Volcanic and magmatic processes at a young spreading centre in Afar, Ethiopia

David J. Ferguson

Hertford College and the Department of Earth Sciences

University of Oxford

Thesis submitted for the degree of Doctor of Philosophy

7th October 2011

Supervisor: Professor David M. Pyle

"Taking into account the general condition of the area, it is quite improbable that the geology (of Afar) will ever be systematically studied"

Dainelli, 1943

Abstract

Volcanic and magmatic processes at a young spreading centre in Afar, Ethiopia

David J. Ferguson

The Dabbahu-Manda Hararo rift segment is a ~25 x 60 km rift zone in Afar, Ethiopia, where a series of axial dyke intrusions has recently occurred. Basaltic eruptions associated with individual dyking events between 2007-2010 have been fed from fissures along the rift axis and been relatively short-lived events lasting less than 60 hours. The volume of melt delivered to the rift surface by these eruptions has been a minor component of the total melt volume supplied to the shallow crust since the onset of the active rifting phase in 2005 and the current intruded to erupted melt ratio for the 2005-2010 period is ~260:1. This is below typical values for magmatic rift zones and may suggest that further volcanism is likely to occur before this activity ceases. $^{40}Ar/^{39}Ar$ geochronology of basaltic lavas from the flank of the rift and from a region of off-axis volcanism to the west of the rift zone gives ages of 25 – 450 ka. These constrain the development of a prominent axial graben in the northern part of the rift to < 30 ka and based on the age-distribution of lavas across the rift flank suggests that volcanism has been focused to the present neo-volcanic zone for at least 200 ka. Geochemical and isotopic constraints on melt generation suggest ~4-6 % partial melting of fertile mantle beneath rift at depth of ~100-75 km. Lavas erupted at the rift axis and from off-axis volcanoes are derived from a common mantle source, however, axial lavas are shown to represent slightly greater extents of partial melting suggesting a focused mantle melting anomaly, such as those seen at ocean ridges, is forming beneath the rift zone.

Extended Abstract

Volcanic and magmatic processes at a young spreading centre in Afar, Ethiopia

David J. Ferguson

Continental break-up is an intrinsic part of the plate tectonic model and leads to the formation of new ocean basins. Magmatism is a common feature of many continental rift zones and is often cited as a key ingredient in the successful evolution from continental rift to oceanic ridge. However, as relatively few rift systems on the Earth are currently at this transitional stage many of the magmatic and tectonic process associated with late-stage rift evolution remain unclear. This thesis examines volcanic and magmatic processes at a mature rift zone in Afar, Ethiopia, and uses geochemical and geochronological data to constrain the processes leading to the generation, storage and eruption of magma and the links between these and the tectonic evolution of the rift zone.

The Dabbahu-Manda Hararo (DMH) rift segment is a ~25 x 60 km mature rift zone in central Afar and since 2005 has been undergoing an active phase of magmatic rifting. The rift zone is almost entirely floored by basaltic lavas and has an overall morphology similar to a slow spreading oceanic ridge. Recent dyke intrusions have demonstrated that a significant portion of extension here is accommodated by magma intrusion along the rift axis. The central part of the segment features a silicic volcano, the Ado Ale volcanic complex (AVC), which has been rifted apart into various isolated fragments. On the western margin of the rift is a separate volcanic lineation, which is oriented approximately perpendicular to the trend of the DMH rift axis. This is primarily composed of two volcanoes, the mostly rhyolitic Badi volcano and an elongate edifice called Dabbayra formed of more basaltic material.

Since the onset of the current rifting phase in 2005 three basaltic dyke-fed fissure eruptions have occurred along the rift axis in 2007, 2009 and 2010. Field and remote sensing observations allow the physical characteristics of these eruptions to be evaluated and comparisons made with other fissure systems. All the eruptions were relatively short-lived events lasting less than 60 hours. The volume of magma emplaced on the rift surface by these eruptions represents a relatively minor component of the total melt volume supplied to the shallow crust, the bulk of which has been emplaced intrusively. Using geodetic estimates of dyke volumes, the current ratio of intruded to erupted melt since 2005 is ~260:1, far below typical values for magmatic rift zones. This suggests that further volcanism may be likely to occur before this phase of activity ceases.

The formation of the DMH rift segment is linked to the geologically recent localisation of strain accommodation along the developing Afro-Arabian plate boundary in Afar.

$^{40}Ar/^{39}Ar$ geochronological analyses of basaltic lavas sampled from the flank of the rift zone and from the Badi and Dabbayra volcanoes on the rift margin record ages of ~30 - 200 ka and ~25-450 ka respectively. The central part of the rift zone currently features a prominent axial graben, which is offset by large fault scarps 30-60 m high. New radiometric ages for lavas cut by these faults constrain the formation of the eastern fault scarp to < 30 ka, giving a (minimum) time averaged slip rate for the large graben bounding fault of ~1 mm yr^{-1}. Although deformation of the lavas by faulting prohibits the identification of paleo-fissures and the volcanic architecture of the study area is unknown, the rift-flank lavas shows a consistent increase in age with distance from the axial graben. When compared to the location of the current magmatic axis, identified from accumulations of young lavas and the recent dyke intrusions, the age-distance profile for lavas since ~200 ka is consistent with emplacement in this neo-volcanic zone and transport outwards at ~10 mm yr^{-1}, similar to the total Afro-Arabian (half) extension rate. The implication of the observed age-distance profile is that the current neo-volcanic zone has been stable in its present location for at least ~200 ka and that melts have therefore been focused along the rift axis over this time, indicating an important stage of rift maturity. It also implies that over this period the relatively narrow DMH rift zone has been accommodating essentially all Afro-Arabian extension. In the northern sector of the rift where these samples were collected the location of the magmatic axis is ~1 km east of the centre of the graben (the 'topographic' axis) and this suggests a decoupling between rifting processes and the development of the graben morphology. The new $^{40}Ar/^{39}Ar$ ages for lavas erupted at the off-rift volcanoes show no consistent age-distance pattern and demonstrate that this region has maintained a constant melt supply over the last ~500 ka, which based on the orientation of the volcanic fissures here is not in equilibrium with the regional stress field.

Geochemical and isotopic analyses of basaltic and silicic lavas provide information on the processes of melt generation and storage beneath both the central rift zone and the off-rift volcanoes. Sr, Nd and Pb isotopic compositions and trace element data suggests that all the magmas erupted across the area are derived from a common fertile mantle source and all show enrichments in incompatible trace elements (i.e. Ba, Nb, La etc) relative to typical mid-ocean ridge basalts. However, important geochemical variations are observed between lava erupted in the two locations. Lavas from the off-rift volcanoes show greater enrichments in incompatible trace elements and greater fractionations between elements of high to lower incompatibility relative to the axial lavas. These variations are consistent with differences in melting regime and these are investigated using major and trace element modelling. Estimations of primary melt compositions made by correcting major element analyses for the effects of crystal fractionation suggest that melting beneath this region occurs in a relatively deep region from ~3.3 GPa to 2.6 GPa, equal to depths of ~100 to 75 km. This result is tested by modelling the beahviour of trace elements sensitive to the pressure and extent of melting. Modelling of the Ce/Yb ratios in partial melts of upwelling peridotite suggests that the observed lava compositions require an initial melt fraction of ~3 % to be generated in the presence of garnet to create the observed fractionations. Modelling of

trace element ratios which are sensitive to extent of melting (i.e. Sm/La and Tb/Yb), suggest that the total melt fraction generated from mantle upwelling beneath the DMH rift is ~4-6 % with slightly higher extents of melting beneath the rift axis, compared to the off-axis volcanoes. These results are in good agreement with the major element evidence on melting processes and it is proposed that that the relative enrichment in incompatible trace elements observed in the off-axis lavas is the result of the magmas that feed this region being separated from the mantle residue at slightly greater depths where total melt fractions are lower. This provides evidence that a focused mantle upwelling, of the kind observed at many mid-ocean ridges, may have begun to develop beneath the axis of the DMH segment.

Major element trends also vary between lavas from the on and off-axis region and shows that they have followed different fractionation paths. Based on modelling of liquid compositions produced by fractionation of the estimated primary melt compositions and comparisons with experimental mineral-melt equilibria data it is proposed that lavas erupted at the rift axis have undergone a two stage fractionation process, where primary melts are initially modified in a deep melt storage region at ~1.3 GPa (45 km depth) and then in a shallow storage region beneath the rift axis at ~0.3 GPa (10 km depth). It is from this shallow chamber that recent dykes have been intruded. For the off-axis lavas, a single stage isobaric fractionation process is proposed with primary melts stalling at the base of the crust (at ~0.6 GPa) (25 km depth). Geochemical data from silicic lavas (peralkaline trachytes and rhyolites) suggest that these evolved melts were derived from extensive low-pressure fractionation of the basalt magmas. In general, the results of the petrogenetic model agree well with recent geophysical data on the distribution of partial melt in the crust and upper mantle beneath the rift zone.

Overall, the data and discussions presented in this thesis provide a new understanding of the magmatic and volcanic processes associated with this transitional rift segment and aid the characterisation of magmatic rift systems close to the continent-ocean transition.

Acknowledgments

Firstly, I would like to thank David Pyle who has been my principal advisor at the University of Oxford and has guided me through all aspects of this project. He has provided valuable ideas and support and has allowed me the freedom to collaborate with other scientists and to develop my own ideas. I am also very grateful to my other advisors, Jon Blundy at the University of Bristol and Clive Oppenheimer at the University of Cambridge, who have both provided me with invaluable advice and support during various parts of this project. While doing this research I have been very fortunate to be a member of a large interdisciplinary research group – The Afar Rift Consortium – and I am very grateful to various members of this group for their help, support, useful discussions, lively research meetings and a very enjoyable distillery visit. In particular I would like to acknowledge support from my fellow Afar PhD students Talfan Barnie and Lorraine Field and also Gezahegn Yirgu, Tim Wright, James Hammond, Jacqui Haughton, Elias Lewi, Barbara Hofmann, Ian Hamling, Derek Keir, Julie Rowland, Mohammed Adem and Charlotte Vye for their help with fieldwork, remote-sensing analysis and sharing their ideas and data with me. I would also like to thank everyone else who helped make fieldwork in Afar both possible and such a great experience.

Andy Calvert at the USGS in Menlo Park, CA, has been very generous with his time and expertise and the geochronological data in this thesis would not exist without his help. Ken Sims at the University of Wyoming allowed me to visit his lab to prepare samples for isotopic analyses and Jurek Blusztajn at Wood's Hole Oceanographic Institution provided invaluable help with the measurements. I have been very fortunate to collaborate with all three of these scientists and they have all taught me a great deal about rock analyses and igneous geochemistry. I would also like to thank Chris Waters at the University of Wyoming for his help and Steve Wyatt, Jeremy Hyde and Norman Charnley in Oxford for their assistance with using lab facilities there. Nick Marsh helped with the XRF at the University of Leicester and Charles Knaack with the ICP-MS analyses at Washington State University.

Finally, I would like to acknowledge Naomi Matthews, Giovanni Fontana, Seb Watt, John Elliott, Susi Ebmeier, Paul Savage and the many others who helped make Oxford postgrad life great fun and who together comprised a first-rate Frisbee team. I am also very grateful to my Dad, who has been very supportive throughout all my studies, and of course to Hannah, without whom this thesis would probably never have been finished.

Table of contents

CHAPTER 4

List of figures

List of tables

Chapter 1

Introduction and geological background

1.1 Introduction

Rifting of the crust is a fundamental geological process that continually re-shapes the Earth's surface. Rift zones scar almost all continental regions and two-thirds of the Earth's outer shell is composed of oceanic lithosphere, formed along the mid-ocean ridge system. The transitional process from a continental rift zone to an oceanic spreading ridge is therefore central to the plate tectonic model. Refining models of late-stage rift evolution requires observational constraints from studies on active rift systems close to the continental-oceanic transition, however rift systems at this stage in their development are not a common feature of the present day Earth's terrestrial tectonics. The Afar depression in northern Ethiopia (Fig 1.1) is a unique region of late-stage continental break-up, where rifting processes associated with the advanced stages of rift evolution can be observed and models of rift development tested (Tazieff et al., 1972; Mohr, 1978; Barberi et al., 1972, 1974; Makris and Ginzburg, 1987; Hayward and Ebinger, 1996; Bastow and Keir, 2011). In Afar rifting along on-land sections of the Red Sea and Gulf of Aden rift systems occurs across narrow magmatic rift segments, considered to be proto-oceanic ridges (Hayward and Ebinger, 1996). This thesis examines the volcanic and magmatic processes associated with one such magmatic rift segment in central Afar, the Dabbahu-Manda Hararo (DMH) magmatic segment (Fig 1.2). It presents geochemical and geochronological data for basaltic lavas erupted along this rift zone and explores ideas relating to the generation and eruption of magma at an embryonic spreading centre and the implications of this new data for rift evolution in

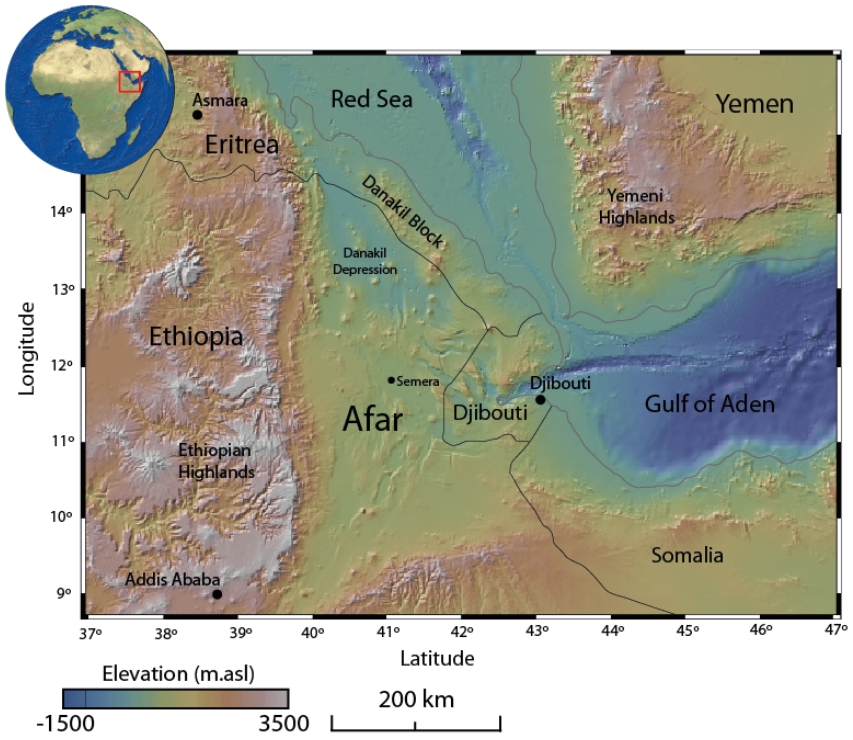

Figure 1.1. Topographic map of northeast Africa. Afar is a triangular shaped low-elevation depression covering parts of Ethiopia, Eritrea, Djibouti and Somalia. The mean elevation decreases northwards and much of the Danakil region in northern Afar lies below sea level

Afar. The DMH rift segment is the location of the largest recorded phase of magmatic rifting, which began in September 2005 and involved a series of ~14 dyke intrusions, several volcanic eruptions and the largest rates of crustal extension ever observed (Ebinger et al., 2010).

1.1.2 Layout of this thesis

- The latter part of this chapter contains important relevant background information on the geology and tectonics of Afar and also a summary of the recent magmatic rifting activity observed in the field area since 2005.
- Chapter 2 presents a overview of the volcanic geology of the field area, the DMH rift segment, which has not been described before in detail.
- Chapter 3 examines the physical characteristics of recent basaltic volcanism (2007-2010) in the DMH rift segment and investigates the general relation between fissural eruptions and magmatic rifting.

- Chapter 4 presents $^{39}Ar/^{40}Ar$ geochronological data for basaltic lavas from the central part of the rift zone and also an adjacent volcanic region and examines the implications of the age data for the formation of the rift segment and for the evolution of rifting in central Afar.
- Chapter 5 presents major and trace element and radiogenic isotope data for basaltic lavas erupted across the field area and develops a model of magma generation and supply to the rift zone and off-axis volcanoes.
- Chapter 6 presents a brief overview of the geochemistry of compositionally evolved melts erupted across the study area and discusses evidence for magmatic differentiation processes.
- Chapter 7 summarizes the main findings of this thesis and outlines potential avenues for future research.

1.2 Afar

Afar is a vast (~200, 000 km^2) arid depression covering most of northeastern Ethiopia and including parts of Eritrea and Djibouti (Fig 1.1). It has the highest recorded annual average daily temperatures on Earth (34°C) and is one of the most sparsely populated places on Earth (~14 people per km^2). The majority of the regions inhabitants are ethnically, socially and linguistically distinct from the rest of the Ethiopian population and many still maintain a semi-nomadic lifestyle. Southern Afar is well known for the discovery of the earliest known *hominid* fossils, preserved in the sediments of the Awash valley (Wolde-Gabriel et al., 2001; White et al., 2009) and the region was an important location for human evolution. Interesting, though very dated, accounts of early European expeditions into Afar in the 1920's and 1930's can be found in memoirs of the British explorers W. Thesiger (Thesiger, 1998) and L. M Nesbitt (Nesbitt, 1935), the latter of whom gave his memoirs the dramatic title "Hell-hole of creation".

Although Afar is an exceptional location for studies on continental break-up and rifting processes it has been relatively un-explored by modern geoscientists. This is largely the result of political instability in Afar and Ethiopia and, importantly, the long-standing, and ongoing, border dispute with neighboring Eritrea, which gained independence from Ethiopia in 1993. The logistical challenges of field campaigns in the harsh desert environment have probably also inhibited scientific studies and many of the samples collected during this project would not have been obtained without transportation via helicopter. After the end the most recent period of active conflict between Ethiopia and Eritrea, the Ethiopian-Eritrean War, which lasted from 1998 to 2000, most of Ethiopian controlled Afar has again become accessible to outside visitors.

1.3 Overview of the geology and tectonics of Afar

This section presents important background information on the tectonic and geodynamic setting of Afar. It provides an overview of the geology of the depression and a detailed description of Quaternary volcanism and volcano-tectonics associated with rifting. It also outlines some concepts relating to rift evolution, which are relevant to understanding the geology of Afar and for which the data presented in later chapters has implications.

1.3.1 Regional tectonics

An outline of the regional tectonics of Afar is shown in Fig 1.2. A sketch geological map outlining the important stratigraphic divisions within Afar is shown in Fig 1.3. The depression lies at the intersection between the Nubian, Somalian and Arabian

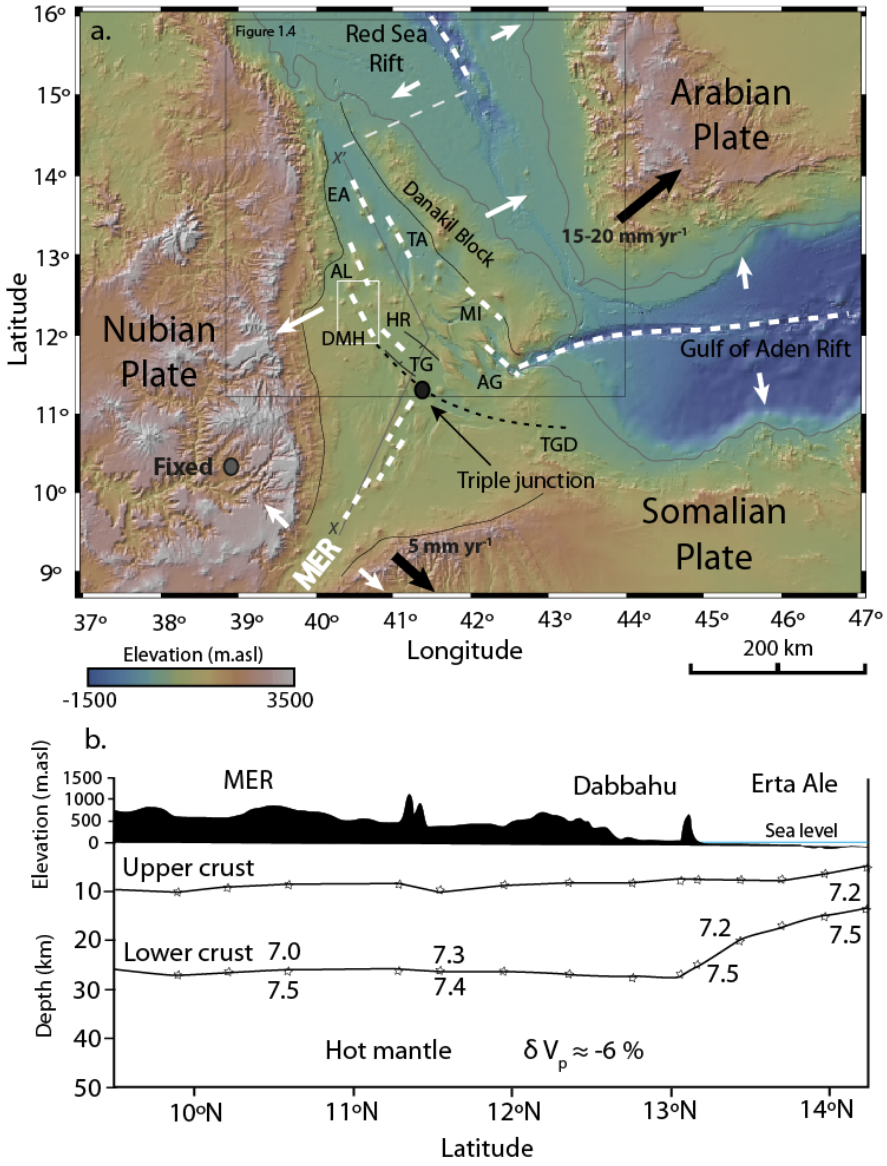

Figure 1.2 Overview of the tectonic setting of Afar. (a) Afar marks the triple junction between the Red Sea, Gulf of Aden and Main Ethiopian Rift systems, which separate the Nubian, Arabian and Somalian plates. Extensional processes in Afar are dominated by the ~NE directed removal of Arabia from Africa. Rifting near the triple junction in all three rift systems is characterised by focused extension along axial rift segments (marked by the white dashed lines). Magmatic rift segments formed along the on-land Red Sea and Gulf of Aden rift systems are the Erta Ale (EA), Tat Ali (TA), Alayta (AL), Dabbahu-Manda Hararo (DMH), Hararo Rift (HR), Asal-Ghoubbet (AG) and Manda Inakir (MI) segments. The Tendaho Graben (TG) is a prominent fault bounded graben at the southern end of the Red Sea rift system. The white box marks the general location of field area for this project, the DMH rift segment. Plate motions are from Vigny et al (2006) and McClusky et al (2010) and this geodetic data indicates that all Afro-Arabian extension is accommodated within Afar. Triple junction location is drawn after Wolfenden et al., (2005). (b) Crustal thickness profile through Afar from Bastow and Keir (2011) and based on data by Makris and Ginzburg (1987). The location of the profile is shown as a grey line from *X-X'* in the map figure. The thickness of the upper and lower crust is largely maintained from the northern MER through Afar and only decreases in the northern part of the depression around Erta Ale.

plates, where the East African, Red Sea and Gulf of Aden rift systems meet (Tazieff et al., 1972; Mohr, 1978). Rifting in the Red Sea was initiated around ~30 Ma (McKenzie et al., 1970) and followed the emplacement of a flood basalt province (Mohr, 1983). Extension along most of the length of the Red Sea and Gulf of Aden systems has largely progressed to seafloor spreading while the Main Ethiopian Rift (MER) is still formed largely from stretched and highly intruded continental lithosphere (Hayward and Ebinger, 1996; Daly et al., 2008). The MER runs northwards into Afar where the triangular depression opens out and becomes dominated by the tectonic and magmatic structures relating to the two oceanic systems.

The rift zones in Afar represent a transitional stage between the continental rift system to the south and the oceanic ridges to the north (Red Sea) and northeast (Gulf of Aden) (Makris and Ginzburg, 1986). On its eastern side the depression is bordered by the uplifted plateau of the Ethiopian highlands, composed of the remnants of the Cenozoic flood basalt province which were erupted onto the neo-Proterozoic basement of the Arabian-Nubian shield, the Pan-African crust (Mohr, 1983). Corresponding basaltic units are found in the Yemeni highlands on the eastern margin of the Red Sea. In Ethiopia, the highlands rise to 4500 metres while Afar itself has an average elevation of 200 m and in its northern region, the Danakil depression, descends to 120 metres below sea level. To the east the depression is bounded by the NNW oriented Danakil block, an isolated and rotated fragment of stretched pre-rift crust and trap basalts that rises to elevations of >2 km (Eagles et al., 2002), and to the south by the Somalian plateau. Both are similar in composition to the Ethiopian highlands, though with a thinner basaltic succession (Mohr, 1978). An important factor in the opening of the depression over the last ~9 Ma is the rotation of the rigid Danakil block. This has become isolated

as the locus of rifting in the southern red Sea migrated westwards and has been rotating independently of Africa and Arabia for at least 3 Ma (Eagles et al., 2002; McClusky et al., 2010). At its northern end the Danakil block marks the southwards bifurcation of the Red Sea rift between the oceanic section and the on-land Afar lineation (Fig 1.2). Further information on the tectonic setting of Afar can be found in a recent review by Beyene and Abdelsalam (2005). Below two important features of the tectonic/geodynamic setting of Afar are discussed in more detail: the Afar plume/hotspot and the nature of the Afar crust.

1.3.1.1 The Afar Plume/hot spot

The pre-rift volcanic history of northeast Africa and Arabia is dominated by the eruption of significant volumes (in Ethiopia ~350,000 km^3) of predominantly basaltic lavas (Mohr, 1983). Attributed by many authors to be the consequence of a mantle plume impinging upon the African lithosphere (Schilling, 1973; Morgan, 1972; Richards et al., 1979; Mohr, 1983; Pik et al 1998, 1999; Hofmann et al., 1997; Ebinger and Sleep, 1998), the original lava pile covered an area of over 600,000 km^2 and reached a thickness of ~2 km (Mohr and Zanettin, 1988; Pik et al., 1998). Initial K-Ar age constraints by Berhe et al., (1987) suggested three prolonged periods of emplacement for the basalt series between 50-40 Ma, 40-30 Ma and 30-21 Ma. However, more recent and more accurate $^{40}Ar/^{39}Ar$ analyses have indicated a much shorter emplacement period of ~1 Ma at around 30 Ma (Hofmann et al., 1997). Although the greatest volumes of lava were erupted in the region that now forms the Ethiopian plateau (Fig 1.3), Cenozoic volcanism was also widespread across North Africa. The spatial and chemical variability observed in these Cenozoic volcanic rocks has led to speculation by various authors on the exact number of distinct plumes/thermal anomalies present below the lithosphere (e.g. Ebinger and Sleep, 1998;

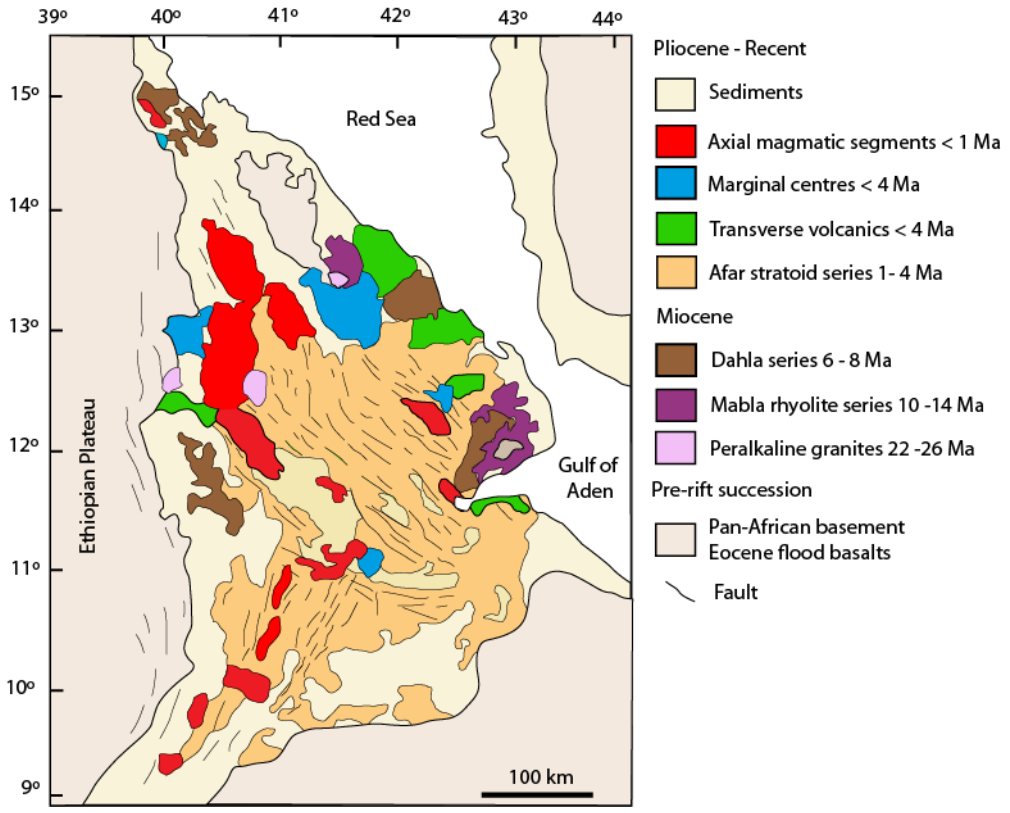

Figure 1.3 Summary geological map of Afar showing important stratigraphic divisions. Recent volcanism has been focused along axial magmatic segment along the axes of rift systems and transverse/marginal zones around the margins of the depression. Map partly re-drawn from Beyene and Abdelsalam (2005) and is primarily based on the geological map by CNR-CNRS, 1973.

George et al., 1998; Ritsema et al., 1999; Gurnis et al., 2000; King and Ritsema, 2000; Davis and Slack, 2002; Pik et al., 2006; Rogers, 2006; Rogers et al., 2002). Pik et al., (2006) for example used isotopic evidence to infer the existence of two distinct plumes sourced from varying depths, whereas modelling by Ebinger and Sleep (1998) suggested the possibility of one large thermal anomaly with melt channeled to distal regions along lithospheric discontinuities. However, notwithstanding on-going debates on the physical and/or chemical nature of the African plume(s), it has been well established that a large melting anomaly centred around the present location of the Afar region led to the rapid emplacement of significant volumes of lavas around 30 Ma and that this preceded the onset of rifting. Similar to other flood basalt provinces causal links have been made therefore between the Cenozoic volcanism in North Africa and

the initiation of continental break-up and formation of the triple junction (Courtillot et al., 1999; Menzies et al., 2002; Wolfenden et al., 2005).

The geochemical character of the Afar plume or melting anomaly has largely been established through isotopic data for lavas from Ethiopia and Yemen. Using ratio-ratio plots of various isotopic systems (e.g. $^{87/86}$Sr vs. $^{144/143}$Nd; $^{87/86}$Sr vs. $^{206/204}$Pb; $^{144/143}$Nd vs. $^{207/204}$Pb) several authors have identified a source component considered to represent either the Afar plume or some other distinct mantle reservoir (Betton and Civetta, 1984; Hart et al., 1989; Barrat et al., 1990, 1993, 1998; Vidal et al., 1991; Schilling et al., 1992; Chazot and Bertrand, 1993; Deniel et al., 1994; Baker et al., 1996; Marty et al., 1996; Pik et al., 1998, 1999, 2006; Kieffer et al., 2004; Furman et al., 2006; Rogers, 2006). However, petrogenetic interpretations of isotopic, and other geochemical, datasets have typically also invoked inputs from other source components. For those studies where a plume origin is considered, contamination of the deep enriched plume source by upper mantle and crustal components has been envisaged to explain deviations in magma chemistry from the suspected 'Afar plume' composition (Schilling et al., 1973, 1992; Vidal et al., 1991; Deniel et al., 1994; Barrat et al., 1990; Marty et al., 1996; Pik et al., 1999; Bertrand et al., 2003; Furman et al., 2006). Alternative non-plume interpretations for the genesis of Afar lavas involve a vertically zoned lithosphere with an evolving bulk composition due to the increasing attenuation of different layers during rifting (Barberi et al., 1980; Betton and Civetta, 1984; Hart et al., 1989).

The complications in interpreting geochemical data from north-east Africa with respect to magma source regions arise partly due to the competing nature of the processes being

considered; that is, an evolving rift system with temporal gradients in source chemistry with or without input from a deep long-lived plume source. A clear example of this is the chemical gradient (in isotopic and trace element concentrations) observed between the oceanic rifts of the Red Sea and Gulf of Aden and the on-land rift lavas from Afar. These have been interpreted to reflect both the distance from the plume head (e.g. Schilling et al. 1973) and the on-going erosion, and therefore decreasing involvement, of the lithosphere as rifting progresses (e.g. Hart et al. 1989). A primary observation, however, that has emerged from the isotopic studies discussed here is that lavas from Afar have distinct characteristics with respect to radiogenic isotopes of Sr, Nd, He and (to a lesser extent) Pb compared to basalts erupted in the Red Sea and Gulf of Aden array and these show similarity to some pre-rift flood basalts.

1.3.1.2 The Afar crust

A key constraint in understanding the tectonic and magmatic processes operating in Afar is knowledge of the thickness, structure and composition of the crust. The thickness and origin of the Afar crust clearly has important implications for rifting processes, while petrogenetic studies must consider potential magma sources, storage and contaminants. Existing knowledge of the Afar crust largely stems from data gathered during a gravimetric and active-source seismic profile measured across Afar in the 1970's (Berckhemer et al., 1975; Makris et al., 1975; Behle et al., 1975; Makris and Ginzburg, 1987; Bastow and Keir, 2011). More recently, the seismic array installed across Afar and the Ethiopian highlands following the onset of the rifting activity in 2005 has provided new datasets for seismic tomography (e.g. Hammond et al., 2011).

Fig 1.2b shows variations in crustal thickness and structure between the Ethiopian plateau, the northern MER, Afar and the Red Sea (profile shown in Fig 1.2). The

Ethiopian highlands region has a crustal thickness of ~44 km which can be seen to decrease significantly across the boundary scarp into Afar. Beneath southern and central Afar the crust is ~26 km thick (Makris and Ginzburg, 1987), while the thinnest/most attenuated crust is found north of ~13.5 °N, around the Erta Ale rift system, which is ~14 km thick. It is only in the northern part of the depression therefore that crustal thicknesses approximating that of the oceanic lithosphere are found. Interpretations of seismic refraction and receiver function data from Afar have described the crust using a three-layered model, comprising a cover layer of sediments and volcanics sitting above an upper and lower crust (Makris and Ginzburg, 1987; Prodehl and Mechie, 1991; Mackenzie et al., 2005; Maguire et al., 2006; Hammond et al. 2011). The surface layer is composed of siliciclastic sediments, evaporites and lava flows and is typically a few km's thick, although local thicknesses of up to 5 km are observed. Below this cover layer is the upper crust, which is interpreted to be composed of stretched pre-rift Pan-African crystalline basement (Makris and Ginzburg, 1987; Mackenzie et al., 2005; Maguire et al., 2006). This varies in thickness from ~8 km in the northern MER, ~4 km in southern and central Afar and is ~2 km north of 13.5 °N (Fig 1.2b). In comparison, the un-stretched Pan-African crust beneath the Ethiopian highlands is ~20-25 km thick.

The thinning observed in the upper crust from the MER into southern Afar is not matched in the lower crust which maintains an almost constant thickness of ~18 km along the MER into southern Afar. In Afar itself some thinning is observed, decreasing from a thickness of ~16 km in the south to ~10 km in the north (Makris and Ginzburg, 1987; Hammond et al. 2011). Makris and Ginzburg (1986) interpreted this lower crustal layer to be new igneous material, whose thickness from the MER to Afar is conserved

by the addition of new magmatic material. The ratio of seismic wave-speeds (Vp/Vs) in the lower crust is uniformly high across Afar (Vp/Vs > 2) and strongly suggests the presence of a melt phase in this layer (Hammond et al., 2011). Seismic wave speeds in the upper mantle underlying this crust show it to be some of the slowest, and therefore hottest, mantle material worldwide (Bastow et al., 2008). A recent study by Hammond et al (2011) has used receiver function analysis to map variations in crustal thickness and Vp/Vs across Afar. These results are in agreement with the crustal models of earlier work (e.g. Makris and Ginzburg, 1986) but provide higher spatial resolution to variations in thickness and Vp/Vs and identify zones of thinner crust/higher Vp/Vs associated with the axis of the on-land Red Sea rift system.

1.3.2 Geology of Afar

This section provides a brief overview of the surface geology of Afar, with particular focus on the volcanic rocks associated with the most recent phase of rifting. A comprehensive survey of the geology of Afar was first published in 1973, following joint Italian-French mapping expeditions (CNR-CNRS, 1973) and the maps and publications produced by members of this group (led by F. Barberi and J. Varet) have largely formed the basis for all subsequent studies on the geology and/or tectonics of Afar. Currently, a new mapping effort is underway led by the British Geological Survey, which will utilize the wealth of remote sensing data that has become available since the 1970's. The surface geology of Afar is ideally suited to observation by remote sensing imagery, as there is relatively little vegetation or sediment cover and when combined with field observations, high-resolution spectral and/or morphological datasets can provide detailed information on otherwise inaccessible areas. It is worth noting, however, that much of the region has either never or has only briefly been visited by geologists.

1.3.2.1 Overview of surface geology

A summary geological map of Afar is shown in Fig 1.3. The floor of the depression is almost entirely covered by volcanic rocks, with the exception of local accumulations of alluvial or aeolian sediments or saline evaporates (CNR-CNRS, 1973; Varet, 1978). The pre-rift neo-Proterozoic basement rocks of the Arabian-Nubian shield are only visible in the faulted marginal scarps separating Afar from the Ethiopian Highland plateau and the Danakil block. Limited outcrops of Miocene volcanic rocks are found around the margins of the depression. The most extensive stratigraphic unit is a series of basaltic sheet flows termed the 'stratoid lavas', which are exposed over most of central Afar and consist primarily of fissural basaltic lava flows, accumulations of which reach thicknesses of up to 1500 m (Barberi et al., 1974; Kidane et al., 2003; Lahitte et al., 2003b). These lavas were erupted from fissures oriented either NE-SW in southern Afar, aligned with extension in the northern MER, or NW-SE in central Afar, aligned with the axes of the Red Sea and Aden rift systems. Several silicic volcanoes, with associated ignimbrite deposits, are also found within the stratoid succession. K-Ar ages for basaltic stratoid samples constrain the main period of emplacement to between 1-3 Ma (Barberi et al., 1975; Lahitte et al., 2003b; Kidane et al., 2003). In central Afar this phase of activity has linked to the formation of a series of grabens, such as the Tendaho and Dobi grabens (Acocella et al., 2008; Acocella, 2010).

1.3.2.2 Quaternary volcano-tectonic structures

Following the main phase of stratoid emplacement volcanism in Afar became more closely associated with discrete zones of localised volcanic-tectonic activity. Fig 1.4 shows the orientation of prominent volcanic lineaments in Afar and the locations of significant Quaternary volcanoes. The most important of volcanic-tectonic structures are the axial rift zones or segments formed along the axes of the Red Sea or Gulf of

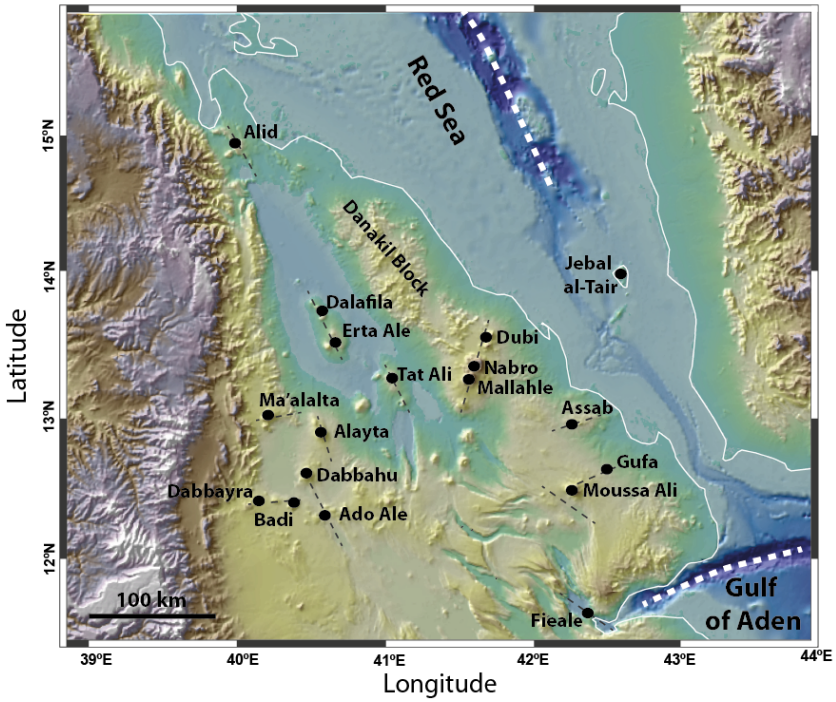

Figure 1.4 Location of prominent Quaternary volcanoes in Afar. Recent volcanism is closely associated with two classes of tectonic structures: axial rift segment and marginal transverse volcanic ranges. See text for further discussions.

Aden rift systems (Barberi et al., 1972; Manighetti et al. 1998; Lahitte et al., 2003). The development of these ~NW-SE trending ~60 x 20 km rift segments (also called axial ranges) marks an important stage of rift evolution as it signifies the localisation of the processes of strain accommodation to narrow zones of faulting and magma intrusion (see section 1.4). In addition to these, recent volcanism has also occurred around the margins of the depression, either along ~EW trending volcanic lineations known as 'transverse structures' or at large eruptive centres termed 'marginal volcanoes' (Barberi et al., 1974).

1.3.2.3 Transverse volcanic zones and marginal centres

The 'transverse' volcanic structures and 'marginal' eruptive centres were first described in detail by Barberi et al (1974) and are found on the margins of the depression (as shown in Fig 1.3). Collectively these terms refer to recent volcanism that is not directly associated with axial rift zones. The structural significance of these volcanic zones and

their relation to the axial rift zones is investigated in chapter 4 (see Fig 4.1 for detailed map). Volcanism in these regions is associated with aligned basaltic cones and volcanoes and also large silicic caldera systems (e.g. Wiart and Oppenheimer, 2005; De Fino et al., 1973). The distinction between 'transverse' and 'marginal' volcanics, as shown in Fig 1.3 is based on the geological map by CNR-CNRS (1973) and Barberi et al (1974) and reflects a general distinction between large individual (silicic) volcanoes versus aligned basaltic cones/fissures. However, as discussed by Wiart and Oppenheimer (2005) and also in further detail in Chapter 4, these divisions are not entirely clear and probably not useful for understanding the volcanic-tectonic significance of transverse/marginal volcanism. Although, unlike the axial volcanic zones, transverse/marginal volcanoes are not directly associated with rifting processes, the volcanic flux associated with these zones is significant and may be equivalent to that from axial volcanism (Wiart and Oppenheimer, 2005).

1.3.2.4 Axial volcanic ranges

The on-land propagation of the oceanic systems has been more prominent along the Red Sea system, which has 5 recognized segments (Erta Ale, Tat Ali, Alayta, Dabbahu-Manda Hararo, Manda-Hararo; Fig 1.2a). The on-land Aden rift consists of only two mature rift segments (Asal-Ghoubbet and Manda Inakir) and several fault-controlled grabens (Vellutini, 1990; Manighetti et al., 2001; Lahitte et al., 2003a). The Asal-Ghoubbet rift zone was the site of a rifting event in 1978, the first intrusion event observed in Afar (Abdallah et al., 1979; Cattin et al., 2005). The magmatic rift segments are defined by accumulations of recent lavas and closely spaced faults and are separated along-axis by transition zones with offsets of ~20 km. There is considerable morphological variation between these, the result of variations in the rates and

morphological consequences of tectonic versus magmatic processes. The Erta Ale rift segment for example, the most northerly on-land segment, has significant along-axis relief, consisting of volcanic cones and a prominent basaltic caldera, which hosts one of the planets few persistently active lava lakes (Oppenheimer and Francis, 1997; 1998; Acocella, 2006). Conversely, the DMH segment, ~100 km to the south, has a well-developed axial graben and is more defined by faulting and fracture than volcanic constructions (Rowland et al., 2007). Immediately north of the DMH, the Alayta rift segment is chiefly dominated by the edifice of the Alayta volcano, while the Tat Ale rift segment has a structure and morphology similar to the Erta Ale segment.

1.3.2.5 Petrology of Afar

Fig 1.5 shows a total-alkali versus silica (TAS) plot for a compilation of Quaternary lavas from across Afar. Overall, the erupted magmas from both the axial rift zones and at the transverse zones/marginal centres have a bimodal basalt-rhyolite compositional distribution. However, a significant volume of lavas with intermediate compositions have also been erupted and these are found both at volcanoes along transverse volcanic zones (e.g. Assab, Dubbi and Dabbayra; Fig 1.4) and at volcanic centres along the axial rift segments (e.g. Dabbahu and Dalafila; Fig 1.4). The Dabbahu volcano is the best studied of these and is notable for having erupted a full basalt to rhyolite compositional series (Barberi et al., 1975; Field, 2011). Intermediate lavas have also been reported from volcanic centres along the Erta rift axial rift segment (Barrat et al., 1998). The data presented in Fig 1.5 represents almost the entire catalogue of published analyses for Afar lavas and is very limited relative to the volume and extent of Quaternary volcanism. On the TAS classification basaltic lavas from axial segments are typically transitional between the alkaline and tholeiitic types identified by

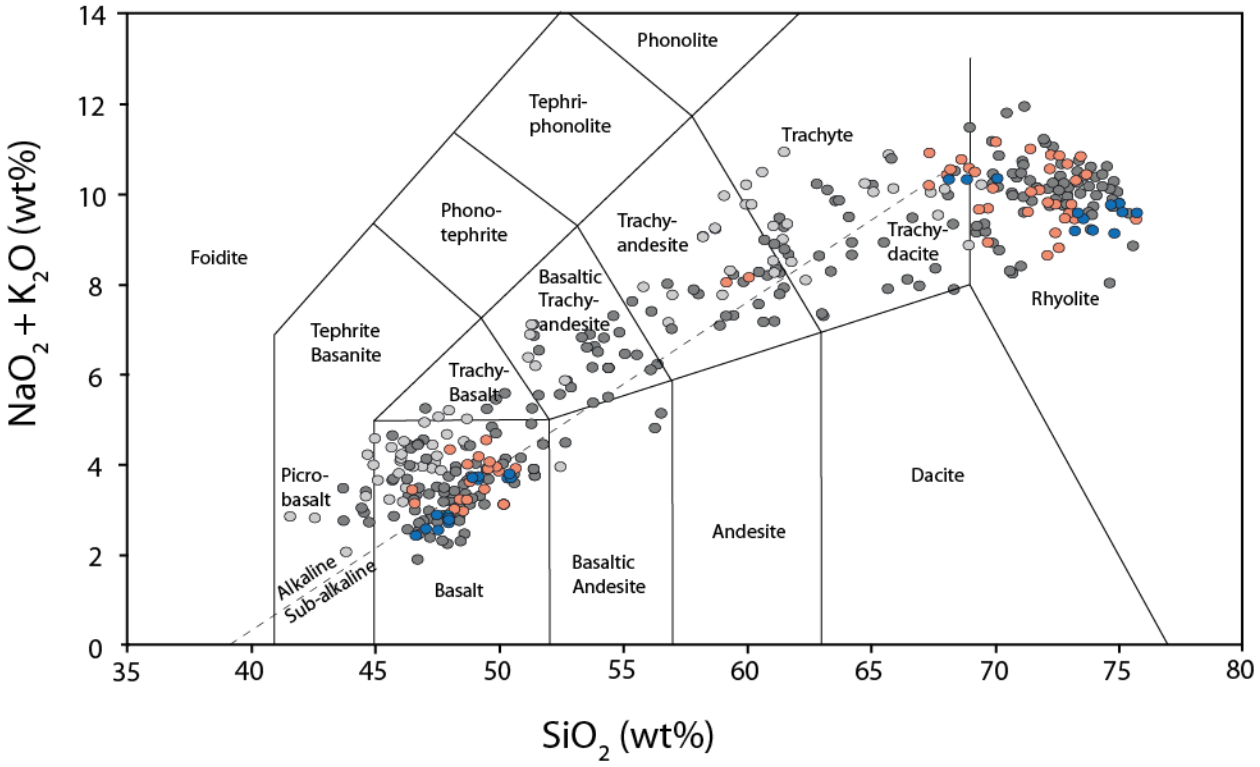

Figure 1.5 Total-Alkali vs. Silica (TAS) plot for lavas erupted across Afar. In general there is a strong bi-modal basalt-rhyolite character to lava compositions, however lava with intermediate compositions are found at several volcanoes located along both axial rift zones (i.e. Dabbahu) and at transverse zones (i.e. Assab). Red and blue symbols indicate lavas analysed in this thesis (red symbols: DMH axial segment, blue symbols: Badi-Dabbayra volcanic region). Dark grey symbols represent lava erupted along axial segment, light grey are for lavas from transverse/marginal volcanic zones. Data sources: Barberi and Varet, 1970; Barberi et al., 1974, 1975; Bizourd et al., 1980; Civetta et al., 1974; De Fino et al., 1978; Deniel et al., 1994; Barrat et al., 1998, 2003; Wiart and Oppenheimer, 2000; Field, 2011; and this study. Alkaline-subalkaline divide after Macdonald, 1968.

MacDonald (1968), while basalts erupted away from the rift axes on the depression margins are slightly more alkaline. Intermediate lavas follow an alkaline trend and cover a broad compositional range from basalt to rhyolite. Rhyolitic lavas are largely peralkaline in compositions (Barberi et al., 1974, 1975; Field, 2011) (i.e. molar Na+K > Al) and following the work of Barberi et al (1975), the Dabbahu volcano became a type locality for generation of peralkaline rhyolites via low-pressure fractionation.

1.3.2.6 Basaltic volcanism

Basaltic lavas are by far the dominant rock type with respect to areal extent and the Quaternary rift zones are almost entirely floored by basaltic flows erupted from fissures

(Barberi et al., 1972). Rates of volcanism are not well constrained along the subaerial Red Sea system, however there appears to be considerable variability in both the time averaged flux and eruption magnitudes between segments. Fissural eruptions in the DMH rift do not seem to typically exceed ~0.02 km^3 and are erupted from fissures <5 km and have flow lengths <1 km (see chapter 3). Conversely the Alayta rift segment, immediately to the north, host a large basaltic fissure-fed flow field covering an area of 30 x 70 km, with flow distances of up to 20 km. Likewise the Erta Ale axial range has abundant evidence for large volume flows with long transport distances. A fissure eruption in the northern part of this segment near the Dalafilla volcano in 2008 erupted 14 km^2 of lava over a 2 day period from fissures ~1 km in length (Pagli et al, 2009). The main Erta Ale edifice has also erupted large volumes of lavas, including at least one caldera-forming event (Acocella, 2006). The lava lake within this caldera last erupted in late 2010 (Field et al., submitted). Both field evidence and the few observations that exist for recent basaltic eruptions (since 2005) in Afar suggest a northward increase in the time-averaged eruption volumes along rift segments. Bastow and Keir (2011) suggested that this trend represents a pulse of decompression melting produced during late stage crustal thinning at the final stage of rift evolution. Observations of the recent eruptions in the DMH rift (2007-2010) and the general characteristics of basaltic volcanism at slowly extending magmatic rifts are presented and discussed in more detail in chapter 3.

1.3.2.7 Silicic volcanism

Numerous volcanic centres erupting more evolved magma compositions are also found across Afar. Several large caldera complexes with associated ignimbrite deposits, termed ‘marginal-centres’, occur along the border scarps between Afar and the Ethiopian highlands and also at the margins of the Danakil block (Barberi et al., 1974;

Oppenheimer and Wiart, 2000, 2004). Like many of their counterparts in the MER (e.g. Rampey et al., 2010) these large caldera systems remain relatively unstudied, however, remote-sensing studies on the Nabbro volcanic range at the southern end of the Danakil block and the Ma'alalta caldera on the western margin of Afar suggests erupted volumes can be significant (>20 km^3) (Wiart and Oppenheimer, 2005). The largest historical eruption in Africa occurred at the Dubbi volcano in the Nabro range in 1861. During this event, explosive silicic activity was followed by basaltic fire fountains, producing a total erupted lava volume of ~3.5 km^3 and a largely complete basalt-rhyolite lava series (Wiart and Oppenheimer, 2000). This volcano began erupting explosively again in June 2001, producing a ~13 km high ash plume, dispersing ash across NE Africa, and basaltic fire fountains within the main caldera feeding lava down-flank lava flows (Smithsonian Institution, 2011).

Silicic volcanism has also occurred at many eruptive centres located along the axes of the Quaternary rift zones (Barberi et al., 1974; Lahitte et al., 2003ab). Field evidence suggests a dominantly effusive, rather than explosive, emplacement style for the vast majority of the trachytic-rhyolitic flows forming these centres and hypocrystalline and holohyaline textures are commonplace. As with effusive silicic flows and domes elsewhere (e.g. California; Fink, 1983) the basal sections of these flow units, when exposed by faulting or road construction, consist of bedded pumiceous deposits. Flow banding at various scales (a few cm's to several 10's of metres) is also common in many silicic units as is textural banding between layers of varying crystallinity, present at similar wavelengths. Although many of the silicic centres appear to be composed almost entirely of glass rich rhyolitic lavas, more complete basaltic-rhyolitic magma series are found at several volcanoes, such as Dabbahu (Barberi et al., 1975; Field et al.,

submitted) and in parts of the Erta Ale range (Bizourd et al., 1979; Barberi and Varet, 1970). A regional study examining K-Ar ages for basaltic and silicic lavas across Afar by Lahitte et al. (2003ab) has proposed that in each rift graben the emplacement of volcanoes erupting more evolved lava compositions systematically precedes the onset of fissural basaltic activity. They interpret this pattern to signify a causal link between the emplacement of silicic volcanoes and subsequent rift propagation/development. However, it is unclear how mechanically feasible this mode of rift propagation is or what linkages would exist to deeper melting structures.

1.4 Rift evolution in East Africa

Rifting of continental regions and the formation of new ocean basins is a fundamental part of the plate tectonic model. However, understanding of the many of the processes and controls involved in rifting and crustal growth remains an active area of research and debate (e.g. McKenzie, 1978; White and McKenzie, 1989; Buck, 1991; van Wijk et al, 2001; Nielsen & Hopper, 2002; Ebinger, 2005). Since the East African rift system is one of the few localities worldwide where rift development can be readily observed many studies on rift evolution have been focused here (e.g. McKenzie et al, 1970; Barberi et al., 1972, 1974; Black et al., 1974; Mohr, 1978; Courtillot et al., 1984; Makris and Ginzburg, 1987; Hayward and Ebinger, 1996; Manighetti et al., 1997; Audin et al., 2001; Lahitte et al, 2003ab; Bastow et al., 2005, 2008; Ebinger, 2005; Kendall et al, 2005; Wolfenden et al, 2005; Buck, 2006; Casey et al., 2006; Keir et al., 2006; Rooney et al., 2007, 2010, 2011; Corti, 2008; Beutel et al., 2010; Bastow and Keir, 2011; Keir et al., 2011). Models that accurately explain the development of the East African rift systems must explain the array of rift-related phenomena observed along strike from the continental rifts in the south to oceanic ridges in the north. These include variations in volcanism, magmatism, magma chemistry, faulting, seismicity,

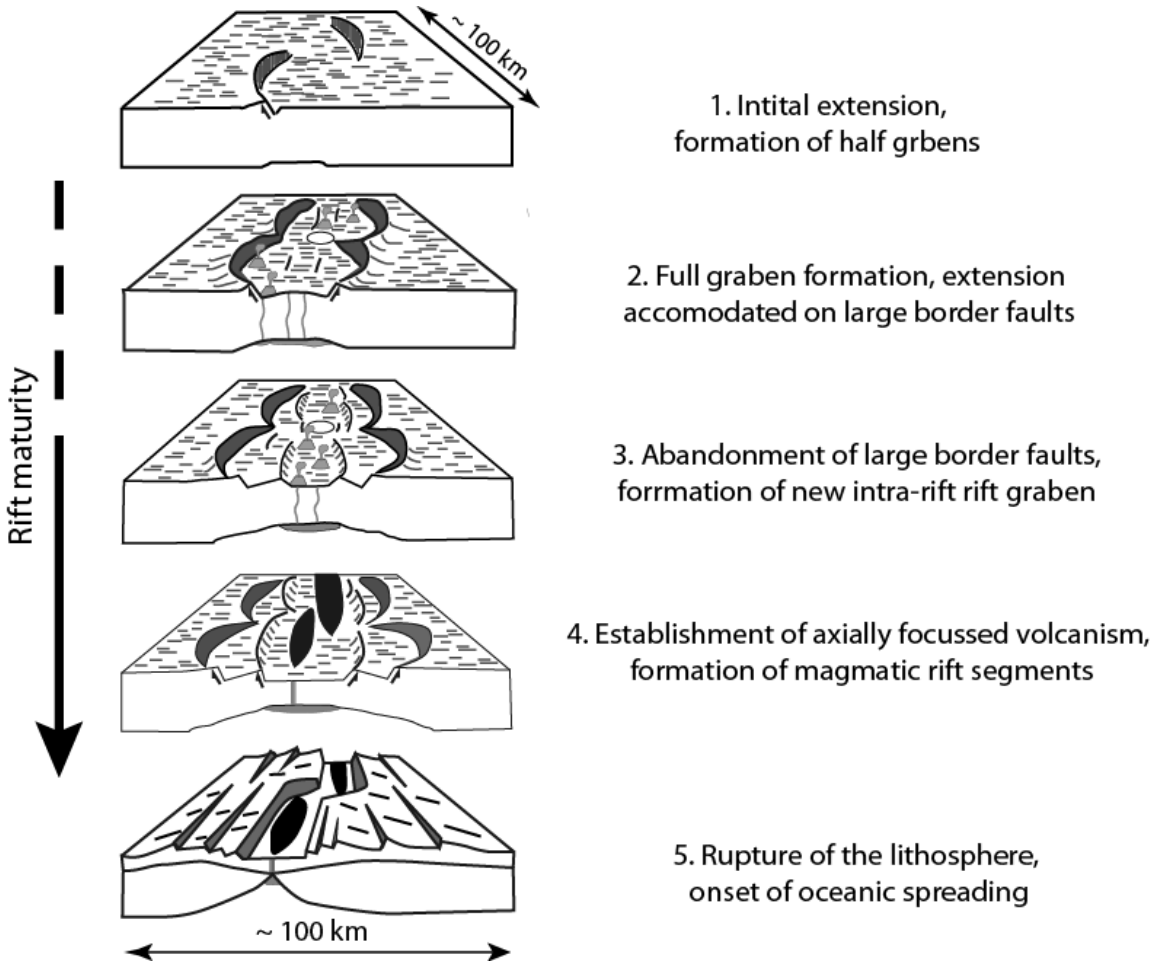

Figure 1.6 Schematic model of rift evolution by Hayward and Ebinger (1996). This conceptual model is based on analysis of rift systems in East Africa. Rift development is marked by a narrowing region of strain accommodation and the abandonment of large faults in favour of smaller closely spaced structures and focused melt intrusion along the rift axis. As rifting proceeds the along-axis structure becomes increasingly segmented, with discrete zones of strain accommodation offset by transverse discontinuities. Oceanic spreading occurs once the lithosphere has been completely attenuated.

crustal thickness and composition and the upper mantle velocity structure. A strong theme to have emerged from recent studies is that in East Africa rift initiation and development appears to have been closely linked to the availability of magma, both for accommodating extension via intrusion and also the thermo-mechanical weakening of the lithosphere (e.g. Ebinger, 2005; Buck, 2004, 2006; Kendall et al., 2010; Rooney et al., 2011).

1.4.1 Models of rift development

A key empirical model describing rift development is that of Hayward and Ebinger (1996), which provides a framework in which to evaluate geological observations of rift related phenomena. Based primarily on structural observations of the along-strike segmentation of rift zones and spatial variations in strain, magmatism, faulting and graben development, this model describes the evolution in the characteristics of rift zones as they mature, shown in Fig 1.6. The key feature of Hayward and Ebinger's analysis is that as the rheology of the lithosphere evolves the response to extension changes from broad grabens and movement on large graben-bounding faults to smaller offset closely spaced fault system within the original graben. A thinner lithosphere causes strain accommodation to be increasingly achieved via magma intrusion rather than faulting, and that the locus of intrusion becomes focused along the new narrow intra-rift rift zone. A temporal trend therefore exists between wide grabens with large offset faults and dispersed volcanism to narrow rift zones, dominated by axial intrusions and only minor faulting. As this model is principally concerned with the shallow crustal processes that result in the formation and maintenance of discrete along axis segments it provides a useful predictive tool that can be used to evaluate geological observations made at a particular rift zone (i.e. the characteristics of faulting and volcanism/magmatism).

A notable observation from seismic refraction studies in Afar is that crustal thickness is largely maintained between the northern MER into southern and central Afar and significant thinning is not observed until ~13 °N (as shown in Fig 1.2) (Makris and Ginzburg, 1987; Hammond et al., 2011). This is in contradiction to the thinning predicted by traditional stretching models (e.g. McKenzie, 1978). As a result stretching

(β) factors in Afar, which plate reconstructions predict to be $\beta \approx 3$ (Eagles et al., 2002) are much lower at $\beta \approx 1.7$. This has been attributed by Bastow and Keir (2011) to be the result of intrusion in accommodating extension rather than stretching and thinning and they propose that the marked increase in crustal thinning north of 13 °N, around the Erta Ale rift segment, is the result of a rapid thinning event that followed successive weakening of the lithosphere from a sustained period of intrusion and underplating. The high volcanic flux observed at the Erta Ale rift segment is interpreted to be the result of a pulse of mantle melting prompted by decompression as the crust thins. The lava pile created during a final thinning event will eventually form the so-called 'seaward-dipping reflectors', a near ubiquitous feature in seismic profiles of passive margins worldwide. The implication for rift evolution is that the continent-ocean transition does not occur until the crust has been substantially weakened by magmatism and in Afar therefore is only crossed north of ~13 °N, where the final stage of lithospheric thinning/erosion is underway.

Finally, it is worth noting that although widely used, including in the thesis, the term rift 'segments' is not always considered an appropriate description for magmatic rift zones in Afar. At mid-ocean ridge segments, where the phrase originates, surface/shallow crustal segmentation is typically matched by discrete upwelling of the upper mantle (e.g. Phipps-Morgan and Chen, 1993). However, seismic evidence from southern Afar clearly shows that a coupled upper mantle velocity structure is not yet present beneath rift segments here (Bastow et al., 2008). Furthermore, the constraints on the nature of the crust (discussed in section 1.3.1) demonstrate that a significant volume of pre-rift material remains (Makris and Ginzburg, 1987; Hammond et al., 2011) and discussions on the tectonics of Afar should describe extension, rather than the often-used 'plate-

separation'. Though essentially semantic, these distinctions can prove important as they shape discussions on the tectonic context of geological observations and although the term segment is used in this thesis it is with these caveats in mind.

1.5 Recent magmatic rifting

The final section of this chapter describes the recent magmatic rifting activity that has been observed since 2005 along the 25 x 60 km Dabbahu-Manda Hararo rift zone in central Afar (Fig 1.7a). The geology of the DMH rift segment is described in detail in Chapter 2. Although dyke intrusion along rift zones is probably the most common of all magmatic process occurring in the shallow crust, it is usually confined to oceanic regions and very few previous observations of active intrusions exist. Rare exceptions to this are the 1975-1984 Krafla rifting phase in Iceland (Bjornsson et al., 1977, 1979; Tryggvason, 1984) and the 1978 Asal-Ghoubbet rifting event in eastern Afar (Abdallah et al., 1979). The recent magmatic activity at the DMH rift has therefore presented a unique scientific opportunity to gain a detailed understanding of the processes associated with dyke intrusion, extension and crustal accretion (e.g. Ebinger et al., 2010). The combination of remote sensing studies, particularly radar interferometry (InSAR), and data from the array of seismic and geodetic instruments installed across Afar since 2005 has provided constraints on this dyking sequence with uncommonly high temporal and spatial resolution. This includes well-located time-series of seismicity and deformation, associated with the propagation of individual intrusions. As such, the contemporary magma system at the DMH rift has been very well constrained and this provides a useful framework in which to evaluate other observations (i.e. geochemical, geochronological etc).

1.5.1 Dyke intrusions: 2005-2010

Fig 1.7 illustrates various field, remote sensing and geophysical observations of the recent rifting activity in the DMH segment. The rifting phase began in September 2005 with the intrusion of a very large dyke (~2 km^2 of magma) along the entire ~60 km length of the DMH rift zone. Initially recognized from seismicity recorded ~450 km away in Addis Ababa (Ayele et al., 2007, 2009), the magnitude and mode of the ground deformation was established by InSAR (Wright et al., 2006; Grandin et al. 2009; shown in Fig 1.7b). Horizontal surface opening along the length of the intrusion was up to ~5 m (Grandin et al., 2009) and numerous fault ruptures and fissuring occurred (Rowland et al., 2007; Barisin et al., 2010; Fig 1.7cd). Accompanying this intrusion was a small eruption of rhyolitic ash and pumice from a vent called Da' Ure, located NE of the Dabbahu volcano (Yirgu et al., 2006; Ayele et al., 2007).

Following the September 2005 intrusion, a series of 13 further dyking events were observed along the DMH rift zone. Occurring between June 2006 and May 2010, all of these dykes involved lesser volumes of magma (0.04-0.2 km^3), shorter propagation lengths (10-15 km) and less horizontal opening (0.8-3.5 m) than the initial September 2005 dyke (Hamling et al, 2009; Grandin et al., 2010a). The total cumulative opening along the rift zone since 2005 has been around 6-8 m (Hamling et al., 2009; Ebinger et al., 2010). Seismic evidence suggest that the source region for all the intrusions is located beneath the central part of the rift, below the Ado' Ale volcanic complex (Fig 1.4.) (Keir et al., 2009; Ebinger et al., 2008; Belachew et al., 2011). Dykes fed from this zone propagate either north, south or in both directions along the rift zone. Geodetic studies have demonstrated an inflation of this region since the rifting phase commenced and this has been interpreted as recharge of the feeder zone (Grandin et al., 2010b).

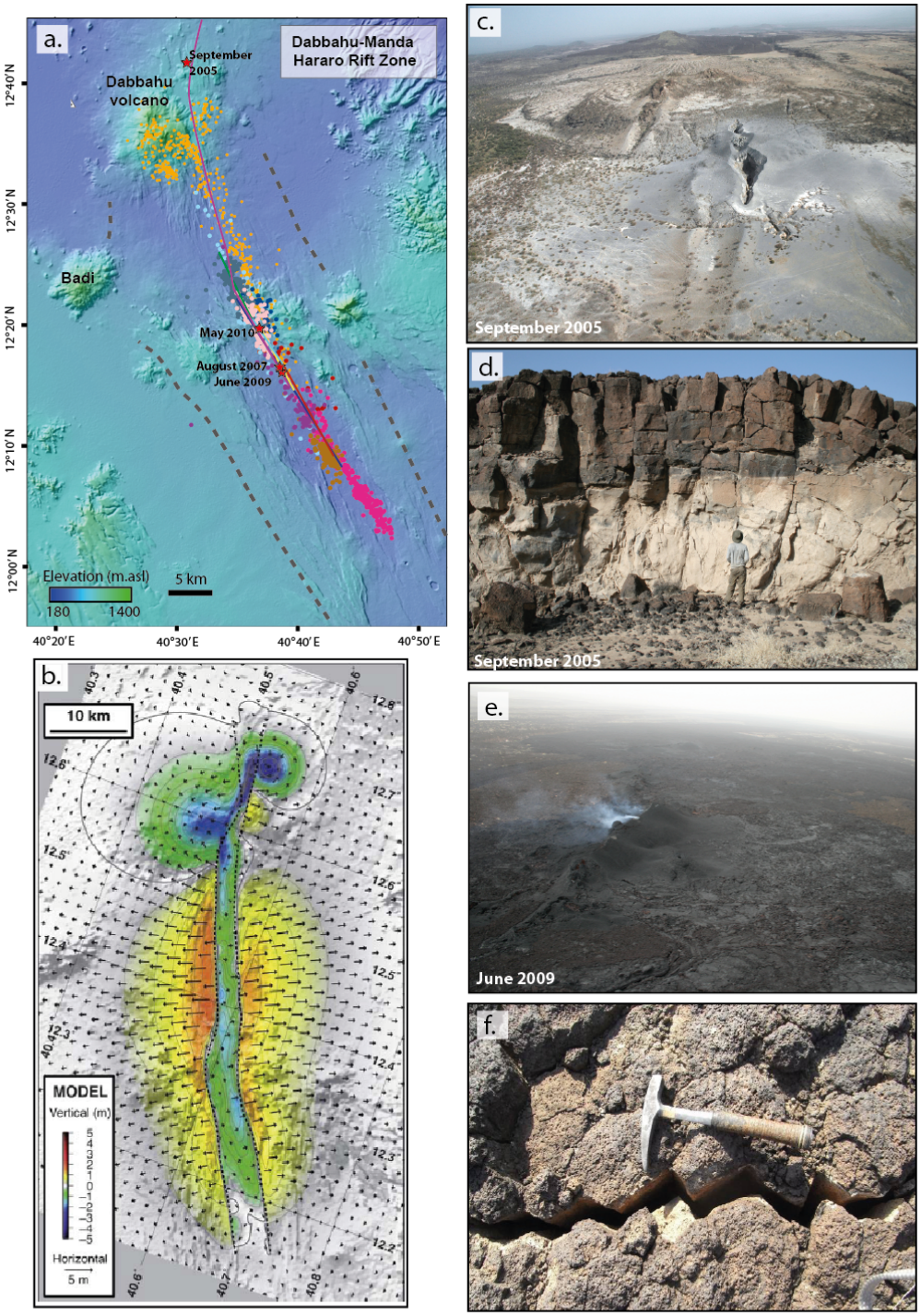

Figure 1.7 Observation of recent magmatic deformation in the DMH axial segment. (a) Topography of the DMH rift segment (location shown as white box in Fig 1.2). Coloured dots show the locations of earthquakes along the DMH rift zone during successive magma intrusion events between 2005-2009 (see Ebinger et al., 2010 for data sources and other details). Solid coloured lines are the paths of individual dyke intrusions from geodetic data by Hamling et al., 2009. Four volcanic eruptions have occurred since 2005, three basaltic eruptions in the rift centre and a small rhyolitic eruption north of the Dabbahu volcano (vent shown in photo) (b) Example of deformation model based on ground motions observed by satellite geodesy during the largest dyke intrusion in September 2005 (model by Grandin et al., 2009). In both (a) and (b) the magmatic activity can be seen to be closely focused along the DMH axis. (c-f) field photos illustrating the structural and volcanological effects of the rifting activity: (c) eruptive fissure for rhyolitic eruption in 2005 (~500 metres length). Recent tephra deposits can be seen around the fissure. (d) Fault break observed following the 2006 dyke intrusion. The base of the dark region in the top half of the fault marks the previous ground surface prior to the latest slip event (person for scale) (e) Basaltic fissure during an eruption in 2009 (location marked in (a)). (f) Example of smaller ground fissures commonly found across the rift zone. Lava flows forming the rift substrate often fracture along the surfaces of internal columnar jointing.

An additional source region in the northern part of the segment beneath Dabbahu is also thought to have supplied a minor portion of the magma intruded during the initial 2005 event (Wright et al., 2006; Grandin et al., 2010).

The small rhyolitic eruption (<0.0001 km^3) that occurred during the September 2005 intrusion was probably the result of a thermal or mechanical perturbation to an existing crustal melt body, caused by the proximity to the large dyke injection and/or the intense seismicity (Pyle et al., 2006; Ayele et al., 2007). Since then, three further eruptions have occurred. These have all been basaltic fissure eruptions associated with three separate intrusion events in August 2007, June 2009 and May 2010. The eruptive fissures have been located close to the rift centre, south of the Ado Ale centre (Fig. 1.7a). Unlike the 2005 eruption these have been fed directly by dykes breaching the surface. These events are significant as they provide confirmation of the results of the geodetic inversion models (i.e. deformation resulting from dyke injection) and also allow sampling and analysis of the magma. Lava samples from the first two of these eruptions were collected during the fieldwork for this thesis and the results and implications of various chemical and isotopic analyses are presented in the following chapters. The physical characteristics of the recent eruptions have also been analysed and are discussed in Chapter 3.

Chapter 2

Geology of the Dabbahu-Manda Hararo Rift zone

2.1 Introduction

This chapter provides an overview of the geology of the field area for this thesis, the Dabbahu-Manda Hararo (DMH) axial rift segment in west-central Afar. This ~25 x 60 km magmatic segment forms part of the on-land Red Sea rift system and marks the location of the evolving Afro-Arabian plate boundary (Fig 1.2). Quaternary volcanism in the region of the DMH segment has mainly occurred along the central part of the rift zone, in the form of axial fissure eruptions and central volcanoes, and also along a transverse volcanic lineation to the east of the segment. This transverse zone is orientated at a high angle to the rift axis and is dominated by two volcanoes, Badi and Dabbayra (see Fig 1.4). The geology of this part of Afar has not previously been described in detail and the information in this chapter provides important context for the data and discussions presented in the subsequent chapters. An exception to this is the Dabbahu volcano at the northern end of the segment, which has been previously studied by Barberi et al (1975), and more recently in greater detail in a PhD thesis by Field (2011), undertaken at the University of Bristol within the framework of the Afar consortium. Once published the new data from Dabbahu will complement the work presented here and although it is not discussed in detail in this thesis, some of the new geochemical data by Field (2011) is included in various geochemical plots (i.e. TAS plot; Fig 1.5) to provide a comparison with the data presented here.

Figure 2.1 False colour Landsat ETM+ (Enhanced Thematic Mapper) image of the Dabbahu-Manda Hararo (DMH) Rift Segment overlaid on a SPOT elevation model. The segment is defined by a ~25 km wide region of intense faulting and recent volcanism. In these spectral bands the important lithological variations observed identified from field observations can be easily recognized. In general the basaltic lavas that form the main substrate across the region appear dark grey/blue, while silicic lavas forming the dome/flow units dispersed across the rift zone appear red. The most recent basaltic flows are darker in colour and can be identified along the rift axis. Sediments appear light coloured. The silicic flows that form the upper part of the Dabbahu volcano are less weathered than those in the central part of the rift and have a light grey rather than red appearance. Some basaltic scoria cones such as those on Dabbayra are a similar colour to the silicic lavas although these are in fact basaltic in composition. An interpreted geological map is shown in Figure 2.2.

2.2 Overview of field area

The DMH rift segment is the most southerly of the 5 axial rift zones that have formed along the axis of the on-land Red Sea rift system (see Fig 1.2). Fig 2.1 shows a false colour Landsat ETM+ image of the DMH segment overlaid onto a digital elevation map. This image allows some of the important compositional and textural distinctions between lavas to be recognized, such as the general division between rhyolitic and basaltic compositions. In this thesis the structural divisions previously made between axial and transverse volcanism (i.e. Barberi et al., 1974; section 1.3) are followed and the DMH segment *sensu stricto*, i.e. the ~25 km wide rift zone marked by intense faulting and fissural basaltic lavas, is referred to using the term 'DMH segment/rift zone', while the transverse volcanoes/lavas are described as 'off-axis volcanoes/lavas'. When used, the term 'DMH volcanic system' refers to the entire field areas comprising both these volcanic-tectonic structures. A geological map of the study region is shown in Fig 2.2.

2.2.1 The Dabbahu-Manda Hararo Rift Segment

The DMH rift segment lies near the southern end of the Red Sea system in Afar at around 12.5 °N, 40.5 °E (Fig 2.1). The mean elevation of the segment is ~400 m.asl, although there is considerable local variation due to volcanic topography. The surface of the rift zone is almost entirely covered in basaltic lavas, erupted from fissures and heavily deformed by normal faulting. Field photos illustrating the structures in the central part of the rift segment are shown in Fig 2.3. Overall the segment covers an area of ~2000 km^2 and has over 1200 distinct faults (Hayward, 1997). The mean strike of faults is 333° although there is significant local variability. South of the Ado Ale

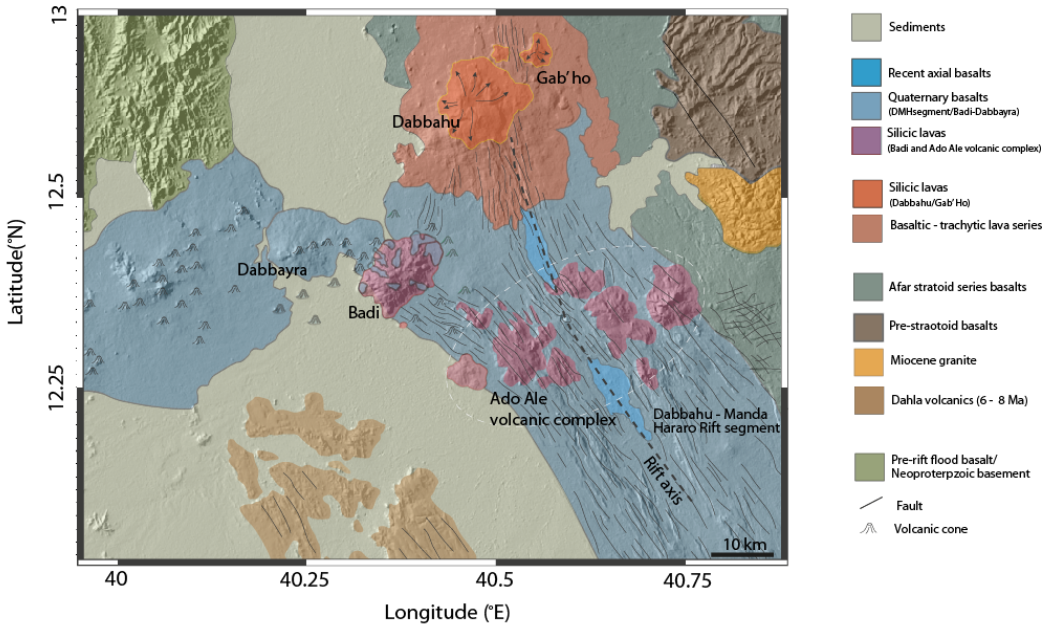

Figure 2.2 Geological map of the field area for this project. Map is based on remote sensing imagery and other previous maps (CNR-CNRS, 1973; Barberi et al., 1975). See text for discussion.

Volcanic Complex (AVC; Fig 2.1) the rift trend is essentially orthogonal to the mean extension oriented NW-NE, while in the northern sector the axial trend becomes more northerly, oblique to mean regional extension (Rowland et al., 2007). There is a well developed axial graben (shown in Figs 2.3a and c) although this is disrupted in the region of the AVC where the axis runs to a central high, marked by a small basaltic crater. Brittle deformation observed on the surface of the rift during a dyking event in 2005 (see section 1.5) led Rowland et al. (2007) to conclude that this was probably the chief mechanism of topographic growth and that magma intrusion is therefore likely to be the principle method of strain accommodation. The overall morphology of the segment is very similar to a slow (~20 mm yr^{-1}) spreading mid-ocean ridge (Rowland et al., 2007).

In addition to the widespread basaltic volcanism associated with dyke intrusion and rifting, it also apparent that more evolved lava compositions (predominantly rhyolitic)

have also been erupted and these are associated with central volcanoes located along the axis. The Dabbahu volcano, formerly known as Boina, lies at the northern end of the segment and has a summit elevation of ~1400 m. Dabbahu forms an essentially complete basaltic-rhyolitic lava series and following the work of Barberi et al (1975) became a type locality for extensive low pressure fractionation and the generation of peralkaline lavas. The area around Dabbahu also hosts several smaller rhyolitic lava domes and flows. This region marks the northern limit of the structures associated with the DMH segment and north of here rifting along the Red Sea system is offset to the east and focused along the Alayta rift segment. Further south in the centre of the DMH segment is a dissected silicic volcano, the various fragments of which form the AVC (Figs 2.1 and 2.2). The outer units of the AVC now flank the rift one on either side and therefore presumably pre-date its formation. Although heavily deformed parts of the AVC still rise to elevations of 1200 m.asl. Although usually described as a dissected volcano it is unclear to what extent these individual volcanic units initially formed a coherent structure. The shape and physical appearance of the inner units, Gommoyta and Diyyilu (Fig 2.1), suggests that these flows/domes once formed volcanic complex of similar scale to Badi, while the two outer units, Eger Aleyta and Ado' Ale, have a slightly different physical appearance and are separated from these by basaltic lavas. It seems more probable therefore that the AVC represents two phases of silicic volcanism, one prior to or during the early stages of the formation of the segment and another following the onset of basaltic volcanism associated with rifting. The emplacement of silicic volcanoes prior to the formation of rift zones has also been observed in other parts of Afar (Lahitte et al., 2003ab).

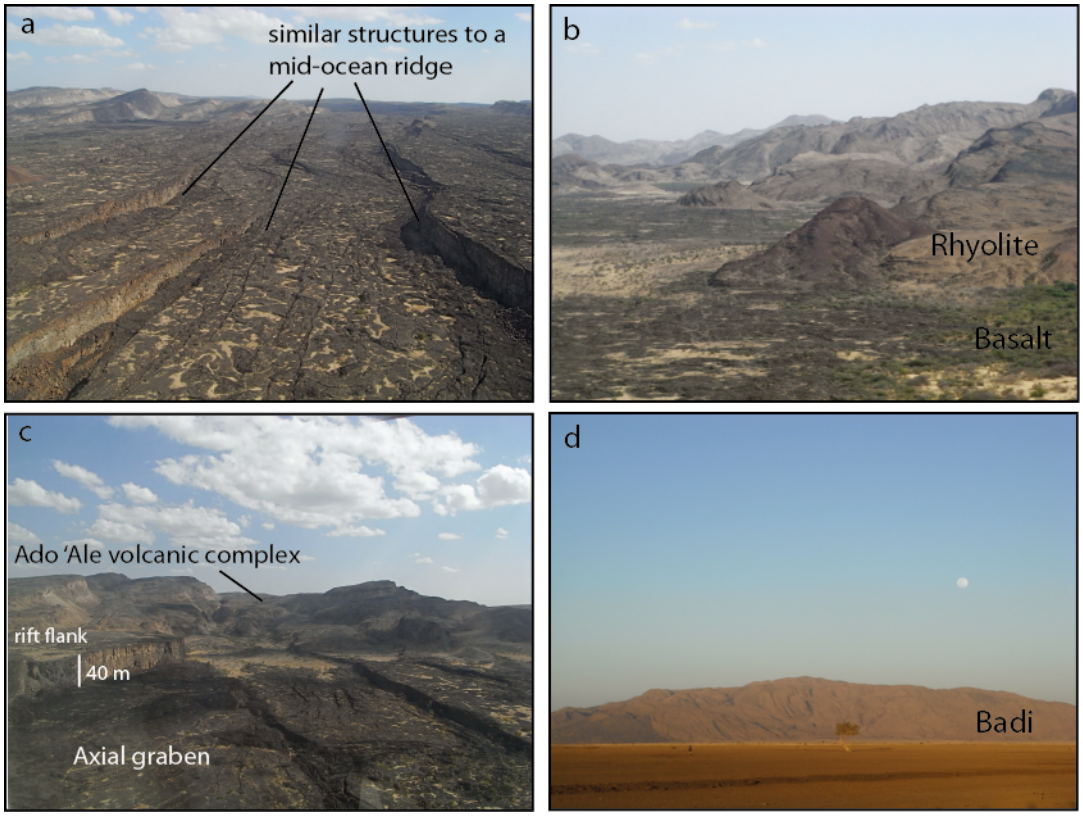

Figure 2.3 Field photos illustrating the volcanic and structural features of the field area. (a) The structures and morphology of the axial zone of the DMH rift segment closely resembles those observed at slow spreading ocean ridges such as the Mid-Atlantic ridge. (b) Photo demonstrating the topographic variations caused by basaltic and rhyolitic volcanism in the rift centre. (c) The edge of the axial graben in the NE part of the AVC (photo looking south) (d) the off-axis silicic volcano Badi. This complex of rhyolitic domes and flows forms a broad low-lying edifice. The darker region on the left is a basaltic lava flow erupted onto the silicic units.

2.2.2 Badi-Dabbayra transverse volcanic structure

On the western margin of the DMH rift segment, NW of the AVC, the rift zone is intersected by the Dabbayra-Badi transverse structure. Badi volcano, shown in Fig 2.3d, lies immediately adjacent to the DMH rift zone and is predominately composed of rhyolitic domes and flows. There is no central eruptive vent and the volcano is instead composed of an amalgamation of individual lava domes, the highest point on the edifice is around 1200 m.asl, 600 m above the surrounding desert plain. Several basaltic eruptions have also occurred here, from monogenetic vents located in the upper parts of the edifice. One previously published K-Ar age of 290 ± 4 ka (Lahitte et al., 2003a) is available for a rhyolitic flow near the base of Badi. To the NE of Badi is Dabbayra,

another complex of volcanic cones and lava flows, in this case of more basaltic composition. Although there is a central massif with a summit crater, eruptions have also occurred from various ~EW trending fissures and the overall edifice has an elongate shape and is ~10 x 5 km, with a large apron of lava flows on the northern side. There is no clear division between the volcanoes and the basaltic cones of Dabbayra merge into the ~NE side of Badi. There are no obvious fault structures visible along the Dabbayra-Badi volcanic structure and the trend of the lineation is defined by the alignment of eruptive vents and fissures. The area south of Dabbayra, to the west of the DMH segment, is a flat plain covered by ~50 m of fluvial sediments (borehole log for Digdiga available from Ethiopian Geological Survey) and is where the village of Digdiga, the nearest settlement to the DMH segment, is located (Fig 2.1).

2.3 Volcanism

On the basis of field observations it is possible to draw a clear distinction between the basaltic and rhyolitic lavas in the field area and both the central part of the rift and Badi-Dabbayra volcanoes appear to have a strong bimodal character with respect to erupted compositions. These observations are confirmed by the chemical analyses of the lavas presented in this thesis (Chapters 5 and 6) and illustrated in the TAS diagram shown in Fig 2.4. Sampling locations are shown in Fig 2.5. Unlike the Dabbahu volcano, where a complete compositional series has been erupted (Barberi et al., 1975; also shown in Fig 2.4), intermediate compositions are scarce in this part of the rift system and only two samples analysed (from the base of Dabbayra) have SiO_2 contents in the range 51-62 wt%. Studies on other transverse volcanic in western Afar have also found lavas of intermediate composition (e.g. Civetta et al., 1974) and in general these appear to be more common along these structures than at the axial rift zones (see Fig 1.5). The bimodal compositional variations between lavas can be readily recognized in certain

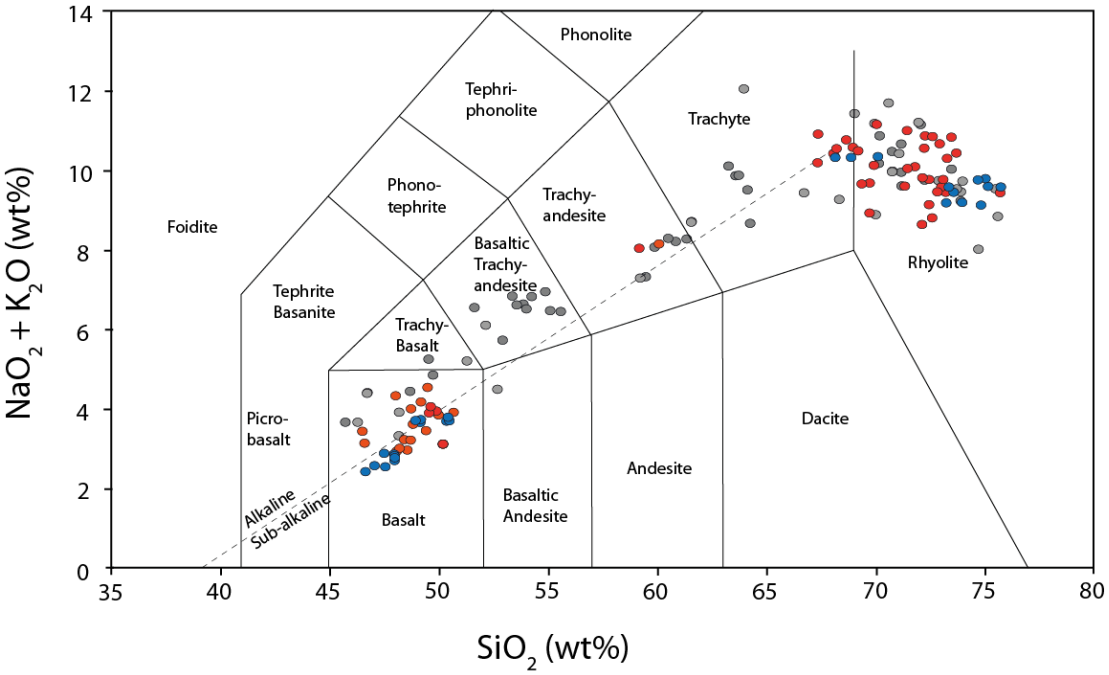

Figure 2.4 Total alkali vs. Silica (TAS) plot of samples from the DMH rift system. Samples analysed in this thesis are marked by blue (lavas from main part of the DMH segment) and red (Badi/Dabbayra region) symbols. Analyses of lavas from the Dabbahu volcano by Barberi et al (1975) and Field (2001) are shown for comparison (grey symbols). The locations of the samples analysed in this thesis are shown below in Figure 2.5.

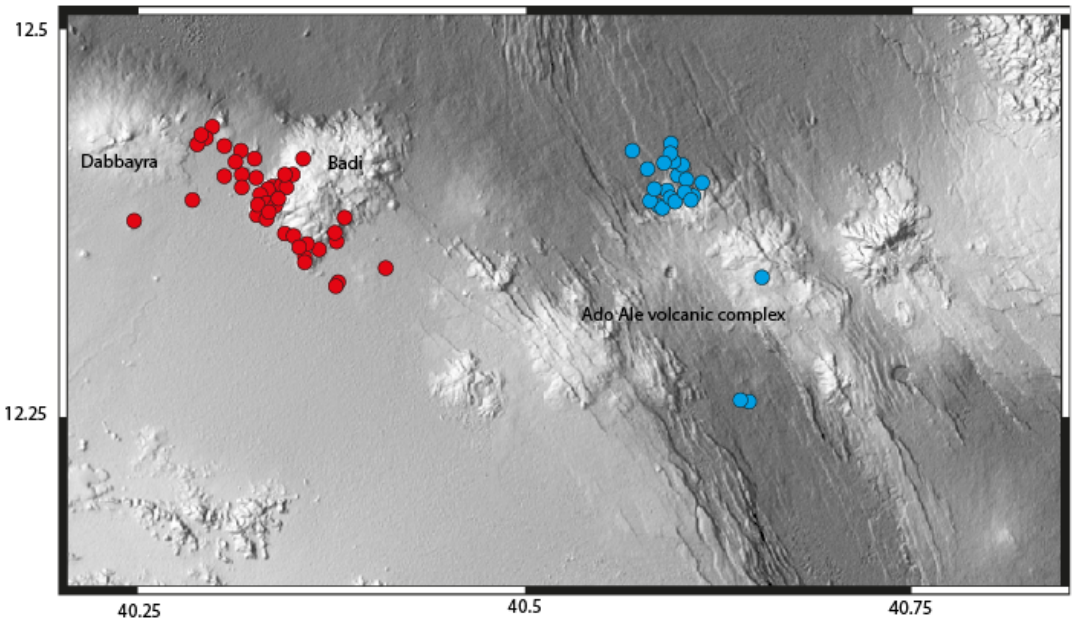

Figure 2.5 Locations of rock samples collected during fieldwork for this thesis. Sampling in the main part of the segment is very challenging and in some cases only practical via helicopter. The compositional range of lava in the sample suite are shown in the TAS plot above (Fig 2.4).

remote sensing imagery, such as the false colour Landsat ETM+ imagery (Fig 2.1), calibrated with field observations. Combining field observations of lava compositions, morphology and textures with remote sensing data allows this imagery to be interpreted to provide a fuller overview of the geology than is possible by fieldwork alone. The geological sketch map of the field area shown in Fig 2.2 is interpreted from remote sensing data, field observations and previous studies (e.g. CNR-CNRS, 1973)

2.3.1 Basaltic volcanism

This section provides an overview of the distribution and emplacement styles of basaltic lavas in the field area. Other aspects of basaltic magmatism, such as the geochemistry and geochronology, are investigated in Chapters 3, 4 and 5.

2.3.1.1 Field observations

With the exception of the rhyolitic lavas associated with the AVC the entire surface of the DMH segment is covered by basaltic lava flows (Figs 2.1 and 2.2). The youngest lavas are found in the axial graben and are distinct in the Landsat imagery due to the lower extents of weathering and dust accumulation and can also be seen to cover faults and fissures that offset older flows (Fig 2.1). Three recent basaltic eruptions have occurred in the southern part of the segment in 2007, 2009 and 2010 and these are examined in detail in chapter 3. The eruptive fissure for the 2009 eruption is shown in Fig 1.7e. Younger flows typically have rubbly or slabby pahoehoe textures (Fig 2.6cd) and are a few metres thick. Inflated pahoehoe lobes are common in the older more weathered flows forming the rift flanks and internal columnar jointing is often visible, exposed by faults and fissures, which typically fracture along the vertical joint surfaces (Fig 1.7f) Evidence from the recent eruptions and the younger less deformed lava in the central graben indicate that dyke-fed fissural systems are the primary mechanism of

emplacement (see Chapter 3). The clear morphological/spectral variation between the younger less eroded flows and the older surrounding lavas is important at it allows a general constraint to be placed on the width of the current neo-volcanic zone. Apart from these recent lavas all the other basaltic lavas exposed on the rift surface have been heavily deformed by the intense faulting and fissuring across the segment. The deformation of these lavas renders mapping of the majority of the individual flow units either highly uncertain or unfeasible. Some features of the volcanic architecture can be extracted from spectral analysis of remote sensing data, however these interpretations can be ambiguous as spectral variations can also be related to patterns of wind blown sediments or fluvial deposits as well as primary geological features.

In contrast to the fissural eruptions along the DMH rift zone, basaltic lavas across the Dabbayra-Badi transverse structure have been erupted from individual vents around which monogenetic cinder cones have been built (Fig 2.6a). Lava flows emanating from these cones reach lengths of up to 5 km when emplaced downhill from the higher elevation cones on Dabbayra and Badi. Immediately SE of Badi on the western margin of the DMH segment basaltic lavas have also been erupted from monogenetic cones, although unlike those east of Badi these have been affected by faulting associated with the rift zone. The variation in eruptive style between the main rift and off-axis region is consistent with magma transport under differing stress conditions (e.g. Takada, 1994). Basaltic volcanism on the Badi edifice has emplaced basaltic material onto the earlier silicic lavas, and this compositional trend in the stratigraphy appears to be very consistent across the volcano and no observations were made of basalts overlain by

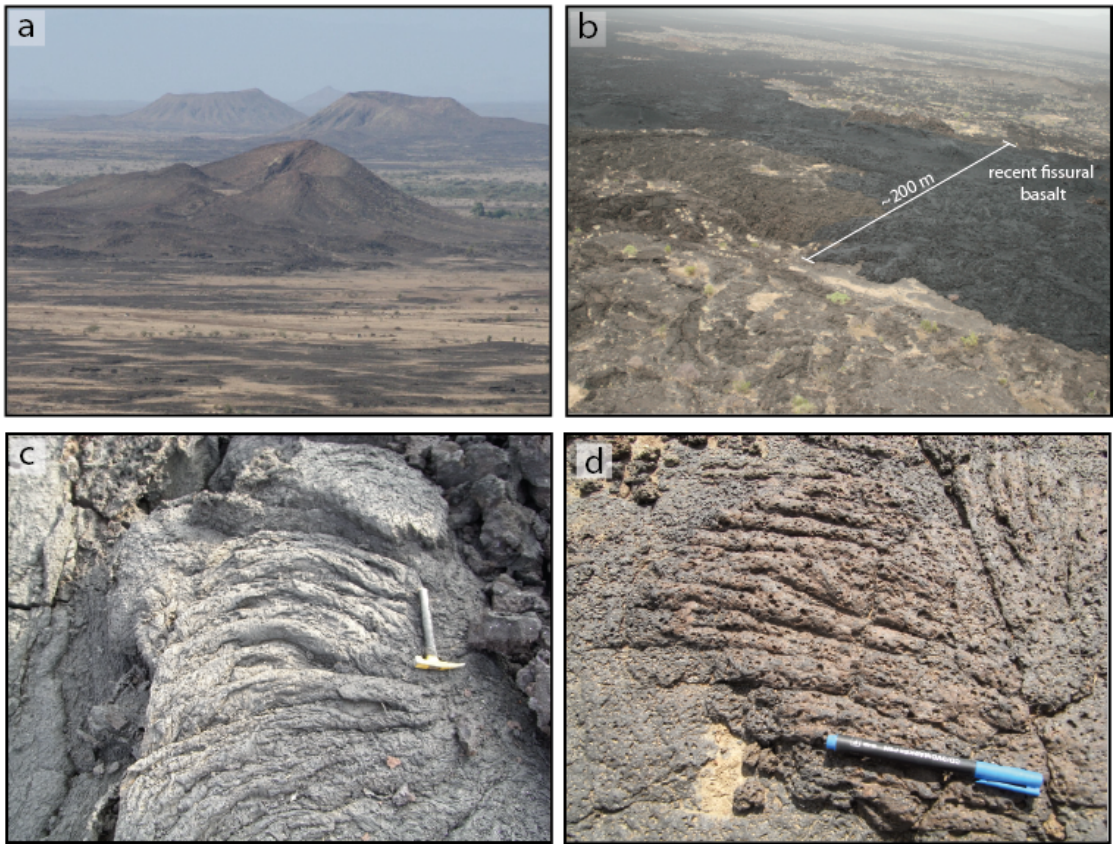

Figure 2.6 Field photo of basaltic volcanism. (a) monogenetic volcanic cones on the rift margin in the region around the Badi and Dabbayra volcanoes. (b) Fissural basaltic lavas in the axial graben, the fresh lava flow in the picture is around 2 days old. These two images illustrate the typical difference in emplacement style between the main rift zone (fissural eruptions) and the off-rift volcanoes (central vents/monogenetic cones). (c) and (d) examples of ropey pahoehoe textures in a new basaltic flow in the rift axis and an older weathered flow on the rift flank.

rhyolite. Several monogenetic cones have also been emplaced onto the fluvial plain south of Dabbayra, around the village of Digdiga.

2.3.2 Silicic volcanism

This section describes observations of lavas identified in the field as 'silicic' and equating to lavas with trachytic and rhyolitic compositions (> 62wt% SiO_2). Although this thesis is primarily concerned with basaltic magmatism some aspects of the geochemistry of these lavas are discussed in Chapter 6.

2.3.2.1 Field observations

Unlike the widespread basaltic activity, the eruption of trachytic and rhyolitic lavas has been restricted to the central part of the DMH segment, forming the units of the AVC, and the lava domes and flows that constituent the bulk of Badi. The silicic lavas of the AVC have been heavily dissected by faulting (Fig 2.2) and are distributed across the segment, however notwithstanding this post-eruptive deformation there are no obvious textural or morphological differences between the majority of the silicic lavas erupted in either location. Representative photos of these lavas are shown in Fig 2.7.

The emplacement of silicic lavas appears to have been predominately effusive rather than explosive and unlike most silicic volcanoes the majority of the erupted material has remained proximal to the vent. These volcanoes are notable for erupting relatively large volumes of rhyolitic lavas without forming the collapse structures usually found at silicic volcanoes, such as those in the MER (e.g. Rampey et al., 2010). Individual flow thicknesses are on the order of several 10 - 100's of metres (Fig 2.7e). Macro-scale textures vary between glass-rich obsidian and de-vitrified or finely microcrystalline lava and flow banding is a near ubiquitous feature of all flows and present at scales from a few centimetres to several metres (shown in Fig 2.7a-d). This layering, and the presence of glassy material, however, is limited to the surface of flows and when exposed by faults flow interiors are composed of homogenous crystalline lava often with columnar jointing (Fig 2.7e). The difference in textural variations and layering between the flow surfaces and interiors suggests that a significant degree of post emplacement crystallization/devitrification has occurred in the flow interiors. Some minor pyroclastic deposits were observed in the upper section of Badi, where several pumice layers interpreted as being emplaced by fallout from a small pyroclastic cone (Fig 2.7f).

Obsidian eruptions elsewhere are often associated with minor explosive phases (i.e. California; Fink, 1983, and Iceland; Tuffen et al., 2002) and it is likely that other minor pyroclastic deposits were also formed during the emplacement of other silicic domes but are either covered by the lavas or have since been eroded. The total subaerial volume of Badi is 31.5 km^3, while the silicic lavas units forming the AVC have a total volume of 48.3 km^3 (calculated from a 15m resolution DEM).

Apart from the one published K-Ar age of 290 ± 4 ka for the base of Badi (Lahitte et al., 2003) no other age constraints exist for silicic lavas from either the AVC or Badi. On the basis of field and remote sensing observations there is little evidence for any recent silicic volcanism and most flows appear to have undergone a similar level of erosion. This age may therefore provide a reasonable benchmark for the emplacement of most of these lavas. The location of the AVC in the rift centre, compared to the off-axis location of Badi, has led to these lavas being heavily deformed by normal faulting and the outer units of the complex flank the segment on either side. It is unclear to what extent these fragments initially formed a coherent edifice, however based on their distribution around the volcanic crater in the rift centre (Figs 2.1 and 2.4) it seems probable that they were erupted from a central vent and have since been rifted outwards.

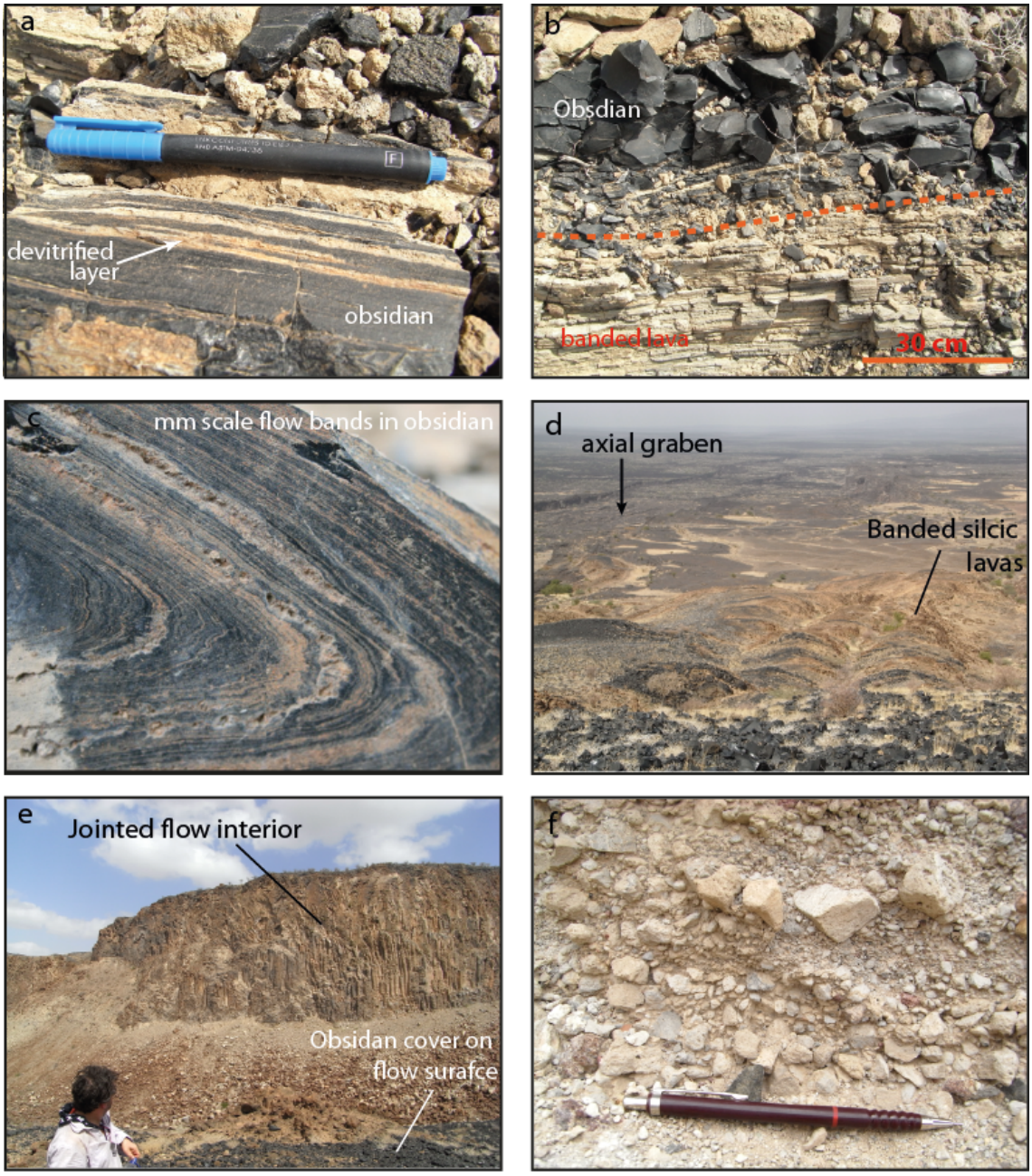

Figure 2.7 Field photos illustrating observations of silicic volcanism in the field area. The products of silicic eruptions predominately consist of effusive glass rich rhyolitic lavas and these form the prominent lava dome/flow units visible in Fig 2.1. (a - d) Flow banding is commonly observed and is present at scales of a few millimetres up to several metres. (e) Unlike the banded textures observed on the flow surface when exposed by faults flow interiors are texturally homogenous and display columnar cooling joints. (f) Although dominated by effusive lavas some minor pyroclastic deposits were observed in the upper parts of Badi volcano. The bedded pumice layers in the photo are inferred to be a pyroclastic fall deposit associated with a small pumice dome.

Chapter 3

Recent rift related volcanism in the DMH rift

3.1 Introduction

This chapter presents observations from three basaltic fissure eruptions along the Dabbahu-Manda Hararo rift zone and discusses the general characteristics of basaltic fissure eruptions at rift zones. These eruptions, which occurred in August 2007, June 2009 and May 2010, are amongst the few documented volcanic eruptions in Afar. After establishing the physical characteristics of individual eruptions the context of volcanism within the 2005-2010 rifting activity is examined via comparison to the intrusive and extrusive magmatism that occurred during the Icelandic Krafla rifting activity in the late 1970's. Some of the observations included here from the 2007 and 2009 eruptions have been published in Ferguson et al (2010), with T. Barnie, D. Pyle, C. Oppenheimer, G. Yirgu, E. Lewi, T. Kidane, S. Carn and I. Hamling as co-authors.

3.2 Basaltic volcanism at magmatic rifts

Rift zones represent the most common magmatic environment on Earth and account for ~75% of global lava production (Crisp, 1984). However, the inaccessibility of most extensional systems and the rarity of on-land magmatic-rifting events result in limited opportunities to characterise rift related volcanism or the balance between intrusive and extrusive magmatism. Some research has shown that the first order volcanic characteristics of magmatic rifts, such as flow volumes (Perfit and Chadwick, 1998) and fissure lengths (Sinton et al., 2002), may display consistent variations with spreading

rate, implying that the measurement of volcanic eruption parameters can assist in understanding extensional systems. Although observations of ocean-floor rift magmatism at the scale of a single eruption and/or lava flow unit exist (e.g. Chadwick et al., 1995; Embley et al., 2000; Soule et al., 2007), they represent snapshots of otherwise coarse datasets. The spatial and temporal resolution required to document accurately a series of eruptions (and the associated intrusive activity) in an active magmatic rift is still only practical for subaerial volcanoes. However, on-land rifting events occur infrequently and only one sustained period of activity has been previously observed in the modern instrumental era (i.e. 1975-1984 Krafla rifting phase, Iceland; Bjornsson et al., 1977; Bjornsson et al., 1979; Trygvsson, 1984). The recent rifting activity in the DMH rift therefore represents an exceptional opportunity to characterise the volcanism associated with an active spreading system and to draw conclusions concerning the partitioning of magma between intrusive and extrusive phases. This chapter presents remote sensing and field observations for the 2007, 2009 and 2010 eruptions and derives first-order physical parameters for the eruptive systems. The Afar eruptions are comparable to some of those reported for oceanic rift systems (i.e. Embley et al., 1999) and may shed light on aspects of magma supply and eruption at oceanic ridges. Comparisons are also made between the Afar eruptions and those associated with the Krafla rifting episode. This analysis is used to evaluate potential temporal trends of magma partitioning between intrusive and extrusive components, and in the magnitude and frequency of basaltic volcanism at the DMH rift.

3.3 Observations of recent basaltic volcanism in Afar

Due to the remoteness of the Afar region the eruptions discussed here were first brought to the attention of the international community thanks to timely reports of

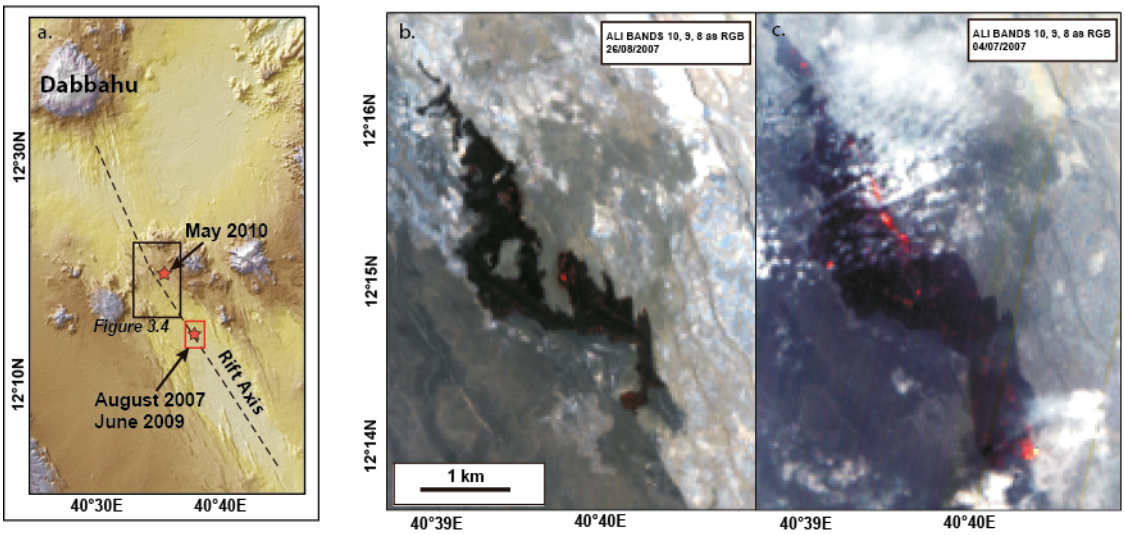

Figure 3.1. (a) Location of August 2007 and June 2009 eruptive fissures along the DMH axis. (b and c) Daytime Advanced Land Imager (ALI) images of August 2007 and June 2009 fissure eruptions, acquired 12 and 4 days (respectively) following the onset of activity. Both images have the same scale and extent (shown by the red box in (a)). Bands in the short wave infrared (SWIR) at 2.08-2.35 µm, 1.55-1.75 µm and 1.2-1.3 µm are displayed as RGB respectively. Note the largest scoria cone and SE toe of the 2007 flow and the fissure, SE toe and patches of the 2009 flow were still hot enough at the time of image acquisition to radiate in the far SWIR, and appear red. The August 2007 fissure system was reactivated and extended during the June 2009 eruptions.

their associated SO_2 emissions observed by the Ozone Monitoring Instrument (OMI) aboard the EOS-AURA satellite. The location of the SO_2 source was subsequently identified via thermal imagery collected by the MODIS (Moderate Resolution Imaging Spectroradiometer) instrument carried on NASA's Terra and Aqua satellites (e.g. Wright et al., 2004). Rapid field access in 2007 and 2009 was possible thanks to helicopter support provided by the Ethiopian Air Force. These two eruptions were in the same location, shown in Fig 3.1, and the June 2009 eruption reactivated the August 2007 fissure system and resurfaced the older lavas. The May 2010 eruption site was further north (Fig. 3.1a) and this event was of a far lower magnitude than the first two. Details of the chronology and physical parameters for each eruption are collated in Table 1. All were short-lived events (< 3 days). Mean effusion rates for the first two (~55 - 70 m^3 s^{-1}) were similar to those reported for fissure eruptions in Iceland (Harris et al., 2000). The May 2010 eruption has a lower mean effusion rate of ~23 m^3 s^{-1}

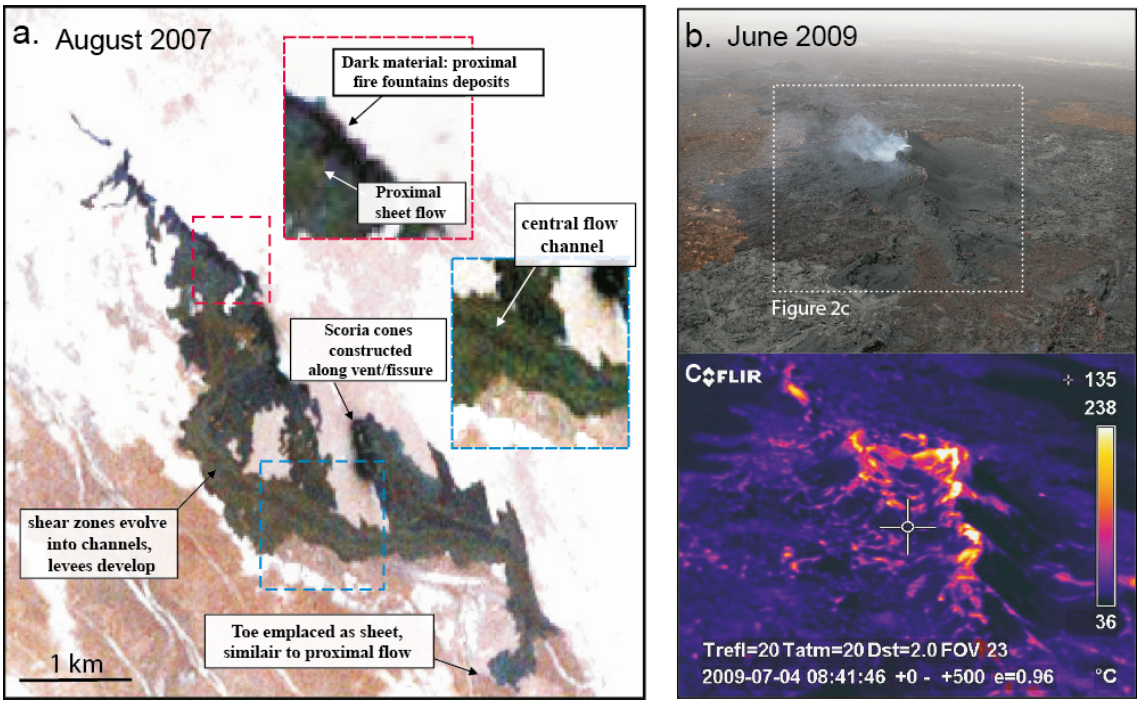

Figure 3.2 (a) Interpreted ASTER image of August 2007 eruption products. Image resolution is 15m and shows visible-near infrared (VNIR) spectral bands. Image histogram for each RGB channel has been stretched to highlight spectral variation over very low reflectance fresh basalts. Eruption products identified from oblique aerial photographs and ground inspection can be recognised in the ASTER image and different emplacement styles identified. Relatively unfractured pahoehoe surfaces appear blue, fractured aa surfaces appear grey-brown, scoria dark blue – black, previous aa lava flows pale brown, old flows and sediment white. (b) Visual and (c) thermal images of the Jne 2009 eruptive vent taken from a helicopter on 04/07/09 (eruption began 29/06/09). Scoria appears smooth and dark grey, pahoehoe light– medium grey, heavily fractured aa material brown. Temperature image acquired with a FLIRThermacam. Parts of the scoria cone reach temperatures of up to 238°C the highest temperatures observed.

3.3.1 August 2007 eruption

The August 2007 fissure system was located south of the centre of the DMH segment (Figs. 3.1ab). This was the first basaltic eruption since the rifting phase began (in September 2005) and occurred during the seventh dyking event (Hamling et al., 2009). It was also the first subaerial fissure eruption at a rift zone since the Icelandic activity in the 1980's. The location of the eruptive fissure coincided with the southern part of the subsurface dyke, as identified through modelling of geodetic data (Hamling et al. 2009) (see section 5). Thermal data from MODIS indicate that the effusive eruption began on

12 August 2007 and lasted less than 48 hours. Visiting the site on 23 August, residual gas emissions were observed but no lava effusion. ASTER (Advanced Spaceborne Thermal Emission and Reflection Radiometer) and Hyperion-ALI satellite imagery of the eruptive system are shown in Fig. 3.1b and parameters for the eruptive system in Table 3.1.

3.3.1.1 Emplacement style

Aspects of the lava flows and their emplacement styles observed during our fieldwork can be recognised by distinctive spectral signatures in the ASTER imagery (~15 m pixel size). This provides the basis for image-based interpretation of the entire flow field and fissure system (Fig. 2a). The fissure system has a total lateral extent of ~4 km, and fed two main lava flows. The northern flow field was sourced from an intermittently active fissure, 2 km in length, whilst a southern fissure around 500 m in length, fed a 1-km-long flow. Constructed along the northern fissure were low (~10 m high) elongate scoria cones that fed pahoehoe flows and sheets that transformed down-flow into channelised aa flows. Activity along the southern fissure constructed three much larger scoria cones (20–30 m in height) and also fed a proximal pahoehoe flow/sheet that became channelled and disrupted down-flow. The tip of the southernmost flow appears to have a pahoehoe texture. Although activity along the southern section appears to have been more explosive (signified by higher scoria cones) and therefore presumably involved more volatile-rich magma, possibly sourced from the head of the intrusion, varying eruptive styles have been observed to occur synchronously along basaltic fissures (e.g. Etna; Spampinato et al., 2008) and the resolution of the MODIS thermal data is insufficient to determine the temporal pattern of activity along the fissure. The total area covered by the new lava flows is 2.2 km^2 and the bulk erupted volume is 4.4 –

Table 3.1 Summary of the physical parameters for recent DMH eruptions discussed in the text

Eruption date	Duration of main effusive phase[a]	Total fissure Length	Area (km^2)	Bulk Volume (10^6 m^3)	Intrusive: Extrusive	Mean effusion rate	Bulk SO_2 flux[b]
August 2007	36-48 hrs	4	2.2	4.4 – 8.8	~10:1	55	26±5
June2009	48 – 60 hrs	6.5	4.5	13 - 18	~ 5:1	70	34 ±7
May 2010	<10 hrs	<1	<0.25	< 1	~80:1	<30	-

[a] Estimated from MODIS thermal data
[b] Measured by the Ozone Monitoring Instrument (OMI)

8.8×10^6 m^3 (based on flow thickness measured in the field).

3.3.1.2 SO_2 Emissions

The Ozone Monitoring Instrument (OMI) is a space-based hyperspectral UV/visible spectrometer aboard NASA's Aura satellite (Levelt et al., 2006). Here we use SO_2 total columns derived from the operational OMI SO_2 algorithm (Yang et al., 2007) to calculate SO_2 burdens in the volcanic clouds (graphical example of SO_2 data shown for 2009 eruption in Fig 3.3). The first OMI acquisition following the onset of the eruption was on 13 August at 10.15 UTC which detected an SO_2 cloud, emanating from the DMH region, over Ethiopia and Sudan. A further acquisition on the 14 August showed these emissions to be continuing, however the thermal signal in the MODIS data has significantly decreased by this point, indicating that the effusion of lava had probably ceased. Estimates of the SO_2 burden from the OMI data are very sensitive to the altitude of the SO_2 cloud. A forward trajectory model for the plume (using the HYbrid Single-Particle Lagrangian Integrated Trajectory model, HYSPLIT; Draxler and Rolph 2003) suggests an altitude of 3-5 km. Downwind lofting of the cloud observed in this model is probably caused by the large increase in elevation over the Ethiopian highlands (max elevation ~4.5 km). Assuming a maximum altitude of 5 km gives an approximate SO_2 mass of 26 ± 5 kt. No data are currently available on the un-degassed volatile

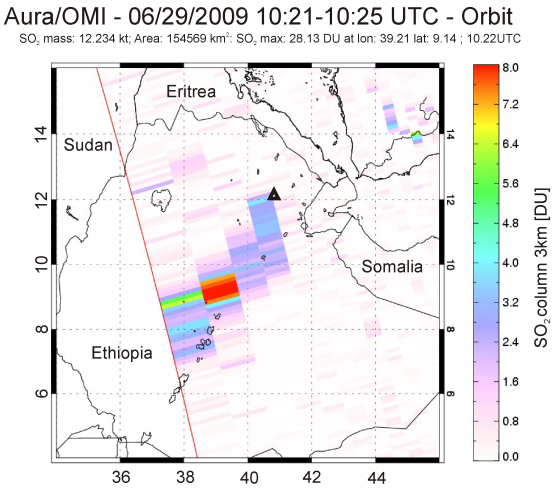

Figure 3.3. SO2 column imaged by Ozone Monitoring Instrument (OMI). SO_2 column amounts (in Dobson Units [DU]; 1 DU= 28.5 mg m^{-2}) retrieved from OMI measurements at ~10.23 UTC on 29 June (colour-coded pixels) superimposed on a map showing national boundaries. Location of eruptive vent is illustrated by the triangle. A concentrated region of SO_2 can be seen within the plume around 384 km downwind.

contents of the DHM magmas, however peak sulfur concentrations from olivine-hosted melt inclusions from young basalts in the nearby Asal rift reach ~0.12 wt% (Clocchiatti et al., 1980). Analysis of glassy scoria from this eruption show that the sulfur content of the erupted and degassed magma is 0.023 - 0.038 wt% (Ferguson et al., 2010). If we assume a typical sulphur loss of ~0.09 wt% during ascent and eruption, the observed emission of 26 kt (26 x 10^6 kg) of SO_2 would require around 5.5 x 10^6 m^3 of magma. The bulk erupted volume of 4.4 - 8.8 x 10^6 m^3 is therefore sufficient to account for all of the observed SO_2 released without needing to invoke volatile loss from un-erupted melt.

3.3.2 June 2009 Eruption

Following the August 2007 fissure eruption, the central and southern section of the DMH rift was re-intruded by five further dykes with an average return time of ~4 months. The sixth dyke intrusion since August 2007 (and 13th since September 2005) coincided with a second extrusive event in June 2009. During this event, the August 2007 eruptive fissure was reactivated, the new eruption products almost entirely covering the earlier flows (Fig. 3.1c). The first thermal alerts from MODIS were recorded on 28 June at 23.20 UTC and had subsided by 2 July 2009. An Advanced Land Imager (ALI) image acquired on 4 July 2009, the same day as a field visit, clearly

shows the newly emplaced flows and the residual heat along the main fissure and across the lava flows. This was also imaged from a helicopter using an infrared camera (FLIR Thermacam) and a maximum temperature of 238°C recorded at the surface of the fissure (Fig 3.2bc). On site, newly constructed scoria cones ~50 m in height were observed, from which low-level gas emissions were still occurring (visible in Fig. 3.2b). New ground fissures, with surface openings of ≤0.5 m, were also observed around the vicinity of the eruption, as were fresh looking fault breaks with vertical throws of ≤1.5 m.

3.3.2.1 Emplacement style and physical parameters

As with the August 2007 eruption, the proximal lava flows were emplaced as pahoehoe type flows that evolved into aa flows away from the vent. Channelisation of the flows was less distinct than in the 2007 eruption. Eruptive activity was concentrated in the northern section of the fissure, the site of the most intense degassing and thermal signature in the ALI image (Figs. 3.1c and 3.2b,c). The eruption reactivated the entire length of the 2007 fissure and extended the system by ~500 m to the south and 1 km to the north. The active fissure was more continuous than observed for the 2007 eruption, and had a total length of 5.2 km. Although largely overlying the previous lava flows, the areal extent of the new eruption products can be estimated from ASTER night-time thermal data. The new lava flows and proximal scoria deposits cover an area of 4.5 km^2 with a total erupted bulk volume of 13.5 – 18 × 10^6 m^3 (using field observation of flow thickness). Physical parameters are summarised in Table 3.1.

3.3.2.2 SO_2 emissions

The first SO_2 detection by OMI was on the 29 June at 10.23 UTC (Fig 3.3). Infrared satellite instruments that have poor sensitivity to the lower troposphere (e.g., AIRS and

IASI) detected no SO_2 during the eruption, from which we infer a plume altitude of <5 km. On this occasion radiosonde data is available from a launch site in Saudi Arabia (18.2N, 42.7E), which indicates a wind speed at <5 km of 10.3 m s-1 from the NE. Above this altitude a strong shear wind was present, which is also consistent with a lower tropospheric plume. HYSPLIT modelling also suggests an altitude of 3 - 5 km. In the first OMI detection, shown in Fig 3.3, the plume was drifting ~SW and contained 15-36 kt of SO_2 (depending on altitude). In this image a concentrated pulse of SO_2 is visible in the centre of the cloud, around 384 km downwind of the source, presumably relating to the most vigorous stage of the eruption. With a wind-speed of 10.3 m s^{-1} this relates to around 10.36 hours of transport. This is very close to the time of the first MODIS thermal alerts and presumably the onset of lava effusion. The next OMI acquisition on 30 June at 11.06 UTC also detected tropospheric SO_2 over western Ethiopia and Sudan, however due to a data gap the measurements did not cover the plume in the area around the eruption site. Assuming an altitude of 5 km gives a total SO_2 burden of 34 ± 7 kt. Due to the data gap in the second acquisition this is likely a minimum estimate. Using our inferred value for sulfur loss during decompression (~0.09 wt%), the observed emissions of 34 x 10^6 kg of SO_2 would require degassing from ~7 x 10^6 m^3 of magma. Considering the gap in the OMI data it seems reasonable to assume that all the emitted SO_2 can be accounted for by the erupted bulk volume of 13.5 - 18 x 10^6 m^3.

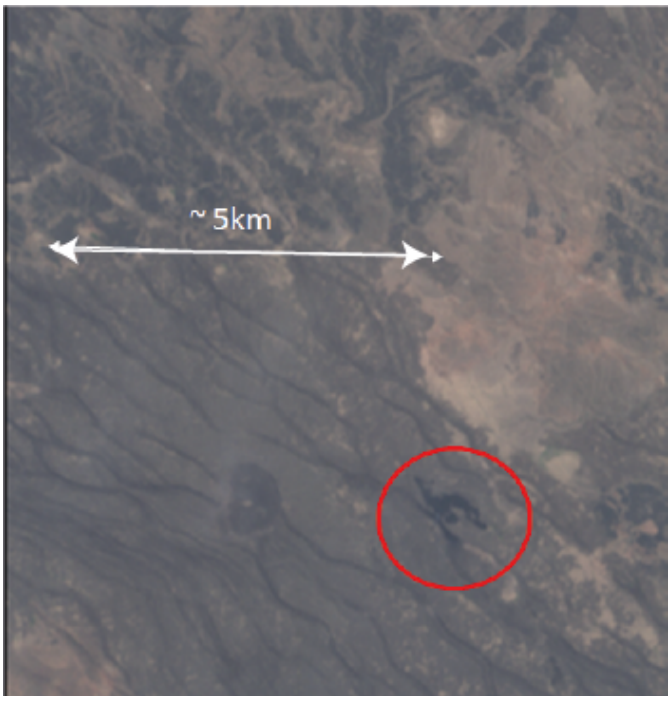

Figure 3.4 Landsat image of lava flow erupted May 2010 (dark region in red circle). Location shown in Figure 3.1. The magnitude of this eruption was very small and the erupted volume is estimated to be < 1 x 10^6 m^3. The location of the fissure near the summit of the along-axis topographic high (marked by the small crater) is notable as it indicates that this intrusion had the greatest vertical propagation of any in the 2005-2010 intrusion series.

3.3.3 May 2010 eruption

The June 2009 dyke intrusion and eruption marked the end of the regular cycle of dyke intrusions along the DMH rift that began in 2005 (average return time ~4 months). No further activity was detected in the rift until May 2010 when several thermal alerts were identified by the MODIS instrument near the along-axis summit. The first data acquisition to record these was at 19.40 UTC 21 May 2010, a residual thermal signal was present in data collected the following day but had diminished by 23 May. An EO-1 image acquired at 07.18 UTC 22 May (Fig. 3.4) reveals newly emplaced basaltic flow near the central crater at the along-axis summit of the rift.

3.3.3.1 Duration and magnitude

The onset of the eruption was initially constrained by MODIS data to have occurred between 22.45 UTC on 20 May and 19.40 UTC 21 May. The Landsat image (Fig 3.4) acquired at 07.18 UTC 22 May shows that the bulk of the lava had been erupted by this time and no temperature above 180 °C was registered. Reports were also made from

local inhabitants of a smoke plume and active lava flows, however it is unknown exactly when these sighting occurred. The precise duration of the eruption has, however, been further constrained from analysis of high temporal resolution infrared imagery collected by a geostationary meteorological satellite by T. Barnie, University of Cambridge using the technique of Barnie and Oppenheimer (2010). This indicates that the main period of lava effusion began around 01.15 UTC 21 May and ended around 3.5 hours later at 03.45 UTC (T. Barnie, pers com).

No scientific visit has been made to the May 2010 eruption site and the location in the centre of the rift is not easily accessible. Approximate physical parameters can be derived form the remote sensing data and are listed in Table 3.1. Compared to the previous eruption in 2007 and 2009 this event was particularly short-lived and produced a minor volume of lava ($< 1 \times 10^6$ m^3).

3.4 Partitioning of magma between intrusion and eruption

3.4.1 Dyke and lava volumes for 2007 and 2009 events

Intrusive and extrusive melt volumes in active magmatic systems are typically hard to constrain with any degree of confidence (see White et al., 2006 and references therein). The most accurate estimates of intruded melt volumes come from inversion models of geodetic data on surface deformation. In the case of the recent Afar dyking events the high-resolution geophysical data available (i.e. Ebinger et al., 2008; Hamling et al., 2009; Keir et al., 2009; Grandin et al., 2010) have allowed the volumes of successive intrusions to be modeled with unusually high precision. The locations, opening profiles and volumes of the first thirteen dykes since 2005 have been calculated from elastic

dislocation models based on InSAR and GPS measurements (Wright et al., 2006; Hamling et al., 2009; Grandin et al., 2009, 2010). Dykes typically extend to a depth of ~10 km, coincident with a magmatic source region identified from high-resolution seismic measurements (Keir et al., 2009), and therefore likely approximate the volume of the entire intrusion. Parameters from the August 2007 modeled intrusion suggest

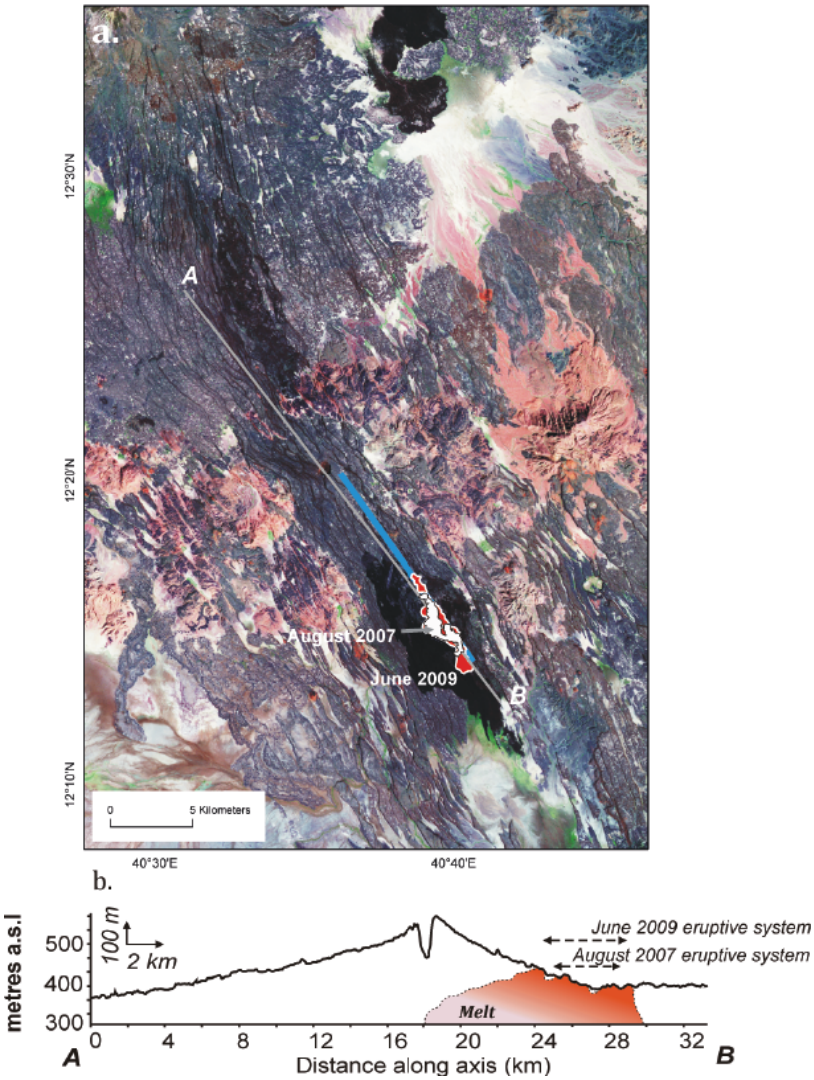

Figure 3.5. Location of 2007 and 2009 dykes along rift axis. False colour Landsat ETM+ (Enhanced Thematic Mapper) image of the central part of the Dabbahu-Manda Hararo rift (regional location shown in chapter 1). Basaltic rocks generally appear dark whilst the more siliceous lava flows that flank the rift centre appear red. Blue line is the modelled track of the August 2007 dyke (by Hamling et al. 2009). Both the 2007 (white outline) and 2009 (red outline) basaltic eruptions occurred along the southern part of the intrusion. The most recent basaltic volcanism prior to 2007 (identified as the most un-deformed basaltic flows) can be seen on the northern and southern margins of the central axial topography (b) cross section showing topographic profile along the rift axis, locations of the recent eruptive fissures and schematic illustration of the feeder dyke. In the central part of the rift zone the axial graben is replaced by a region of enhanced volcanic topography, coincident with a seismically imaged subsurface region of magma storage (identified by Keir et al. 2009).

a dyke of volume of 48 - 55 × 10^6 m^3, oriented 334° and 9.1 km in length, causing surface opening of ≤1.6 m (Hamling et al., 2009; Grandin et al., 2010). The region of maximum extension along the intrusion track is coincident with the eruptive fissure. The June 2009 dyke model suggests a volume of 44 – 50 × 10^6 m^3 with maximum surface opening of ≤1.5 m. Both these eruptive fissures opened along the southern sections of their feeder dykes, at the furthest lateral extent from the source region (locations shown in Fig 3.5). The volume of the dyke May 2010 intrusion has been estimated from a similar inversion of InSAR data b to be 81 ± 18 x 10^6 m^3, with an average opening of 1.6 m along the intrusion (I. Hamling, pers com). It is notable that location of the vent was almost directly on the summit of the along-axis topographic high and the feeder dyke therefore had the greatest vertical propagation of any intrusion in the 2005-2010 series.

Magma volumes for intrusive and eruptive events during the 2005-2010 Afar phase are listed in table 3.2 and the temporal trend of intrusive and extrusive magma volumes shown in Fig 6b. The intrusive volumes used are those of Grandin et al., (2010), who have produced the most complete analyses of the intrusive sequence. The individual volume ratios between intrusive and extrusive emplacement for the August 2007, June 2009 and May 2010 events are approximately 10:1, 5:1, 80:1 respectively, assuming that all of the erupted melt was extracted directly from the magma chamber during each dyking event. Using a simple model for the cooling time, t, of a 2 metre wide dyke to half its initial temperature of 1200°C of $t = w^2/\kappa$, where t is time, w is the half width of the dyke and κ is the thermal diffusivity (10^{-6} m^2 s^{-1}, Fowler, 1990), significant cooling of each individual intrusion will have occurred within ~12 days. As the return time of

the post-2005 (~1 m width) dyke intrusions in the DMH was around 1 to 6 months (Hamling et al., 2009; Grandin et al., 2010) it is unlikely therefore that any eruptions involved magma intruded into shallow part of the rift by a previous dyke.

3.4.2 Cumulative volume ratios during a rifting episode

The best-studied rifting period in an analogous setting prior to the current Afar activity was the 1975-1984 Krafla rifting cycle in Iceland (e.g. Bjornsson et al., 1979; Trygvsson, 1984; Einarsson, 1991). During nine years of activity at Krafla 20 individual dykes were intruded along the rift, accompanied by nine basaltic eruptions.

Estimates of intruded volumes are available from geodetic models of inflation and deflation of the inferred magma source by Ewart et al., (1991). The volume of erupted material can also be estimated via field and remote sensing observations (Bjornsson et al., 1977; Bjornsson et al., 1979; Harris et al., 2000 and references therein). The temporal pattern of magma partitioning between intrusive and extrusive activity during the Krafla cycle (shown in Fig. 3.6) demonstrates a distinct change from a dominantly intrusive to a dominantly extrusive regime after ~4 years of activity (Harris et al., 2000). During the initial and chiefly intrusive phase the volume ratio of cumulative intrusive to extrusive melt varied from 444:1 and 148:1. By the fifth basaltic eruption, in 1980 (coincident with the ~15th dyke intrusion), the majority of melt supplied from the central magma source was being erupted rather than intruded. Numerical modelling of the Krafla activity by Buck et al. (2006) attributed the increasing volcanic output to a continual relaxation of along-axis stresses by successive dyke injections, allowing for greater vertical (vs. horizontal) propagation during later intrusion events.

Table 3.2 Intruded and erupted volumes for dyking/eruptive events in the DMH rift segment since 2005

	Sept 2005	June 2006	July 2006	Sept 2006	Dec 2006	Jan 2007	Aug 2007	Nov 2007	April 2008	July 2008	Oct 2008	Feb 2009	June 2009	May 2010	Total
Intruded volume (x 10^6 m^3)	3014	129	48	53	44	37	55	372	99	47	198	73	44	81	4294
Erupted volume (x 10^6 m^3)							4.6						11	~1	16.6

Intrusive volumes from modelling of geodetic data: Sept 2005 – June 2009 (Grandin et al. 2010), May 2010 (I. Hamling, unpublished data)

dyke injections, allowing for greater vertical (vs. horizontal) propagation during later intrusion events. The final (cumulative) extrusive to intrusive magma ratio for the entire nine year period was ~3:1 (Harris et al., 2000). Long-term intrusive-extrusive melt ratios for the (slow spreading) Mid Atlantic Ridge and the (fast spreading) East Pacific Rise have been estimated, based on structural studies, to be between 5-10:1 and 5-8:1 respectively (White et al., 2006). These estimates are currently too imprecise to resolve any differences resulting from variations in spreading rate. It is still unclear how typical the episodic rifting style seen in Iceland and Afar is to oceanic systems.

The rifting phase in the DMH rift produced fourteen dykes with a cumulative volume of 4294×10^6 m^3 (4.294 km^3) (Grandin et al., 2010) and three basaltic eruptions with a total volume of ~16.6 $\times 10^6$ m^3, giving by mid 2010 a cumulative intrusive-extrusive balance of ~260:1. The temporal pattern of the cumulative intrusive-extrusive volume ratio for Afar is shown alongside the corresponding data for Krafla in Fig 3.6. Both rifting phases began as predominantly intrusive events, with very high intrusive volumes relative to the volcanic output (ratios of 100's:1). At Krafla this was subsequently 'balanced', to obtain a final ratio of 1:3, by a period of dominantly eruptive activity.

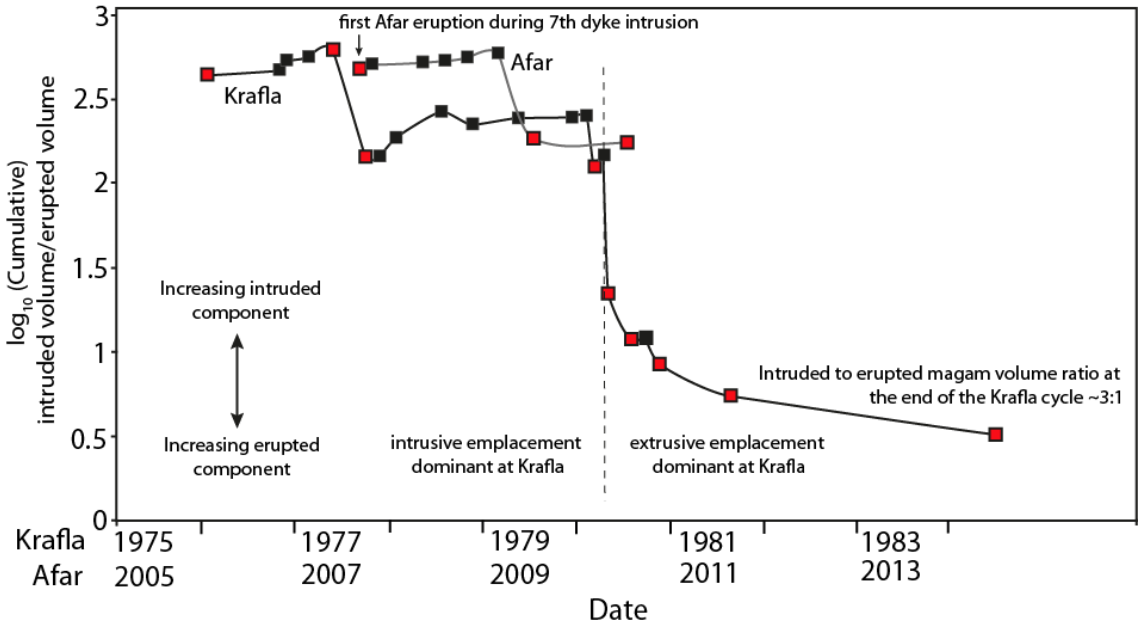

Figure 3.6 Temporal trend of cumulative intrusive to extrusive magma volume ratios. Ratios shown for the Krafla rifting cycle and from the currently (post 2005) on-going activity in Afar. Magma supplied to the Krafla system during the initial part of the rifting phase was dominantly emplaced via intrusive processes. The bulk of the volcanic flux occurred during the latter stage of the cycle where almost all supplied melt was erupted. The recent Afar activity has a similar regime for the corresponding stage of the Krafla cycle. Both extrusive volumes have been corrected for a porosity of 30%. Red symbols indicate dyking events that included eruptions. Intrusive volumes at Krafla from Ewart et al, 1991. Erupted volumes from Bjornsson et al., 1977, 1979 and Harris et al, 2000 and references therein.dyke injections, allowing for greater vertical (vs. horizontal) propagation during later intrusion events. The final intrusive and extrusive magma ratio for the entire nine year episode was ~3:1 (Harris et al., 2000).

3.5 Surface characteristics of eruptions

3.5.1 Volcanic features of magmatic rifts

This section compares observations of first-order physical volcanic parameters for the Afar and Krafla rifting events. Fig 3.7 shows the evolution of eruptive parameters for each rifting phase. At Krafla, all observed physical features (fissure length, duration, areal extent and volume) increased in magnitude as rifting progressed. Some studies (e.g. Perfit and Chadwick, 1995; Sinton et al, 2002) have suggested that such physical characteristics can have a proportional relationship to the spreading rate. If such relations do exist then observational data on volcanism could provide important, and accessible, constraints on subsurface processes, such as intrusive melt volumes and

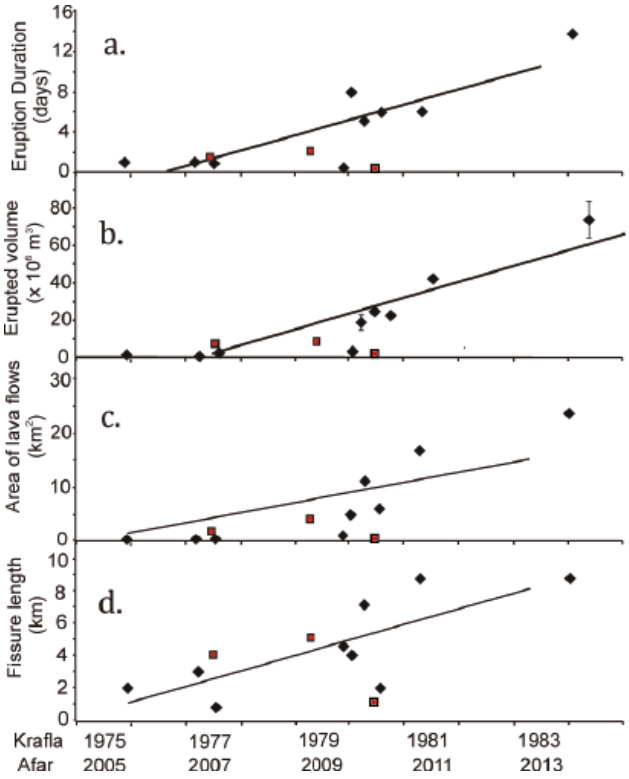

Figure 3.7. Temporal patterns of first order physical parameters for basaltic eruptions. Data for the Afar (squares) and Krafla (diamonds) rifting phases. (a) Eruption duration, (b) erupted volume (DRE corrected for 30% porosity), (c) area of eruption products, (d) fissure length. Trend lines are for Krafla data only. All observed parameters show an overall increase during the Krafla cycle as individual eruptions became larger in magnitude. See text for discussion.

previous active rifting phases. The current catalogue of volcanic data for oceanic rifts, although growing, is still limited and is clearly biased towards large events and fortuitous discoveries during submersible dives. If oceanic volcanism occurs largely during discrete rifting cycles, such as seen in Iceland and Afar, this will also restrict attempts to compile accurate datasets on the scale of single eruptions, as opposed to 'packages' of closely spaced events (see Sinton et al., 2002). If the DMH rift had only been surveyed after June 2009, the products of the two recent Afar eruptions would have most likely been mapped as one single event.

3.5.2 Relations between rifting activity and volcanic parameters

The trend of physical parameters for Krafla (Fig. 3.7) suggests that, in the case of episodic rifting, the magnitude of any one volcanic event depends on the most recent preceding activity, and that eruptions of varying sizes are not randomly distributed through time but show a progression throughout a cycle. If a similar trend of

eruption magnitudes was consistently repeated over successive rifting cycles, each accommodating roughly equal amounts of extension, then two scenarios, depending on the timescale of observation, can be envisioned for relating volcanism to spreading rates. 1) A short-term trend, over one rifting cycle, where the likely magnitude of eruptions is dependent on the stage in the cycle and the magma flux to the rift. If the temporal and volumetric relations between intrusive and extrusive activity observed at Krafla are consistent, either internally to the Krafla system or to other rifts (both currently untested), then data on an eruption, and possibly those preceding it, could provide a qualitative/semi-quantitative constraint on recent magmatic extension. 2) A long-term (i.e. multi-cycle) relation, where an overall scaling exists between the time-averaged spreading rate, controlled by the magmatic flux, and the range of eruption magnitudes. An important factor is whether there is (eruptible) melt available below the rift axis. A permanent sub-axial magma chamber is generally considered to only be a feature of faster spreading systems (>50 mm yr^{-1}; Sinton and Detrick, 1992; Phipps-Morgan and Chen, 1993), although long lived melt bodies may also exist along sections of slower spreading system (Singh et al., 2006). The contrast between the intermittent versus permanent availability of magma may be a fundamental control on the size and frequency range of eruptions (Sinton et al., 2002).

Extension across the Red Sea system in Afar is currently ~16-20 mm yr^{-1} (Vigny et al., 2006; McClusky et al., 2010). Rifting since 2005 has caused ~10 m of extension across the DMH rift zone (Hamling et al., 2009; Grandin et al., 2010) and has been accompanied by a volcanic flux of ~16.6 × 10^6 m^3. From the predicted long term spreading rate, this gives a volcanic flux of ~0.03 × 10^6 m^3 yr^{-1}. In the case of the Krafla episode, (9 m of extension accompanied by a bulk lava volume of ~ 281 × 10^6 m^3 of

lava and a long-term extension rate of 20 mm yr^{-1}) this gives an order of magnitude larger time-averaged flux here of 0.6×10^6 m^3 yr^{-1}. Whether this difference simply reflects variation in magma production rates in different geodynamic settings is unclear. On a global scale, the long-term lava production rates in different tectonic settings remain poorly constrained, however 0.03×10^6 m^3 yr^{-1} is far below the range of mean rates available for continental or oceanic rifts of $1\text{-}10 \times 10^6$ m^3 yr^{-1} (White et al., 2006).

3.6 Volcanic topography and eruption locations

Structural analysis of recent (post September 2005) and existing fault structures along the DMH segment suggests that the majority of brittle surface deformation visible across the rift may be magmatic (i.e. dyke induced) in origin (Rowland et al., 2007). Recent seismic studies (Keir et al., 2009) demonstrate that, similar to slow spreading ocean ridges, dykes intruded into the DMH rift are fed from a central magma chamber. The location of this source region corresponds with the highest along-axis topography around the Ado' Ale Volcanic Complex (AVC) (Fig 3.5a). The existence of a central magma source has been identified as a key factor in maintaining the segmentation of the rift zone along the Red Sea system (Wright et al., 2006; Keir et al., 2009). The coincidence of a central zone of magma accretion with the axial topography (Fig. 3.5b) agrees with predictions made by numerical modelling of successive intrusive events from a centralised magma source by Buck et al., (2006). The model of Buck et al. predicts that eruptions will most likely be associated with dykes with shorter lengths, thereby creating topography around the central magma source and that the loading effect of significant axial topography act to focus future eruptions at the margins of the central topographic load. Conversely, dismantling by normal faulting makes eruptions more likely at greater distances along the axis. The eruptions in 2007 and 2009 were fed

by dykes ~9 km long, which is typical of many of the recent dykes (8-9 km), but much shorter than the initial September 2005 intrusion (~60 km) and also slightly shorter than intrusions in July 2006 (~ 10km) and November 2007 (~11 km) (Hamling et al., 2009).

Imagery from the spaceborne Landsat ETM+ instrument (Fig 3.5a) shows that the locations of the most recent basaltic volcanism in the DMH rift (i.e. where lava flows are least deformed) correspond to the slopes/margins of the central edifice. A consequence of the apparent focusing of volcanic activity in these regions is the resulting difficulty in identifying previous eruptions, the products of which are continually resurfaced. For example, if there had been no observations of the August 2007 event at the time, it is likely the products would subsequently have been attributed to the later 2009 event. The use of thermal data acquired during, or shortly after, eruption has proved to be remarkably useful in identifying the products of the most recent event (e.g. Figs 3.2bc). If the characteristics of volcanic systems fed from a central magma source are to be used to constrain understand subsurface magmatic processes and rift systems, then it is desirable to reconstruct accurately the volume and extent of previous individual eruptions.

3.7 Discussion

3.7.1 Size and frequency of eruptions during a rifting episode

The basaltic eruptions observed thus far during the rifting phase in August 2007, June 2009 and May 2010 show many similarities to those that occurred during the comparable stage of the Krafla cycle. Magma partitioning at Krafla operated under two distinct regimes, with the bulk of each batch of melt supplied from the central chamber

being emplaced either intrusively or volcanically. Overall, the nine year cumulative volcanic flux accounted for ~25% of the total magma supply (Harris et al., 2000). As magma transport to the shallow part of the rift zone is not continuous (i.e. during discrete dyke injections) then any marked increase in the trend of the cumulative erupted volume must be accommodated by either larger single eruptions or through a greater number of dyking intrusions that feed small to medium-sized eruptions. The temporal pattern of intrusive to extrusive magma volumes and of physical eruptive parameters observed at Krafla (Fig. 3.6 and 3.7) (Harris et al., 2000) clearly shows that in this system the former was the case. Numerical models based on the Krafla dykes (Buck et al., 2006) show that once tensile stress along a rift zone has been sufficiently relieved, via repeated dyke injections, the ability of successive intrusions to propagate upwards rather than laterally is increased and hence extrusion becomes more likely. This model predicts that an initial accumulation of melt is then depleted via repeated intrusion into the rift.

In order to derive meaningful correlations between eruptive parameters and spreading rates (e.g. Sinton et al., 2002), physical features relating to a single eruption must be accurately resolved. In case of an episodic rifting style, focusing the volcanic component to the latter stages of a rifting phase increases the likelihood that newly emplaced flows and eruptive systems will be rapidly resurfaced, limiting the time available for detection. Even on the subaerial rift systems in Iceland and Afar, the subsequent identification of a single eruptive unit would be problematic without contemporaneous observations. The volumetric relations presented here for the partitioning of magma between intrusive and volcanic processes, consistent thus far between corresponding periods of the Afar and Krafla cycles, have intriguing

implications for assessing both the volumes of subsurface melts, and relating intermittent volcanic observations to a sustained period of active rifting. The ability to acquire a high-resolution time series of the magmatic flux in Afar yields unprecedented accuracy in assessing the intrusive to extrusive relations for the magmatic system.

3.7.2 Forecasting future basaltic eruptions in the DMH rift

Pursuing the dyking model of Buck et al. (2006) with respect to DMH rift system suggests that once a critical threshold of extension is attained along the DMH rift, the dominant emplacement style for most the magma supplied to the rift would be by eruption rather than endogenous growth from intrusion. The major period of intrusion in the DMH rift was from September 2005 to June 2009 and with the exception of the May 2010 intrusion/eruption, no seismic or volcanic activity has been reported since. As discussed volcanism has been a volumetrically minor component of this active phase, with < 1% of the magma supplied to the shallow crust being erupted. As the rate of dyke intrusions has now decreased it could be concluded that the along axis stress has been relaxed and conditions favouring magma injection no longer exist. Alternatively, the sub-rift melt supply may have been exhausted. In the case of the former, future eruptions may well be expected, as future dykes propagate upwards rather than horizontally along the axis. The evidence for volcanism from previous rifting activity preserved in the axial graben suggests that the presently observed volcanic flux of ~0.03 $\times 10^6$ m^3 yr^{-1} (assuming a long-term extension rate of 20 mm yr^{-1}) comprising two small and one minor eruption is less than would be expected.

It is therefore expected that, should magma still be available beneath the DMH rift then the volcanic flux will increase from its current level and may be accommodated by

eruptions of increasingly larger magnitude (i.e. of greater volume, duration and spatial extent). These are most likely to be located in the central rift, within 10-15 km of the rift centre, on either the northern or southern margins of the central Ado' Ale volcanic complex (Fig. 3.5). The pattern of eruptions at Krafla clearly shows that a large volume of eruptible melt remained following the major period of dyke induced extension and that this was erupted during two large eruptions, the largest occurring almost 5 years after the last significant extensional event. If future eruptions are to occur at the DMH during this active period it seems likely they will occur within the next ~10 years, however the dominant factor is clearly whether the melt supply from the sub-rift chamber will be sustained. The minor nature of the May 2010 intrusion/ eruption could be interpreted as suggesting that the magma supply has been exhausted and future activity will not occur until melt has re-accumulated, by which time tensile stresses will have increased to again favour intrusion. Alternatively, the May 2010 dyke may represent the final relaxation of local tensile stress and future volcanic activity will occur once sufficient overpressure exists within the existing magma reservoir, which has been depressurized over the previous 5 years of activity. The pattern of eruptive parameters observed at Krafla can be well explained by the competing forces of magma overpressure and tectonic (tensile) stress in driving upwards versus horizontal dyke propagation (Buck et al., 2006). It seems likely therefore that if eruptions do occur in the immediate future at the DMH rift they have a high probability of being the largest that typically occur here. On the basis of the recent activity this would mean an eruption of $>15 \times 10^6$ m^3. At Krafla for example the volume of the largest (and final) eruption (84×10^6 m^3) was around 3.5 times larger than the preceding four events. In the DMH rift, however, evidence from preserved lavas in the axial graben suggests that single

eruptions probably do not often exceed ~20 × 10^6 m^3 and an event of this magnitude may be around the upper limit for typical DMH volcanism.

3.8 Summary

Opportunities to observe an active rifting cycle and the associated volcanism are extremely rare. The 2005-2010 Afar phase is the first to be observed on land since the 1975–1984 Krafla cycle and the first in the age of high-resolution multispectral satellite observations. By integrating analysis of satellite imagery, field observations and available geodetic data it has been possible to record and characterise the basaltic eruptions that have occurred (thus far) during the Afar rifting cycle. All the eruptions were relatively short lived events and had volumes, durations, fissure lengths and mean effusion rates similar to basaltic fissure eruptions that occurred during similar stages of the Krafla phase. The SO_2 emissions observed by OMI during the 2007 and 2009 events are consistent with volatile loss from the respective erupted volumes. Combing physical observations with geodetic inversions of the intrusive activity allows the cumulative mass balance between intrusive and extrusive magmatism for the rifting period between 2005-2011 to be constrained at ~260:1. Although the activity has been primarily intrusive in nature, observations of the Krafla cycle (i.e. Bjornsson et al, 1979; Tryggvason, 1984) and models of repeated dyke emplacement (Buck et al. 2006), suggest that, should melt supply be maintained, future intrusions are more likely to result in eruptions.

Chapter 4

$^{40}Ar/^{39}Ar$ Geochronology of basaltic lavas

4.1 Introduction

The main focus of this chapter is the chronology of basaltic volcanism in the region of the DMH rift segment. Eruption, or emplacement, ages are investigated via $^{40}Ar/^{39}Ar$ geochronology of lava samples collected from both the central part of the DMH rift and also from the adjoining Dabbayra-Badi volcanic lineament. There is very little existing geochronological information for volcanic or tectonic process in this area and the formation and eruptive history of the DMH segment and surrounding volcanoes are both essentially unconstrained by radiometric age data.

A comprehensive geochronological study of this region would be extremely challenging in both analytical and logistical terms, and is beyond the scope of this project. However, given the dynamic nature of the tectonic environment in Afar a degree of knowledge on the temporal context of the volcanic/magmatic processes being investigated is important for developing a clear understanding of the links between volcanism and tectonics. The age data presented here for lavas from the central part of the rift segment record volcanism across a section of the northeastern flank and provide some important constraints on the formation and structural development of the DMH segment. Ages for lavas erupted at the Badi and Dabbayra volcanoes, near the eastern edge of the rift segment, provide a broader understanding of the history of volcanism in this part of Afar and also on the development of the volcanic zones termed 'transverse' volcanic ranges. The $^{40}Ar/^{39}Ar$ data presented here is the result of collaborative work with Andy

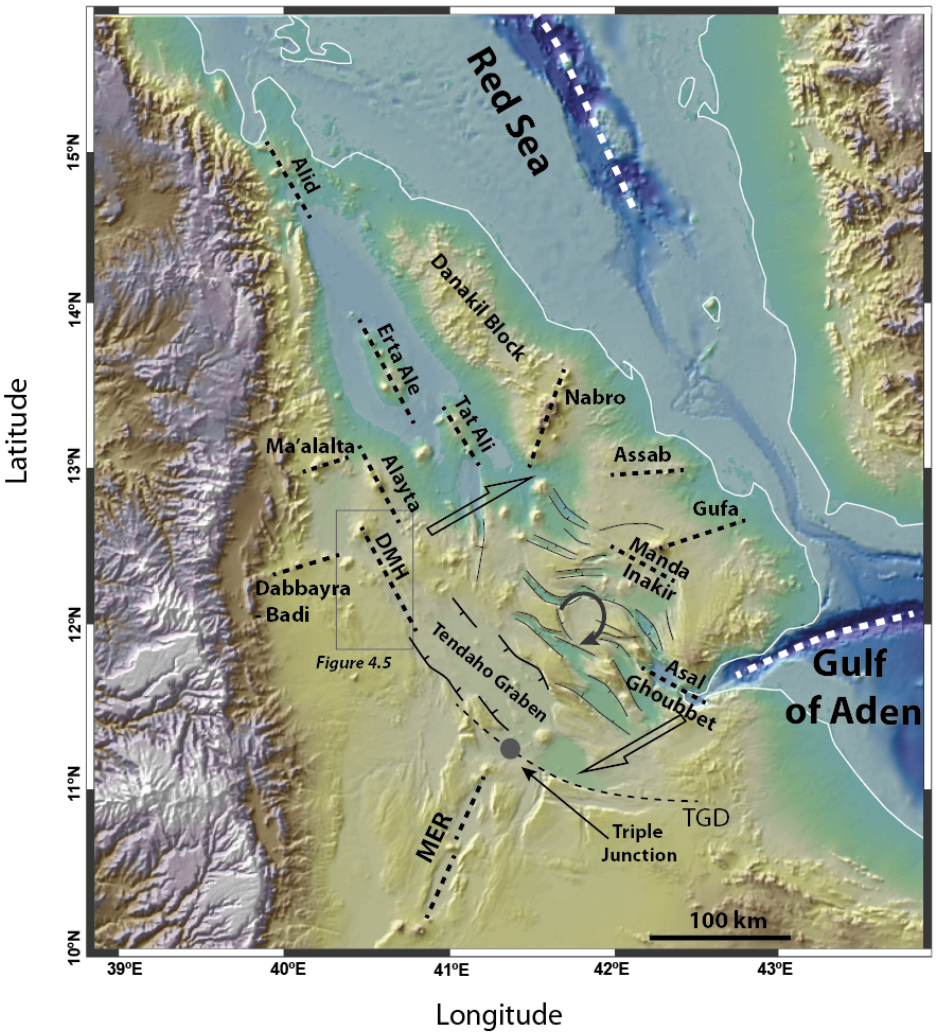

Figure 4.1 Relief map of Afar showing important volcano-tectonic structures and grabens. As described in chapter 1 (section 1.3.2) Quaternary volcanism has been focused along two kinds of volcanic-tectonic structures; axial rift segments and transverse/marginal volcanic zones. The region between the southern part of the on-land Red Sea system in western Afar and the on-land Gulf of Aden system in eastern Afar is marked by complex zone of faulting and block rotations (see Manighetti et al., 2001; Kidane et al., 2003).

Calvert at the USGS argon lab in Menlo Park, California and his help and support are gratefully acknowledged.

4.2 Volcano-tectonic structures in Afar

Quaternary volcanism in central and northern Afar has chiefly occurred along two types of tectonic structure, shown in Fig 4.1: the axial rift segments, formed along the axes of the on-land Red Sea and Gulf of Aden rift systems, and the so-called transverse volcanic ranges/marginal volcanoes, which form volcanic-tectonic lineations oriented

roughly perpendicular to the axial segments/ rift zones and are found around the margins of the depression.

4.2.1 Axial volcanic segments and grabens

The developing Afro-Arabian plate boundary in Afar consists largely of en-echelon magmatic rift segments, formed in highly attenuated and under-plated continental crust (Makris and Ginzburg, 1987; Bastow and Keir, 2011; Hammond et al., 2011) and where extension is primarily achieved via magma intrusion (Abdallah et al., 1979; Cattin et al., 2005; Wright et al., 2006; Hamling et al., 2009; Grandin et al., 2009, 2010; Ebinger et al., 2010; Keir et al., 2009; Keir et al., 2011). Morphologically these segments are defined by ~60 x 20 km zones of intense faulting and volcanism and are oriented approximately NW-SE (Fig 4.1). The morphology of individual segments varies and reflects the competing processes of volcanic construction versus deformation by extensional tectonics. The high lava flux at the Erta Ale segment in northern Afar for example, where the crust is most attenuated (Makris and Ginzburg, 1987), has created a region of locally high topography, rising up to 600 m above the surrounding desert. At other rift zones, such as the Dabbahu-Manda Hararo (DMH) and Asal-Ghoubbet (AG), faulting has been more dominant and these segments are defined as regions of locally negative topography. The long-term structural development of the rift systems in East Africa (described in Chapter 1, section 1.4) is marked by the systematic evolution in the characteristics of rift zones; from broad (~50 km) fault controlled grabens in the Main Ethiopian Rift (MER), to narrow (<20 km) volcanic rift segments in the Afar depression and finally to spreading ridges in the Red Sea and Gulf of Aden (Hayward and Ebinger, 1996). An important stage in the transition from continental rifting to oceanic spreading is strain localisation to a narrow rift zone and the development of an axially focused

magma system (Hayward and Ebinger, 1996; Wolfenden et al., 2005; Beutel et al., 2010) (shown in Fig 1.6 in Chapter 1). This process confines deformation and crustal growth to a narrow region, leading to the eventual creation of the magnetic anomalies characteristic of ocean ridges.

4.2.2 Previous work on rift evolution in central Afar

The DMH segment is the most southerly of the magmatic rift zones forming the on-land Red Sea rift system. Quaternary extension south of the DMH has primarily occurred across the Tendaho Graben (TG), a wide (~30 km) fault controlled graben, with large offset border faults (>200 m). The formation of the TG is associated with the eruption of a large volume of lavas, erupted between 0.5-2 Ma belonging to the Afar stratoid group (Barberi et al. 1975; Kidane et al., 2003; Lahitte et al., 2003; Acocella et al., 2008). In eastern Afar, the on-land Gulf of Aden rift has one well-developed axial segment, the Asal-Ghoubbet (AG) rift segment (Manighetti et al., 1998), located on the coast at Ghoubbet bay and the site of a rifting event in 1978 (Abdallah et al., 1979). North of the AG another segment, the Manda-Inakir (MI) segment, appears to be forming, however, this currently lacks well-defined structures or volcanic fissures (Manighetti et al., 1998; Lahitte et al., 2003). The AG and MI rifts are connected by a series of grabens, which have formed successively in a ~NE direction (Lahitte et al., 2003). In central Afar the southern section of the on-land Red Sea system, consisting of the DMH rift and the TG, overlaps with the on-land part of the Gulf of Aden rift (Fig. 4.1). The overlap region is marked by a strain transfer zone of narrow fault controlled grabens and rotated blocks formed between 1-3 Ma around the time of the eruption of the Stratoid series lavas (Manighetti et al., 2001; Kidane et al., 2003).

Analysis of temporal patterns of faulting at the AG rift segment by Manighetti et al (1998) has shown that the structures defining this segment have formed since ~850 ka and this broadly marks the localisation of faulting and volcanism along this part of the Aden rift system. The corresponding timescale of strain localisation along any part of the Red Sea system is currently unknown. It is also unknown what the temporal relation between the localisation of faulting processes and the formation of a focused sub-rift melt supply. On a regional scale it has been proposed by Lahitte et al (2003ab) that a causal relation exists between the emplacement of silicic volcanoes and the development of Quaternary rift zones/grabens along both the Red Sea and Aden system. Using K-Ar ages for silicic and basaltic lavas from across southern Afar this study proposed that a consistent temporal pattern exists at individual rift zones between the onset of silicic volcanism at central volcanoes and the subsequent fissural basaltic activity, the latter signifying the development of the rift zone/graben. In this model the thermal weakening of the crust by emplacement of a silicic volcano is considered sufficient to 'guide' rift development/propagation. However, it is unclear how feasible this scenario is with respect to the mechanics of rifting and a more realistic interpretation may be that increasing extension corresponds to an increased melt flux and the eruption of less evolved compositions. The age constraints of Lahitte et al. (2003ab) provide a very valuable, and in the context of Afar, comprehensive dataset on the timing of volcanism across the region. However, geochronological studies focused along individual rift segments are required to fully investigate temporal trends in the chemical and spatial characteristics of volcanism.

4.2.3 Transverse volcanic zones

In addition to the axial rift segments and grabens of the Red Sea and Gulf of Aden rifts Quaternary volcanism has also occurred at volcanic centres on the margins of the depression, termed 'marginal centres', and along E-W oriented zones, termed 'transverse structures' (Barberi et al. 1970, 1974). Shown in Fig 4.1, these are the Dabbayra-Badi and Ma'alalta structures in western Afar and the Nabro, Assab and Gufa volcanic zones in eastern Afar. In volumetric terms, the erupted products of these volcanoes, particularly from large silicic eruptions, suggests that the melt flux to these off-rift regions may be as significant as that along the rift segments (Wiart and Oppenheimer 2000ab, 2005). Individual volcanoes along transverse zones vary between large silicic caldera systems (e.g. Ma'alalta), elongate edifices (e.g. Dabbayra) and fields of monogenetic basaltic cones (e.g. Gufa) (Civetta et al., 1974; Wiart and Oppenheimer, 2005). The distinction between a 'marginal centre' and a 'transverse range/zone' was made following the French-Italian mapping expeditions in the 1960's (e.g. Barberi et al., 1970). However, as some 'marginal centres' essentially form part of a transverse zone (i.e. Dubbi volcano along the Nabro range) and others although dominated by a silicic caldera (i.e. Ma'alalta), are also associated with lines of basaltic cones, the actual distinction is not entirely clear and is probably unimportant (see Chapter 1). In this thesis the term 'transverse' will be used to describe all these structures.

Barberi et al (1974) proposed that the formation of transverse structures was caused by the presence of pre-existing zones of weakness in the crust and suggested that these were similar to the fracture zones that offset the mid Atlantic spreading ridge.

Geochemical studies of basaltic lavas from the Assab volcanic range in eastern Afar (De Fino et al., 1974; Civetta et al., 1974) and Nabro (Wiart and Oppenheimer, 2005) show that basaltic lavas erupted here are more alkaline than the transitional-tholeiitic lavas erupted along the axial rift segments. A remote sensing survey of the eight eruptive centres forming the Nabro range by Wiart and Oppenheimer (2005) suggests that volcanism involving more evolved magma compositions here is linked to the proximity to the pre-rift crust of the Danakil block. Only two historical eruptions have been reported along transverse volcanic ranges, both at volcanoes along the Nabro range; the first at Dubbi volcano in 1851 is the largest recoded silicic eruption in Africa and involved pyroclastic flows emplacement and basaltic fire fountains, resulting in over 100 fatalities (Wiart and Oppenheimer, 2000); the second, at Nabro volcano, started in June 2011 with a plinian eruption, causing ash-fall over NE Africa and, like the Dubbi eruption, was followed by basaltic fire fountains feeding lava flows (Smithsonian Institution, 2011). The existing scientific literature on transverse and/or marginal volcanism in Afar is limited to a handful of studies (i.e. Barberi et al., 1970, 1974; De Fino et al., 1974; Civetta et al., 1974; Wiart and Oppenheimer, 2000ab, 2005) and very little is known about their formation, or how the timescales of volcanism and processes of melt generation compare to those at the axial rift segments.

4.3 $^{40}Ar/^{39}Ar$ Geochronology

In order to provide some quantitative temporal constraints on volcanism and rift development in the DMH rift segment and on the formation of the adjoining Badi-Dabbayra transverse structure, age determinations were made on a suite of lavas using the $^{40}Ar/^{39}Ar$ radiometric dating method. Samples from the main section of the rift were collected on the northeastern flank, where access was possible via helicopter, while off-

axis samples were collected from the Badi volcano, the base of the Dabbayra volcano and from monogenetic cones surrounding these volcanoes (locations shown in Fig 4.3). All lavas analysed were basaltic with the exception of one andesite (sample 2909; 59 wt% SiO_2) collected from the southeast base of Dabbayra.

4.3.1 Overview of $^{40}Ar/^{39}Ar$ technique

The $^{40}Ar/^{39}Ar$ dating method is based on the decay of the radioactive isotope ^{40}K to stable radiogenic ^{40}Ar. ^{40}K decays to ^{40}Ar with a half-life of 1.25 Ga and the longevity of the ^{40}K isotope, coupled with the relative abundance of potassium in geological materials, makes the K–Ar decay scheme widely applicable to many geological processes and timescales. The $^{40}Ar/^{39}Ar$ technique was developed from the original K-Ar dating method and was first used by Merrihue and Turner (1966). The introduction of $^{40}Ar/^{39}Ar$ dating, and particularly the step-heating method, greatly reduced the uncertainties associated with the original K-Ar technique, which requires dual measurements on separate sample aliquots rather than a single isotopic ratio analysis, and is also less amenable to testing model assumptions. The relevant background information for the application of $^{40}Ar/^{39}Ar$ to basaltic lavas is presented below. For a more comprehensive overview of the principles, technical aspects and different applications of $^{40}Ar/^{39}Ar$ geochronology see McDougall and Harrison (1999).

4.3.1.1 Application of $^{40}Ar/^{39}Ar$ geochronology to lavas

When investigating the eruption ages of lava samples, the underlying assumption for the K-Ar decay system is that all the radiogenic argon ($^{40}Ar^*$) produced in situ from the decay of ^{40}K since the time of sample cooling has been retained within the solid phases in the rock. However, samples will also contain a proportion of pre-existing radiogenic

^{40}Ar, which must be corrected for during the age calculation. Magma at or near the Earth's surface is generally assumed to have degassed and equilibrated with the isotopic composition of atmospheric argon. The initial ratio between argon isotopes in the sample upon cooling will therefore approximate the atmospheric value of $^{40}Ar/^{36}Ar$ = 295.5. Assuming complete pre-solidification degassing and equilibration, the total ^{40}Ar measured in a cooled lava sample ($^{40}Ar_T$) will be equal to the product of the ^{40}Ar produced during in-situ decay of ^{40}K since the time of cooling ($^{40}Ar^*$) plus the portion of atmospheric ^{40}Ar present following degassing ($^{40}Ar_A$). Using the ^{36}Ar isotope to quantify the amount of $^{40}Ar_A$ present, the radiogenic argon produced in situ is given by $^{40}Ar^* = {}^{40}Ar_T - ({}^{36}Ar_A \times 295.5)$. However, if degassing prior to cooling is incomplete, some extra or 'excess' ^{40}Ar may remain in the sample and lead to an anomalously old apparent age (as it will be considered to be $^{40}Ar^*$). One approach to testing this assumption and identifying any excess ^{40}Ar is to analyse samples using an incremental or step heating method, rather than one single fusion and analysis. Data collected during step heating experiments allows the initial $^{40}Ar/^{36}Ar$ ratio of the sample to be estimated and therefore deviations from the atmospheric value to be identified (Lanphere and Dalrymple, 1976). Removing phenocrysts, or avoiding porphyritic samples, can help reduce the risk of analyzing material that has not completely degassed.

The original K-Ar dating technique required the measurement of the total concentration of elemental K in the sample. This value was then used to calculate the amount of ^{40}K present using the known (natural) ratio between $^{40}K/^{39}K$. The $^{40}Ar/^{39}Ar$ technique avoids dual measurements for K and Ar by using the ^{39}Ar isotope as a proxy for ^{40}K. To achieve this, samples must first be irradiated in a nuclear reactor, converting a proportion of the ^{39}K present to ^{39}Ar ($^{39}Ar_K$). Measurement of $^{39}Ar_K$ in an irradiated sample can then be used as a proxy for ^{39}K, which, using the known $^{39}K/^{40}K$ ratio, is

then used to calculate the concentration of ^{40}K. Since during neutron bombardment only a small percentage of ^{39}K will be converted to $^{39}Ar_K$ a reactor constant (the *J-value*) is also required for this calculation. The *J-value* is determined by co-irradiation and analysis of a standard material with an accurately known K/Ar ratio and age. In addition to the production of $^{39}Ar_K$ from ^{39}K, irradiation also induces numerous other nuclear reactions. Some of these are relevant to the $^{40}Ar/^{39}Ar$ measurement, as their products cause interferences during the isotopic analysis. The most important of these are the production of ^{36}Ar, ^{37}Ar, ^{39}Ar from Ca, ^{40}Ar from K and in some cases ^{36}Ar from Cl. For example, as the correction for atmospheric $^{40}Ar_A$ is made using the measured ratio of $^{40}Ar/^{36}Ar$, any additional ^{36}Ar produced from Ca must be quantified and corrected for. Correction factors for Ar isotopes produced by irradiation of Ca can be found by irradiation and analysis of a pure Ca salt (e.g. fluorite). As ^{37}Ar is a negligible component of atmospheric argon, any measured ^{37}Ar is likely to be produced from Ca and can be used to calculate correction factors for $(^{39}Ar/^{37}Ar)_{Ca}$ and $(^{36}Ar/^{37}Ar)_{Ca}$. Data on the interference isotopes can also be used to calculate apparent K/Ca and K/Cl ratios for each temperature step, providing information on the degassing behaviour of different phases throughout the heating experiment.

4.3.1.2 Age interpretation

During step-heating experiments samples are progressively heated (at ~10-50 °C increments) in a vacuum and the gas released during each step extracted and analysed with a mass spectrometer. As higher temperature increments are reached nuclides from lattice sites with progressively stronger bonds are released and analysed. Five argon isotopes are measured, ^{36}Ar, ^{37}Ar, ^{38}Ar ^{39}Ar and ^{40}Ar, allowing both the sample age and interferences to be calculated. Following the corrections for interferences, atmospheric

argon and system blanks discussed above the $^{40}Ar^*$ and $^{39}Ar_K$ values can be calculated and the sample age (t) found using the $^{40}Ar/^{39}Ar$ age equation:

$$t = \frac{1}{\lambda}\ln\left(\frac{^{40}Ar*}{^{39}Ar_K}J + 1\right)$$

where λ is the ^{40}K decay constant and J the reactor constant. For a detailed derivation of this relation see McDougal and Harrison (1999). During the step heating experiments an apparent age can be determined using this equation for each temperature step. Fig 4.2 shows a schematic example of two commonly used plots to interpret data from step heating measurements. Plotting the age spectrum against the cumulative percentage of ^{39}Ar gas released (Fig. 4.2a) allows, if present, a 'plateau' of concordant ages to be recognized in the age spectra. A weighted mean plateau age can be calculated from these steps and a test of statistical significance applied. Although there is no universally accepted criteria, age plateaus should typically consist of temperature steps where consecutive ages for individual step do not vary beyond the 2σ error and at least 50% of the released ^{39}Ar is incorporated within the plateau steps (McDougall and Harrison, 1999). An isochron diagram can also be constructed by dividing the measured ^{40}Ar and ^{39}Ar from each heating step by ^{36}Ar and plotting $^{39}Ar/^{36}Ar$ vs. $^{40}Ar/^{36}Ar$ (Fig 4.2b). In a concordant sample, or series of plateau forming temperature steps, the slope of a line through these points will be proportional to the sample age and the initial $^{40}Ar/^{36}Ar$ ratio given by the y-axis intercept. If the sample has fully degassed and equilibrated with the atmosphere prior to cooling then this initial $^{40}Ar/^{39}Ar$ value will equal the atmospheric value of 295.5. A plateau age interpretation is only considered meaningful if the data from its constituent temperature steps can be used to construct an isochron with a concordant age and an initial $^{40}Ar/^{39}Ar$ value within 2σ of the atmospheric value.

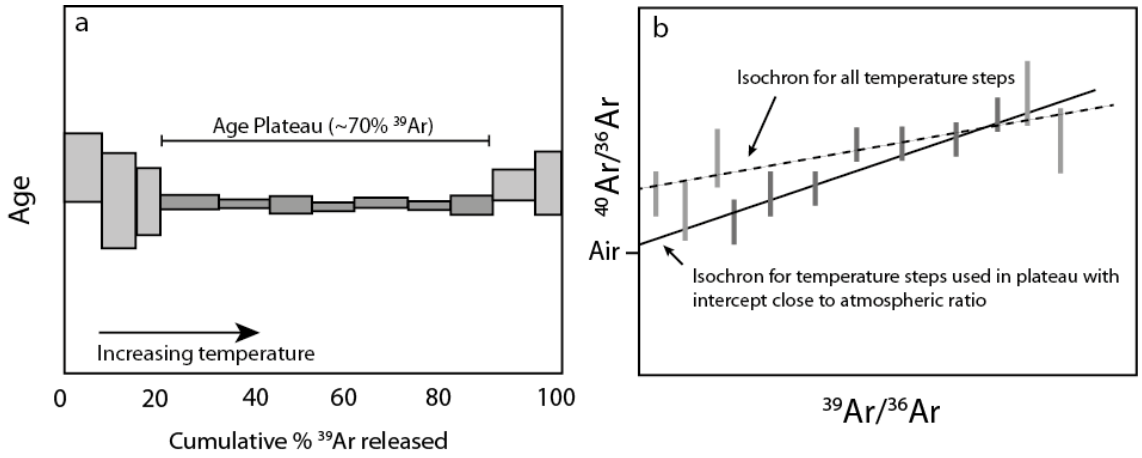

Figure 4.2 Schematic examples of graphical interpretation of $^{40}Ar/^{39}Ar$ age data for step heating analyses. (a) Plot of cumulative ^{39}Ar gas released during step heating versus apparent age for each temperature step. Each box represents one heating interval during which all the gas released is extracted and analysed. An age for each step is calculated using the age equation in the text and the size of the box reflects the 2-sigma error in the age calculation. A plateau age is calculated from temperature steps which incorporate at least ~50% of ^{39}Ar released and where consecutive steps have ages within 2-sigma error. (b) Isochron diagram constructed by plotting $^{39}Ar/^{36}Ar$ vs. $^{40}Ar/^{36}Ar$. The model assumption of complete degassing prior to cooling can be assessed by the y-intercept of the regression line, which should approximate the atmospheric values (air). A plateau age is generally only accepted if the constituent steps can be used to construct a suitable isochron line.

4.3.1.3 Analysis of young low-K lavas

The $^{40}Ar/^{39}Ar$ technique has been well established as a method for determination the age of volcanic rocks and has been successfully applied to dating young geological materials (e.g. Chen et al, 1996; Singer and Pringle, 1996; Renne et al., 1997; Heizler et al., 1999; Singer et al., 2004; Calvert and Lanphere, 2006; Lanphere et al., 2007; Lipman and Calvert, 2011). As this technique is based on the decay of ^{40}K, mafic lavas, which are typically low in K, present particular analytical challenges due to the lower radiogenic yields and measurements must be of sufficient precision to resolve the $^{40}Ar/^{39}Ar$ in the sample from the atmospheric value. Obtaining isotopic data of sufficient precision for young low-K basalts therefore requires careful sample preparation and analysis to minimize other sources of error. The use of a step-heating approach (rather than total fusion) when analysing young basaltic samples allows a more robust interpretation of the analytical data and resulting age calculation. The preparation and analytical methods used here were developed at the USGS argon lab in

Menlo Park, California (e.g. Calvert & Lanphere, 2006), where these analyses were also performed.

4.3.2 Sample preparation and analysis

A major issue when analyzing basaltic lavas is the effect of hypocrytalline textures on the retention of the $^{39}Ar_K$ isotope within the sample. An assumption of the age model used for the step-heating analysis is that the $^{39}Ar_K$ is distributed in similar way to the ^{40}K. However, the reactor-induced decay of ^{39}K to $^{39}Ar_K$ has a range of associated recoil energies, which may result in migration (recoil) of the $^{39}Ar_K$ nuclide. This effect can be problematic when using fine-grained or glass rich samples, where the recoil distances are likely to be largest (e.g. Dalrymple and Clague, 1976). The effect of recoil may be the loss of the $^{39}Ar_K$ isotope altogether due to migration out of the sample or it may be re-distributed within the sample, moving from low temperature high-K minerals to high temperature low-K phases. The first scenario will result in anomalously old apparent ages for some temperature steps, while the latter can significantly disturb the age spectra. Samples for this study were selected following thin section analysis in order to attempt to minimize the detrimental effects of glassy, porphyritic and vesicular textures and to identify the appropriate target size fraction for a groundmass separate.

Following sample selection, a few 100 grams of material was crushed and sieved to separate out the desired size fraction (typically ~250-350 μm). This fraction was then cleaned thoroughly in an ultrasonic bath with several rinses of deionized water and isopropyl alcohol. After drying, the proportion of groundmass material was increased by passing the sample through a magnetic separator. Around 250 mg of material was then handpicked from the final residue using a binocular microscope. The picked

sample was wrapped in 0.5 mm thick Cd foil and placed in a quartz vial and irradiated for 1-2 hours (depending on sample batch, see appendix A) in the central thimble of the USGS's TRIGA reactor in Denver, Colorado, along with a sample of the mineral standard Taylor Creek sanidine (TCR-2; accepted age of 27.87 Ma) as a neutron flux monitor. K-glass and fluorine were also co-irradiated to correct for interfering isotopes from K and Ca. The isotopic analyses were performed on the irradiated samples at the USGS argon lab in Menlo Park. A complete description of the analytical procedure can be found in appendix A.

4.3.3 Results

The results of the geochronological analyses are listed in table 4.1 and the locations of samples with interpreted ages on the map in Fig 4.3. Graphical results of the $^{40}Ar/^{39}Ar$ analysis for 14 samples are shown in Fig 4.4. Tabulated data from each step of all the step-heating experiments can be found in appendix A. With the exception of two samples all of the interpreted ages used here are weighted mean plateau ages that include at least 60% of the total ^{39}Ar gas released. Plateau ages however were not possible for two samples, SA02 and 2802. 2802 appears to have been strongly affected by recoil in the reactor and the total gas interpretation is therefore considered the most reliable. For sample SA02 the isochron age (with a low intercept) is the preferred age interpretation, as the plateau produces a negative age; however the isochron has a large uncertainty and this age is not used in the analysis below. Samples from the main section of the rift have an age range of ~30 to 200 ka, while those from the off-rift Badi-Dabbayra region yield ages of ~25 to 450 ka. Uncertainties in the age data are typically ~10 - 20% (2σ).

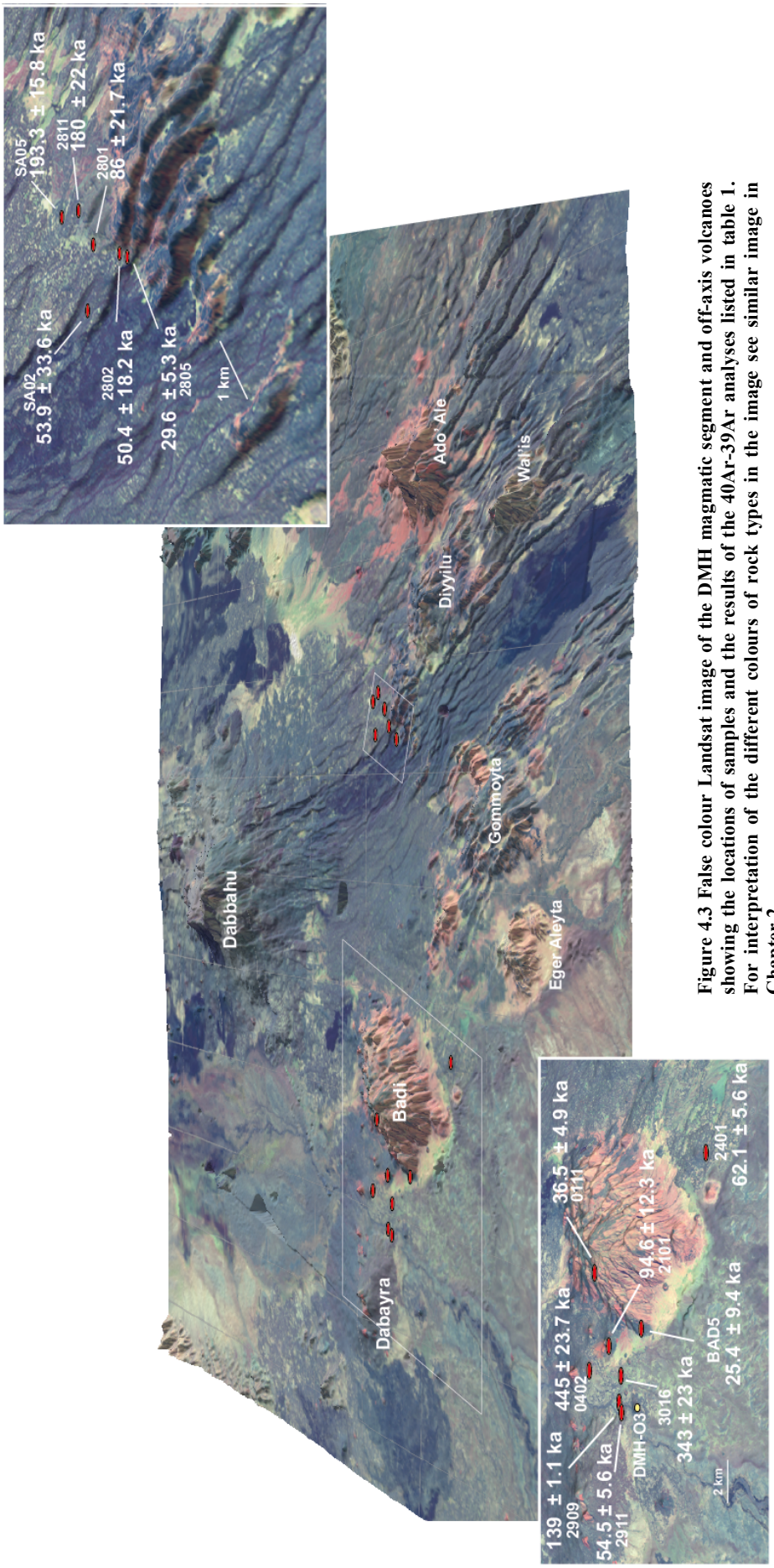

Figure 4.3 False colour Landsat image of the DMH magmatic segment and off-axis volcanoes showing the locations of samples and the results of the 40Ar-39Ar analyses listed in table 1. For interpretation of the different colours of rock types in the image see similar image in Chapter 2

Table 4.1 $^{40}Ar/^{39}Ar$ age data for lavas from DMH segment and Badi-Dabbayra volcanoes

Sample	Mg#	Plateau			Interpreted	Isochron				Total Gas
		%^{39}Ar[steps, °C)	Age (ka)	MSWD	Age (ka)	%^{39}Ar[steps, °C]	Age (ka)	MSWD	$^{40}Ar/^{36}Ar_i$	**Age (ka)**
2805	57	100 (10 of 10)	**29.6 ± 5.3**	0.18	**29.6 ± 5.3**	100[550-1100]	23.9 ± 8.8	0.15	296.5 ± 2.7	34.9 ± 8.1
SA02	60	63 (700-1000)	-6.6 ± 11.2	1.34	**52.9 ± 33.6***	67(650-1000]	**52.9 ± 33.6**	1.45	291.9 ± 1.8	-36.0 ± 11.3
2802	57	63 (8 of 13)	-8.8 ± 24.7	0.71	**50.4 ± 18.2**†	63[550-895]	-109.9 ± 62.3	1.03	297.4 ± 2.5	**50.4 ± 18.2**
2801	59	100 (20 of 20)	**86.0 ± 21.7**	2.87	**86.0 ± 21.7**	100[550-1100]	97.0 ± 39.5	5.67	295.2 ± 1.7	76.4 ± 11.6
2811	59	60 (7 of 14)	**179.8 ± 22.0**	0.18	**179.8 ± 22.0**	60[675-975]	165.0 ± 78.5	0.4	295.8 ± 3.6	43.7 ± 16.2
SA05	49	64 (9 of 16)	**193.3 ± 15.8**	0.2	**193.3 ± 15.8**	64[615-940]	231.2 ± 50.9	0.33	294.5 ± 2.9	150.2 ± 10.7
BAD5	59	77 (9 of 10)	**25.4 ± 9.4**	0.37	**25.4 ± 9.4**	77[550-975]	55.0 ± 26.2	0.46	293.9 ± 3.1	51.6 ± 8.3
3016	54	100(12of 12)	**342.5 ± 23.4**	2.44	**342.5 ± 23.4**	100[550-1100]	312.3 ± 118.6	3.94	296.4 ± 8.4	353.2 ± 12.1
0402	61	94 (12 of 13)	**444.9 ± 23.7**	0.5	**444.9 ± 23.7**	94[550-1050]	429.3 ± 41.1	0.94	295.8 ± 1.4	462.7 ± 25.7
2911	57	59 (6 of 10)	**54.5 ± 5.6**	0.81	**54.5 ± 5.6**	59[750-1100]	64.410 ± 19.373	0.93	294.5 ± 4.6	100.4 ± 4.4
0111	62	98 (13 of 14)	**36.5 ± 4.9**	1.22	**36.5 ± 4.9**	98[550-1275]	40.5 ± 11.0	2.1	295.1 ± 2.1	42.7 ± 4.5
2401	64	61 (6 of 11)	**62.1 ± 5.6**	0.4	**62.1 ± 5.6**	61[800-1100]	59.1 ± 13.0	0.55	296.0 ± 4.5	91.7 ± 5.0
2101	57	62 (8 of 13)	**94.6 ± 12.3**	0.4	**94.6 ± 12.3**	62[550-900]	179.9 ± 116.0	0.65	292.0 ± 8.5	142.8 ± 8.6
2909	27	78 (8 of 11)	**138.9 ± 1.1**	0.78	**138.9 ± 1.1**	78[700-1150]	140.6 ± 1.6	0.82	294.0 ± 2.4	139.9 ± 1.1

$^{40}Ar/^{36}Ar_i$ is the ratio at intercept and MSWD is the mean squared weighted deviate. All accepted plateaus are defined by at least 60% of ^{39}Ar released and have a $^{40}Ar/^{36}Ar_i$ value within 2-sigma of the atmospheric value (295.5) on an isochron plot (see plots in Figure 4.5).
Full analytical descriptions and data tables are in the appendix.
***SA02 yields an isochron age with a low $^{40}Ar/^{36}Ar$ intercept.**
†2802 was strongly affected by ^{39}Ar recoil in the reactor; we therefore interpret the total gas age as most reliable.
Mg#'s are taken from table 5.1

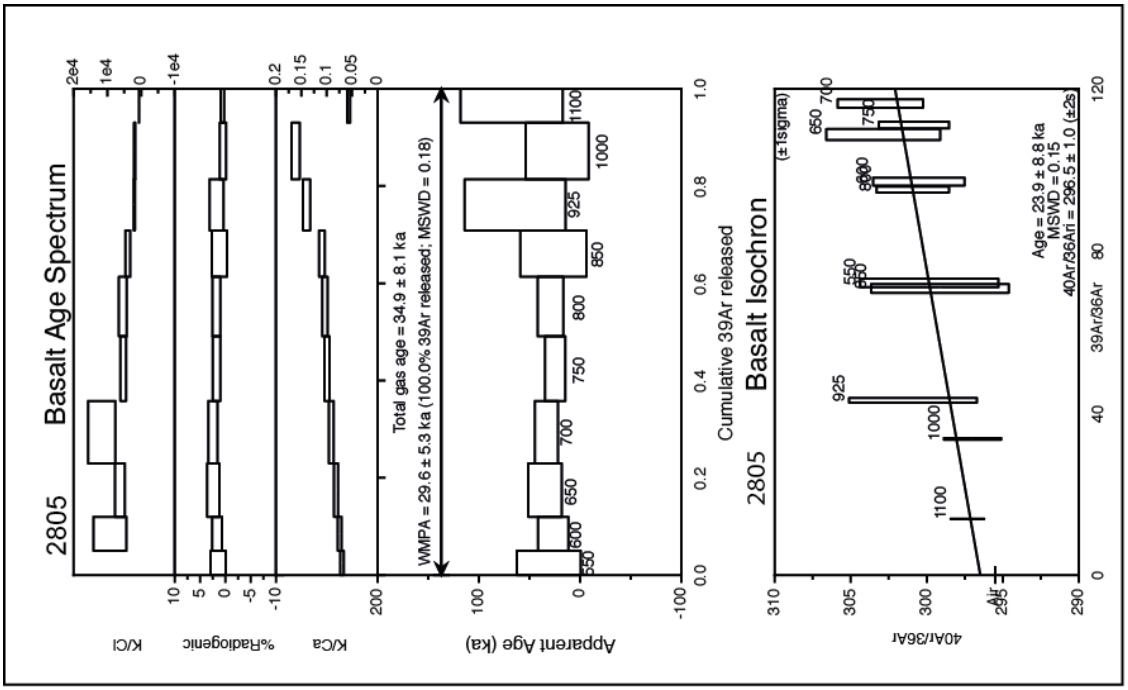
2805 Basalt Age Spectrum
Total gas age = 34.9 ± 8.1 ka
WMPA = 29.6 ± 5.3 ka (100.0% 39Ar released; MSWD = 0.18)
Apparent Age (ka)
Cumulative 39Ar released
2805 Basalt Isochron
(±1sigma)
Age = 23.9 ± 8.8 ka
MSWD = 0.15
40Ar/36Ari = 296.5 ± 1.0 (±2s)
40Ar/36Ar
39Ar/36Ar

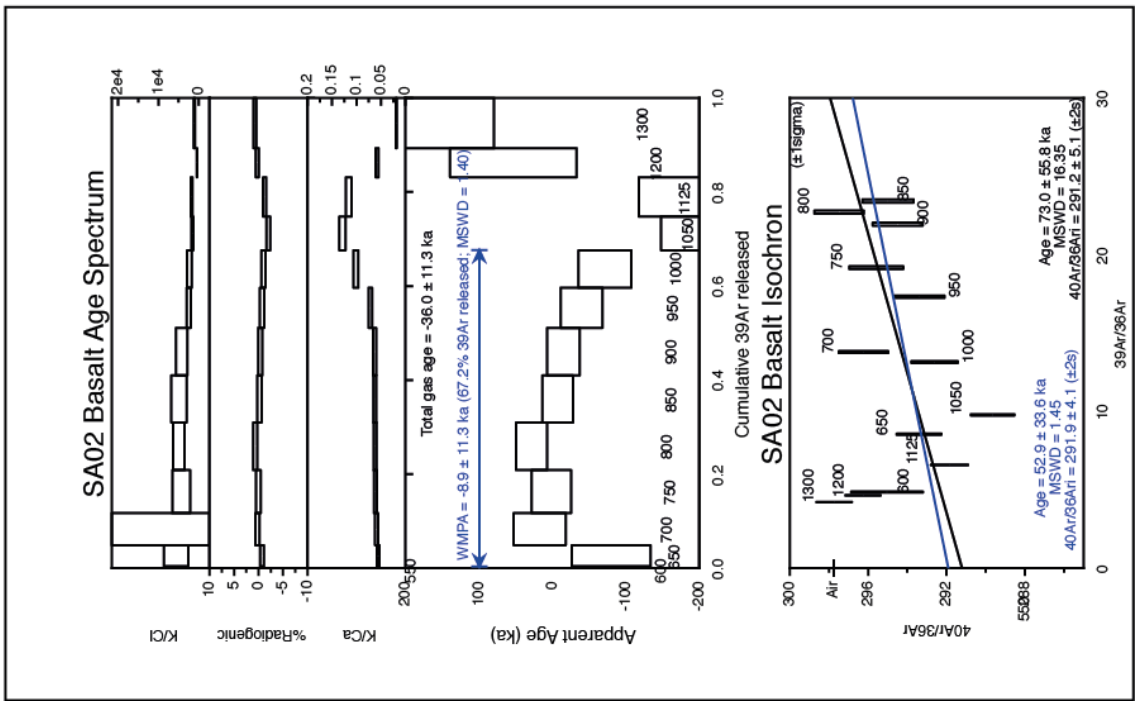
SA02 Basalt Age Spectrum
Total gas age = -36.0 ± 11.3 ka
WMPA = -8.9 ± 11.3 ka (67.2% 39Ar released; MSWD = 1.40)
Apparent Age (ka)
Cumulative 39Ar released
SA02 Basalt Isochron
(±1sigma)
Age = 73.0 ± 55.8 ka
MSWD = 16.35
40Ar/36Ari = 291.2 ± 5.1 (±2s)
Age = 52.9 ± 33.6 ka
MSWD = 1.45
40Ar/36Ari = 291.9 ± 4.1 (±2s)
40Ar/36Ar
39Ar/36Ar

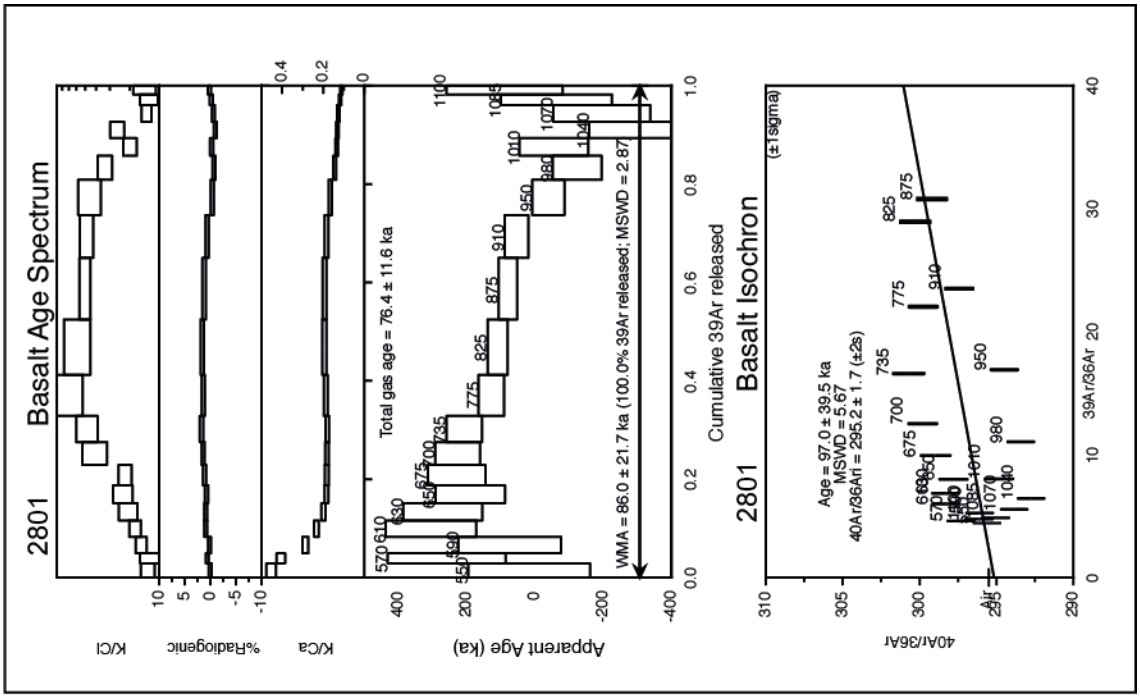
2801
Basalt Age Spectrum
Total gas age = 76.4 ± 11.6 ka
WMA = 86.0 ± 21.7 ka (100.0% 39Ar released; MSWD = 2.87
Apparent Age (ka)
K/Ca
%Radiogenic
K/Cl
Cumulative 39Ar released
2801
Basalt Isochron
(±1sigma)
Age = 97.0 ± 39.5 ka
MSWD = 5.67
40Ar/36Ari = 295.2 ± 1.7 (±2s)
40Ar/36Ar
39Ar/36Ar

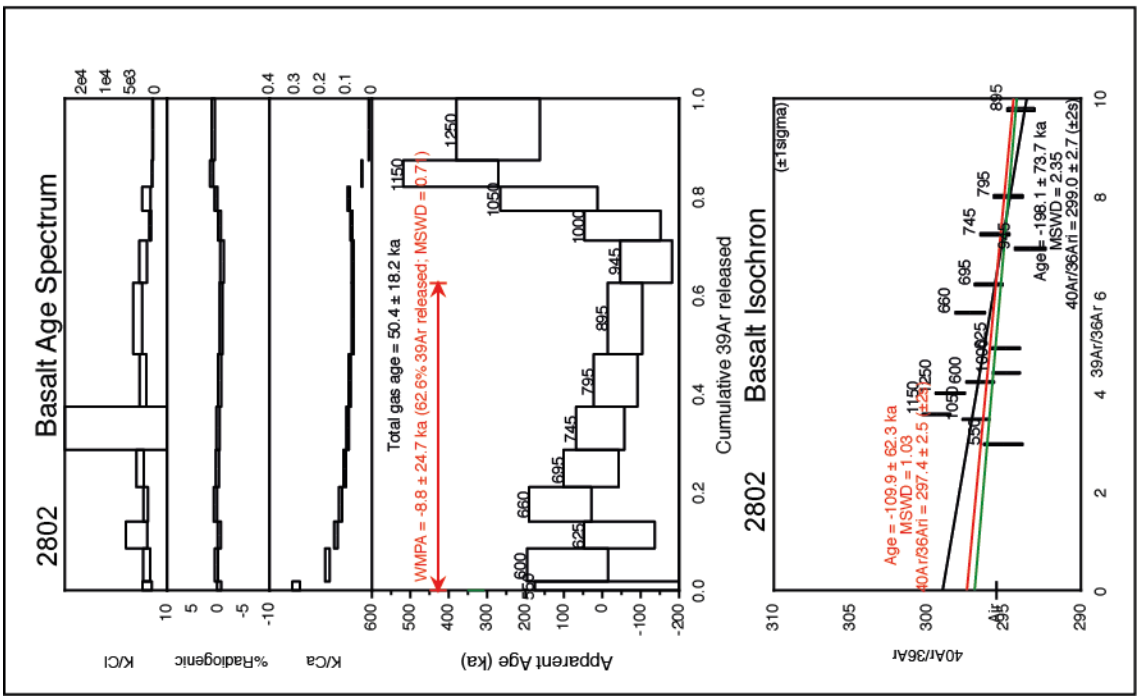
2802
Basalt Age Spectrum
Total gas age = 50.4 ± 18.2 ka
WMPA = -8.8 ± 24.7 ka (62.6% 39Ar released; MSWD = 0.71)
Apparent Age (ka)
K/Ca
%Radiogenic
K/Cl
Cumulative 39Ar released
2802
Basalt Isochron
(±1sigma)
Age = -109.9 ± 62.3 ka
MSWD = 1.03
40Ar/36Ari = 297.4 ± 2.5 (±2s)
Age = -198.1 ± 73.7 ka
MSWD = 2.35
40Ar/36Ari = 299.0 ± 2.7 (±2s)
40Ar/36Ar
39Ar/36Ar

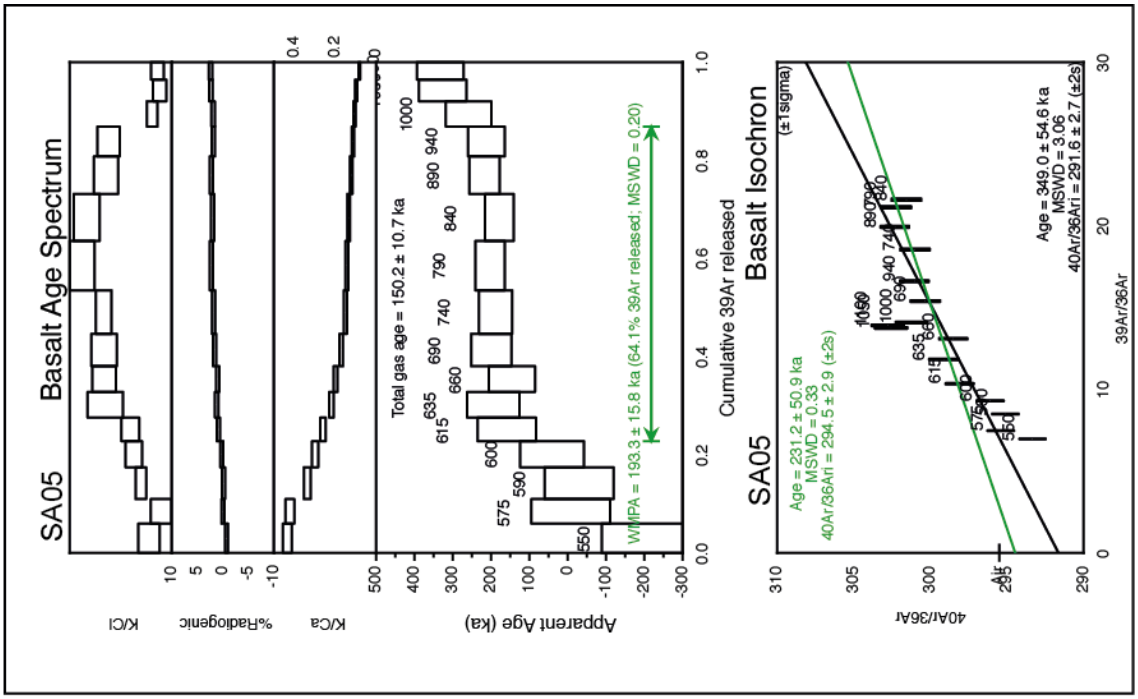
SA05
Basalt Age Spectrum
Total gas age = 150.2 ± 10.7 ka
WMPA = 193.3 ± 15.8 ka (64.1% 39Ar released; MSWD = 0.20)
Apparent Age (ka)
Cumulative 39Ar released
%Radiogenic
K/Ca
K/Cl
Basalt Isochron
(±1 sigma)
Age = 231.2 ± 50.9 ka
MSWD = 0.33
40Ar/36Ari = 294.5 ± 2.9 (±2s)
Age = 349.0 ± 54.6 ka
MSWD = 3.06
40Ar/36Ari = 291.6 ± 2.7 (±2s)
40Ar/36Ar
39Ar/36Ar

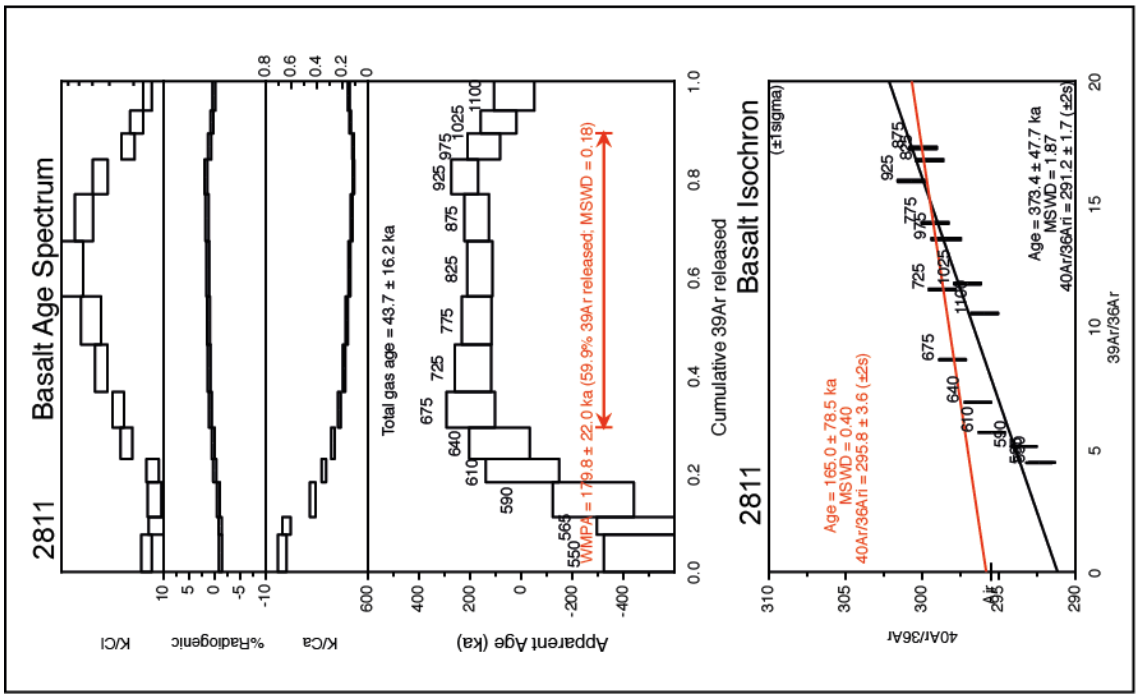
2811
Basalt Age Spectrum
Total gas age = 43.7 ± 16.2 ka
WMPA = 179.8 ± 22.0 ka (59.9% 39Ar released; MSWD = 0.18)
Apparent Age (ka)
Cumulative 39Ar released
%Radiogenic
K/Ca
K/Cl
Basalt Isochron
(±1 sigma)
Age = 165.0 ± 78.5 ka
MSWD = 0.40
40Ar/36Ari = 295.8 ± 3.6 (±2s)
Age = 373.4 ± 47.7 ka
MSWD = 1.87
40Ar/36Ari = 291.2 ± 1.7 (±2s)
40Ar/36Ar
39Ar/36Ar

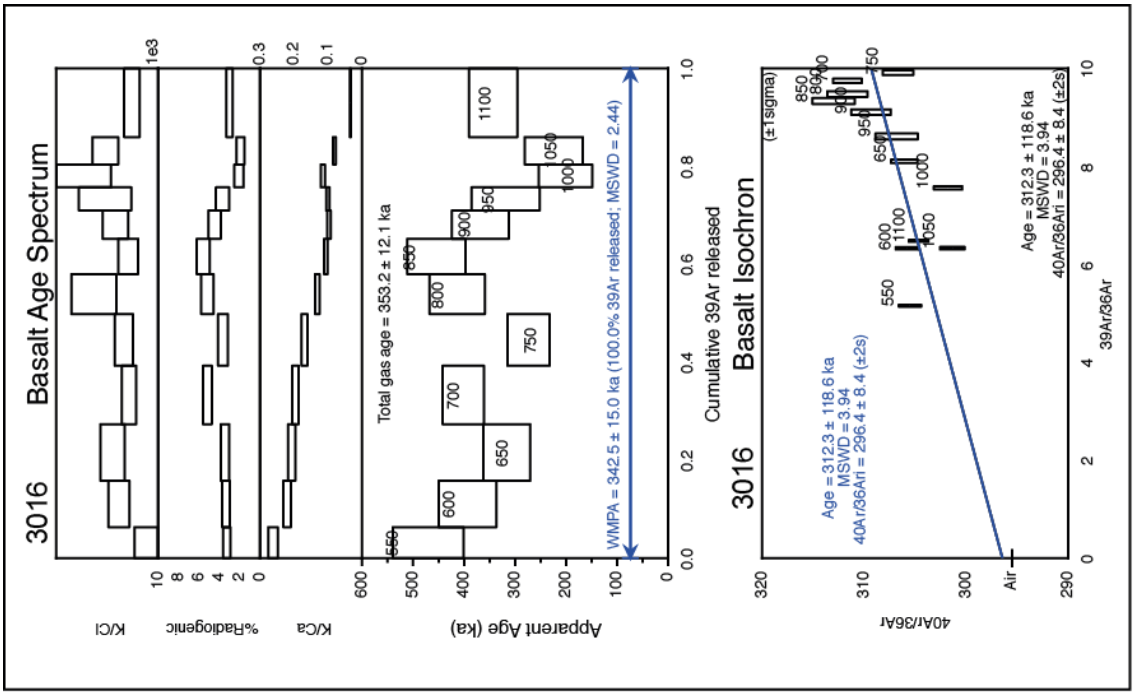
3016
Basalt Age Spectrum
Total gas age = 353.2 ± 12.1 ka
WMPA = 342.5 ± 15.0 ka (100.0% 39Ar released: MSWD = 2.44)
Apparent Age (ka)
Cumulative 39Ar released
K/Ca
%Radiogenic
K/Cl
3016
Basalt Isochron
(±1 sigma)
Age = 312.3 ± 118.6 ka
MSWD = 3.94
40Ar/36Ari = 296.4 ± 8.4 (±2s)
40Ar/36Ar
39Ar/36Ar
Air

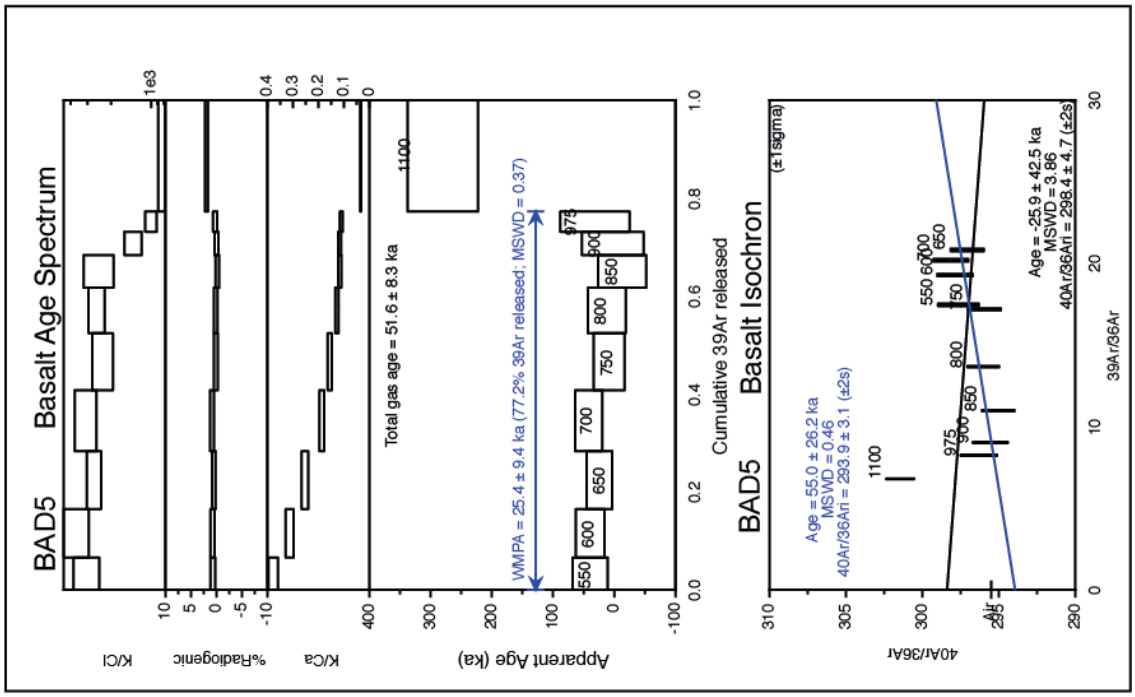
BAD5
Basalt Age Spectrum
Total gas age = 51.6 ± 8.3 ka
WMPA = 25.4 ± 9.4 ka (77.2% 39Ar released: MSWD = 0.37)
Apparent Age (ka)
Cumulative 39Ar released
K/Ca
%Radiogenic
K/Cl
BAD5
Basalt Isochron
(±1 sigma)
Age = 55.0 ± 26.2 ka
MSWD = 0.46
40Ar/36Ari = 293.9 ± 3.1 (±2s)
Age = -25.9 ± 42.5 ka
MSWD = 3.86
40Ar/36Ari = 298.4 ± 4.7 (±2s)
40Ar/36Ar
39Ar/36Ar
Air

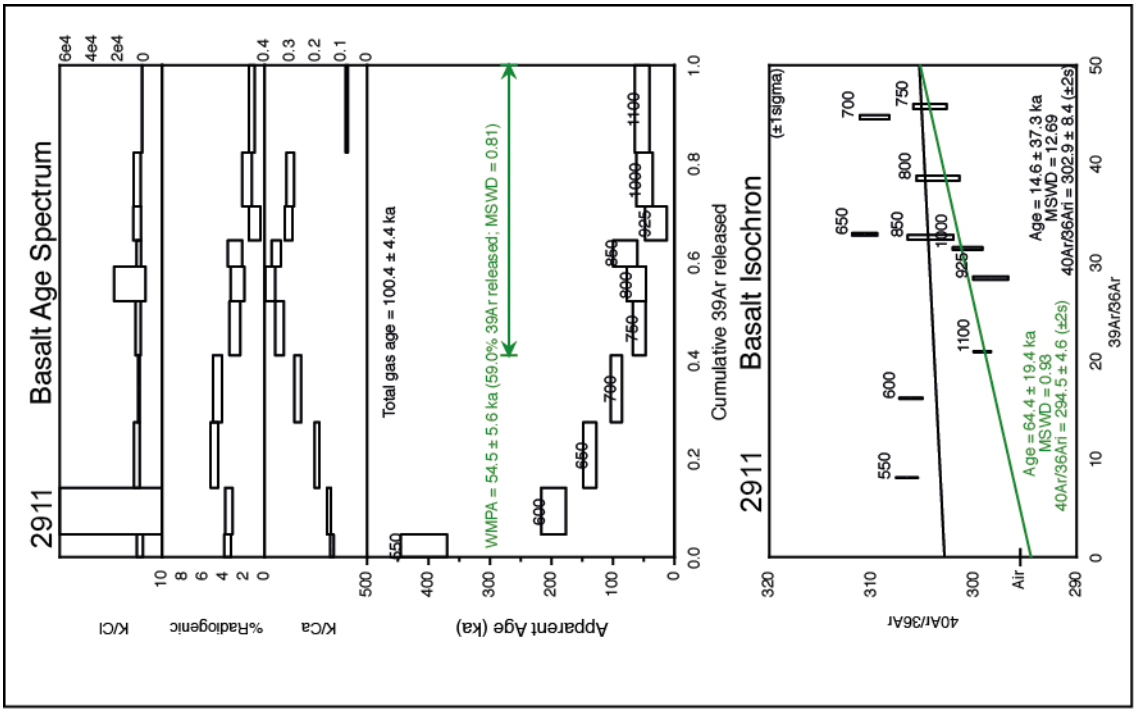
2911
Basalt Age Spectrum
Total gas age = 100.4 ± 4.4 ka
WMPA = 54.5 ± 5.6 ka (59.0% 39Ar released; MSWD = 0.81)
Apparent Age (ka)
Cumulative 39Ar released
K/Ca
%Radiogenic
K/Cl
2911
Basalt Isochron
(±1sigma)
Age = 64.4 ± 19.4 ka
MSWD = 0.93
40Ar/36Ari = 294.5 ± 4.6 (±2s)
Age = 14.6 ± 37.3 ka
MSWD = 12.69
40Ar/36Ari = 302.9 ± 8.4 (±2s)
40Ar/36Ar
39Ar/36Ar
Air

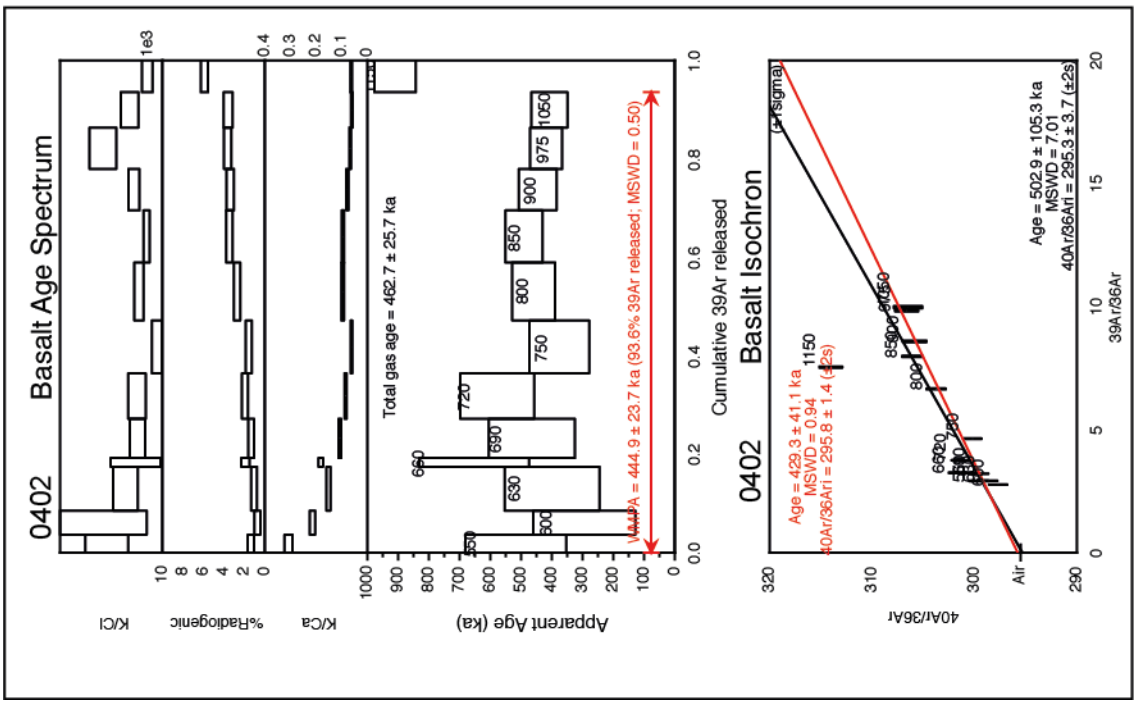
0402
Basalt Age Spectrum
Total gas age = 462.7 ± 25.7 ka
WMPA = 444.9 ± 23.7 ka (93.6% 39Ar released; MSWD = 0.50)
Apparent Age (ka)
Cumulative 39Ar released
K/Ca
%Radiogenic
K/Cl
0402
Basalt Isochron
(±1sigma)
Age = 429.3 ± 41.1 ka
MSWD = 0.94
40Ar/36Ari = 295.8 ± 1.4 (±2s)
Age = 502.9 ± 105.3 ka
MSWD = 7.01
40Ar/36Ari = 295.3 ± 3.7 (±2s)
40Ar/36Ar
39Ar/36Ar
Air

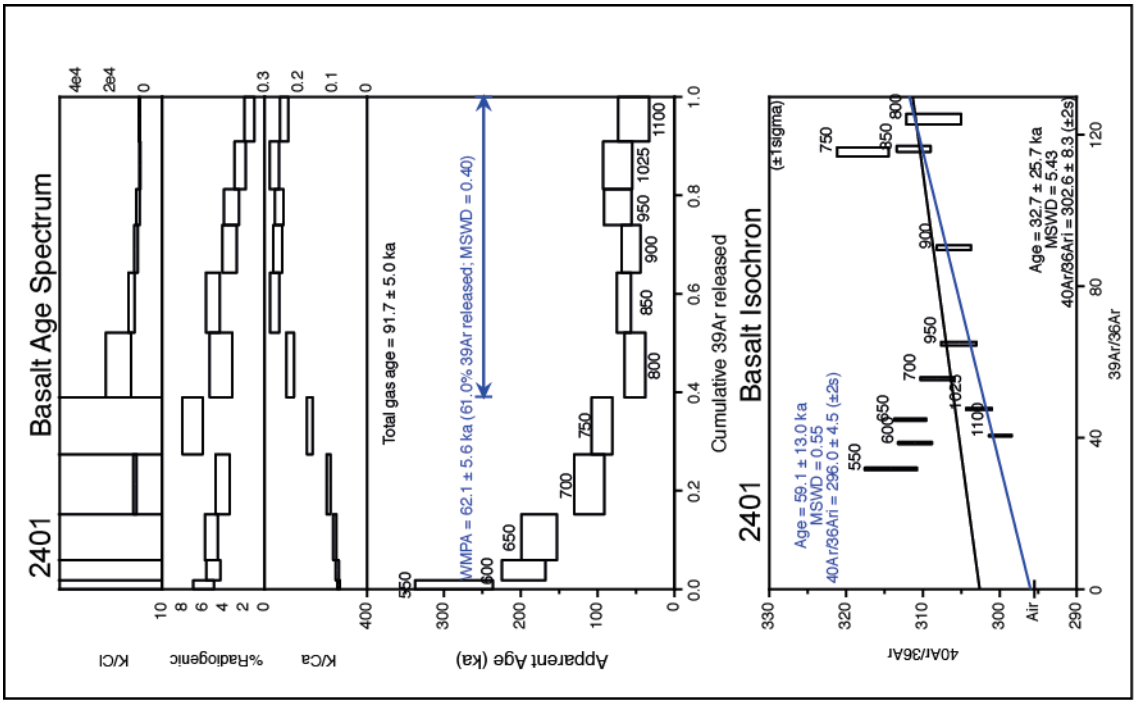
2401
Basalt Age Spectrum
Total gas age = 91.7 ± 5.0 ka
WMPA = 62.1 ± 5.6 ka (61.0% 39Ar released; MSWD = 0.40)
Apparent Age (ka)
Cumulative 39Ar released
K/Ca
%Radiogenic
K/Cl
2401
Basalt Isochron
(±1sigma)
Age = 59.1 ± 13.0 ka
MSWD = 0.55
40Ar/36Ari = 296.0 ± 4.5 (±2s)
Age = 32.7 ± 25.7 ka
MSWD = 5.43
40Ar/36Ari = 302.6 ± 8.3 (±2s)
Air
40Ar/36Ar
39Ar/36Ar

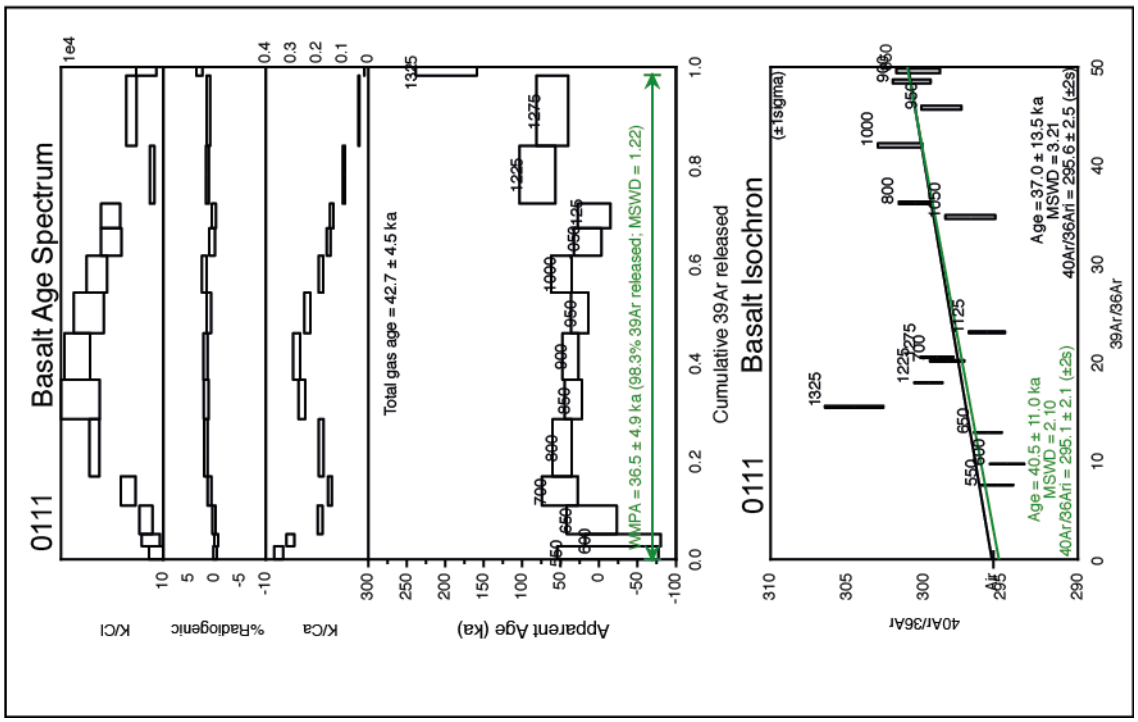
0111
Basalt Age Spectrum
Total gas age = 42.7 ± 4.5 ka
WMPA = 36.5 ± 4.9 ka (98.3% 39Ar released; MSWD = 1.22)
Apparent Age (ka)
Cumulative 39Ar released
K/Ca
%Radiogenic
K/Cl
0111
Basalt Isochron
(±1sigma)
Age = 40.5 ± 11.0 ka
MSWD = 2.10
40Ar/36Ari = 295.1 ± 2.1 (±2s)
Age = 37.0 ± 13.5 ka
MSWD = 3.21
40Ar/36Ari = 295.6 ± 2.5 (±2s)
Air
40Ar/36Ar
39Ar/36Ar

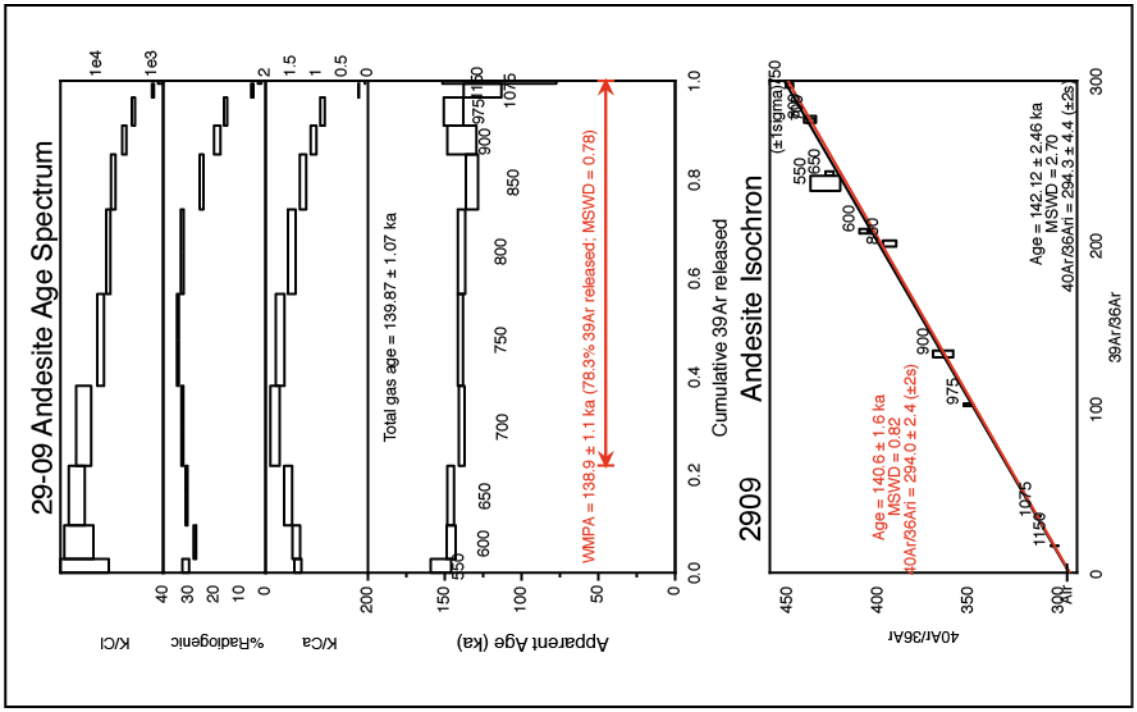

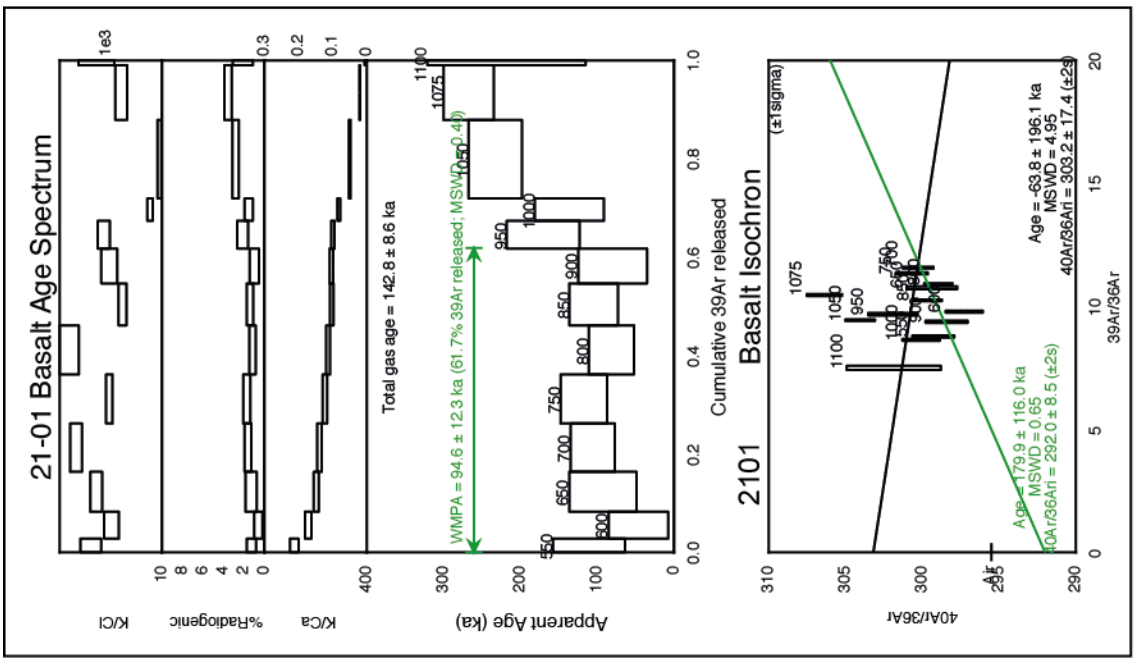

Figure 4.4 ^{40}Ar-^{39}Ar age spectra and isochron plots for lavas from the eastern flank of the DMH segment (samples: SA02, 2805, 2802, 2801, 2811, SA05) and off-axis basalts around the Badi-Dabbayra volcanoes (Samples: BAD5, 3016, 0402, 2911, 0111, 2401, 2101, 2909). See Figure 4.2 for a schematic example of these plots. Also included are K/Cl and K/Ca ratios measured during degassing, which aid the age interpretation (see text). WMPA stands for Weighted Mean Plateau Age and indicates the temperature steps used for the age plateau. MSWD is the Mean Square Weighted Deviate. Text in isochron plots is colour coded according to the colour of the regression lines, which are plotted for both the plateau steps (coloured lines) and the total gas released (black). The Locations of samples is shown in Figure 4.3 and interpreted ages listed in Table 4.1. Age plateaus were not possible for samples SA02 and 2802. SA02 yields an isochron age with a low $^{40}Ar/^{36}Ar$ intercept and this is used as a guideline age only. 2802 was strongly affected by recoil in the reactor and it is considered therefore that the total gas age is the most reliable.

4.4 Discussion 1

The discussion part of this chapter is divided into two sections: the first examines the age data from the main DMH segment and the implications of this for the formation/development of the rift zone history of Afro-Arabian extension; the second investigates the volcanic history on the rift margin at the Badi-Dabbayra transverse volcanic lineation and structural interactions between this and the DMH segment.

4.4.1 The formation of magmatic rift segments

A major outstanding issue in understanding the development of the axial rift segments in Afar is a lack of quantitative temporal constraints on their formation. The model of rift evolution by Hayward and Ebinger (1996) (illustrated in Chapter 1, Fig 1.6), which is based on empirical observations in East Africa, predicts that as rifting progresses and the elastic thickness of the lithosphere decreases, the response of the thinning lithosphere to extension will evolve from movement on large graben bounding faults to the formation of a narrow intra-graben fault system. Providing there is a sufficient melt supply, magmatism then becomes focused along this new narrow axial zone and extension via dyke intrusion becomes dominant. The implication of this model is that the formation of an oceanic type magma system, i.e. with melts delivered efficiently to the rift axis, develops as a result of the lithospheric response to extension. Although Models of rift formation such as Hayward and Ebinger (1996) are often based on empirical physical observations, they have not yet been tested by quantitative observational data on the surface processes they describe and the actual details of segment formation remain unclear. This is particularly true of the relation between the development of characteristic rift structures/morphology and the evolution in magmatic

processes. As the goal of these models is to explain a highly dynamic tectonic process, a key constraint when applying/testing these models is knowledge of the timescales over which important magmatic and structural features develop.

4.4.2 Contemporary magmatic activity at the DMH segment

The contemporary shallow level magma system at the DMH rift has been well characterised by seismic (Ayele et al. 2007; Ebinger et al. 2008; Ayele. et al. 2009; Keir et al. 2009; Belachew et al. 2011; Grandin et al., 2011), geodetic (Wright et al. 2006; Hamling et al. 2009, 2010; Grandin et al. 2009, 2010) and volcanological (Chapter 2) studies on the ~14 dyking events between 2005-2011. Earthquake locations and the modeled intrusion tracks from these studies are shown in Fig 4.5 and these events have provided clear evidence that the present day melt supply is strongly focused along the axial zone. The magma-dominated extension observed during this period has demonstrated that the DMH rift is currently at a level of maturity akin to an incipient spreading ridge (Hayward and Ebinger, 1996; Ebinger et al., 2010). A notable feature of the recent rifting is that in the northern part of the rift the observed instantaneous axis of extension is not at the centre of the axial graben, the assumed long-term axis, but is offset to the east by ~1-2 km. In contrast, intrusions (Hamling et al., 2009; Grandin et al., 2010) and eruptions (see Chapter 3) in the southern sector have been largely centred within the graben. However, faulting in both sectors during the largest intrusion in 2005 was asymmetric (Barisin et al., 2009), dominated by movements on westward dipping structures (Grandin et al., 2009).

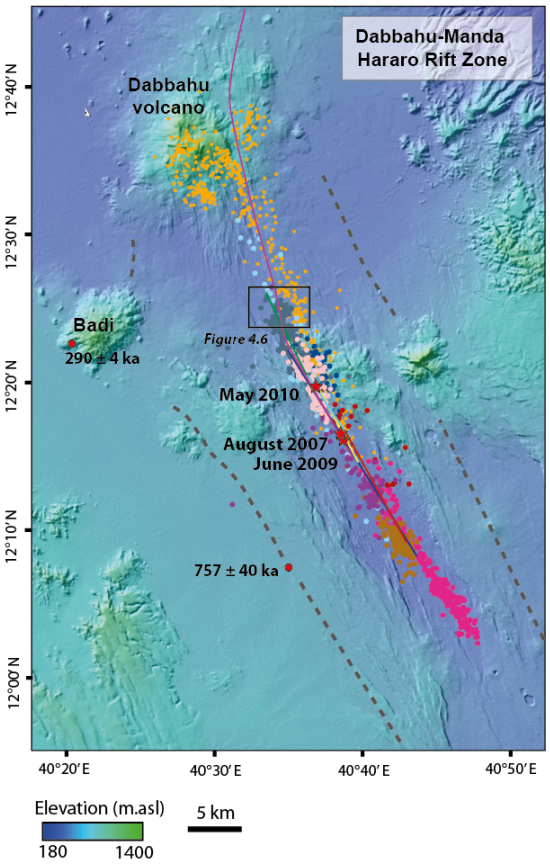

Figure 4.5 Locations of recent earthquakes (circles), dyke intrusions (coloured lines) and fissure eruptions (stars) long the axis of the DMH rift segment. Earthquakes are coloured according to groups of events during discrete dyke injections between 2005-2009. See Ebinger et al (2010) for details on individual events. Together this data all indicates that melt supply is strongly focused along the DMH axis, as is is the case for mature oceanic ridges. Two previous K-Ar ages are available for this region, one for a rhyolitic lava from Badi volcano (290 ± 4 ka) and one from a basaltic flow on the western margin of the rift (757 ± 40 ka) (Lahitte et al., 2003). Dyke models are by Hamling et al., 2009 and Grandin et al., 2009, 2010.

4.4.3 Geological constraints on volcanic processes

Field and remote sensing data shows that in terms of lava morphology there is little evidence of recent volcanism occurring outside of the axial graben (Fig. 4.3; see also Chapter 2), however, the intensity of faulting in flows on the rift flanks makes estimates of relative age based on erosional state very difficult and importantly makes reconstructions of individual flow units highly uncertain. It is therefore unclear where the lava flows forming the rift flanks originated and to what extent they are related to the present neo-volcanic zone. In common usage, the term "DMH magmatic segment" is applied to describe a region of closely spaced faulting that is formed from (primarily basaltic) lavas, which are inferred to be directly associated with rift-related volcanism along this rift zone. For example, early studies in Afar described these lavas as the

products of 'oceanic type volcanism' (i.e. Barberi et al., 1972) implying that they were emplaced in a similar way to lavas at mid-ocean ridges. However, faulting and brittle deformation associated with the emplacement of the largest dyke in the current phase in 2005 demonstrated that dyke-induced deformation, leading to the development of ocean-ridge type morphology, can affect areas located at least 4 km from the rift axis (e.g. Wright et al. 2006; Grandin et al. 2009; Rowland et al. 2007; see fault in 1.6d). Older, pre-DMH rift, lavas could therefore develop such structures *in situ* without being related to volcanism at the current rift segment. Understanding the magmatic development of the rift zone therefore involves understanding the history of volcanism and how it links to the extensional processes associated with the current tectonic regime.

Without a clear understanding of the volcanic architecture, which is not possible due to deformation, the interpretation of the age data with respect to rifting process is difficult, as factors such as flow length, direction etc are unknown. However, it is possible to construct some generalized constraints on the volcanic character of the rift zone, based on field/remote sensing observations and the recent magmatic activity, which can be used to guide the interpretation of the geochronological data.

4.4.3.1 Faulting and volcanism in the DMH segment

An important implication of the magmatic extension observed since 2005 is that magma intrusion along the DMH axis is capable of accommodating all Afro-Arabian extension (16-20 mm yr^{-1}; Vigny et al., 2006; McClusky et al., 2010) with a ~500 year intrusion cycle and there is no requirement for significant periods of amagmatic extension on faults (Rowland et al., 2007). Analysis of brittle deformation following the 2005 dyke intrusion led Rowland et al (2007) to conclude that dyke induced faulting (i.e. Rubin

and Pollard, 1988) may be the predominant mode of fault growth across the segment, demonstrating the important link between magmatism, extension and faulting. A notable feature of the present structure of the DMH rift is the well-defined axial graben, which is bounded by 30-100 m high fault scarps. In the northern sector, where the sample profile was collected, these faults represent a distinct topographic boundary between the graben and rift flanks are no structures of similar size exist between the graben and rift margin. The development of these faults therefore clearly marks an important phase in the structural evolution of the segment.

It is clear from field/remote sensing observations, such as those outlined in Chapter 2, that the most recent volcanic activity has occurred within the central graben at base of the central volcanic edifice. These observations are consistent with the eruptive activity observed since 2007 in the southern part of the rift zone (documented in Chapter 3). In the northern sector the youngest lavas are notable concentrated in the eastern part of the graben, while in the southern sector they are distributed across the graben centre. The 2007-2010 eruptions and the evidence from the less-deformed/eroded flows in the graben suggests that eruptions along the axis are typically of small magnitude, with relatively small erupted volumes (< 0.02 km^3) and short flow lengths (< 1 km), and that the transport of lava across the high graben bounding scarps is unlikely. It may be reasonable therefore to adopt the view that to a first-order lava transport over large distances is unlikely to have significantly disrupted the age profile of lavas. However, it may also be important to discriminate between lavas found inside and outside of the central graben, as this imposes a significant constraint on eruption locations (i.e. flows erupted after its formation are almost certainly confined there). The current accumulation of lavas in the axial graben adjacent to the sample profile suggests a neo-

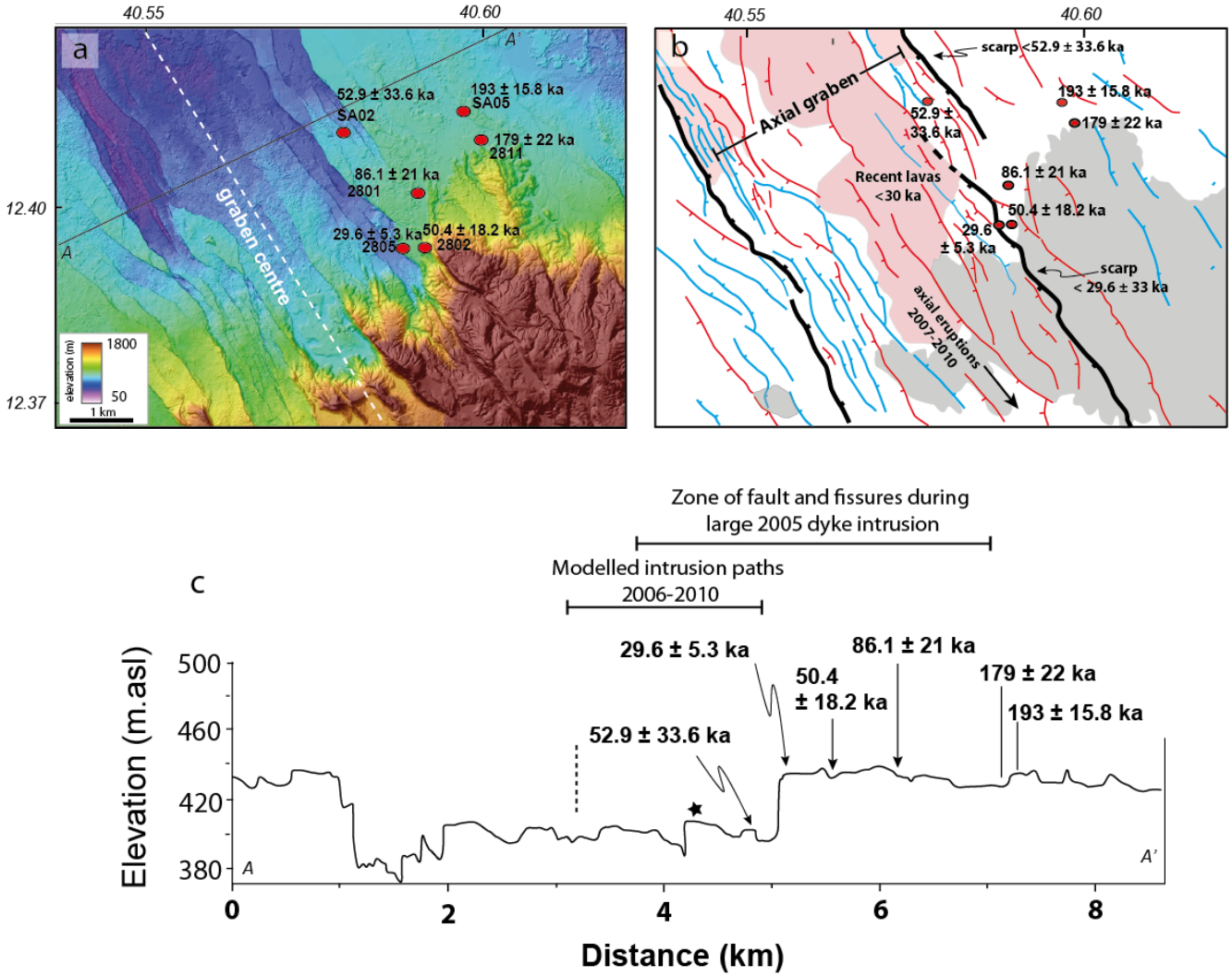

Figure 4.6 Detailed location map of 40Ar/39Ar ages from the eastern flank of the DMH rift. (a) LiDAR elevation map showing sample locations on the rift flank north of the Ado Ale Volcanic Complex. The central depression of the ~4 km wide axial graben can be clearly seen in the LiDAR data. (b) Map of the same region interpreted from the LIDAR data and SPOT imagery. Faults are coloured according to orientation; red faults have downthrows to the west and blue faults to the east, the thick black lines mark the large scarps marking the edge of the graben. The freshest looking basaltic lavas in the central graben are coloured red, silicic lavas of the AVC are coloured grey. The new Ar/Ar ages constrain the formation of the marginal faults in this region to < ~30 ka. (c) topographic section along the profile shown in (a). Ar/Ar ages projected onto the section are partly schematic due to the offset in the large fault and are drawn to reflect the position of sample relative to the axial graben. During the current rifting phase intrusions have been injected beneath the eastern part of the graben. The location of dykes injected between 2006 - 2009 are the best constrained as the 2005 intrusion was of such large magnitude that the location, from seismic or geodetic observations, is harder to model. Information on brittle deformation during the 2005 intrusion is from Rowland et al (2005). Dyke models from Hamling et al (2009) and Grandin et al (2009, 2010). The black star indicates the location of the 'zero-age' point identified by the regression of the Ar-Ar data discussed in the text and shown in fig 4.7.

volcanic zone ~2 km wide that is concentrated east of the topographic centre of the graben (see Fig 4.6).

4.4.4 Interpretation of new geochronological data

4.4.4.1 Temporal-spatial distribution of lavas

Fig 4.6a shows LiDAR topographic data for the axial graben and eastern rift flank and the six lava samples with $^{40}Ar/^{39}Ar$ ages. A structural map based on the LiDAR and other geological observations is shown in Fig 4.6b and a cross section in Fig 4.6c. Two of the dated samples are located at the edge of the graben and are displaced by the large graben bounding faults and these give ages of 52.9 ± 33.6 ka (sample SA02) and 29.6 ± 5.6 ka (sample 2805), which due to the low precision on sample SA02, are the same within analytical uncertainty. These constrain the development of this graben bounding fault scarp to less than ~25 – 35 ka, and give a (minimum) time averaged slip rate of ~1 mm yr^{-1}. This also constrains the youthful looking lava within the graben to be younger than ~ 30 ka and it can be inferred therefore that the axially focused melt supply, evident during the recent activity, has been a feature of this rift zone for at least ~ 30 ka. The oldest ages obtained for samples from the rift flank are 193 ± 15.8 ka and 179 ± 22 ka for lavas sampled ~2.5 km from the edge of the graben (Fig 4.6). Between these and the ~30 ka graben edge are flows with intermediate ages of 50.4 ± 18.2 ka and 86.1 ± 26 ka.

Although they do not provide a comprehensive overview of the volcanic history, the new ages obtained for the lavas across the rift flank do impose certain constraints on volcanism since ~200 ka. The increase in age of the lavas with increasing distance from

the axis, although un-corrected for flow length, does imply a correlation between the age of these lavas and their proximity to the present rift axis.

4.4.4.2 Analysis of age data

At mid-ocean ridges it is common to assess the age distribution of lavas by comparing an age-distance profile against a spreading curve drawn from the rift axis (e.g. Goldstein et al., 1994; Sims et al., 2003). Similar to some oceanic systems (i.e. Sims and Standish, 2010) it is possible at the DMH segment to identify a topographic axis in the graben centre (similar to an oceanic 'bathymetric' axis) and also a magmatic axis based on the accumulation of recent lavas that define the neo-volcanic zone, which in the northern part of the rift zone is located ~1 km east of the topographic axis. However, a potential problem with this approach at the DMH rift zone is that for the older lavas the location of the assumed axis is not necessarily applicable, i.e. volcanism may not have been focused along the axial zone at this time. Therefore, in addition to comparing the age-profile to the possible axis location (topographic and magmatic) an alternative approach has also been taken where the significance of the spatial distribution of ages *within* the sample suite has been investigated from a regression analysis of the age profile. In this analysis a weighted least squares regression was used to find the best linear fit for a solution with two independent fit parameters, which are equal to the velocity component of the age-distance distribution and the x-axis intercept. These were used as they reflect the two potentially significant aspects of the age profile, the spreading rate/velocity and the location of the spreading axis (i.e. the 'zero-age' point). The results of this analysis is shown in Fig 4.7 and show that the observed age distribution across the sample profile can be explained by axis perpendicular transport at a velocity of 12.5 ± 1 mm yr^{-1} (with a high correlation coefficient of $r^2 = 0.99$), which closely approximates the

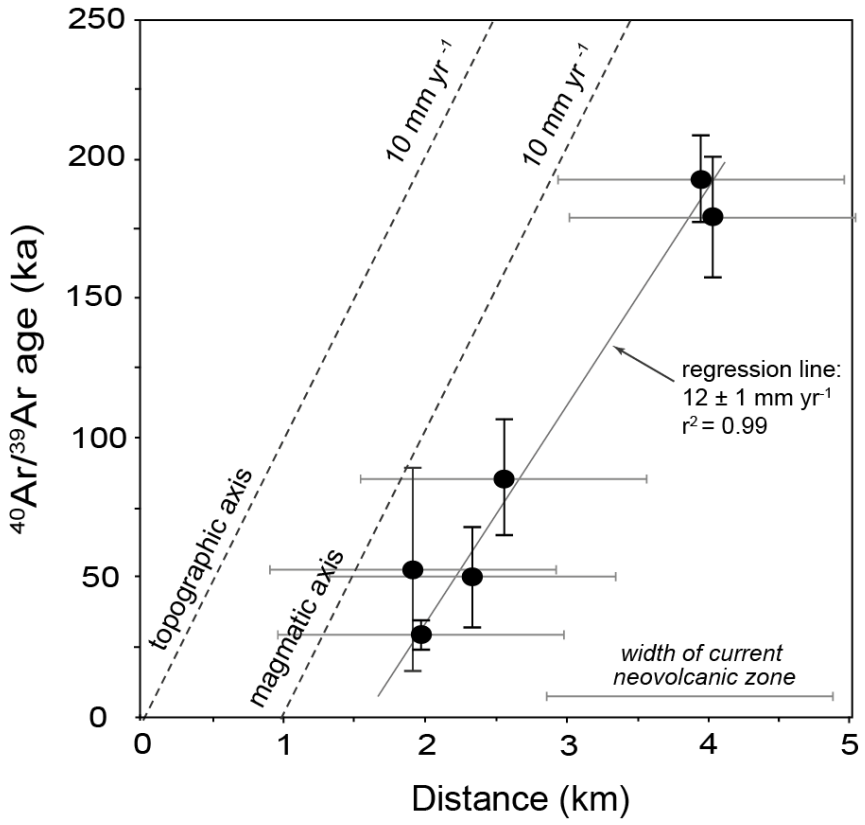

Figure 4.7 Plot of ^{40}Ar-^{39}Ar age versus distance from the centre of the axial graben. Sample locations shown in Fig 4.6. Distance is measured from the sample site along a path perpendicular to the axis. The regression is a least squares fit weighted to the error in the ^{40}Ar-^{39}Ar age and is solved for two fit parameters, equal to the velocity and x-axis intercept (see text for further explanation). Sample SA02 (52.9 ± 33.6 ka) was not included in the regression analysis due to the large uncertainty in the age measurements (although the effect on the results is negligible). The velocity (extension rate) given by the regression is very close to the Afro-Arabian half rate of ~8-10 mm yr^{-1}. Also shown are spreading rate curves for a (half) extension rate of 10 mm yr^{-1} from the topographic axis (graben centre) and magmatic axis (centre of neo-volcanic zone). As the location of eruptive fissures for individual samples is unknown the x-axis error bars used are equal in width to the current neo-volcanic zone. There is good agreement between both the regression results and the extension rate curve (when the width of the emplacement zone is considered) to extension at ~10 mm yr^{-1} from the magmatic axis. This is also in agreement with the location of the instantaneous axis observed during recent dyke intrusions (Hamling et al., 2009; Grandin et al., 2010).

Afro-Arabian half rate of 8-10 mm yr^{-1}. The location for the origin of the age trend (i.e. the axis) is in the eastern side of the axial graben (marked by a small star in Fig 4.6c) and is broadly coincident with the most accurately located dykes intruded during the recent rifting phase, insofar as these were injected beneath the eastern side of graben (Hamling et al., 2009; Grandin et al., 2010). If axial magmatism is assumed for all the samples the current age distribution can also be well explained by extension of ~10 mm yr^{-1} from the 'magmatic' axis' providing the width of the potential zone of volcanic

accretion is considered (i.e. the neo-volcanic zone) (Fig 4.7). A similar curve drawn from the topographic axis does not provide a good explanation for the age distribution unless the neo-volcanic zone was substantially wider.

The results of the regression analysis and comparison of the age-distribution with the magmatic axis both suggest that the lavas erupted since ~200 ka are related to the location of current dyke injections by an extensional velocity close to the Afro-Arabian half rate. This is significant as it suggests that, 1) a focused magma system has existed at the DMH rift segment since at least ~200 ka, and 2) this narrow segment has been accommodating all Afro-Arabian extension during this time, possibly to a large extent by axial magma intrusion.

4.4.4.3 A preliminary model for the volcano-tectonic evolution of the DMH segment

A key piece of information given by the age profile is that the large faults that currently define the axial graben did not form until after ~30 ka and this represents a significant event in the topographic development of the rift zone, particularly with respect to development of ocean ridge type morphology. A model of lava emplacement based on the age data must therefore include the non-steady state topographic evolution suggested by the formation of these faults, which have significantly larger offsets than most faults across the rift (i.e. Fig 4.6). Fig 4.8 presents a potential scenario for the volcanic and tectonic history of the DMH segment that could account for the geochronological observations. In this model lavas accumulate in the neo-volcanic zone and are transported outwards via plate-spreading type processes. The two important features of this are 1) magmatism is focused to a neo- volcanic zone over the last 200 ka

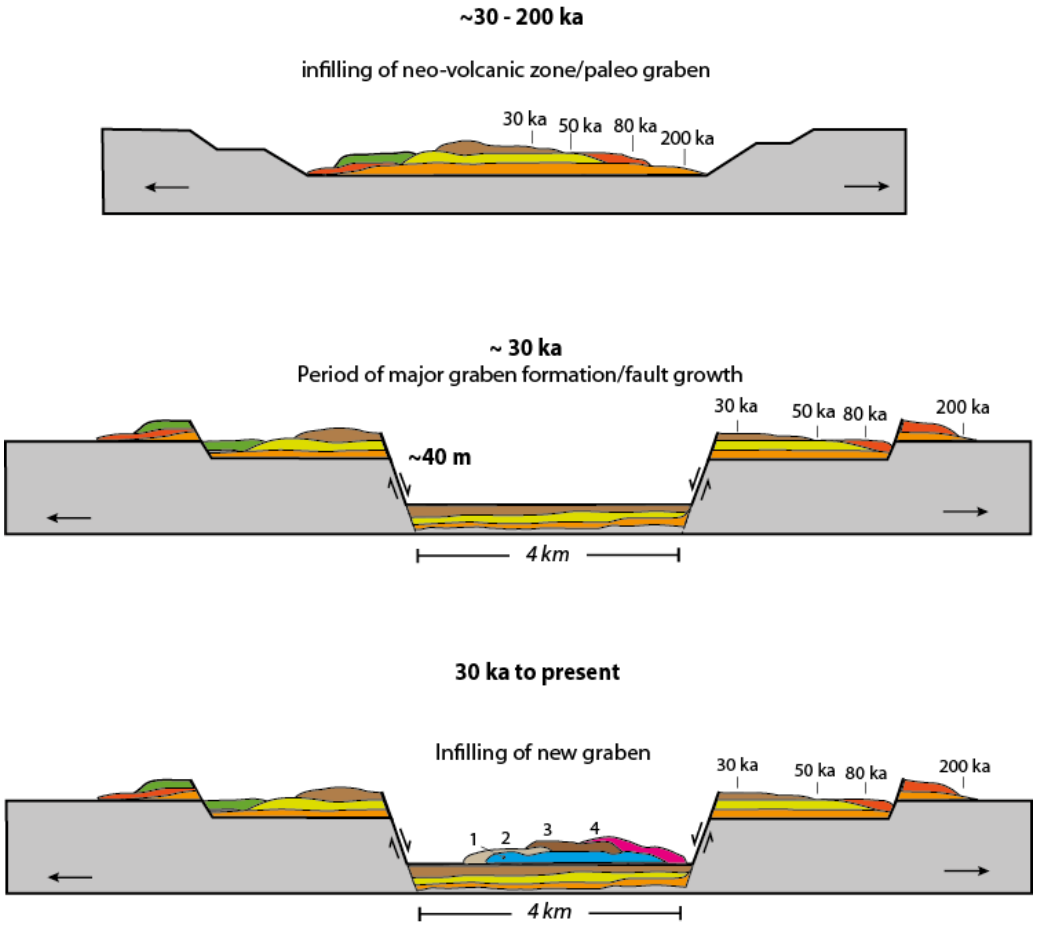

Figure 4.8 Possible scenario for volcanism and faulting in the DMH segment since 200 ka (not drawn to scale). Model is based on the new age constraints presented above. The ages indicated on lavas are ages before the present (not the time indicated in the model) and demonstrate how the observed age profile could have formed. In this model volcanism occurs in a neo-volcanic zone around the rift axis with limited off-axis flow. The history of the segment in punctuated by the formation of the prominent axial graben after ~30 ka. The age of the youngest flow offset by this fault limits the growth of the current topography to < 30 ka, however it is unclear whether this is the result of increased fault growth of a decrease in infilling of the graben by volcanism. The final distribution of ages on the eastern flank is similar to the observed pattern shown in Fig 4.6.

and 2) at < 30 ka the development of the rift is punctuated by the formation of the current axial graben. Possible reasons for why graben formation occurred at this period include a change in the extensional regime linked to a decrease in melt supply, leading to a period of tectonic (amagmatic) extension, or the effects of the increasing attenuation of the lithosphere leading to change in rifting processes.

The oldest DMH samples (SA05 and 2811) analysed give $^{40}Ar/^{39}Ar$ ages of ~200 ka and lie ~7 km from the outer edge of the segment. If it is assumed that age-distance profile

is related in some way to axial volcanism and subsequent transport outwards then extrapolation to the eastern edge of the segment gives an estimated age of ~760 ka for the formation of the entire magmatic segment (at a half extension rate of 12.5 mm yr^{-1}). This is in close agreement with one previous K-Ar age of 757 ± 40 ka available for a lava flow at the southwestern margin of the DMH segment (Lahitte et al., 2003) (shown in Fig 4.5) and may therefore broadly constrain when magmatism became focused along the axis of this part of the Red Sea system. Testing this conclusion will be possible with further geochronological work to increase sample density and distribution.

4.4.5 Summary

Earlier in this section it was noted that although focusing of magmatism to an axial region is a fundamental part of rift evolution it was not clear to what extent the current magmatic processes observed in the DMH segment reflected the emplacement of lavas across the entire rift zone. Although a detailed chronology has not been presented the age data presented here can be used to argue that for at least ~200 ka volcanism has been largely focused around the axial region and that during this period, as is the case today, this narrow rift zone has accommodated essentially all Afro-Arabian extension at a rate similar to the current (full) rate of 16 - 20 mm yr^{-1}.

4.5 Discussion 2

4.5.1 Off-axis volcanism and faulting: the Badi-Dabbayra transverse structure

The previous section discussed the significance of the chronology of axial volcanism in the DMH rift segment for the processes of segment formation/development. This section focuses on the timescale of volcanism along the ~EW trending transverse volcanic structure encompassing the Badi and Dabbayra volcanoes and the structural interactions between this and the ~NS trending DMH rift segment.

4.5.2 Geochronology of Badi and Dabbayra

The $^{40}Ar/^{39}Ar$ age data for lavas from the central part of the DMH rift segment demonstrates that volcanism associated with magmatic extension across this rift has probably been focused to some extent to the axial region since at least ~200 ka and possibly since ~760 ka when the structures forming modern rift zone may have begun to develop. However, during this time contemporaneous volcanism has also occurred along the Badi-Dabbayra transverse volcanic structure between the western part of the DMH rift and the regional scarp separating Afar from the Ethiopian highlands. This section examines the age data from these volcanoes and the significance of this region for faulting in the main part of the DMH segment.

In total eight new ages have been obtained for lavas from this region; five from lavas erupted at volcanic cones on the eastern edge of Dabbayra, two from basaltic flows

erupted onto the silicic units of Badi and one from a flow on the rift margin SE of Badi. Sample locations and interpreted ages are shown in Fig 4.3 and record volcanism here between 450 and 30 ka. Samples from three volcanic cones at the eastern edge of Dabbayra give ages of 445 ± 24 ka, 343 ± 23 ka and 94.6 ± 12.3 ka. Two other samples, taken from flows exposed in the Awra River give ages of 139 ± 1 ka and 55.4 ± 5.6 ka, the youngest of these forms the present-day surface in this location. Although the emplacement history of the silicic lavas that form the bulk of Badi is not known, the existing age of 290 ± 4 ka for a rhyolitic flow at the base of the volcano on the western side (Lahitte et al., 2003) provides a benchmark for the silicic part of the volcano. The erosional state of this flow is very similar to those forming the main part of the volcano and suggests the bulk of the edifice may have been emplaced around this time. To the SE of Badi, where the structures of the transverse lineation merge into the central part of the DMH rift a faulted basaltic flow gives an age of 62.1 ± 5.6 ka. The youngest eruption ages in the sample suite are for basaltic cones on Badi, with two flows from separate vents on the western side giving ages of 36.5 ± 4.9 ka and 25.4 ± 9.4 ka.

A comprehensive understanding of the growth of the Badi or Dabbayra volcanoes is not currently possible, however the new age data presented here provides useful constraints on the timescale of volcanism in this region. The lavas sampled at the eastern edge of Dabbayra complex record eruptive activity here from ~450 to 55 ka and although the overall stratigraphic position of our oldest samples (0402, 445 ± 24 ka and 3016, 343 ± 23 ka) is unknown, these lie furthest from the centre and are stratigraphically below the two flows to the west (2909, 139 ± 1 ka; 2911, 55.4 ± 5.6 ka). The 2911 flow directly overlies the 2909 flow, which has been exposed by the Awra River. Assuming an overall younging trend of lavas with increasing elevation the entire volcano would have formed approximately within the last ~500 ka. On the basis of the weathering of lavas

there is no evidence in the main part of the volcano for Holocene eruptions. The most youthful looking lavas occur to the west of Dabbayra and immediately north of Badi. Lavas erupted from the oldest dated basaltic cone are in contact with the rhyolitic flow at the margin of Badi previously dated at 290 ± 4 ka (Lahitte et al., 2003). Whether basaltic activity significantly pre-dated rhyolitic volcanism is unclear, but the age data show that basaltic and rhyolitic lavas were erupted simultaneously within a few km's of each other. The young basaltic lavas that cap the rhyolitic flows on Badi, dated at < 40 ka, demonstrate that basaltic volcanism has been a long-lived feature of this region. The consistent weathering of the rhyolitic flows suggests that these may have all been erupted around the same time, at approximately 300 ka, however confirmation of this requires further age constraints.

4.5.3 Structural interaction with the DMH segment

The vents and fissures forming the Dabbayra complex are oriented ~EW, essentially perpendicular to the strike of the DMH rift segment and the Afar-Highland boundary scarp (Fig. 4.1). At its eastern side around Badi this becomes more SE, and merges with the DMH rift near the Ado Ale volcanic complex (AVC). The AVC marks the along axis centre of the rift and overlies the source region from which recent intrusions have been fed. There is a notable similarity between the effusive glass rich rhyolitic flows of Badi and those erupted ~25 km away in the central part of the rift, forming the now heavily faulted silicic lavas of the AVC (described in Chapter 2). Apart from the Dabbahu volcano at the northern end of the DMH rift segment these are the only locations where rhyolites have been erupted. No absolute age constraints exist for the

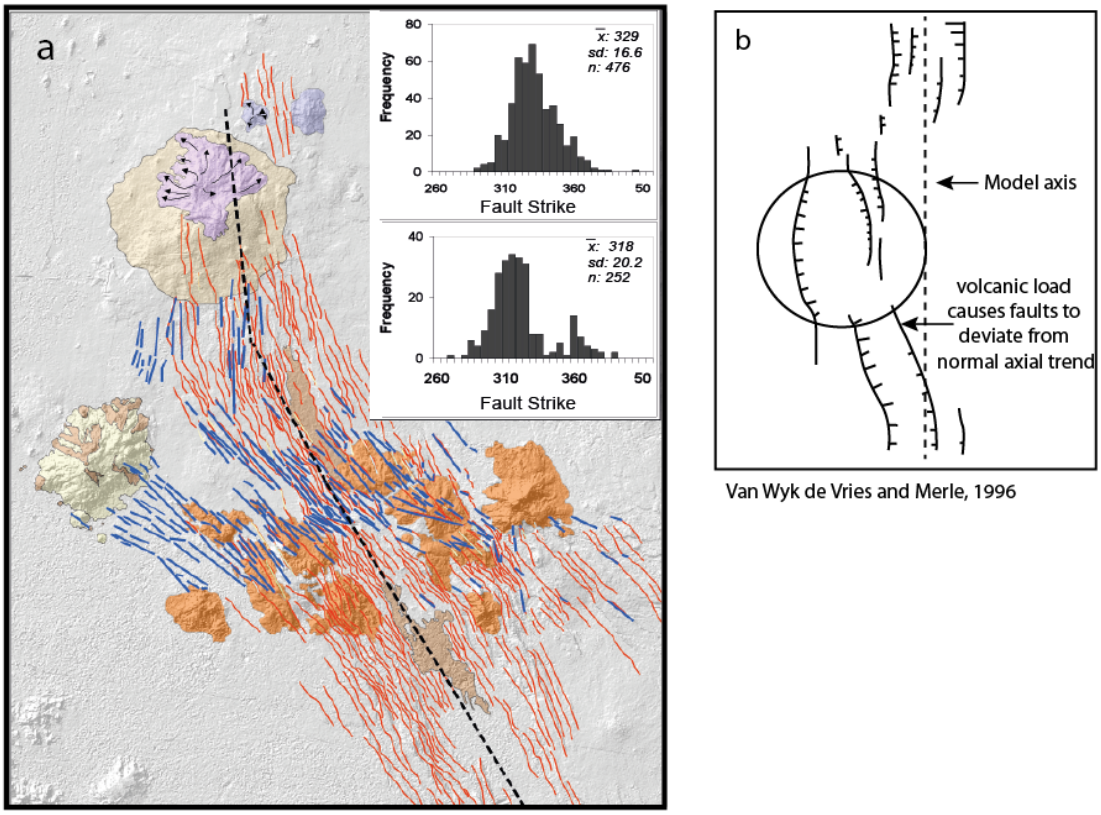

Figure 4.9 (a) Fault map of the DMH segment. Map made using ~5 m resolution SPOT imagery and showing major volcanic/topographic loads. Faults are coloured according to orientation with structures that deviate by more than 15° from the axial trend coloured blue. The axis orientation is marked by the black line and and is drawn along the centre of the axial graben. The top histogram shows the strike of all faults (mean of 329°), the bottom histogram show the orientation of faults in blue (mean strike 316°). The greatest variation is seen in the rift centre where faults deviate from the axial trend towards the Badi volcano on the rift margin. This pattern is similar to analogue models of the stress effects of volcanic loading by off-rift volcanoes as shown in (b). The location of this map is similar to Fig 4.5.

silicic lavas of the AVC, however the geometry of the two units on either side of the axial graben, named Gommoyta and Diyyilu (Fig 4.3), suggests that these previously formed a continuous unit and have been rifted apart. These are currently ~6 km apart, separated by basaltic lavas in the axial graben. Using the long-term (half) extension rate predicted by geodesy of ~10 mm yr^{-1} (Chu and Gordon, 1998; Vigny et al., 2006; McClusky et al., 2010), which is consistent with the analysis of age data for the eastern flank basalts presented in the previous section, and assuming eruption at the axis, the estimated age of theses rhyolitic flows is ~300 ka. This would make emplacement of these lavas coincident with the rhyolitic flow unit at the base of Badi, which has an K-

Ar age of 290 ± 4 ka (Lahitte et al., 2003a), and implies that rhyolitic volcanism in the central part of the rift may have been contemporaneous with similar activity ~25 km to the NW at Badi.

4.5.3.1 Patterns of faulting and volcanism

The DMH segment is defined by intense faulting and as discussed in the previous section has a well-developed central axial graben. The mean elevation of the segment rises towards the central point due to the silicic and basaltic lavas that form the Ado' Ale volcanic complex, erupted above the central magma reservoir. The along-axis summit is marked by a basaltic crater ~0.8 km in diameter. The segment has over 1200 distinct faults (Hayward, 1997) (recognized in <30 m resolution imagery), with typical spacing of a few 100 m's. Analysis of brittle deformation observed during the 2005 dyking event by Rowland et al (2007) demonstrated that at the surface in addition to vertical slip there is a significant component of horizontal opening across fault surfaces and that this style of faulting was the principal mechanism of extension. This also appears to be the case for many of the other faults in the central DMH rift and highlights the important link between magma intrusion and extension/brittle deformation.

The mean orientation of the segment changes slightly along axis across the central AVC complex and the southern section trends NW-SE essentially orthogonal to the mean extension direction, while north of the AVC it develops a more northerly trend, slightly oblique to mean extension (Rowland et al., 2007). Fig 4.9a shows fault traces in the central part of the DMH rift mapped onto SPOT (5 m resolution) and Landsat (30 m resolution) satellite imagery. The mean strike of all faults mapped here is 329 ± 17° (1σ), similar to the ~333° found by Hayward, (1997). Faults coloured in blue in Fig 4.9a

are those that deviate from the mean axial trend by >15° and the greatest variation can be seen to occur around the silicic lavas of the AVC and Badi. Analogue sandbox experiments suggest that the presence of volcanic loads, either along the axis of a rift or off-axis, can cause local variations in fault orientations (Fig 4.9b) (van Wyk de Vries and Merle, 1996). In the case of a volcano adjacent to the rift, faulting was observed over a wider zone and fault orientations rotated from being axis perpendicular towards the volcanic load. There is notable similarity between these experimental results, shown in Fig 4.9b and the variation in fault orientations around Badi, where faulting deviates away from the main rift towards the volcano. An age of 62.1 ± 5.6 ka was obtained for a faulted basaltic flow (sample 2401; Fig. 4.4) offset by these faults demonstrating that the emplacement of the volcano, broadly constrained at 290 ± 4 ka by Lahitte et al (2003), preceded the formation of this particular structure. There is evidence therefore to suggest that the emplacement of Badi has affected rifting processes on the western side of the DMH rift segment, causing strain accommodation here to occur over a wider zone. However, the new age data also shows that basaltic volcanism in the region around Badi was occurring at least by 445 ka and if the topographic load of the present largely silicic edifice has affected fault orientations this effect is independent of the mechanism of melt supply to these eruptions (discussed below).

4.5.3.2 Localisation of volcanism along the Badi-Dabbayra zone

The new $^{40}Ar/^{39}Ar$ ages presented here for the Badi-Dabbayra lavas and those from the central part of the DMH segment (in addition to the two existing K-Ar ages from Lahitte et al, 2003) demonstrate that broadly speaking volcanism was localised at the same time along these two lineations. The development of the ~E-W Badi-Dabbayra lineation has occurred in a region previously dominated by extension on ~N-S structures and the localisation of volcanism along these structures may have only been

possible after rifting processes became confined to the axis of the DMH segment. The coeval volcanism in these two region identified in the age data demonstrates that while magmatism along the Red Sea axis is strongly linked to rifting processes, the emplacement of melts erupted a few km's away is not as strongly governed by either rifting processes or the regional stress field. The proximity of the off-axis volcanoes to the central part of the DMH segment is probably not coincidental, as seismic (Keir et al., 2009; Belachew et al., 2011) and geodetic (Hamling et al., 2009; Grandin et al., 2010) studies of the recent magma intrusions have shown that magma feeding these intrusions accumulates beneath this part of the rift.

Assuming melts generated during mantle upwelling are focused to some extent beneath the DMH axis, as suggested by the age-distance data for the axial lavas and other evidence for long-term focused strain accommodation here, then the interaction of these melts with a pre-existing fracture zone could result in transport away from the DMH segment feeding eruptions at Badi and Dabbayra. Theoretical work suggests that pre-existing fractures may influence magma transport in the crust, providing they are oriented nearly perpendicular to the least compressive stress direction (e.g. Ziv et al., 2000), which is consistent with the orientation of the Dabbayra-Badi structure with respect to the DMH axis. Geochemical evidence for melt supply to the off-axis volcanoes is discussed in the following chapter.

4.5.4 General significance of 'transverse' volcanism in Afar

Overall there are several notable features of the transverse volcanic zones; they are aligned E-W or NE-SW, approximately perpendicular to the trend of the rift zones; they are only found at the margins of the depression; and unlike the axial volcanic ranges

they show little evidence of faulting (Fig 4.1). The regional tectonic significance of transverse volcanic structures was initially discussed by Barberi et al (1974), who, in light of the recently discovered offsets to spreading ridge in the Atlantic (e.g. Bonatti, 1973), proposed that they represented similar proto-offset zones, responsible for creating along-axis discontinuities. Barberi et al proposed a model for the formation of transverse structures, whereby volcanism was localised along pre-existing fractures oriented roughly perpendicular to the axis of rifting and which eventually created along-axis offsets between the newly forming rift segments that would be inherited by future spreading ridges. Since then it has become clear that MOR discontinuities are most likely related to melt supply and mantle upwelling patterns (e.g. Schouten et al., 1985; Macdonald et al., 1988; Batiza, 1996) and studies on the rift segmentation in the northern MER and in Afar have shown that these offsets are probably also controlled by similar magmatic processes (e.g. Hayward and Ebinger, 1996; Wright et al., 2006; Keir et al., 2009; Ebinger et al., 2010). However, although they do not control rift segmentation the association of the transverse volcanism with the margins of Afar suggests that their formation is likely to be linked to pre-existing lithospheric structures. In western Afar, both the Dabbayra-Badi volcanic lineation and the Ma'alalta complex are located along ~E-W offsets to the regional ~N-S scarp separating Afar from the Ethiopian highlands (Fig 4.1). Likewise, in eastern Afar, the Nabro volcanic range has formed in a ~NW-SE orientation along a topographic break in the Danakil block (Wiart and Oppenheimer, 2005). South of the Nabro range are the Assab and Gufa volcanic fields, consisting of basaltic cones erupted onto Miocene lavas, however, any association between these and basement structures is unclear due to coverage of any pre-rift structures by the Miocene lavas. The lack of visible faulting of transverse volcanoes compared to axial rift zones is unsurprising, as they are oriented

approximately parallel to the principal Afro-Arabian extension direction, however the alignment of vents demonstrates that magma transport is these zone clearly has a preferred orientation that is not controlled by the regional stress field. As proposed above for the Dabbayra and Badi volcanoes, the influence of pre-existing fracture zones, oriented perpendicular/highly oblique to the least compressive stress direction, on melt transport (i.e. Ziv et al., 2000) could explain the localisation of volcanism along structures oriented in this way. The association of the Nabro, Ma'alalta and Dabbayra-Badi volcanic zones with ~E-W structures in the pre-rift basement suggests that this is a strong possibility.

4.5.4.1 Relation between transverse volcanism and axial rift zones

Prior to the age data presented here for the Badi-Dabbayra lavas no other published geochronological datasets exists for any other transverse volcanism and with the exception of the two historical eruptions in the Nabro range, in 1861 (Wiart et al., 2000; Wiart and Oppenheimer, 2000) and 2011 (Smithsonian, 2011), the volcanic history of these structures was unknown. Field and remote sensing evidence suggests that the products of most transverse volcanoes are of similar age to the axial segments and most appear younger than the ~1-3 Ma stratoid lavas (i.e. Barberi et al., 1974; Wiart et al., 2000; Wiart and Oppenheimer, 2000, 2005). The new $^{40}Ar/^{39}Ar$ ages for the DMH segment and Badi-Dabbayra volcanoes show that the onset of volcanism along both structures was essentially coeval (i.e. since ~800 ka). The growth of the off-axis volcanoes was probably only possible once extensional processes became confined to the narrow DMH axis, allowing off-axis plumbing systems to develop that were not directly related to the regional stress field. The petrogenetic relation between melts erupted at Badi and Dabbayra compared to the DMH axis is investigated in detail in

Chapter 5. North of Dabbayra, the Ma'alalta volcanic complex has a similar structural relationship with the Alayta segment, although in this case the off-axis volcanism is chiefly characterised by a large silicic caldera system, with minor basaltic cones. In eastern Afar the Nabro and Assab volcanoes are not as closely related to axial segments, while the Gufa structure is next to the Manda-Inakir (MI) segment terminating at a large off-axis volcano (Fig 4.1). The MI segment is not well developed and is not as structurally well defined as the other, such as the DMH or AG segments. However, the orientation of faulting along the MI segment does alter around this volcano (Manighetti et al., 1998), which may be attributed to a similar effect to the Badi edifice on faulting in the DMH rift zone. It seems therefore that when in close proximity structural interactions do occur between axial segments and transverse structures, however the localisation of volcanism along transverse structures is not necessarily connected to the focused melt supply to the axial rift zones, as several large transverse volcanoes, such as those along the Nabro range, have developed at considerable distance from the rift axes.

4.5.5 Summary

The new age data for the Badi and Dabbayra lavas provides a framework for understanding the growth of these volcanoes and importantly shows that volcanism here has been contemporaneous with rift related activity in the nearby DMH segment. The close spatial and temporal association between the onset of activity along these volcanic structures strongly suggests that volcanism could be not be localised along the Dabbayra-Badi lineation until nearby rifting was focused to the narrow DMH segment, allowing pre-existing structures to influence melt supply away from the axis. The location of the off-axis volcanoes near the central part of the DMH segment, where melts are thought to accumulate, may reflect a connection between these plumbing

systems at depth. Geochemical constraints on melt generation and storage are investigated in the following chapter. On a regional scale there appears to be a close relationship between the formation of transverse volcanic zones and ~E-W oriented structures in the depression bounding faults, both along Ethiopian highland scarp in western Afar and the Danakil Block in the east. Although several transverse volcanoes are in close proximity to axial segments, some are not and it remains unclear why focused plumbing systems were developed along these specific structures.

4.6 Conclusions

The important conclusions from this chapter are as follows:

1. The age constraints for the axial lavas from the DMH rift segment suggest that the onset of focussed volcanism and faulting occurred after ~800 ka and that volcanism has been confined to the rift axis for at least 200 ka. During this time the extension accommodated by the DMH segment, either by magma intrusion or faulting has accounted for essentially all Afro-Arabian extension. The temporal patterns of faulting and volcanism in the region since ~2 Ma, i.e. the opening of the Tendaho graben followed by the formation of the DMH segment, are in agreement with the predictions of rift evolution made by the model of Hayward and Ebinger (1996).

2. The age data for lavas from the Dabbayra-Badi region shows that volcanism had begun here by at least 445 ± 24 ka and it seems likely that this structure grew simultaneously with the DMH segment. The localisation of magmatism along this structure probably relied on the narrowing of the region of active rifting along the adjacent Red Sea axis, allowing pre-existing fracture systems, related to the major

offsets in the regional scarp, to control off-axis melt transport. This may provide a good working model for the existence of transverse volcanic zones across Afar.

3. The proximity of the Badi edifice to the DMH segment appears to have influenced patterns of faulting in the centre of the rift zone, which are similar to the results of analogue experiments on the structural effects of off-axis volcanic loads.

Chapter 5

Petrogenesis of basaltic lavas

5.1 Introduction

The previous chapters have discussed the petrology (Chapter 2) and volcanology (Chapter 3) of the DMH rift segment and adjacent volcanoes and have investigated the growth of these volcanic-tectonic structures and their significance to rift development (Chapter 4). The geochronological data demonstrated that the melt supply to the main part of the rift has been focused along the axial zone for at least 200 ka and that this system has probably been accommodating almost all Afro-Arabian extension during this period, possibly to a large extent by dyke intrusion (e.g. Wright et al., 2006; Rowland et al., 2007). It was also shown that melts have been supplied to feed contemporaneous eruptions along the off-axis Badi-Dabbayra volcanic structure to the NE. The development of the focused magma supply along the DMH axis is a vital part of rift maturation (Hayward and Ebinger, 1996), as it confines magma intrusion and extension to the rift axis and over time creates a consistent age progression of new crust across the rift axis. This chapter develops the understanding of the DMH magmatic system by investigating the petrogenesis of the basaltic lavas erupted along the DMH rift zone and at the off-axis volcanoes. Major and trace element and radiogenic isotopic data is used to constrain petrogenetic processes and, along with existing geophysical constraints, forms the basis for a model of melt generation and supply to the rift.

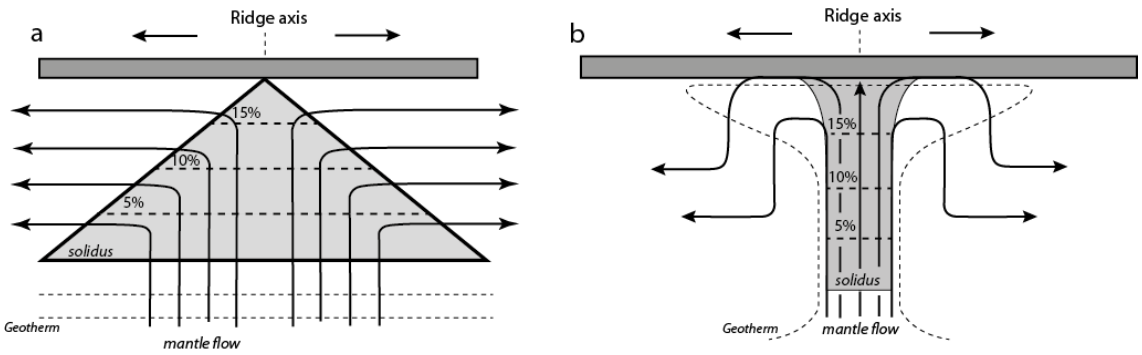

Figure 5.1 Schematic examples of possible mantle-melting regimes for (a) passively upwelling mantle beneath a rift zone (the corner flow model) and (b) melting associated with active upwelling in a plume. Dashed lines show contours of partial melting along decompression paths (black arrows). In the passive case the mantle is at a constant potential temperature and ascends due to the separation of the overlying plates. Adiabatic melting occurs during decompression once the solidus is crossed. In (b) the upwelling of hot material distorts the mantle geotherms and all decompression paths reach high extents of partial melting. One consequence of the variation between these two regimes is that the averaged melt product from (a) will contain a greater contribution of melts generated at higher pressures. Based on illustrations in Langmuir et al (1992).

Relatively few previous geochemical studies exist for lavas from Quaternary rift zones in Afar and no previous work has presented a detailed source-to-surface model for melting and magma supply to a rift segment. The chapter begins with an overview of partial melting in the mantle and of the previous work on petrogenesis in northern Ethiopia. This is followed by the new geochemical data for DMH rift system and development of a petrogenetic model. These new petrological results are then compared to recent geophysical constraints on melt migration and distribution beneath the DMH rift.

5.2 Background

5.2.1 Melt generation at oceanic rifts

Melting beneath mid-ocean ridges (MOR's) occurs due to adiabatic decompression of the mantle as it rises passively in response to the separation of the overlying plates (e.g. Carmichael et al., 1974). Numerous studies have investigated the details of this melting process and have shown how the partial melts generated during mantle decompression beneath ridges ultimately form the oceanic crust (e.g. Langmuir et al., 1977; O'Hara,

1985; McKenzie and Bickle, 1988; McKenzie and O'Nions, 1991; Langmuir et al., 1992; Keleman et al., 1997; Niu, 1997). Melting begins as the ascending mantle intersects the peridotite solidus and typically ceases once there is no longer any vertical component to the solid flow (i.e. decompression stops) when the residual mantle material starts to move away in a horizontal direction. The cross-section of the melting region created by this process, illustrated in Fig 5.1a, is approximately triangular in shape with a flat base (the solidus) and centred beneath the rift axis (McKenzie, 1985a; Plank and Langmuir, 1992).

The maximum depth range over which melting occurs is controlled by both the mantle potential temperature, which determines at what pressure the solidus is crossed, and also the point at which heat loss upwards makes melting no longer possible, which may coincide with the base of the overlying rigid plate (McKenzie and Bickle, 1988). The melting rate, and therefore maximum extent of melting, is typically considered to depend on mantle temperature (e.g. Klein and Langmuir, 1987; McKenzie and Bickle, 1988), although this may also be related to the spreading rate of the plates (cf. Niu and Hekinian, 1997). Mid-ocean ridge basalts (MORB's) erupted at spreading ridges typically preserve geochemical signatures, such as trace element concentrations, that reflect melting conditions deep in the melting region and transport processes must therefore be sufficiently fast and/or chemically isolated to prevent equilibrium with shallower mantle material (Kelemen et al., 1997). MORB's are also rarely in equilibrium with mantle olivine compositions and are not therefore primary magmas, the compositions of which can be estimated by applying corrections for fractional crystallisation (e.g. Klein and Langmuir, 1987; Herzberg and O'Hara, 2002).

5.2.2 Melting in plumes and beneath continental rift zones

In addition to mantle decompression occurring as a passive response to plate separation, decompression melting can also occur due to the active upwelling of hot buoyant mantle material (i.e. a mantle plume/hotspot) (e.g. White and McKenzie, 1995). Melting here differs from the purely passive upwelling models due to variations in the orientation of geotherms and higher fluxes of material through the melting region (Fig 5.1b) (White, 1993; Ito et al., 1999). Several instances exist where rifting occurs above plumes/hotspots and this can lead to large volumes of melt being generated as hotter than normal mantle material is decompressed (White and McKenzie, 1993). In regions where spreading ridges are underlain by hot mantle, which has an additional active upwelling component, melting occurs due to both passive and active decompression and the deviation from purely passive behaviour can have important differences for melting regimes (e.g. Ito et al., 1999). In Iceland for example, passive upwelling models based on plate separation alone can adequately explain the observed trace element signatures and crustal thickness at the edge of the island, however, an active upwelling component, which fluxes greater volumes of material through the deeper part of the melting region is required to model the same parameters in the centre of the island, near the plume/hotpsot centre (Maclennan et al., 2001).

Melt generation beneath continental rifts is less well understood than at oceanic ridges, primarily because it can be unclear whether asthenospheric upwelling occurs due to passive or active processes (e.g. White et al., 1987; Nielsen and Hopper, 2004; Armitage, et al., 2009). Similar methods to those used to model melting at MOR's have, however, successfully reproduced observations related to melt generation at continental rift zones, such as the Basin and Range region in the western USA (Wang et al., 2002)

and the Baikal rift in Siberia (Johnson et al., 2005). In practice, discriminating between different melting models in any setting is typically limited by the availability of constraints on key factors affecting melting processes, such as source composition and lithology and rates and depths of melting. As a result, differences in factors such as upwelling rates or melting geometries do not always strongly affect the overall results of common partial melting models (e.g. Plank and Langmuir, 1992). Identifying an active upwelling component that contributes to melt generation requires knowledge and/or consideration of other factors sensitive to upwelling rates, such as the thickness of new crust generated (e.g. Maclennan et al., 2001) or the geometry and thermal structure of the melting region (e.g. Watson and McKenzie, 1991).

The tectonic and magmatic features of the Afar segments (i.e. focused zones of magmatic extension still underlain by pre-rift crust) show them to be transitional between continental and oceanic type rifts. However, it is unknown to what extent melting in the sub-rift mantle shows similarity to either MOR's, other evolved rift zones above oceanic hotspots, such as in Iceland, or regions of continental rifting and volcanism, such as the Basin and Range province, USA. In practice, however, variations in melting processes associated with these different settings does not strongly affect the general petrogenetic constraints that can be derived from geochemical observations. For example, partial melt fractions calculated from geochemical models represent a mean value for the melting processes and can be related to the maximum extents of melting once other constraints become available on melting processes or geometries (e.g. Niu, 1997). The effect of active upwelling can have important implications for melting processes, however without additional constraints, such as knowledge of melt volumes, are difficult to asses (Maclennan et al., 2001).

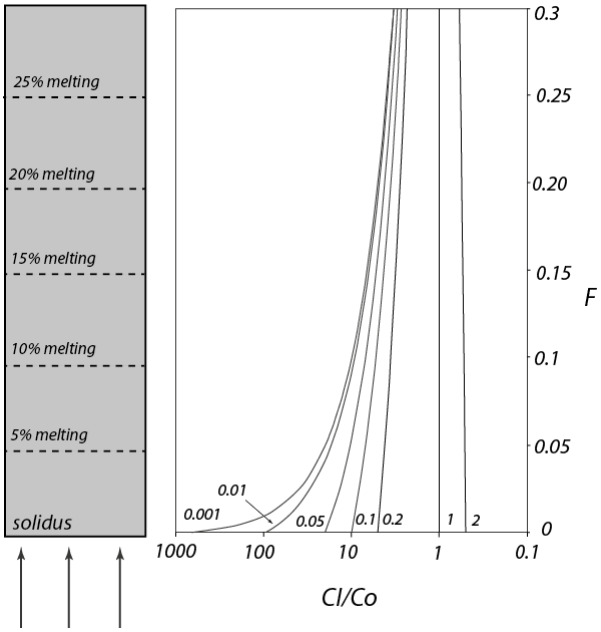

Figure 5.2 Effect of partition coefficient on partial melt compositions. Graph shows the change in the concentration ratio (Cl/Co) between liquid and solid phases during batch melting (F = % partial melting) of upwelling mantle for elements with different partition coefficients (D-values). Values of D are indicated next to the respective curves. Highly incompatible elements (D <<0) are highly enriched in the initial melts (at low F) compared to more compatible elements.

5.2.3 Geochemical constraints on melting processes

5.2.3.1 Geochemical modelling

Knowledge regarding melting processes typical comes from modelling the behaviour of various chemical species during partial melting. Forward and inverse models based on the composition of erupted lavas can be used to infer melting conditions, such as depth and extent of melting or important variations in source lithology. The behaviour of a chemical constituent during melting is described by a partition coefficient (K_d), which is equal to the concentration in the solid divided by the concentration in the melt at equilibrium. In the case of simple batch (equilibrium) melting, the concentration of an element or chemical species in the melt (C_l) can be related to the concentration in the source (C_o) by:

$$C_l = C_o / (F + D_o (1-F)) \qquad (1)$$

Where F is the melt fraction and D_o the bulk partition coefficient for element of interest in the solid and is given by $D_o = \Sigma x^i K_d^i$, where x is the modal abundance of mineral i

and K_d^i the relevant mineral/melt partition coefficient for the element of interest in mineral *i* (Shaw, 1970). Fig 5.2 illustrates how the ratio of an element between the solid and melt varies with different values of *D* during for batch melts generated at a range of *F's*. Trace elements that are highly incompatible (i.e. $D_o << 1$) will be strongly partitioned into the liquid phase during the first increments of melting compared to those with *D's* closer to 1 and low degree melts (i.e. at low values of *F*) are therefore strongly enriched in the most incompatible elements. In the case of non-modal melting, where mineral phases do not melt in their modal proportions, this expression becomes:

$$C_l = C_o / (F + D_o (1-P_o)) \qquad (2)$$

Where P_o is the bulk partition coefficient in the melt and is calculated in the same way as D_o but using melting modes. The composition of the residue (C_s) after non-modal melting can be found from:

$$C_s = C_o / 1 - F (1 - PF/D_o)^{1/Po} \qquad (3)$$

These expressions describe the simple case where chemical equilibrium is maintained with the solid reside until the moment of wholesale melt extraction. Similar expressions also exist for other melting styles, such as fractional and dynamic melting (e.g. Shaw. 1970; McKenzie, 1985), where melt fractions are separated from their residue during melting. Although all these models are to some extent unrealistic with respect to certain aspects of melt extraction and melt-solid equilibria they have been successful in explaining many geochemical observations of melt and residue compositions during mantle melting (e.g. Langmuir et al., 1992; Niu, 1997) and as such are considered to be

good approximations of the melting process. The variables used in melting models (i.e. D, P, C_o etc) are largely derived from experimental (e.g. Kinzler and Grove, 1992; Kushiro, 2001) and theoretical (e.g. Blundy and Wood, 1994) studies.

5.2.3.2 Trace element constraints on melting

The most commonly used methods for approximating primary melt generation processes involve models of trace element partitioning between solids and their partial melts using melting equations such as the ones shown above. Highly incompatible elements (i.e. where $D < 0.01$) such as Ba, Th and La are concentrated in the melt phase during the initial increment of melting (i.e. Fig 5.2) and low degrees of melting will therefore produce large fractionations between these and less incompatible elements with larger *D's* such as Nd, Zr and Sm. Initial melts may therefore have high values for ratios such as Ba/La and La/Sm, which decrease as F increases. For example, Fig 5.3a illustrates the variation in Ba/La and Sm/La in partial melts from a peridotite source generated by variable extents of batch and fractional melting. In addition to melt fraction, the composition of any partial melt is also clearly dependent on the initial composition of the source material and, in the case of non-modal melting, also on the relative participation of the constituent crystalline phases in the melting reaction. Incompatible element concentrations provide an indication of source fertility, however, as these are also sensitive to melt fraction (i.e. Figs 5.2 and 5.3a), other information, such as radiogenic isotope ratios, are required for source discrimination. The key lithological variation during melting of mantle peridotite is the transition during decompression in the stable alumina-bearing phase from garnet to spinel to plagioclase. Several of the heavier rare earth elements (REE's) (Dy-Yb) are compatible in garnet and the presence of this phase in the solid therefore strongly influences fractionations

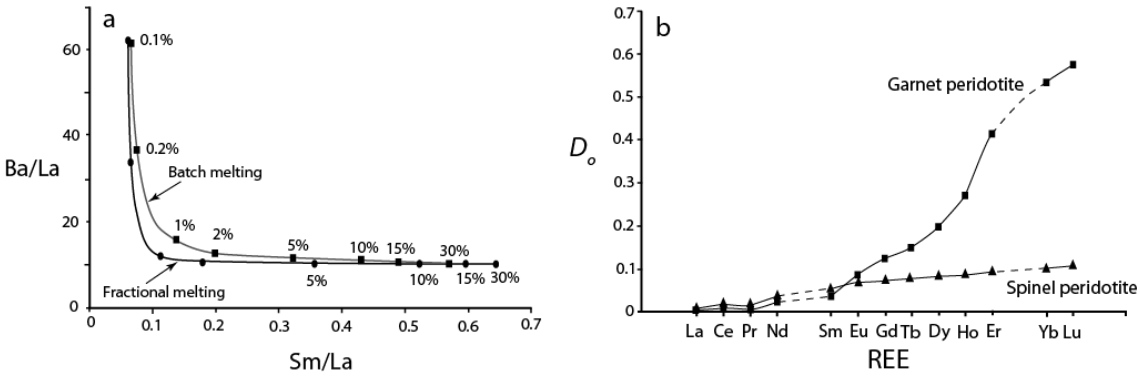

Figure 5.3. (a) Sm/La vs. Ba/La calculated for different extents of fractional and batch melting of a fertile peridotite source. Symbols along curves mark degrees of partial melting. Initial melts are strongly enriched in highly incompatible Ba relative to La and therefore have high Ba/La values. Melts with high Ba/La are therefore characteristic of small melt fractions or melting of fertile material. La/Sm ratios show a more consistent variation with melt fraction and can provide an indication of extent of melting. (b) Illustration of the effect of peridotite lithology on the bulk partition coefficients (D_o) for selected rare earth elements. The compatibility of the HREE's in garnet has a strong effect on the bulk partition coefficient and therefore the composition of partial melts.

between the light and middle rare earths (LREE and MREE) and the heavy rare earths (HREE) and leads to high ratios such as Tb/Yb. Fig 5.3b shows bulk partition coefficients (*Do*) calculated for a range of REE's in spinel and garnet bearing peridotite and illustrates the effect on garnet on the partition behaviour of the HREE (Dy – Lu). The occurrence of large MREE/HREE fractionations in melts is typically interpreted to represent a stronger garnet field signature and therefore deeper melting and is often used as a melting geobarometer (e.g. O'Neil, 1981). It has also been shown that some HREE's can be moderately compatible in Ca and Na rich clinopyroxene during high pressure melting of fertile spinel peridotite solidus and melts generated under these conditions can therefore produce REE fractionations similar to garnet field melting (Blundy et al., 1998). Forward models of trace element concentrations, i.e. using equation (2), can be tuned to a particular melting scenario by incorporating physical constraints, such as the effect of melting pressures on the relative importance of garnet versus spinel peridotite melting (e.g. Wang et al., 2002; Johnson et al., 2005). These parameters can be estimated from geophysical and experimental studies or from modelling of major element concentrations sensitive to certain parameters, such as the

initial depth (e.g. FeO and MgO) and the final extent (e.g. Na_2O and SiO_2) of melting (i.e. Langmuir et al., 1992; Herzberg and O'Hara, 2002; Herzberg, 2006).

5.3 Previous work

5.3.1 Pre-rift Eocene flood basalts

In NE Ethiopia pre-rift Eocene volcanism is widely attributed to a mantle plume beneath the pan-African crust (e.g. Marty et al., 1996; Ebinger and Sleep, 1998; Pik et al., 2006; see also section 1.3.1.1 in chapter 1). This resulted in the eruption of a thick (1-3 km) succession of basaltic lavas that now form the Ethiopian highland plateau and parts of the Yemeni highlands (Mohr, 1983; Mohr and Zanettin, 1988; Hofmann et al., 1997; Pik et al., 1998, 1999; Kieffer et al., 2004). There is significant geochemical diversity among the Eocene flood basalt lavas and the range of major and trace element and isotopic compositions suggest considerable source heterogeneity and/or variable extents of melting (Marty et al., 1996; Pik et al., 1998, 1999; Kieffer et al., 2004). A detailed investigation of the Eocene flood basalts by Pik et al (1999) suggested that several source possible source components were involved in the generation of these lavas, inferred from apparent mixing trends in geochemical plots; 1) the deep sourced Afar plume component, 2) a depleted mantle reservoir, and 3) the upper and 4) lower crust. The Afar plume source is akin to a moderately enriched mantle source, characterised by $^{87}Sr/^{86}Sr$: 0.7040,$^{143}Nd/\ ^{144}Nd$: 0.51295 and $^{206}Pb/^{204}Pb$: 18.8. He isotopic data suggests that at least some of the material involved in the genesis of the flood basalts was sourced from below the 670 km seismic discontinuity (Marty et al., 1996; Pik et al., 2006) and this likely represents the enriched plume component. Distinct from the plume material is a HIMU-type component (low $^{87}Sr/^{86}Sr$, high $^{206}Pb/^{204}Pb$) identified in some Eocene lavas in Ethiopia and Yemen (Baker et al., 1996; Stewart and

Rogers, 1996) and also in more recent lavas in Afar (Vidal et al., 1991; Deniel et al., 1994). Although originally attributed to the Afar plume, this HIMU signature is in fact widespread along the Red Sea/Yemen coast and may actually reside in the Arabian lithospheric mantle (Bertrand et al., 2003). Contrary to the conclusions of Pik et al (1999) and other plume-related models (i.e. Furman et al., 2006; Pik et al., 2006; Rogers, 2006), Kieffer et al (2004) have interpreted the geochemical variation observed amongst the Eocene Ethiopian basalts to reflect melting of heterogeneous mantle material across a broad thermal anomaly associated with the African superswell, a regional feature supporting dynamic topography across much of southern and eastern Africa (Nyblade and Robinson, 1994). Distinguishing between these models, which differ with respect to the regional geodynamic implications of different petrogenetic interpretations, requires better geophysical characterisation of the mantle structure beneath Ethiopia and a better understanding of the geochemical reservoirs invoked to explain variable melt compositions. An important step towards the latter would be further analyses of crustal and mantle xenoliths from Ethiopian lavas, as very few have yet been analysed. Modelling of trace element data from the most voluminous lava group forming the flood basalt succession (the low-Ti basalts; Pik et al., 1998) suggests that these magmas were generated by ~13% partial melting of a slightly depleted mantle source (Ayalew and Gibson, 2009).

5.3.2 Melt generation in the MER

Following the emplacement of the flood basalts and the initiation of rifting, volcanism in Ethiopia has been confined to the Main Ethiopian Rift (MER) and the rift zones in Afar. Recently the structure of the crust and upper mantle in the central and northern part of the MER, where magmatic rift segments have formed within the broad graben bounded by Miocene faults, has been well characterised by studies of seismic refraction,

velocity and anisotropy (e.g. Bastow et al., 2005, 2011; McGuire et al., 2006). These reveal a low velocity upper mantle, which is at elevated temperatures and contains partial melt (e.g. Bastow et al., 2005, 2008) and high-density intrusions in the crust beneath rift segments (e.g. Cornwell et al., 2006, 2010). Along the MER axis the crust varies in thickness from ~40 km in the southern part of the MER (~8°N) to ~30 km in the north (~11°N) (McGuire et al., 2006). The petrogenesis of lavas erupted in the MER has not been well studied and volcanism here involves numerous silicic volcanoes (e.g. Pyle, 1999; Peccerillo et al., 2003, 2007; Rampey et al., 2010) and fissural basalts and basaltic cones associated with magmatic rift zones (e.g. Chernet and Hart, 1999; George and Rogers, 1999; Rooney et al., 2011).

The isotopic compositions of MER basalts are broadly similar to the flood basalts but have a more restricted range (Furman, 2007). It has been suggested that some MER magmas have experienced a significant degree of crustal contamination (e.g. Boccaletti et al., 1995; Trua et al., 1999), however, as discussed by Rooney et al (2007), these studies did not account for compositional variation in primary melts (e.g. Rooney et al., 2005; Furman et al., 2006) and assumed crustal compositions based on crustal samples from elsewhere. In reality assessing melt-crust interactions is currently difficult in both the MER and Afar, due to the heterogeneous nature of the Pan-African crust and sparse coverage of compositional data from crustal exposures of xenoliths. Based on general indicators of crustal contamination, such as Ce/Pb and La/Nb ratios, contamination of MER lavas appears to be either very minor or absent (Furman, 2007; Rooney et al., 2007, 2010). Melting beneath the MER is typically considered to involve fertile peridotite related to the Afar plume (e.g. Furman et al., 2006; Furman, 2007) and at depths close to the garnet-spinel transition zone (Furman, 2007; Ayalew and Gibson,

2009; Rooney et al., 2010). Rare-earth element inversion modeling of the Eocene flood basalts and the younger MER basalts by Ayalew and Gibson (2009) suggest that since the Eocene the extent of partial melting in the mantle beneath the MER mantle has decreased from ~13 to 7% along with a decrease in mantle temperature.

5.4 Analytical methods

Samples of dense lavas for geochemical analysis were collected from the eastern flank and axial graben of the DMH rift segment and from the Badi-Dabbayra volcanic region to the east. A few 100 grams of material was crushed in a steel jaw crusher and powdered using an agate mill. Bulk major and trace element concentrations were determined for all samples using a PANalyticalAxios-Advanced XRF spectrometer at the University of Leicester, UK, using standard XRF glass disc and powder pellet preparatory techniques. Further trace element analyses were also performed for selected samples by solution ICP-MS using a Finnigan Element2 HR-ICP-MS at the Washington State University, USA. Further analytical details are in appendix B.

Sr-Nd-Pb isotope analyses were performed for 12 samples at Wood's Hole Oceanographic Institution, USA, using a ThermoFinnigan Neptune MC-ICP-MS. Powdered samples for Sr and Nd isotopic measurements were leached in an HF/perchloric acid mix prior to digestion. These were then dissolved in HCl and dried down several times before being centrifuged and passed through resin columns. Afte column separation samples where dried and re-dissolved in nitric acid. Samples for Pb isotopic analysis were exposed to an HF/HNO_3 acid mix and dried down several times

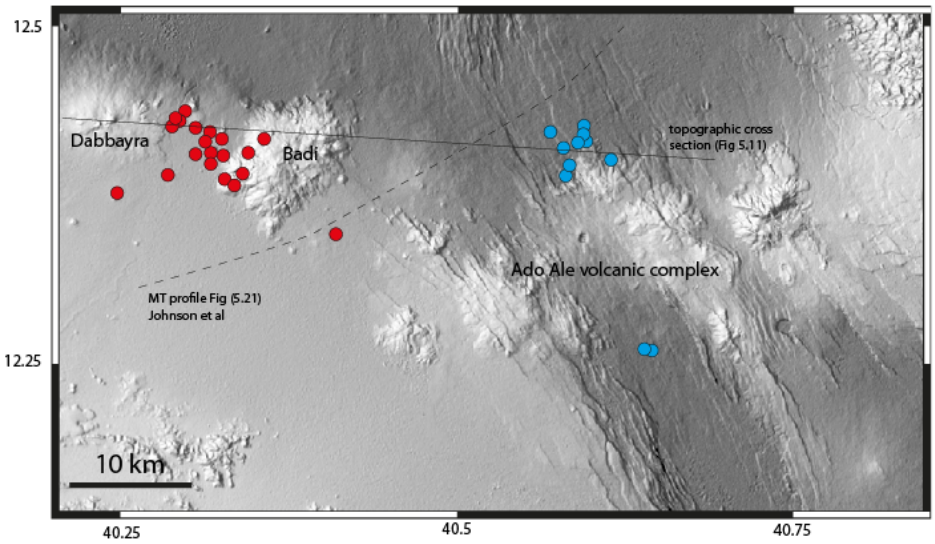

Figure 5.4 Location of lava samples discussed in this chapter from the main section of the DMH rift segment (blue symbols) and around the off-axis volcanic region (red symbols). For regional context see maps in chapters 1 and 2.

before further dissolution in HCl and HBr and column separation. Analytical details for these measurements are reported in the footnotes to Table 5.2.

5.5 Results

5.5.1 Major elements

The results of the major element analyses are reported in Table 5.1. All lava samples analysed are basaltic with the exception of one trachyandesite from the base of the Dabbayra volcanic complex. The location of sampling sites are shown in Fig 5.4. On a total alkali versus silica plot (Fig 5.5a) they straddle the alkaline/sub-alkaline divide, similar to other basalts from Afar (Barberi et al., 1975; Barrat et al., 1998, 2003). Plots of major element oxides versus MgO for all basaltic samples are shown in Fig 5.6 and lavas from each region follow separate major element trends. Mg# (Table 5.1) varies between 43 – 60 for the axial basalts and 47 – 69 for Badi-Dabayra

Table 5.1 Bulk major (wt%) and trace (ppm) element concentrations measured by XRF.

Location	DMH	DMH	DMH	DMH	DMH	DMH	DMH	DMH	DMH
Sample	**2007**	**2009**	**2805**	**SA05**	**SA02**	**SA01**	**2801B**	**2802**	**SAO4**
Latitude	12.263	12.256	12.393	12.415	12.413	12.413	12.413	12.404	12.415
Longitude	40.652	40.652	40.589	40.597	40.578	40.598	40.578	40.589	40.598
SiO_2	48.49	48.09	46.64	49.49	47.24	47.18	47.22	46.64	49.62
TiO_2	3.21	3.00	2.40	2.49	2.20	2.20	2.25	2.40	2.49
Al_2O_3	13.83	14.12	14.37	14.14	14.75	14.81	14.70	14.37	14.07
Fe_2O_3	16.08	15.41	13.88	13.81	13.75	13.71	13.85	13.88	13.65
MnO	0.246	0.236	0.209	0.219	0.206	0.204	0.209	0.209	0.216
MgO	5.43	5.30	8.26	5.93	9.42	9.12	8.96	8.26	6.03
CaO	9.57	9.88	10.35	9.71	10.09	10.00	10.06	10.35	9.91
Na_2O	3.01	3.03	2.46	2.83	2.41	2.48	2.47	2.46	2.88
K_2O	0.718	0.688	0.403	0.889	0.328	0.380	0.382	0.403	0.840
P_2O_5	0.518	0.477	0.366	0.347	0.300	0.332	0.346	0.366	0.343
SO_3	0.047	0.011	0.022	0.036	0.011	0.033	0.022	0.022	0.010
LOI	-0.77	-0.42	0.24	-0.35	-0.77	-0.59	-0.55	0.24	-0.03
Total	100.37	99.83	99.61	99.54	99.93	99.86	99.91	99.61	100.03
Mg#	42.60	43.10	56.70	48.57	60.12	59.41	58.74	56.70	49.27
CaO/Al_2O_3	0.69	0.70	0.72	0.69	0.68	0.68	0.68	0.72	0.70
K_2O/TiO_2	0.22	0.23	0.17	0.36	0.15	0.17	0.17	0.17	0.34
Ba	270	253	161	266	136	147	168	161	281
Ce	61.7	53.1	40.2	60.9	32.7	39.8	37.8	40.2	62.8
Co	48.6	46.4	52.3	42.4	52.5	52.2	51.6	52.3	38.1
Cr	38	54	266	162	270	271	269	266	140
Cu	61	61	114	60	91	105	109	114	52
Ga	20.1	23.0	19.0	20.9	19.7	20.0	20.5	19.0	23.3
La	24.0	22.2	13.6	25.8	14.1	15.0	15.3	13.6	23.0
Mo	1.29	1.29	2.11	1.29	2.06	2.38	2.43	2.11	1.29
Nb	30.1	23.2	20.9	22.9	17.0	18.6	18.6	20.9	22.9
Nd	30.3	26.6	22.2	31.7	19.9	23.1	20.9	22.2	30.3
Ni	15	16	91	33	115	110	106	91	32
Pb	3.38	23.89	2.33	33.79	2.26	1.64	1.53	2.33	33.79
Rb	172	171	8	172	7	8	8	8	172
Sc	48.8	49.2	36.0	43.8	31.5	30.5	31.8	36.0	41.6
Sr	225	224	301	225	301	304	307	301	225
V	429	413	334	331	286	290	295	334	295
Y	59.1	45.4	34.4	45.3	30.5	32.7	33.2	34.4	45.3
Zn	132	124	98	112	86	92	91	98	98
Zr	173	171	156	173	130	143	144	156	173

All data determined using a PANalytical Axios Advanced XRF spectrometer at the University of Leicester, UK.
Samples prepared using standard XRF preparation techniques (described in appendix B)
Mg# calculated from molar Mg/(Mg+Fe) assuming 90% Fe as Fe^{2+}.
BD = Badi-Dabbayra, DMH = Dabbahu-Manda Hararo Segment

Location	DMH	DMH	DMH	BD	BD	BD	BD	BD	BD
Sample	**28-11**	**28-12**	**SAO3**	**BADI0**	**0111**	**24-01**	**21-01**	**2911**	**2909**
Latitude	12.410	12.414	12.396	12.378	12.398	12.333	12.396	12.425	12.42
Longitude	40.601	40.598	40.590	40.328	40.355	40.389	40.321	40.292	40.29
SiO_2	46.53	50.10	47.02	48.80	50.61	48.03	49.52	48.54	59.15
TiO_2	2.26	2.58	2.34	2.06	1.67	1.80	2.09	1.89	1.29
Al_2O_3	14.23	14.17	14.73	15.87	15.81	15.30	15.35	15.79	15.75
Fe_2O_3	13.57	13.97	13.96	11.18	9.70	10.79	11.53	11.20	9.57
MnO	0.206	0.218	0.211	0.177	0.158	0.169	0.188	0.176	0.223
MgO	8.69	6.64	8.48	7.16	7.22	8.95	6.99	6.70	1.59
CaO	10.32	9.58	10.20	10.26	9.92	11.85	9.43	12.05	3.93
Na_2O	2.27	2.90	2.45	2.79	2.88	2.44	2.97	2.41	5.02
K_2O	0.274	0.877	0.343	0.846	1.054	0.515	0.922	0.557	3.039
P_2O_5	0.381	0.363	0.330	0.342	0.276	0.299	0.352	0.297	0.499
SO_3	0.455	0.023	0.017	0.090	0.076	0.031	0.212	0.052	0.023
LOI	0.15	-0.50	-0.56	0.05	0.36	-0.11	0.20	-0.14	-0.19
Total	99.34	100.05	99.52	99.62	99.73	100.06	99.76	100.52	99.89
Mg#	58.49	51.12	57.20	58.50	62.08	64.61	57.16	56.82	26.80
CaO/Al_2O_3	0.73	0.68	0.69	0.65	0.63	0.77	0.61	0.76	0.25
K_2O/TiO_2	0.12	0.34	0.15	0.41	0.63	0.29	0.44	0.29	2.35
Ba	135	281	158	287	285	208	281	226	917
Ce	37.1	59.3	33.2	47.5	45.4	35.3	57.9	41.7	142.9
Co	53.2	38.9	48.5	42.0	38.2	38.7	42.5	40.9	9.6
Cr	271	142	243	93	215	338	31	185	<0.7
Cu	115	52	109	62	54	78	14	66	5
Ga	18.1	22.8	21.2	18.2	17.4	17.1	18.6	17.7	26.6
La	13.8	27.8	16.5	20.4	22.4	18.5	24.8	19.6	64.4
Mo	2.12	1.29	2.16	2.89	2.24	1.12	3.05	1.29	4.89
Nb	18.9	22.9	18.2	29.7	25.2	24.0	34.7	22.9	86.7
Nd	21.7	33.8	19.7	27.9	26.1	20.0	29.1	21.3	67.7
Ni	100	32	93	53	59	115	12	74	<0.7
Pb	2.09	33.79	1.86	1.33	3.27	20.54	2.49	33.79	7.07
Rb	5	172	5	19	26	182	20	172	73
Sc	34.1	41.1	32.0	33.5	30.7	46.9	30.7	46.2	16.3
Sr	292	225	309	368	286	251	360	225	362
V	309	314	285	303	237	253	271	277	19
Y	32.4	45.3	33.6	29.3	30.5	48.2	34.6	45.3	58.2
Zn	97	99	90	79	69	64	92	73	115
Zr	144	173	144	159	166	172	195	173	197

Location	BD	BD	BD	BD	BD	BD	BD	BD	BD
Sample	**2609**	**3016**	**0402**	**25-01**	**20-01**	**3004(3)**	**BAD4**	**26-11**	**29-08**
Latitude	12.384	12.410	12.418	12.358	12.396	12.389	12.371	12.368	12.426
Longitude	40.292	40.306	40.308	40.352	40.391	40.337	40.327	40.262	40.296
SiO_2	47.98	49.14	48.05	48.67	49.41	46.55	49.74	49.44	48.37
TiO_2	2.71	2.59	1.45	1.87	1.90	2.33	1.92	2.89	1.99
Al_2O_3	14.90	14.80	15.29	15.64	15.66	15.88	15.89	15.04	15.64
Fe_2O_3	13.19	12.25	10.12	10.72	10.67	11.24	10.63	13.52	11.37
MnO	0.207	0.201	0.15	0.171	0.170	0.176	0.170	0.215	0.180
MgO	6.59	6.53	9.35	6.42	7.02	8.47	6.39	5.45	7.69
CaO	8.89	8.64	11.47	10.62	10.09	10.87	9.82	7.79	11.23
Na_2O	3.39	3.15	2.57	2.63	2.67	2.41	2.93	3.51	2.57
K_2O	0.939	1.027	0.55	0.601	0.950	0.748	1.114	1.048	0.655
P_2O_5	0.432	0.413	0.19	0.361	0.344	0.366	0.354	0.454	0.310
SO_3	0.618	0.056	0.22	0.066	0.055	0.044	0.087	0.069	0.029
LOI	0.50	0.05	0.56	-0.10	0.56	0.32	0.74	0.66	-0.36
Total	99.62	99.59	99.98	100.35	99.50	99.41	99.78	100.10	99.68
Mg#	52.35	53.97	67.03	56.84	59.16	62.40	56.94	47.00	59.81
CaO/Al_2O_3	0.60	0.58	0.75	0.68	0.64	0.68	0.62	0.52	0.72
K_2O/TiO_2	0.35	0.40	0.38	0.32	0.50	0.32	0.58	0.36	0.33
Ba	321	368	173	264	331	246	322	366	241
Ce	57.4	59.0	30.5	44.0	52.8	44.7	54.0	63.4	40.8
Co	40.0	44.0	45.5	49.1	40.7	46.3	39.7	35.4	44.6
Cr	11	212	236	364	91	208	79	4	173
Cu	15	26	32	69	54	80	54	16	74
Ga	21.5	21.2	16.8	16.4	18.9	17.1	18.9	23.5	19.4
La	25.2	25.5	12.1	19.8	24.8	19.7	25.1	27.7	19.0
Mo	3.20	2.87	2.26	2.37	2.69	2.44	2.44	3.25	2.28
Nb	39.7	36.0	19.4	24.9	31.1	31.4	33.1	44.1	26.3
Nd	28.4	29.7	17.4	24.5	25.7	22.6	25.8	34.2	22.4
Ni	3	63	72	120	58	95	48	<0.9	61
Pb	2.55	2.70	0.71	1.29	3.36	1.71	2.65	0.82	1.93
Rb	22	22	12	12	19	17	26	25	15
Sc	31.2	30.4	32.2	33.1	30.2	31.2	27.7	30.2	33.2
Sr	384	461	474	324	352	469	353	406	340
V	359	313	242	280	255	302	237	321	286
Y	35.9	31.9	17.1	26.1	30.2	21.9	31.0	37.2	27.5
Zn	100	94	58	68	79	72	80	110	73
Zr	194	197	136	120	184	125	196	209	134

Location	BD	BD	BD	BD	BD	BD	BD	BD	BD
Sample	**BAD6**	**30-13**	**21-04**	**26-01**	**26-04**	**26-02**	**04-01**	**21-06**	**2910**
Latitude	12.378	12.392	12.414	12.398	12.400	12.398	12.418	12.388	12.424
Longitude	40.328	40.340	40.313	40.320	40.320	40.320	40.302	40.314	40.292
SiO_2	48.80	46.49	48.92	49.37	49.56	48.67	48.12	49.96	59.96
TiO_2	2.06	2.37	1.97	2.25	2.26	2.26	1.45	2.06	1.19
Al_2O_3	15.87	15.76	16.32	15.49	15.49	15.19	16.51	15.42	15.84
Fe_2O_3	11.18	11.29	10.64	11.79	11.83	11.72	9.06	11.48	9.17
MnO	0.177	0.178	0.172	0.188	0.188	0.188	0.146	0.183	0.210
MgO	7.16	7.78	7.33	7.19	7.08	7.14	8.99	6.74	1.47
CaO	10.26	10.98	10.06	9.31	9.04	9.31	11.51	9.23	3.62
Na_2O	2.79	2.57	2.91	2.62	3.28	3.20	2.39	3.00	4.93
K_2O	0.846	0.868	0.845	0.839	0.787	0.823	0.581	0.848	3.149
P_2O_5	0.342	0.384	0.293	0.361	0.369	0.379	0.190	0.343	0.432
SO_3	0.090	0.074	0.055	0.159	0.033	0.083	0.222	0.048	0.018
LOI	0.05	0.41	0.01	0.65	-0.01	0.83	0.58	0.15	-0.15
Total	99.62	99.15	99.53	100.22	99.91	99.79	99.76	99.47	99.83
Mg#	58.50	60.24	60.27	57.29	56.85	57.28	68.60	56.38	26.1
CaO/Al_2O_3	0.65	0.70	0.62	0.60	0.58	0.61	0.70	0.60	0.23
K_2O/TiO_2	0.41	0.37	0.43	0.37	0.35	0.36	0.40	0.41	2.65
Ba	287	281	275	268	271	257	173	272	965
Ce	47.5	54.9	47.2	48.2	49.4	48.9	30.5	59.2	140
Co	42.0	45.1	41.1	39.5	38.8	41.5	45.5	42.6	11.32
Cr	93	214	131	162	171	163	236	32	<0.7
Cu	62	78	10	19	17	22	32	15	<1.7
Ga	18.2	18.1	17.4	18.6	20.2	20.1	16.8	19.3	3.7
La	20.4	23.0	19.3	22.6	21.2	21.8	12.1	24.8	26.0
Mo	2.89	2.17	2.49	2.04	2.68	2.53	2.26	2.83	69
Nb	29.7	34.1	28.5	32.1	33.1	33.4	19.4	34.2	4.6
Nd	27.9	25.3	22.5	27.0	28.4	26.5	17.4	28.1	90
Ni	53	88	18	25	33	31	72	10	65
Pb	1.33	1.54	2.47	0.98	2.25	2.14	0.71	3.43	<0.7
Rb	19	19	17	17	17	18	12	20	8.3
Sc	33.5	32.1	32.6	31.6	28.4	30.5	32.2	29.1	74
Sr	368	466	465	389	374	391	474	358	356.2
V	303	309	283	290	279	287	242	272	20.68
Y	29.3	23.2	23.9	30.4	31.7	31.4	17.1	35.7	58
Zn	79	74	76	92	90	95	58	96	117
Zr	159	135	139	154	163	161	92	201	593

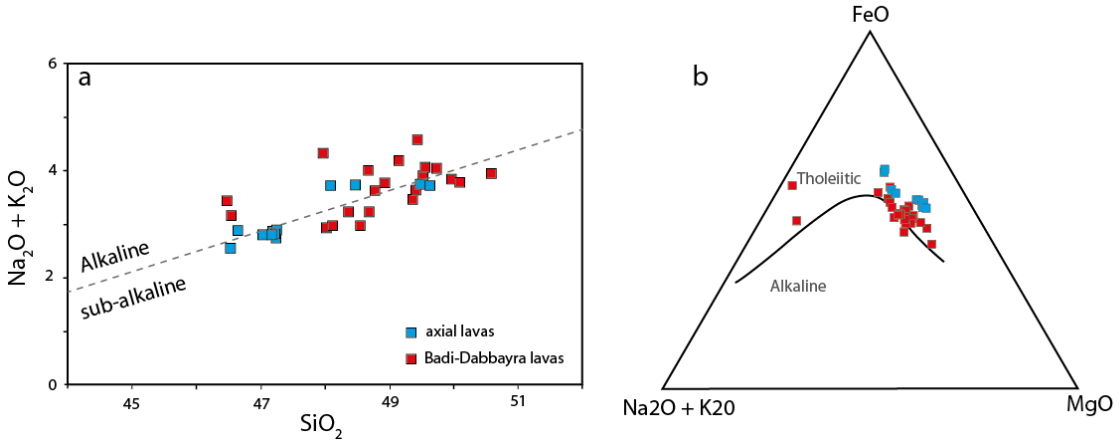

Figure 5.5 (a) Total alkali vs. Silica (TAS) plot for basaltic lavas. Similar to other Afar basalts (i.e. Barberi et al., 1975) these are transitional between the alkaline and sub-alkaline fields of MacDonald (1968). (b) AFM discrimination diagram (including intermediate samples) with alkaline-tholeiitic division of Irvine and Baragar (1971).

basalts, indicating a similar degree of differentiation. At 9 wt% MgO lavas from the DMH rift segment have higher $Fe_2O_3^T$ and lower K_2O, Al_2O_3 and K_2O/TiO_2 compared to those erupted off-axis. Na_2O, SiO_2 and CaO/Al_2O_3 are similar for both groups. Overall SiO_2 contents are relatively low for both lava groups varying between 49.3 ± 1.9wt% for MgO of ~4-10 wt%. TiO_2, Na_2O, $Fe_2O_3^T$ and K_2O increase in all samples with decreasing MgO, while Na_2O and Al_2O_3 increase. CaO also decreases in all samples with decreasing MgO but in the axial basalts this variation is very small (9.6 – 10.4 wt%). On the TAS plot (Fig 5.5a) there is no discernable difference in alkalinity between sample groups, however in the AFM classification scheme, shown in Fig 5.5b, the two groups are more distinct and the axial lavas classed as more strongly tholeiitic, with the Badi-Dabayra samples plotting across the alkaline-tholeiitic divide. This is similar to the difference in alkalinity previously observed between basalts erupted at axial rift zones and off-axis transverse volcanic zones in other parts of Afar (e.g. De Fino et al., 1973; Barberi et al., 1974; Civetta et al., 1978). It should be noted, however, that although the Badi-Dabbayra lavas and other transverse volcanics, such as those from Assab in eastern Afar (De Fino et al., 1973; Civetta et al., 1974) are classed

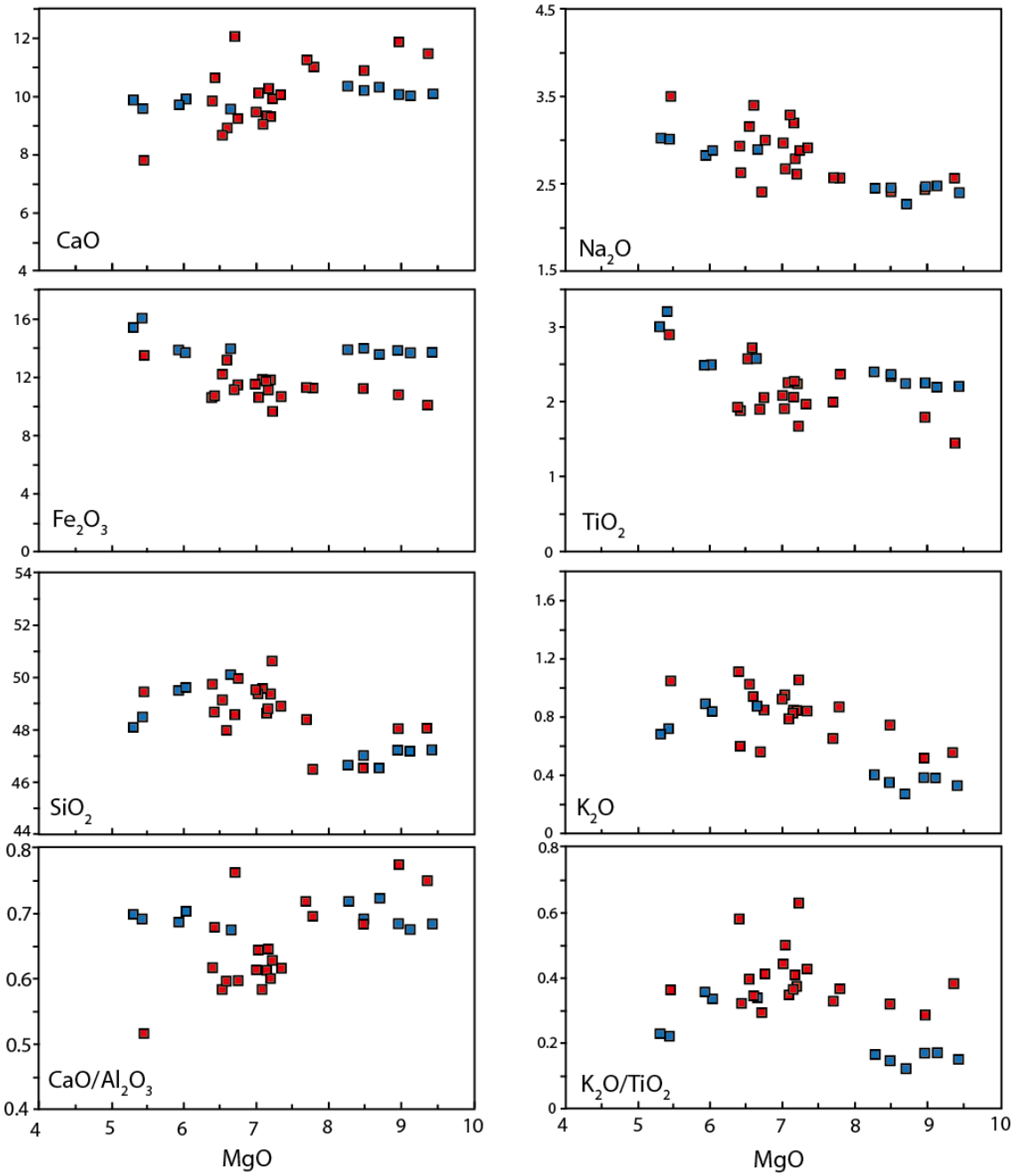

Figure 5.6 Harker style major element variation plots for all basaltic lavas listed in table 5.1. Symbols are the same as in Figure 5.5 (axial lavas: blue; off-axis lavas: red). Coherent trend can be recognized between lava samples groups from each region. All concentrations in wt%. See text for discussion.

as alkaline based on the Irvine and Baragar (1971) AFM scheme, all these suites show enrichment in $Fe_2O_3^T$ during their early evolution and could therefore all be considered to follow a tholeiitic evolutionary trend (see Zimmer et al., 2010).

5.5.2 Trace elements

Trace element concentrations determined by XRF are listed in Table 5.1. Data from ICP-MS analyses are listed in Table 5.2. MORB normalized spidergrams of trace element concentrations are shown in Fig 5.7 and mantle normalized rare earth element (REE) profiles in Fig 5.8. Selected ratio-ratio plots and variation diagrams are shown in Fig 5.9. All the lavas are enriched in trace elements compared to MORB with the exception of some of the least incompatible elements (i.e. Ho, Y, Er etc), which show slight depletions (Fig 5.7). All the axial lavas sampled have very consistent trace element profiles and concentrations and show little variation between individual samples. There is more variability in the Badi-Dabbayra lavas, which have consistently steeper patterns due to relative enrichments in the more incompatible elements and some have cross cutting profiles. Lavas from both groups have the largest peaks (relative enrichments) at Ba and Ta and relative depletions in U. Some off-axis samples have minor peaks at Pb. The off-axis samples have moderate (~1.5 times greater) but significant enrichments in both the highly and moderately incompatible elements compared to those erupted on-axis. On average these are also slightly more depleted in the heavier REE and other less incompatible elements (Fig 5.8). Accordingly there is a systematic variation in ratios between elements with higher to lower incompatibility (i.e. Sm/La, Zr/Y, Ba/Y, Zr/Nb etc) between sample groups (Fig 5.9). Plots of trace elements vs. Mg# also clearly show the consistent difference in incompatible element enrichment between sample groups. Tb/Yb_N ratios vary between 1.58 – 1.83 for all samples, with the highest values in the off-axis samples (Tb/Yb_N >1.73) (shown in Fig 5.11). Ratios of elements with approximately similar geochemical behaviour (i.e. Ba/Nb, Th/U) have similar ranges for all lavas (Fig 5.9).

Table 5.2 Trace element and isotopic compositions for selected samples

Location	DMH	DM	DMH	DMH	DMH	DMH	DMH	DMH	DMH
Sample	**2007**	**2009**	**2805**	**SA05**	**SA02**	**SA01**	**2801B**	**SAO4**	**SAO3**
ppm									
La	24.69	23.1	15.23	25.41	12.75	14.50	14.61	25.27	14.09
Ce	55.51	52.1	35.01	56.41	29.87	33.64	34.07	56.10	32.97
Pr	7.39	6.98	4.76	7.30	4.13	4.64	4.65	7.30	4.52
Nd	32.58	30.8	21.50	31.43	18.80	21.07	20.92	31.14	20.65
Sm	8.16	7.62	5.39	7.67	4.87	5.35	5.25	7.68	5.33
Eu	2.72	2.61	2.03	2.43	1.81	1.95	1.97	2.41	1.99
Gd	8.60	8.2	5.94	8.24	5.30	5.85	5.81	8.17	5.82
Tb	1.42	1.35	0.98	1.38	0.87	0.95	0.96	1.38	0.97
Dy	8.66	8.28	5.95	8.46	5.37	5.89	5.85	8.42	5.86
Ho	1.74	1.69	1.19	1.74	1.08	1.18	1.19	1.75	1.17
Er	4.67	4.41	3.11	4.59	2.81	3.10	3.08	4.60	3.12
Tm	0.65	0.61	0.44	0.67	0.40	0.43	0.43	0.66	0.43
Yb	3.94	3.77	2.67	4.01	2.43	2.60	2.60	4.01	2.61
Lu	0.62	0.59	0.40	0.62	0.36	0.41	0.39	0.63	0.39
Ba	261	247	145	239	123	136	138	238	133
Th	2.01	1.85	0.89	2.43	0.74	0.92	0.88	2.40	0.81
Nb	29.44	27.6	18.16	30.65	15.02	16.92	17.46	30.83	16.73
Y	43.19	41.3	29.37	42.77	26.40	28.70	28.89	42.86	29.14
Hf	5.00	4.67	3.37	5.50	3.02	3.34	3.29	5.55	3.31
Ta	2.00	1.86	1.19	2.07	1.03	1.15	1.16	2.07	1.12
U	0.55	0.52	0.25	0.66	0.22	0.26	0.24	0.66	0.21
Pb	2.32	2.11	1.28	2.49	1.06	1.29	1.37	2.49	1.26
Rb	15.5	14.6	6.1	20.0	5.0	6.2	6.4	19.8	3.9
Cs	0.15	0.14	0.05	0.22	0.04	0.06	0.06	0.20	0.03
Sr	299	295	294	290	283	292	290	289	285
Sc	37.5	38.2	35.3	35.9	38.8	34.5	35.7	36.4	37.0
Zr	197	184	139	216	119	133	136	216	133
$^{87}Sr/^{86}Sr$	0.70383		0.70381	0.70383	0.703813	0.703	0.7038		
$^{144}Nd/^{143}N$	0.51289		0.51292	0.51286	0.512864	0.512	0.5129		
$^{206}Pb/^{204}Pb$	18.5218		18.50	18.49	18.48	18.48	18.50		
$^{207}Pb/^{204}Pb$	15.5616		15.56	15.56	15.56	15.56	15.57		
$^{208}Pb/^{204}Pb$	38.4823		38.51	38.46	38.50	38.51	38.53		

Trace elements determined by solution Inductively Coupled Plasmas Mass Spectrometry (ICP-MS) at the University of Washington, USA using the procedure of Knaack et al (1994). Precision on the trace element analyses based on internal standards and blanks is around ±5% for the REE's and ~±10% for other traces. Sr, Nd and Pb Isotopic analyses were conducted at Woods Hole Oceanographic Institution, USA using a ThermoFinnigan Neptune MC-ICP-MS and similar analytical procedures to Waters et al (2011). See appendix B for full analytical details. Sr and Nd have an internal precision (2-sigma) of 8-15 ppm, external precision is estimated to be between 15-25 ppm after adjusting to SRM987 ($^{87}Sr/^{86}Sr = 0.71024$) and La Jolla ($^{144}Nd/^{143}Nd = 0.511847$) standards. Measurements of Pb isotopes have (2-sigma) internal precision of 20-40 ppm and external precision from 20 ppm for $^{207}Pb/^{204}Pb$ to 120 ppm for $^{208}Pb/^{204}Pb$. For further details see appendix B.

Location	BD	BD	BD	BD	BD	BD
Sample	**BADI05**	**2911**	**2609**	**3016**	**0402**	**2909**
ppm						
La	22.09	17.96	27.71	26.25	20.61	69.32
Ce	46.75	38.41	58.53	56.70	44.11	155.50
Pr	5.88	4.90	7.38	7.24	5.46	18.53
Nd	24.44	20.84	31.01	30.26	22.67	72.04
Sm	5.56	4.75	7.09	6.73	4.99	15.23
Eu	1.93	1.69	2.41	2.24	1.77	2.74
Gd	5.55	4.87	7.04	6.39	4.81	13.75
Tb	0.89	0.79	1.12	1.01	0.75	2.34
Dy	5.33	4.78	6.66	5.94	4.50	14.21
Ho	1.08	0.94	1.34	1.16	0.90	2.84
Er	2.73	2.49	3.40	3.00	2.28	7.82
Tm	0.39	0.34	0.48	0.42	0.32	1.18
Yb	2.36	2.07	2.95	2.51	1.90	7.84
Lu	0.36	0.32	0.45	0.38	0.29	1.29
Ba	262	204	325	338	285	181
Th	2.39	1.74	2.61	2.54	2.15	9.29
Nb	27.27	23.17	36.57	32.69	26.48	87.02
Y	26.31	23.62	33.04	28.70	21.74	62.04
Hf	3.79	3.07	4.61	4.61	3.40	14.70
Ta	1.81	1.54	2.46	2.20	1.80	5.51
U	0.64	0.32	0.73	0.74	0.60	0.29
Pb	2.04	1.45	1.90	2.44	2.71	8.36
Rb	19.1	12.9	19.8	20.6	18.1	95.0
Cs	0.18	0.07	0.19	0.18	0.18	0.22
Sr	360	347	391	464	472	9
Sc	32.4	33.6	31.8	29.2	29.7	3.1
Zr	151	119	184	186	136	619
$^{87}Sr/^{86}Sr$	0.70374	0.70381	0.70376	0.70366	0.70378	0.7037
$^{144}Nd/^{143}Nd$	0.512872	0.51288	0.51289	0.51285	0.512839	0.512864
$^{206}Pb/^{204}Pb$	18.72	18.81	18.79	18.76	18.86	18.69
$^{207}Pb/^{204}Pb$	15.57	15.58	15.58	15.58	15.58	15.57
$^{208}Pb/^{204}Pb$	38.60	38.73	38.72	38.61	38.74	38.52

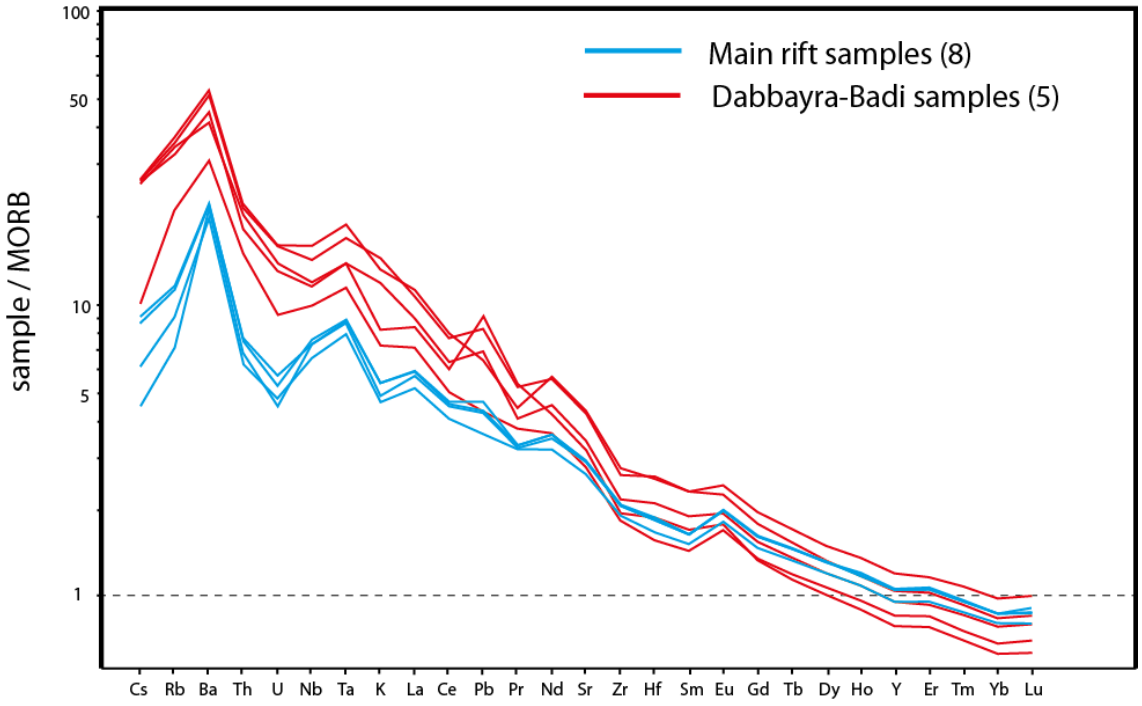

Figure 5.7. MORB normalized trace element patterns for samples with MgO > 6wt% (ICP-MS data; Table 5.2). N-MORB values from Sun and McDonough (1989). Lava from off-axis volcanoes show consistent enrichments in the most incompatible element compared to the axial basalts. All samples are enriched relative to MORB except for the heavy rare earths elements, which are slightly depleted.

5.5.3 Sr-Nd-Pb isotopes

The $^{87}Sr/^{86}Sr$, $^{144}Nd/^{143}Nd$, $^{206}Pb/^{204}Pb$, $^{207}Pb/^{204}Pb$ and $^{208}Pb/^{204}Pb$ results are listed in Table 5.2. Plots of variations between radiogenic isotope ratios are shown in Fig 5.9 Axial lavas from the DMH segment have $^{144}Nd/^{143}Nd$ of 0.512927 to 0.512864 and $^{87}Sr/^{86}Sr$ of 0.703825 to 0.703791, both essentially constant within analytical uncertainties.$^{144}Nd/^{143}Nd$ for the Badi-Dabbayra lava varies from 0.512890 to 0.512839 and is also invariant within analytical error. $^{87}Sr/^{86}Sr$ varies from 0.703814 to 0.703646, larger than the analytical uncertainty but still very small. There are very slight variations observed in Pb isotopes in the axial basalts, with$^{206}Pb/^{204}Pb$ varying from 18.52 to 18.48, $^{207}Pb/^{204}Pb$ from 15.57 to 15.56 and $^{208}Pb/^{204}Pb$ from 38.53 to 38.46. More significant variability in Pb is observed in the Badi-Dabbayra lavas where $^{206}Pb/^{204}Pb$ varies from 18.86 to 18.53, $^{207}Pb/^{204}Pb$ from 15.58 to 15.56 and $^{208}Pb/^{204}Pb$ from 38.74 to 38.38. These are all positively correlated in Pb isotopic space and trend away from

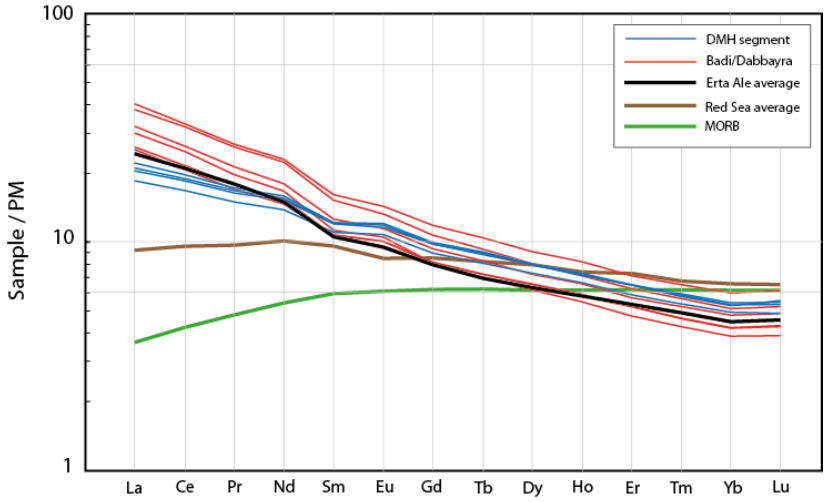

Figure 5.8. Primitive mantle normalized REE profiles for basaltic lava. Normalizing values from Sun and McDonough (1989). Basalt display smooth patterns and are enriched compared to Red Sea Basalts and typical MORB

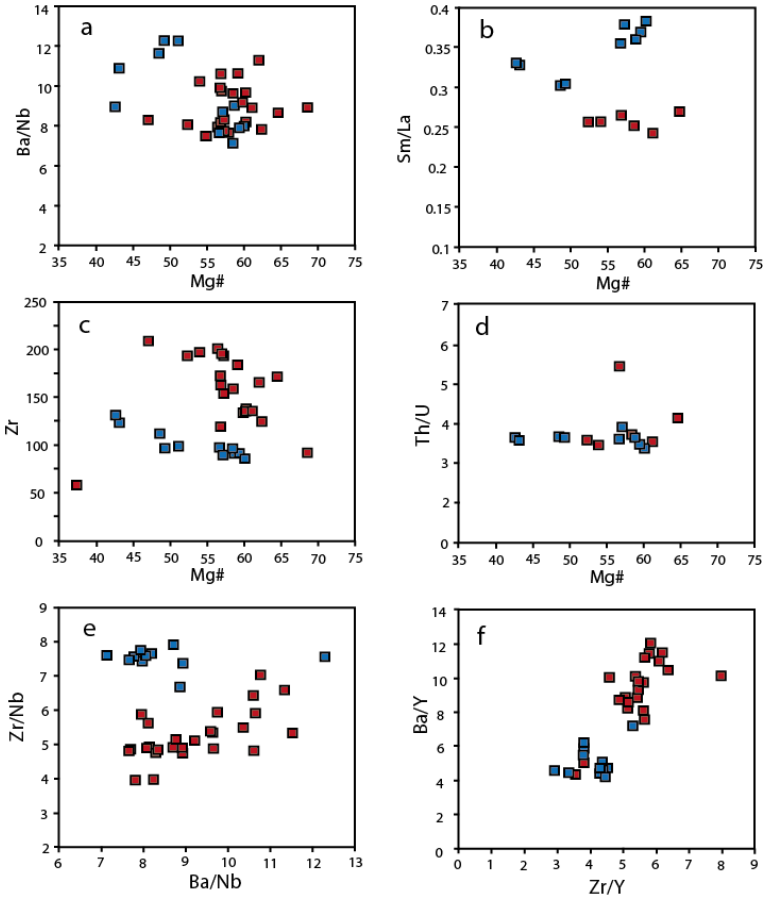

Figure 5.9 Plots showing variation in selected trace element parameters with Mg# and co-variation of Zr/Y vs. Ba/Y and Zr/Nb vs. Ba/Nb. Off-axis lavas (red symbols) are typically more enriched in highly incompatible element such as Zr and Ba compared to the axial lavas (blue symbols). See text for discussion.

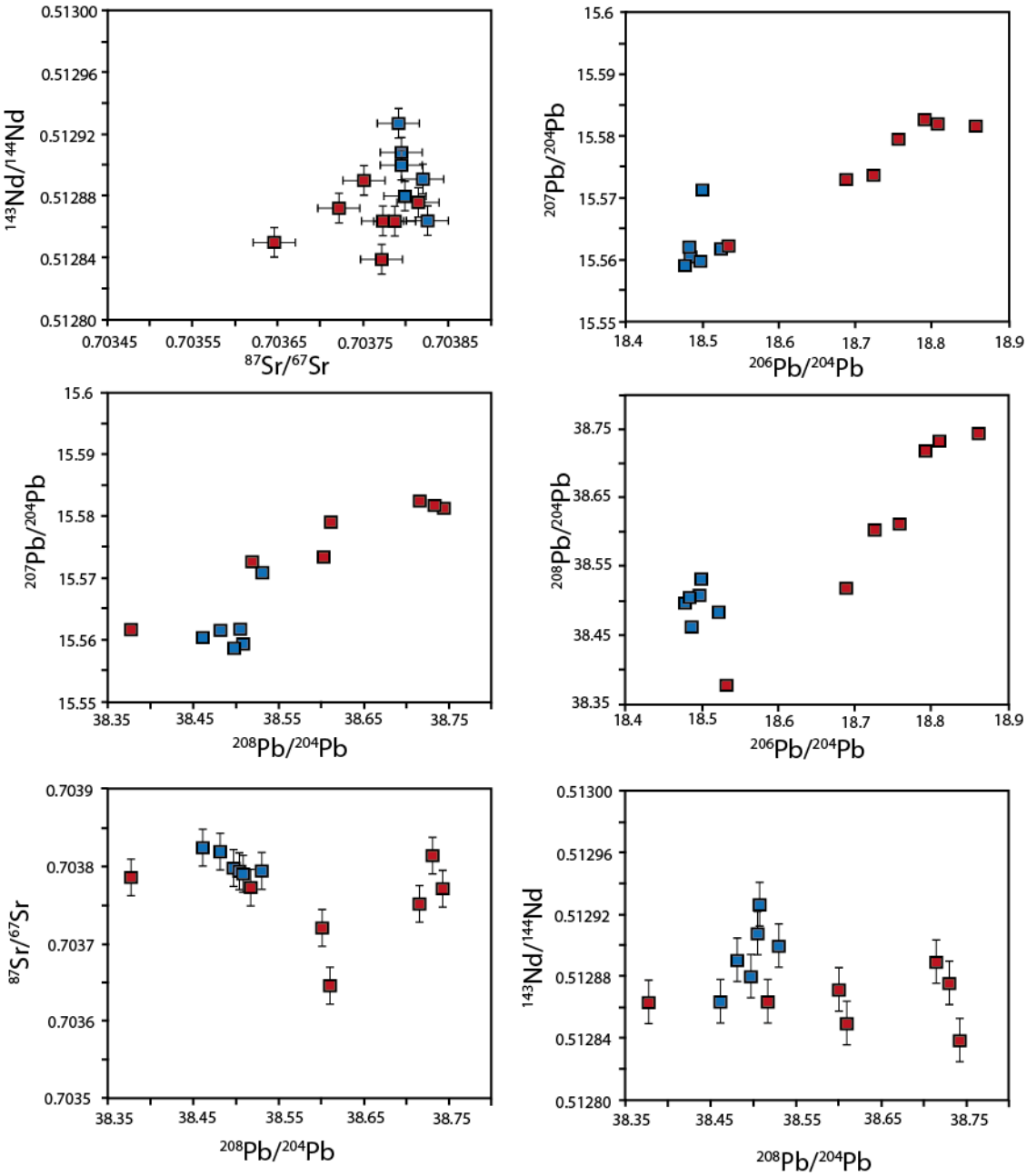

Figure 5.10 Plots of isotopic compositions of samples listed in table 5.2. Both $^{87}Sr/^{86}Sr$ and $^{143}Nd/^{144}Nd$ show only minor variations across the whole sample suite and are mostly uniform within analytical uncertainties. More variation is observed in the Pb isotopic compositions, which are positively correlated in Pb-Pb isotopic plots. Red symbols: off-axis lavas, blue symbols: axial lavas

the axial samples towards higher (more radiogenic) values. In all the isotopic systems investigated values for the trachyandesite lava sample (sample 2909; Table 5.2) from Dabbayra has comparable values to the basaltic lavas and there is no correlation between any isotopic variations with Mg# or sample age. All samples have more radiogenic compositions than typical MORB compositions (i.e. Fig 5.12).

5.5.4 spatial variations in lava chemistry

The major element data demonstrates that the lavas erupted in the main rift zone and at the off-axis volcanoes have followed distinct liquid lines of descent and that melts supplied to these two regions therefore have to some extent differing genetic histories. In the most primitive samples analysed from both regions (Mg# > 55), the on-axis lava have greater initial concentrations of $Fe_2O_3^T$ and lower K_2O, Al_2O_3 and K_2O/TiO_2 (Fig 5.6). Of the 16 samples with high precision ICP-MS trace element data, 12 also have isotopic data and 13 have known eruption ages, based on the $^{40}Ar/^{39}Ar$ geochronology or the recently observed eruptions (2007 and 2009). One further sample (0111) has isotopic data and a $^{40}Ar/^{39}Ar$ age. The total-known age range for all samples is 0 to 445 ka. The axial samples have ages between 0 – 193 ka and based on the extension rate corrected locations (see chapter 4) are inferred to have been erupted in the axial graben. The off-axis lavas have ages of 25 – 445 ka and were erupted from individual cones forming part of, or adjacent to, the Badi or Dabbayra volcanic complexes and do not have a regular spatial pattern of ages. There is a ~20 km gap between sample locations in the main rift zone (taken from the axial graben and eastern flank) and those from the off-axis volcanoes (Fig 5.4).

There are no clear systematic variations in chemical parameters with eruption age, either across the whole study area or within the on and off- axis samples. Fig 5.11

shows selected element-element and isotopic ratios for lavas along a profile perpendicular to the strike of the DMH rift axis. $^{87}Sr/^{86}Sr$ and $^{144}Nd/^{143}Nd$ remain largely constant across the region, however spatial gradients are observed in $^{206}Pb/^{204}Pb$, $^{207}Pb/^{204}Pb$ and $^{208}Pb/^{204}Pb$ (only $^{206}Pb/^{204}Pb$ shown in the figure) all trending to higher values away from the axis. Ratios between element with lower to higher incompatibility (K_2O/TiO_2, La/Sm_N, Tb/Yb_N, Zr/Nb etc) also show variations between the main rift and off-axis volcanoes with consistently higher values for lavas erupted off-axis, while ratios between elements with similar compatibility (Th/U, Ba/Nb etc) are similar for both locations.

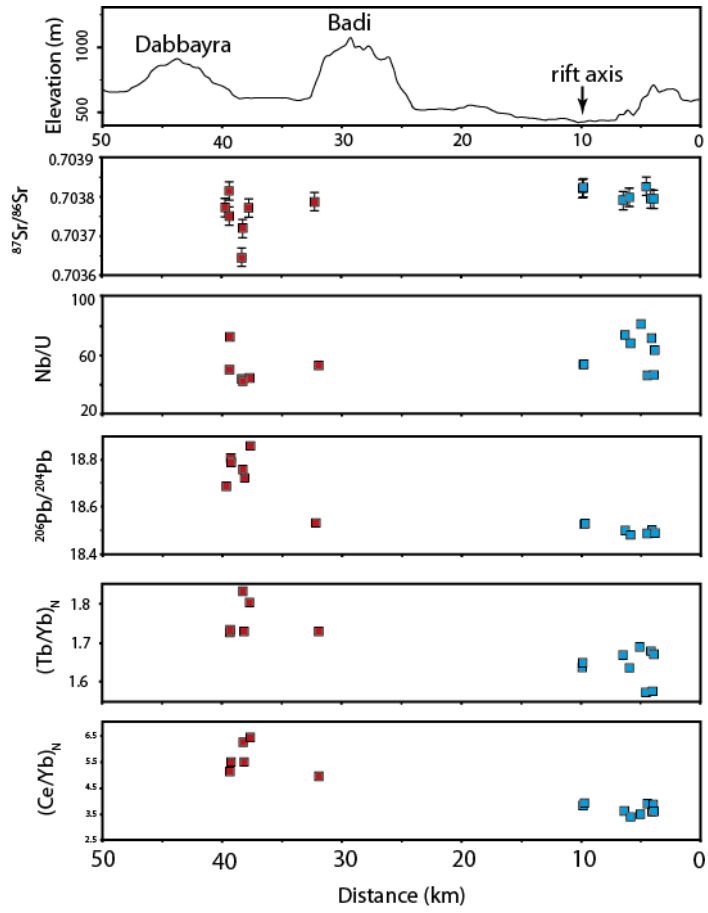

Figure 5.11 Illustration of the variation in certain chemical parameters with distance across the DMH rift system from the rift axis to the off-axis volcanoes on the western margin. $^{86}Sr/^{87}Sr$ and Nb/U values are similar in lavas from both areas, $^{206}Pb/^{204}Pb$, $(Tb/Yb)_N$, $(Ce/Yb)_N$ (MORB normalized) all show consistent variations and are higher in the off-axis lavas. Line of section is shown in Figure 5.4.

5.5.5 Summary of observations

There are some broad geochemical characteristics that are common to all lavas erupted both along the DMH axis and at the off-axis volcanoes. All samples are enriched in incompatible trace elements compared to average MORB's and have a limited range of isotopic compositions. Ratios between highly incompatible elements (Th/U, Ba/Nb, La/Nb etc)are also very similar for all the basalts analysed. However, as discussed above some important differences in geochemical parameters are observed between lavas erupted in the on and off-axis locations. Off-axis lavas consistently have more enriched trace element features (i.e. higher La/Sm, Zr/Nb, K_2O/TiO_2) and show significant variations in Pb isotopic values. The variations in incompatible trace element ratios are important as these are sensitive to source lithology and melting processes. The overall enrichment of all samples compared to average MORB compositions suggests a more fertile mantle source or lower extents of melting than typically occurs during MORB petrogenesis. An important constraint on melting processes is to what extent melting occurs in the presence of garnet (as opposed to spinel or plagioclase at lower pressures). Garnet has an affinity for the HREE and therefore causes fractionations between the incompatible LREE and MREE and the garnet compatible HREE (e.g. Fig 5.3b). The value of Tb/Yb_N in melts is a good indicator of the extent to which peridotite melting has occurred in the garnet or spinel stability fields (e.g. O'Neil, 1981). In lavas from the Basin and Range region in the western USA, Wang et al (1998) found a correlation between Tb/Yb_N and other indicators of melting depth, with garnet-dominated melting producing partial melts with $Tb/Yb_N > 1.8$. Rooney et al (2010) employed a similar criterion to discriminate between melting column depths for lavas erupted in the MER and attributed lower Tb/Yb_N to melting beneath thinner lithosphere.

The observed Tb/Yb_N of 1.58-18.3 for the DMH and Badi-Dabbayra lavas therefore suggests melting near the garnet-spinel transition.

The most important geochemical observations with respect to petrogenesis beneath the DMH rift system are as follows:

1) Radiogenic isotope ratios are very similar for all samples, with the exception of Pb which shows small but significant variations in the off-axis samples. All the samples have more radiogenic Sr-Nd-Pb ratios than typical MORB compositions;

2) Ratios between elements with similar geochemical behaviour show similar ranges between sample groups.

3) All the samples analysed are enriched in incompatible elements relative to MORB and Red Sea basalts, which is consistent with melting of a more fertile source as suggested by the isotopic data.

4) The off-axis (Badi-Dabbayra) lavas show moderate but consistent enrichments in incompatible elements when compared to the axial lavas, suggesting either varying extents of melting or small scale source heterogeneity between the on and off axis melts.

5) Tb/Yb_N ratios suggest some melting near the garnet-spinel transition, with off-axis lavas having slightly higher Tb/Yb_N and therefore more extensive melting with a garnet-bearing residue.

6) The correlation observed between the variation in some geochemical parameters (i.e. Pb isotopes, La/Sm etc) and eruption location (i.e. distance from rift axis) suggests an important link between the process of melt generation and the supply of melts to the shallow crust/surface.

5.6 Magma genesis

Developing a model for the generation and supply of melts beneath the DMH rift system requires constraints on: 1) mantle source composition and lithology, 2) melting parameters, such as depth and melt fraction, and 3) pre-eruptive storage and modification of primary magmas. This section begins by examining isotopic and trace element evidence for mantle source compositions and potential contamination of primary melts. This is followed by major and trace element constraints on primary melt compositions and melting processes beneath the DMH system. Finally, the pre-eruptive storage and fractionation of primary melts are examined.

5.6.1 Mantle source constraints

5.6.1.1 Isotopic evidence

Radiogenic isotope ratios are not strongly fractionated by melting/crystallization processes and are therefore generally a robust indicator of magmatic source components. Almost no variation is observed in the Sr, Nd and Pb isotopic data for the axial samples and this argues strongly for a homogenous source with respect to time-integrated Rb/Sr, Sm/Nd, U/Pb and Th/Pb. The Nd and Sr isotopic data for the off-axis lavas is also very similar with only two samples (3016 and BADI05) with $^{87}Sr/^{86}Sr$ values outside the range for lavas from the main rift when analytical uncertainties are considered. The most significant variations are observed in the Pb isotopic data for the

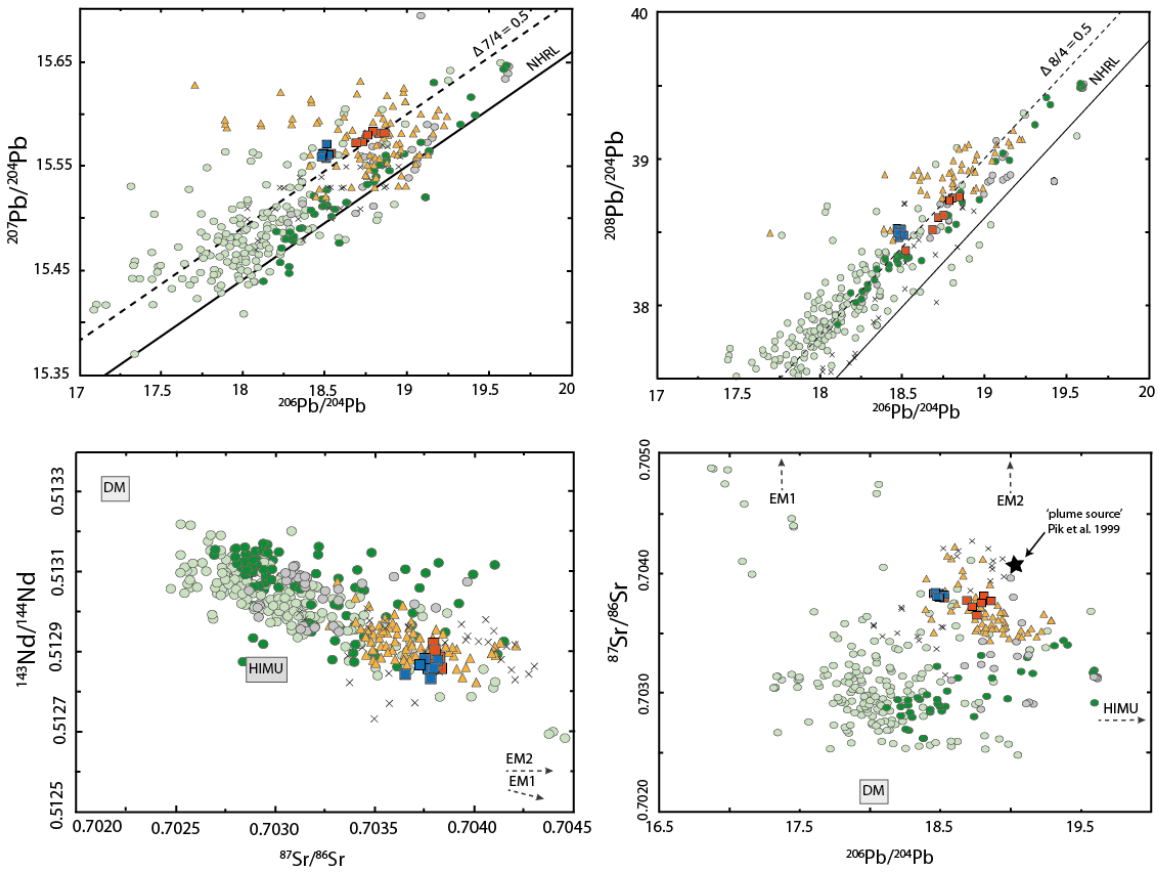

Figure 5.12 Plots of regional isotopic data for Afar and surrounding oceanic regions. The isotopic compositions of the DMH segment lavas and other Quaternary lavas from Afar (triangles), Ethiopian flood basalts (crosses), Red Sea/Gulf of Aden MORB (dark green circles), Red Sea Islands (grey circles) and Indian Ocean MORB (light green circles). The Afar basalts have a distinct isotopic composition compared to Red Sea and Indian Ocean lavas and are more isotopically enriched. The lavas analysed in the thesis from the DMH segment have broadly similar isotopic compositions to previous analyses of basalts from other part of Afar. Data sources: Afar data (Betton and Civetta, 1984; Barrat et al., 1990, 1993, 1998, 2003; Vidal et al., 1991; Schilling et al., 1992; Deniel et al., 1994); Flood basalts (Pik et al, 1999); Red Sea/Aden MORB (Betton and Civetta, 1984; Altherr et al., 1990; Schilling et al., 1992; Volker et al., 1993; Haase et al., 2000); Red Sea Islands (Dupre et al., 1988; Eissen et al., 1989; Roger, 1993; Volker et al., 1997) Indian Ocean data is from a compilation by Stracke et al., (2005).

off-axis lavas. These have positive correlations in Pb-Pb isotopic plots, with the axial samples lying at the less radiogenic end of the range (Fig 5.10). There is no correlation with sample age, but, as noted in the previous section, there is a general trend to more radiogenic values with increasing distance from the axis.

Previously published isotopic data for Quaternary basalts from Afar is limited to a handful of studies (Barberi et al., 1980; Betton and Civetta, 1984; Hart et al., 1989; Barrat et al., 1990, 1993, 1998, 2003; Vidal et al., 1991; Schilling et al., 1992; Marty et

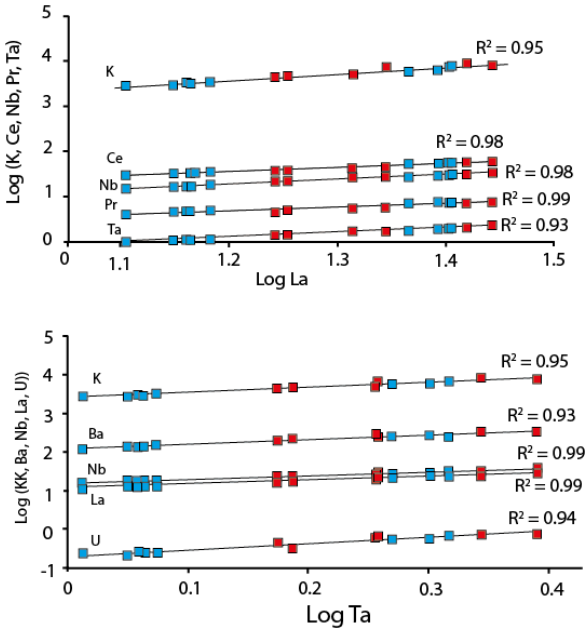

Figure 5.13 Log-Log correlation plot of trace elements. Elements with similar partitioning behavior will form linear correlation in samples derived from the same source (i.e. Sims and DePaolo, 1997). The good correlations between element with similar geochemical behaviour between both on and off-axis lavas suggests they were derived from a common source.

al., 1993; Deniel et al., 1994). This dataset defines an array in Sr-Nd-Pb isotopic space, shown in Fig 5.12, which is distinct from the more depleted characteristics of the basalts erupted along the spreading centres in the Red Sea and Gulf of Aden and at ocean island volcanoes in the Red Sea and is attributed by several authors (e.g. Baker et al., 1996, 2002; Furman et al., 2007) to represent the composition of the modern day 'Afar plume'. All the lavas analysed here from the DMH rift segment and adjacent volcanoes have very similar Sr-Nd-Pb isotopic compositions to the other Quaternary Afar basalts when compared to MORB's from the Red Sea, Gulf of Aden and Indian Ocean (Fig 5.12). The isotopic characteristics of the pre-rift Eocene flood basalts that now form the Ethiopian highland regions also show some similarity to the modern Afar lavas, though there is greater variability here than is seen in the Quaternary lavas from Afar (Pik et al., 1999). Overall, the isotopic compositions of the DMH system lavas have a close resemblance to the plume source identified by Pik et al (1999) ($^{87}Sr/^{86}Sr$: 0.7040,$^{143}Nd/^{144}Nd$: 0.51295 and $^{206}Pb/^{204}Pb$: 18.8) (shown in Fig 5.12). In detail, the Sr and Nd

isotopic ratios for the DMH lavas are slightly less radiogenic than this source, while $^{206}Pb/^{204}Pb$ is similar for the most radiogenic off-axis lavas and slightly more depleted for the axial samples. The isotopic features of the lavas can therefore be adequately explained by either one homogenous mantle source, the partial melts of which are slightly modified with respect to Pb isotopes prior to eruption at off-axis volcanoes, or a source that is essentially homogenous with respect to Sr and Nd isotopic values but has spatial gradients in Pb isotopes. Overall this source is slightly more depleted than the plume end-member composition of Pik et al., (1999) for the Eocene lavas.

5.6.1.2 Trace element evidence

In addition to isotopic evidence, highly incompatible element ratios can also be used to identify mantle source compositions (i.e. Hofmann et al., 1986), providing they have not been strongly fractioned during melting/crystallization. This assumption can be tested using log-log plots of incompatible element concentrations, which, if the elements in question have behaved in a similar way (i.e. with the same bulk partition coefficient), will be linearly correlated, with a slope of 1 (Sims and DePaolo, 1997). Ba/Nb, La/Nb, Ba/Ta, Nb/Ta and U/Th are similar in all the samples analysed and have high correlations in log-log plots (Fig 5.13) and should therefore approximate the ratio in the source. In the pre-rift plume lavas analysed by Pik et al (1999) those with isotopic characteristics similar to the DMH lavas had Ce/Pb, Ba/Nb, La/Nb and Ba/La ratios very similar to values reported elsewhere for ocean island basalts (i.e. Sun and McDonough, 1989; Halliday et al., 1995). The DMH lavas also share this characteristic, with high Ce/Pb (~22-30) and low Ba/Nb (~6-8), La/Nb (~0.8) and Ba/La (~9-11).

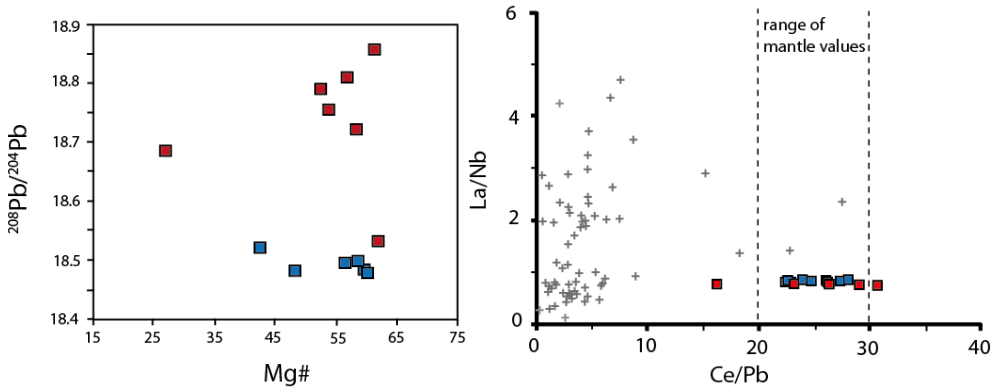

Figure 5.14 (a) Plot of Mg# vs. $^{208}Pb/^{204}Pb$. There is no clear correlation between degree of differentiation and Pb isotopic composition. (b) Ce/Pb vs. La/Nb plot of basaltic lavas. These ratios are often used to indicate crustal contamination of mantle derived melts. The Ce/Pb mantle range of 25 ± 5 is from Hofmann et al., (1986). For comparison samples of Ethiopian crustal material are also shown. The lavas analysed here show close agreement with the mantle ratios and crustal interaction is therefore considered to be minor. Ethiopian crustal analyses from: Kebede et al., 1999; Sifeta et al., 2005; Tadesse and Allen, 2005; Yihunie et al., 2006).

Previous studies on the petrogenesis of basalts in Afar have typically interpreted the geochemical features of these lavas as reflecting generation from an enriched plume source with contamination by asthenospheric and/or lithospheric material (Schilling et al., 1973, 1992; Vidal et al., 1991; Deniel et al., 1994; Barrat et al., 1990; Pik et al., 1998, 1999). As originally noted by Schilling (1973), there is also a systematic regional variation in normalized La/Sm ratios between basalts from the Red Sea/Gulf of Aden (PM normalized $La/Sm_N \approx 1$; e.g. Schilling, 1973; Haase et al., 2000) and those on-land in Afar ($La/Sm_N \approx >1.7$; e.g. Barrat et al., 1998, 2003; this study). These observations suggest that a fertile source component has persisted beneath Afar since the initial Eocene flood basalt volcanism and that it is not, as originally proposed by some authors (i.e. Barberi et al., 1980; Betton and Civetta, 1984; Hart et al., 1989), derived from the pan-African lithosphere interacting with melts from a depleted upper mantle.

5.6.1.3 Crustal contamination?

An important factor to consider when investigating the petrogenesis of Afar lavas is to what extent any chemical diversity within the erupted melts relates to contamination by crustal material. In the region of the DMH rift segment seismic evidence suggests a

crustal thickness of ~22 km (Makris and Ginzburg, 1987; Hammond et al., 2011), composed of three layers; a ~4 km thick lower velocity upper crust, a ~16 km thick high velocity lower crust and a thin cover layer of lava flows and sediments. The lower crust has been interpreted to be mafic material, accreted by underplating during plume/hotspot magmatism, while the upper crust is thought to be crystalline pre-rift Pan-African crustal material (Makris and Ginzburg, 1987; Prodehl and Mechie, 1991; Hammond et al., 2011). A major issue in assessing crustal contamination in Afar and the northern MER is a lack of published analyses of local crustal material. Compositional data is available for crustal xenoliths from Eritrea (Teklay et al., 2010) and exposures in the Ethiopian highlands (Pik et al., 1999), however the heterogeneous nature of the Pan-African crust makes comparison with remote samples uncertain.

As discussed, the Sr-Nd-Pb isotopic data for the axial samples show only very minor variations. The only significant isotopic variability observed is in the Pb isotopic composition of the off-axis lavas. If crustal interactions have affected the erupted melts then this should become more evident in more evolved samples, due to the combined effects of assimilation coupled with fractional crystallization (AFC) processes, however in the current dataset there is no clear correlation between indicators of differentiation (i.e. Mg#) with Pb-isotopic compositions (Fig 5.14a). Pik et al (1999) identified variable extents of crustal contamination in some Ethiopian flood basalt lavas due to co-variations of Ce/Pb, La/Nb and Ba/Nb with Sr isotopes. Both Ce/Pb and La/Nb are commonly used criteria to assess crustal contamination and have been used by Furman (2007) and Rooney et al (2010) to argue against significant contamination in the MER. Uncontaminated mantle-derived melts typically have a Ce/Pb ratio of ~20-30 (Hofmann et al., 1986; Sims and DePaolo, 1997), which is reduced by interaction with Pb-rich

crustal materials. La/Nb is typically low in mantle melts and increased by crustal assimilation. Fig 5.14b shows Ce/Pb vs. La/Nb for the analysed samples, which show no evidence for deviation from the mantle values. Neither the isotopic or trace element data therefore show evidence for any significant modification of these melts by crustal interaction.

5.6.2 Primary melt compositions and partial melting

5.6.2.1 Major element systematics

It is rare for erupted melts to be in chemical equilibrium with their mantle source and primary melts are almost always modified by crystal fractionation/accumulation and/or mixing prior to eruption (e.g. O'Hara, 1968). The lavas analysed from across the DMH rift system have Mg# from 42 - 68 and have undergone variable extents of pre-eruptive fractionation. No lavas with MgO > 10 wt% have been analysed. None of the observed compositions can therefore be considered to reflect primary mantle melts, which if in equilibrium with a peridotite source have an Mg# of ~75. The erupted range of major element composition therefore provides information on processes, such as crystallisation, that have modified the primary melts prior to eruption and in order to use the major element data to investigate melting processes, these must be corrected for. The variation plots, shown in Fig 5.6, demonstrate that on and off axis lavas have followed distinct liquid lines of descent (LLD) and, importantly, that at higher MgO contents (> 7.5 wt%) there are consistent compositional differences between the two sample groups, i.e. higher Fe_2O_3 and TiO_2 and lower Al_2O_3, K_2O and CaO in the axial lavas. Parental melts supplied to these two regions therefore have varying genetic histories prior to the final stage of evolution represented in the observed compositional range.

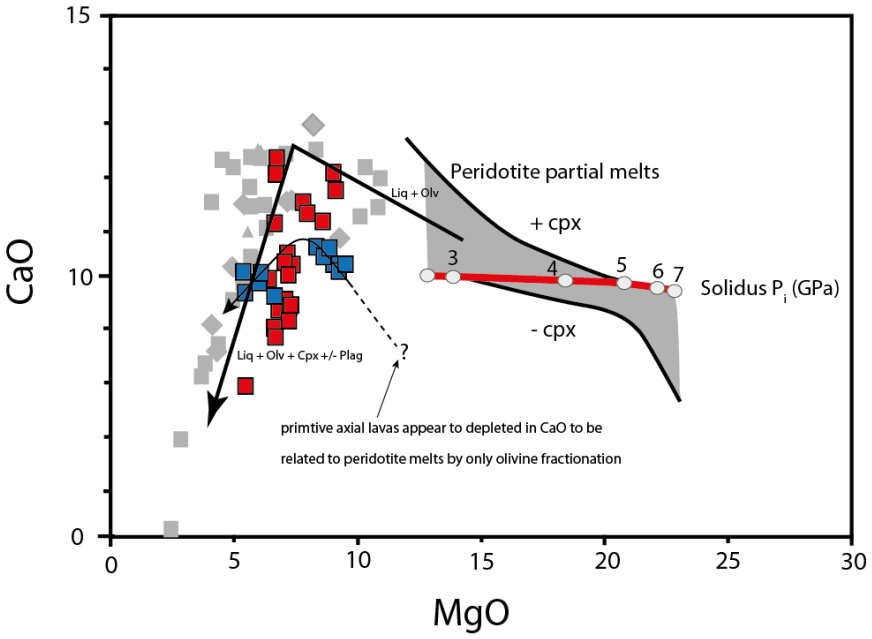

Figure 5.15. MgO versus CaO (both in wt%) used for estimation of pre-eruptive fractionation. The grey field shows the compositions of partial melts of mantle peridotite calculated by Herzberg and O'Hara (2002). The black arrow is a typical fractionation path for melts with these compositions at crustal pressures. The off-axis lavas (red symbols) and other Afar samples (grey symbols) appear to follow this trend and can be related to these primary melts by removal of olv + cpx ± plag. The axial lavas (blue symbols) do not appear to fit this path and seem to trend to compositions that are too depleted in CaO to be related to primary melts in this way. Figure is re-drawn after Herberg and O'Hara (2002).

5.6.2.2 Primary melt compositions and melting parameters

Primary magmas are liquids that initially separate from the mantle following partial melting. At MgO contents > 9 wt% fractionation of basaltic melts is typically strongly dominated by olivine removal (e.g. Grove et al., 1993) and as olivine-liquid Fe/Mg partitioning is well understood (Roeder and Emslie, 1970; Beattie, 1993) it is possible to correct for the removal of with reasonable accuracy. Primary melt calculations commonly involve the addition of olivine to the most magnesian erupted compositions observed until a liquid that is in equilibrium with mantle olivine compositions of ~ Fo_{90} is obtained. For methods involving olivine addition it is therefore important when selecting samples to assess the likelihood that other phases have also been removed. Here, primary melt compositions are calculated using the PRIMELT2 software by

Herzberg and Asimow (2008), which uses the method of Herzberg and O'Hara (2002). This technique involves two main calculations: 1) the inversion of measured compositions by the incremental addition of equilibrium olivine to obtain a series of more primitive liquid compositions; and 2) forward modelling of a series of fractional melts from a fertile peridotite source based on the parameterization of experimental data (from Walter, 1998). An accepted primary melt composition is found when a common liquid is identified from these two calculations, i.e. a partial melt generated under specific melting conditions that can be produced by olivine addition to the observed sample composition. Once the primary melt composition has been established other petrological parameters, such as melting pressures, extent and potential temperature, can then be estimated (e.g. Herzberg and O'Hara, 2002; Herzberg et al., 2007; Frey et al., 2011; Gazel et al., 2011).

The first stage of the primary melt calculation is to identify compositions suspected to lie on an olivine control trend. Unfortunately, relatively few of the samples analysed have high MgO contents and so interpretation of fractionation trends at MgO > 8wt% is uncertain. In the variation plots in Fig 5.5 samples with > 8wt% MgO do show evidence for olivine dominated fractionation and so these may represent suitable candidates for inversion. The Herzberg and O'Hara (2002) method also includes an assessment of fractionation by comparing observed compositions with those predicted from fractionation of a primary peridotite melt. Fig 5.15 shows CaO vs. MgO for primary melt compositions calculated by Herzberg and O'Hara (2002) and a typical LLD for these melts at crustal pressures (e.g. Grove et al., 1993). At MgO > 7wt% fractionation is dominated by olivine (olv) after which time clinopyroxene (cpx) and/or plagioclase (plag) are also removed.

Comparing this with the DMH and Badi-Dabbayra lavas and other lavas from the Erta Ale segment (Barrat et al., 1998) and the Hararo rift (Barrat et al., 2003), which is ~40 km SE of the DMH, suggests that almost all of these lavas, including all of the on-axial samples, have been modified by multi-phase fractionation and are therefore unsuitable for inversion by olv only addition. However, some of the most primitive samples from the off-axis volcanoes and from the other rifts do appear to be primitive enough to be related to peridotite partial melts by olivine removal and may provide robust primary melt compositions. It is also notable on Fig 5.15 that the on-axis samples do not follow the same LLD as the other lavas and appear too depleted in CaO to be directly linked to peridotite partial melt by olv only removal. However, in the observed range of compsotions, the most magnesian axial samples do not show evidence for crystallisation of other phases such as cpx or plag. Possible explanations for this are that the parental melts for these lavas fractionated at higher pressures, where cpx becomes stable at an earlier stage (e.g. Langmuir et al., 1992) or that these were generated by partial melting of pyroxenite mantle, which can result in lower CaO primary melts (e.g. Hirschmann et al., 2003). This latter alternative is considered unlikely, as a major change in source lithology between the on and off-axis lavas of this kind, affecting the major element compositions, should result in incompatible element enriched pyroxenite partial melts, the opposite to the observed trace element pattern. It is considered therefore that the varying major element trends most likely represent variations in fractionation processes and these are discussed in next section.

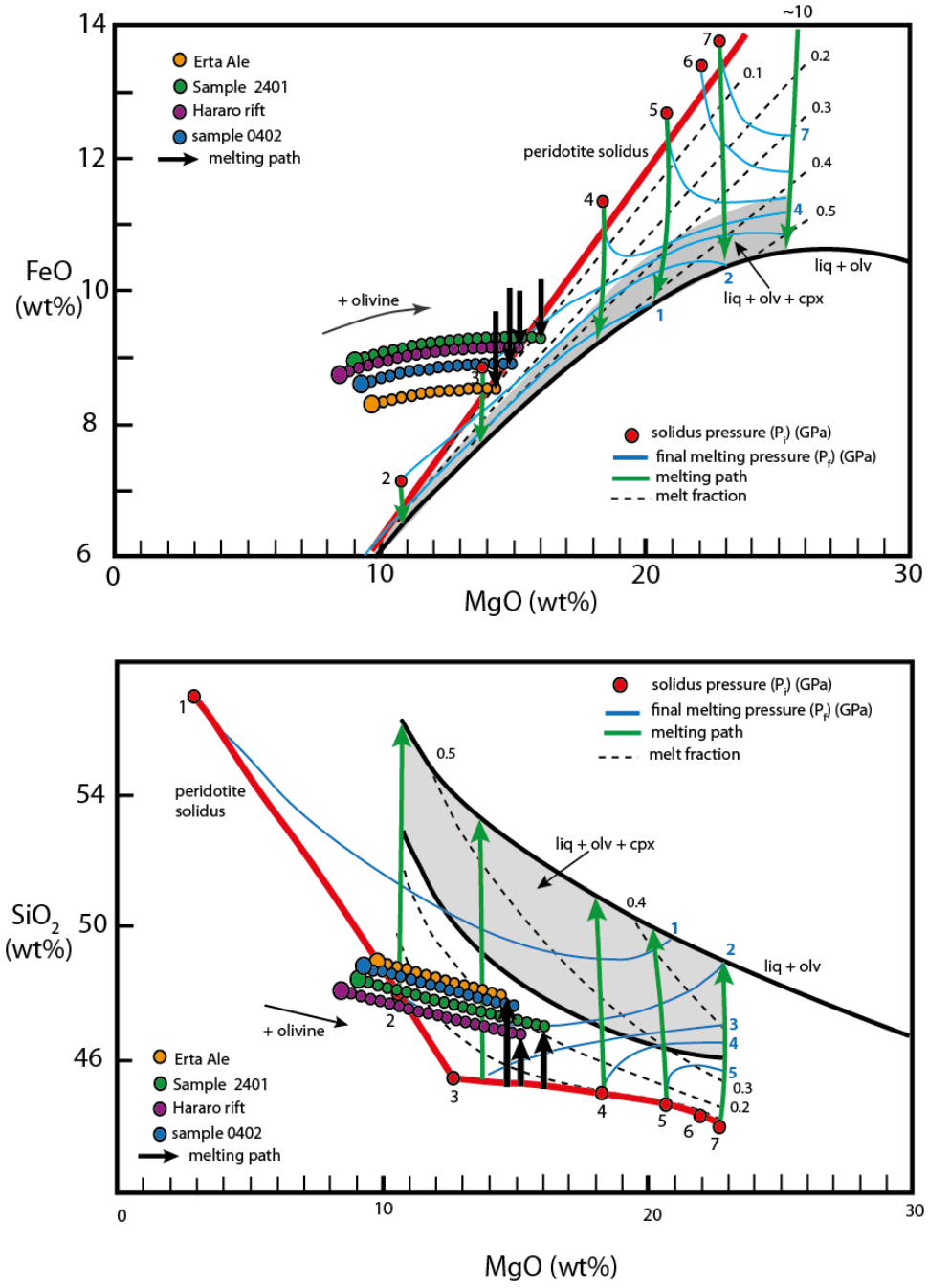

Figure 5.16 Graphical projections after Herzberg (2006) and Herzberg et al (2007) illustrating the method used to estimate primary melt compositions from analyses of lavas (called PRIMELT2; Herzberg et al, 2007). These plots illustrate the different compositions of primary melts generated by peridotite melting at different solidus temperatures and melt fractions. Melting begins once the solidus (red line) is crossed and continues along the paths marked by the green arrows. The blue lines indicate the final pressure of melting for a given composition and the dashed black line the melt fraction. Samples that are considered to have only fractionated olivine (coloured circles) are back corrected by the re-addition of olivine at 1% increments until they are in equilibrium with mantle compositions. Coloured circles show the compositional paths followed by each samples as it is corrected to more magnesium compositions. The primary melt composition and melting parameters are found from the intersection of a forward melting model with the back-corrected lava composition. Hararo sample from Barrat et al (2003), the Erta Ale composition is an average from 5 primary melt calculations using data from Barrat et al (1998).

Table 5.3 Successful primary melt solution using the PRIMELT2 model of Herzberg et al (2007)

Sample	2401	0402	HB*	average DMH-Hararo	EA average (n=5)[§]
SiO2	47.01	47.48	46.74	*47.08*	*47.92*
TiO2	1.49	1.25	1.53	*1.43*	*1.69*
Al2O3	12.66	13.29	13.09	*13.01*	*13.16*
Cr2O3	0.00	0.00	0.00	*0.00*	*0.00*
Fe2O3	0.74	0.62	0.68	*0.68*	*0.84*
FeO	9.30	8.91	9.15	*9.12*	*8.43*
MnO	0.17	0.15	0.18	*0.16*	*0.18*
MgO	16.11	15.14	15.38	*15.54*	*14.13*
CaO	9.84	10.43	11.00	*10.42*	*10.91*
Na2O	2.01	2.08	1.88	*1.99*	*2.09*
K2O	0.43	0.48	0.20	*0.37*	*0.41*
P2O5	0.25	0.16	0.20	*0.20*	*0.24*
T (°C)	1376	1350	1355	*1360*	*1330*
TP_AFM (°C)	1487	1463	1469	*1473*	*1437*
F_AFM	0.14	0.13	0.09	*0.12*	*0.12*
Pi (GPa)	3.36	3.22	3.25	*3.28*	*3.07*
Pf (GPa)	2.48	2.47	2.73	*2.56*	*2.35*

*HB = Hararo basalt from Barrat et al (2003), [§]Average value from calculations for 5 Erta Ale sample from Barrat et al (1998). TP_AFM is potential temperature based on aggregated fractional melting model; F = melt fraction, Pi and Pf are initial and final pressures of melting respectively are calculated from:
$Pi = 11.248MgO - 13700(1/MgO)^3 - 8.13\ (ln(MgO))^3$ and $Pi - Pf = 4.659F + 10.24F^2$ after Herzberg and O'Hara (2002) and Herzberg and Gazel, (2009).

Table 5.3 lists primary melt compositions calculated using the Herzberg and O'Hara (2002) method from samples considered acceptable for olivine-only inversion using their criteria (see Herzberg and Asimow, 2008). Only two of the samples from the DMH system (samples 2401 and 0402) produced acceptable primary melt results, while one lava from the Hararo rift and four from the Erta Ale segment also gave acceptable

primary compositions. Sample 2401 is from a ~62 ka flow on the eastern side of the segment and 0402 is from a ~445 ka monogenetic cone between Badi and Dabbayra. It is unfortunate that so few of the samples, from either the DMH segment of elsewhere, are sufficiently primitive to estimate primary compositions, however the 7 successful solutions obtained (listed in Table 5.3) produce similar results and these should provide reasonable constraints to investigate melting processes. Table 5.3 also list estimates of melting depths, mantle potential temperature (Tp) and melt fractions calculated from the primary melt compositions. Graphical illustrations of the decompression melting paths are shown in Fig 5.16 using the projections of Herzberg (2006) and Herzberg et al (2007). Predicted pressures for the onset of melting (P_i) for the DMH and Hararo rift samples are ~3.3 GPa, while the Erta Ale lavas suggest slightly shallower melt initiation with a P_i of ~3.1 GPa. Final melting pressures (P_f) are estimated be ~2.5 GPa for the DMH/Hararo lavas and ~2.3 GPa at Erta Ale, producing melting columns of similar length (~0.7 GPa). Partial melting beneath both areas is estimated to be between 10-15%. As the crust beneath Erta Ale is ~10 km thinner than in central far beneath the DMH/Hararo rifts (Hammond et al., 2011) the pressure estimates for both areas equate to similar melting regions between ~100 to 75 km depth. Estimates of mantle Tp based on the primary melts compositions are ~1470°C for central Afar and ~1445°C for Erta Ale.

5.6.2.3 Comparison to forward model

The primary melt compositions in Table 5.3 are calculated by comparison of olivine corrected liquids with those from a forward melting model. This model is based on the parameterization of the experimental data of Walter (1998) by Herzberg and O'Hara (2002). It is possible to independently test the primary compositions and melting parameters by comparing them to melts calculated using an alternative model for

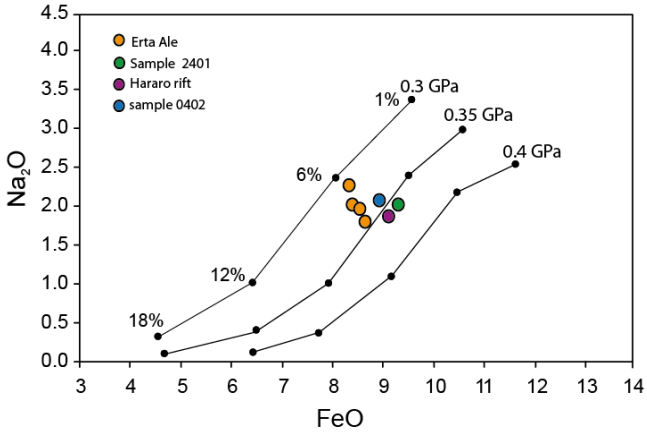

Figure 5.17. Forward model of FeO and Na_2O compositions of polybaric melts of fertile peridotite with varying solidus temperatures. The coloured dots are the primary melt compositions calculated in Figure 5.16 (same symbols). This model is similar to that of Johnson et al (2005). The starting composition used was 0.3 wt% Na_2O and 7.73 wt% FeO. The garnet spinel transition was set at 30 kbar and bulk partition coefficients vary depending on the source lithology: garnet peridotite - 60.1Olv + 18.9Opx 7.3 Gnt; spinel peridotite 58Olv + 25 Opx + 15Cpx + 2 Sp. Partition coefficients are pressure dependent and are listed in the appendix of Johnson et al (2005).

polybaric melting. As the FeO^T and Na_2O compositions of partial melts have been shown to be sensitive to melting pressures and melt fractions respectively (i.e. Langmuir et al., 1992) these can provide good indicators of variations in melting pressures and melt fractions (e.g. Wang et al., 2002; Johnson et al., 2005).

The FeO and Na_2O composition of partial melts have been calculated during polybaric melting of a fertile peridotite using the method employed by Johnson et al (2005). This model is similar to that of Langmuir et al (1992), however as the initial melting pressures given by the primary melt model are in the garnet stability field (i.e. > 3GPa; Robinson and Wood, 1998), which is in agreement with the high $(Tb/Yb)_n$ ratios (Fig 5.11), melting begins in a garnet bearing lithology before continuing in the presence of spinel at lower pressures. Following Langmuir et al (1992) melting during decompression is assumed to occur at 1.2% per kbar and cpx reduces in the residue by 0.7% for every 1% melting. For different values of Pi, solidus and potential temperature are calculated after McKenzie and Bickle (1988) and the garnet-spinel transition pressure after Robinson and Wood (1998). Fig 5.17 shows a series of fractional melts for different values of P_i calculated using this model. Specific details of the model

parameters are given in the caption. The primary melt compositions calculated for the DMH/Hararo lavas can be reproduced by ~9 % partial melting of fertile peridotite with a solidus pressure of 3.5 GPa and Tp of 1470 °C. The Erta Ale primary melts plot between modeled compositions for Pi's of 3 and 3.5 GPa and at melt fractions of ~6-11 %. These results are in good agreement with the primary melt model and give confidence in the melting conditions derived from it. However, as demonstrated by the systematic variations in both major and trace element compositions between lavas erupted in the main rift zone and at the off-axis volcanoes (i.e. Fig 5.11) some variations in petrogenetic processes do occur between these areas. The lack of suitable erupted compositions for primary melt calculations, including all the axial lavas, means that it is not possible at this stage to examine these variations in detail. Trace element modelling provides an important means to test the melting parameters given by the major element data and to examine variations in petrogenesis across the DMH system.

5.6.2.4 Trace element constraints on melting

The primary melt calculations and forward models shown in 8s. 5.16 and 5.17 suggests that melting beneath the DMH rift system occurs in fertile mantle with a Tp of ~1470°C between depths of ~100-75 km. At this Tp the garnet-spinel transition occurs at 2.85 GPa (~92 km) (Robinson and Wood, 1998) and the initial phase of melting should occur in the garnet stability field. Many studies have used constraints from rare earth elements (REE) to investigate melting depths (e.g. Mckenzie and O'Nions, 1991; Shen and Forsyth, 1995; Wang et al., 2002; Johnson et al., 2005; Rooney et al., 2010), due to the variations in partitioning behaviour of the HREE's (Dy to Yb) between garnet and spinel bearing lithologies, as illustrated in Fig 5.3b. In the DMH system $(Tb/Yb)_N$ ratios vary between 1.57 – 1.83 and can be used to differentiate between the on (Tb/Yb <1.7) and off (Tb/Yb >1.7) axis lavas (Fig 5.11). In the MER Rooney et al (2010) used a

$(Tb/Yb)_N$ value of >1.8 to distinguish between garnet lherzolite dominated melting beneath thicker lithosphere and spinel lherzolite melting at shallower depths beneath thinned lithosphere. The range of $(Tb/Yb)_N$ for the lavas analysed here suggests that melting occurs near the garnet-spinel transition and that, for at least some melts, a degree of garnet lherzolite melting is probably required to produce the observed fractionations. Trace element modelling can also be used to constrain the mantle source composition and extent of melting. A more fertile source is relatively enriched in the most incompatible elements and will produce partial melt with higher ratio such as Ba/La compared to a depleted source. At a fixed source composition, variations in the relative concentrations of highly to moderately incompatible trace elements in partial melts (i.e. Ce/Yb, Sm/La) are sensitive to the melt fraction (e.g. Fig 5.3a) as the more incompatible element is more readily partitioned in to the melt during the initial stages of melting. As illustrated in Figs 5.9 and 5.11 ratios such as these show consistent variations between the on and off axis samples.

5.6.2.5 Trace element model

To investigate the behaviour of trace elements in the melting region beneath the DMH rift a melting model was constructed based on the constraints from the major element data. The initial melting pressures suggested by the major elements indicate that melting begins in the garnet field and that this accounts for the first ~5 % of melting after which further melting occurs in the spinel field. To test the role of garnet in melt generation the Tb and Yb concentration of partial melts have been modeled for melting columns involving varying amount of initial garnet field melting. The Ba, Sm, La and Ce concentration were also calculated as these provide information of source composition and melt fractions. Accumulated fractional melting, which produces compositions

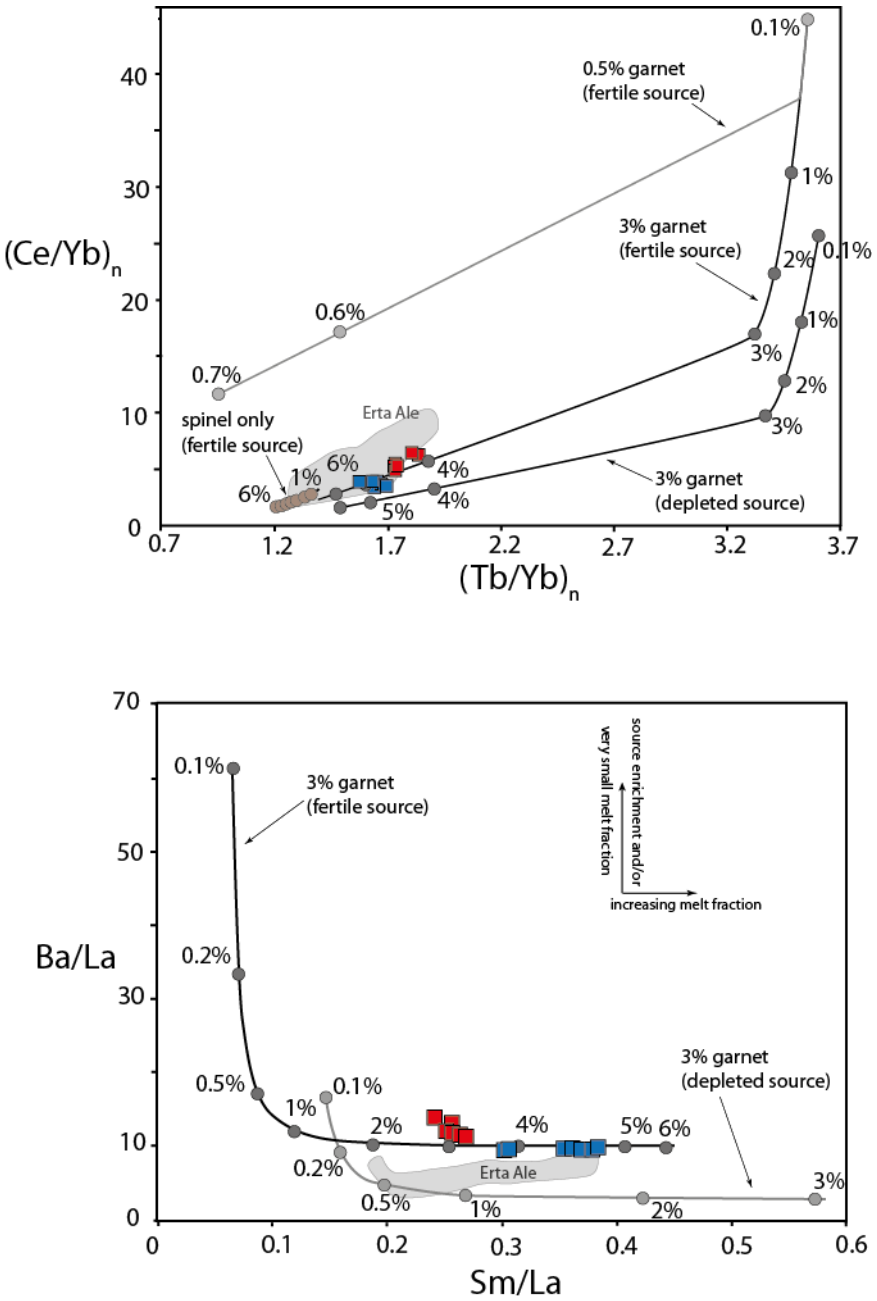

Figure 5.18 Illustrative results of trace element models for different melting scenarios. Depleted and fertile source compositions, partition coefficients and mineralogy and melting modes are listed in table 5.4. Melts are calculated by pooling non-modal batch melts at 0.2% increments. To simulate the effect of varying depths of melt initiation different amounts of garnet field melting were modeled followed by further melting of the residue in the spinel field. Symbols along curves indicate melt fraction (F). Data symbols are as before (off-axis, red; on-axis, blue). Grey field shows Erta Ale data from Barrat et al (1998). The observed compositions for the DMH systems basalts are best modeled with a fertile source and the ~3% initial melting in the garnet field.

between pure fractional or batch melts (both unlikely scenarios in nature), was approximated by pooling batch melts after 0.2 % melting increments. In the case of melting of a garnet lithology followed by a spinel bearing source the garnet-spinel

Table 5.4 Parameters used in the trace element melting model

Source composition						
	Ba	**La**	**Sm**	**Ce**	**Tb**	**Yb**
Fertile	6.98	0.687	0.444	1.775	0.108	0.493
Depleted	0.563	0.206	0.299	0.722	0.077	0.347
Partition coefficients						
Cpx	0.00068	0.071	0.459	0.122	0.382	0.432
Opx	0.00004	0.0008	0.0251	0.0047	0.021	0.047
Gnt	0.00001	0.001	0.21	0.007	1	4.18
Olv	0.000043	0.0000082	0.00032	0.000039	0.002	0.017

Source mineralogy and melting modes				
	Garnet Lherzolite		**Spinel lherzolite**	
	solid	**melt**	**solid**	**melt**
Cpx	0.075	0.87	0.125	0.88
Opx	0.21	-0.28	0.27	0.21
Gnt	0.6	0.38	-	-
Olv	0.115	0.03	0.575	-0.18
Spn	-	-	0.03	0.09

Fertile and depleted mantle source from Sun and McDonough (1989). Partition coefficients are from experimental data by McDade et al (2003) and a compilation by Donnelly et al (2004). Source mineralogy is the same as that used by McDade et al (2003) and melting stoichiometry is from Gudfinnsson and Presnall (1996).

transition was treated as instantaneous. The source compositions, mineralogy, melting modes and partition coefficients used in the model are listed in Table 5.4.

Fig 5.18 show calculated $(Ce/Yb)_N$ vs. $(Tb/Yb)_N$ and Ba/La vs. Sm/La for partial melts generated by various melting scenarios alongside the observed compositions. The Tb/Yb ratios in the erupted lavas are best produced by an initial melt fraction of ~3% in the garnet field, followed by further melting a spinel bearing source. These results are consistent with the melting pressures derived from the major element model as shallower, spinel-only melting cannot produce the observed Tb/Yb fractionations. Comparison of the observed and modeled Ba/La ratios (Fig 5.18b) supports a fertile mantle source beneath the DMH rift as a depleted source composition can only reproduce the observed composition at very low values of F (< 0.2 %). The melt fractions suggested by the trace element models are ~4-6 %, slightly less than those

predicted by the major element model (~10%), and with the higher degree melts erupted at the rift axis. The trace element compositions of the Erta Ale lavas used in the primary melt calculations, shown in Fig 5.18, are also consistent with the major element model, suggesting slightly shallower melting (less garnet) here compared to the DMH samples and melt fractions. The source for these melts may also be slightly more depleted than for the DMH system as suggested by the lower Ba/La ratios. This source depletion may be the result of the higher volcanic flux at Erta Ale compared to the DMH segment (e.g. Bastow and Keir, 2011).

Overall there is good agreement between the constraints on melting processes suggested by the major element data and the results of the trace element models. Both clearly show that melting begins in the garnet field and the Tb/Yb fractionations in the observed and modeled melts are consistent with upwelling mantle with a Tp of ~1470 °C intersects the solidus at ~100 km depth below the garnet-spinel transition at ~92 km. Melting then continues into the spinel field until around ~75 km depth. The modeled melt compositions presented here are calculated for a *1-D* melting column with linear mixing between melts produced at different depths. There is not currently any information on the geometry of the melting region beneath the DMH segment, however the fact that axial lavas represent higher extents of melting is consistent with the shallowest part of the melting region being centred beneath the rift axis, as is the case at MOR's. If melting does not occur over a linear column then the values *F* calculated by the melting model represent mean melt fractions for pooled melts from a range of depths, and are less than the total extent of melting that occurs at the top of the melting zone (i.e. Plank and Langmuir, 1992; Niu, 1997). For example, in the case of a perfectly triangular melting zone and complete melt extraction mean F is equivalent to 0.5 of the

total *F* at the top of the melting zone (Langmuir et al., 1992). Future seismic imaging may provide information on the geometry of the melt zone in the mantle beneath the DMH segment and will allow these results to be modified accordingly.

5.7 Pre-eruptive storage and fractionation

The previous section outlined how partial melting in the upwelling mantle beneath the DMH segment produces primary melts with compositions similar to those listed in Table 5.3 and with the trace element ratios observed in the erupted melts. The compositional range within the erupted lavas and the differences between these and probable primary compositions (i.e. Fig 5.15) shows that composition of these melts are significantly modified by fractionation processes prior to eruption.

As illustrated schematically in Fig 5.15, the LLD followed by the off-axis lavas is broadly typical of basaltic melts evolving at crustal pressures and is in contrast to the axial samples, which form a distinct trend. At CaO contents > 10 wt%, these lavas, unlike the off-axis samples, do not show evidence for clinopyroxene (cpx) crystallisation. However, as noted above, it seems likely based on predicted peridotite primary melt compositions even the most primitive erupted lavas (~9.5 wt% MgO) have been modified by cpx removal (Fig 5.15). Mineral-melt equilbria for olv, cpx and plag vary with pressure, temperature and H_2O content and fractionation and at higher pressures cpx joins the crystallising assemblage earlier (e.g. Langmuir et al., 1992). It seems likely therefore that the axial lavas have been modified to some extent by high-pressure fractionation during which cpx was removed. Evidence for storage and fractionation at both deep and shallow levels is discussed below.

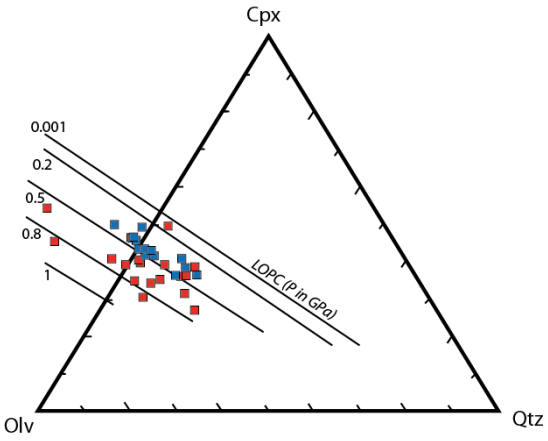

Figure 5.19 Olv-Qtz-Cpx pseudo ternary plot (project from plag) for the Afar basalts plotted according to the method of Walker et al (1979). The position of the Olv-Plag-Cpx cotectic is shown at different pressures, these are based on a compilation of experimental data by Kelley and Barton (2008). Only samples with MgO < 7wt% have been plotted as all three phases must be crystallizing for the results to be meaningful. The axial lavas (blue) appear to be in equilibrium with a lower pressure (< 0.5 GPa) mineral assemblage compared to the off-axis lavas (red) (0.5 – 0.8 GPa).

5.7.1 Liquid-crystal equilibria

In liquids saturated in olv, cpx and plag it possible to estimate the pressures of crystallisation, i.e. where that derivative liquid was produced, by comparing observed melt compositions with liquids lying on the olv-plag-cpx cotectic boundary determined by experimental studies (e.g. Yang et al., 1996; Herzberg, 2004). Before applying this method it must be considered whether the erupted samples represent liquids that are saturated in olv, plag and cpx, otherwise the results are not meaningful. It is also preferable to use compositions of glasses as these best represent quenched liquids. The first of these can be addressed by using samples with suitably low MgO contents, where melts are likely to be saturated in all three phases. In both sample groups lavas with MgO < 7wt% show evidence for crystallisation of olv + cpx + plag (i.e. decreasing Al_2O_3 and CaO with MgO; Fig 5.5) and these samples should give useful results. Unfortunately, it has not been possible to obtain glass compositions as hypocrystalline textures are rare in the samples and almost all the lavas have crystalline groundmass textures and it is therefore necessary to use whole-rock analyses. The effect of this on pressure estimates should not be too severe providing sample with large crystal contents are avoided. The effect of using a whole-rock analyses rather than a glass composition

can be estimated by comparing the results given by a moderately porphyritic crystalline lava sample and a glass rich scoria sample, both erupted during the 2007 axial eruption (scoria data reported in Ferguson et al., 2010). Fig 5.19 shows lavas with MgO < 7wt% plotted on olv-qtz-cpx pseudo-ternary diagram along with experimentally determined locations for the olv-cpx-plag cotectic. In this plot there is no discernible variation between the 2007 lava and scoria. The on-axis samples suggest fractionation for these lavas at 0.2 - 0.5 GPa. The off axis samples show more scatter with most lying between 0.5 - 0.8 GPa, notably higher than the axial group. As these reflect crystallisation in the most evolved liquids erupted they provide constraints on melt storage immediately prior to eruption and identify melt storage within the crust.

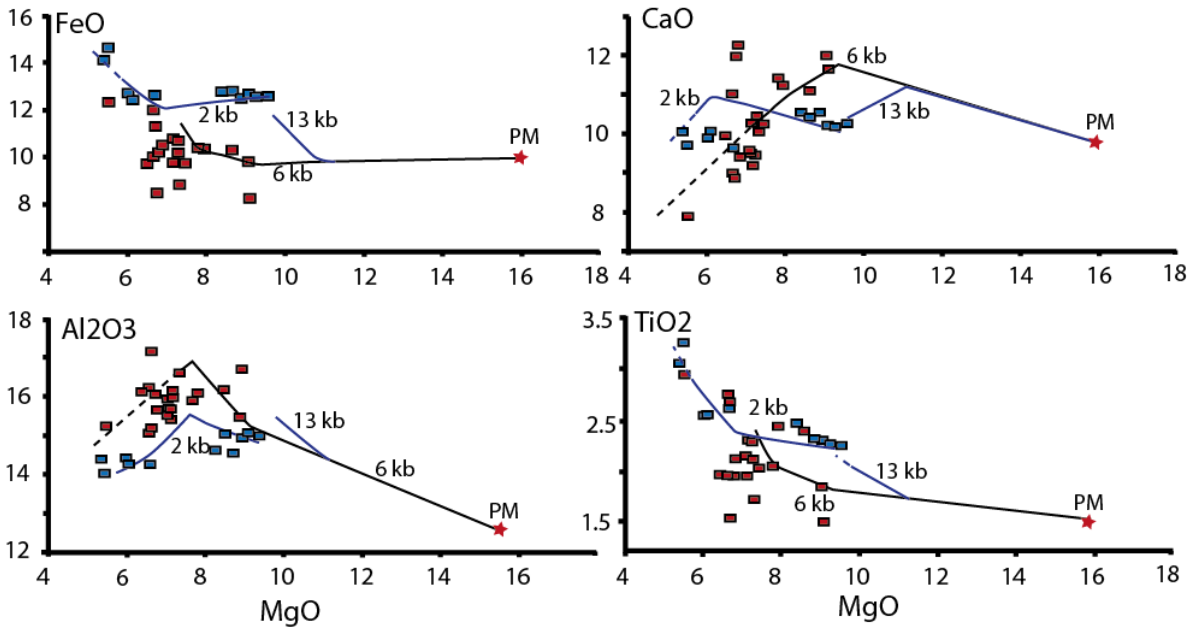

Figure 5.20 Fractionation models showing liquid compositions calculated using the PETRLOG3 modelling software (Danyushevsky and Plechov, 2011). The starting composition used in the model is the calculated primary-melt composition listed in Table 5.3. As the Afar basalts are unlikely to be anhydrous (see text) a nominal water content of 0.3 wt% was added to the primary magma. The compositional trend of the off-axis lavas (red symbols) can be well modeled using a single stage isobaric fractionation process at 6 kb (0.6 GPa) as suggested by the pressure estimate from Olv-Plag-Cpx cotectic diagram (Fig 5.19). The axial basalts (blue symbols) however, do not follow a shallow fractionation trend (as discussed in section 5.7.2.2) trend and the best fit models were found for an initial high pressure fractionation phase (at 13 kb) followed by a secondary low pressure at 2 kb (0.2 GPa) as suggested by the Olv-Plag-Cpx cotectic for the less magnesian samples.

5.7.2 Crystal fractionation models

It is also possible to investigate crystallisation using forward models that predict LLD's for primitive melts under varying pressures and volatile contents. Fractionation paths calculated for the primary melt compositions listed in Table 5.3 and are shown in Fig 5.20. Using the primary melt composition calculated for sample 2401 a series of fractionation trends have been calculated at varying pressures and with different H_2O contents, which can have important effects on crystallisation (e.g. Danyushevsky, 2001). No melt inclusion volatile contents have been successfully measured for these lavas, however recent analyses of melt inclusions from lavas erupted at the Dabbahu volcano at the northern end of the DMH segment suggests potentially high H_2O contents of 3-4 wt% (L. Field, unpublished data) and the axial melts are therefore unlikely to be anhydrous. Modeled fractionation trends for the DMH system lavas are shown in Fig 5.20. The off-axis trend can be well produced from this primary composition by isobaric crystallisation models at pressures of ~0.8 - 6 GPa, which is in good agreement with cotectic boundary on Fig 5.19. However, it is not possible to model the on-axis LLD in this way and an isobaric fractionation process seems unlikely for these melts. As discussed, when compared to potential primary melts even the most primitive axial samples show evidence for cpx fractionation (Fig 5.15), which is suggestive of high pressure fractionation where cpx becomes stable earlier. The most evolved erupted compositions however suggests that these melts fractionated olv, plag and cpx at crustal pressures of ~0.5 - 0.2 GPa (Fig 5.19). A two-stage model is therefore proposed where early removal of cpx at higher pressures, is followed by a second stage of fractionation at lower pressures. Assuming the most primitive erupted composition resembles that of melts ascending from a deeper storage region the observed compositions can be related to the estimated primary melts by an initial stage of

fractionation at 1.3 GPa. This is followed by a further stage of low-pressure fractionation prior to eruption at ~0.2 GPa.

The pressure of 0.8-6 GPa estimated for fractionation of the off-axis lavas corresponds to a depth of ~25 km, which matches the Moho depth in this region estimated by (Hammond et al., 2011) and as such is an obvious location for melt to pond. The shallow melt storage identified for the axial lavas at 0.2 GPa is at ~8 km depth, while the region of deep storage fractionation estimated to be at 40-45 km depths and is where primary melts evolve to ~ 10 wt% MgO. Although there is no direct evidence for this initial stage of fractionation in the erupted compositions it is difficult to relate the most primitive erupted compositions to primary melts compositions without modification by poly-phase crystallisation and this is unlikely to have occurred at crustal pressures. This region of melt accumulation below the crust may be akin to the deep hot zones proposed by Annen et al (2006), where primary melts evolve before fractionated liquids ascend to shallower levels. As lavas erupted in both locations show evidence for large extents of fractionation (> 20 %) significant cumulate residues may exist at the depths identified here for melt storage and these may be observable in seismic velocity profiles.

5.8 Model of melt generation and supply

Fig 5.21 present a schematic summary of the various constraints imposed on melt generation and supply to the DMH system by the petrological data. In this model the mantle solidus beneath the rift is located at ~100 km depth, below the spinel-garnet transition, and melting initiated here continues until ~75 km depth. The variation in melt fractions between axial and off-axis lavas suggest that melts feeding the off-axis volcanoes separate from the mantle residue at greater depths and do not mix with the primary melts that feed the rift axis. These melts ascend to the lower crust where they

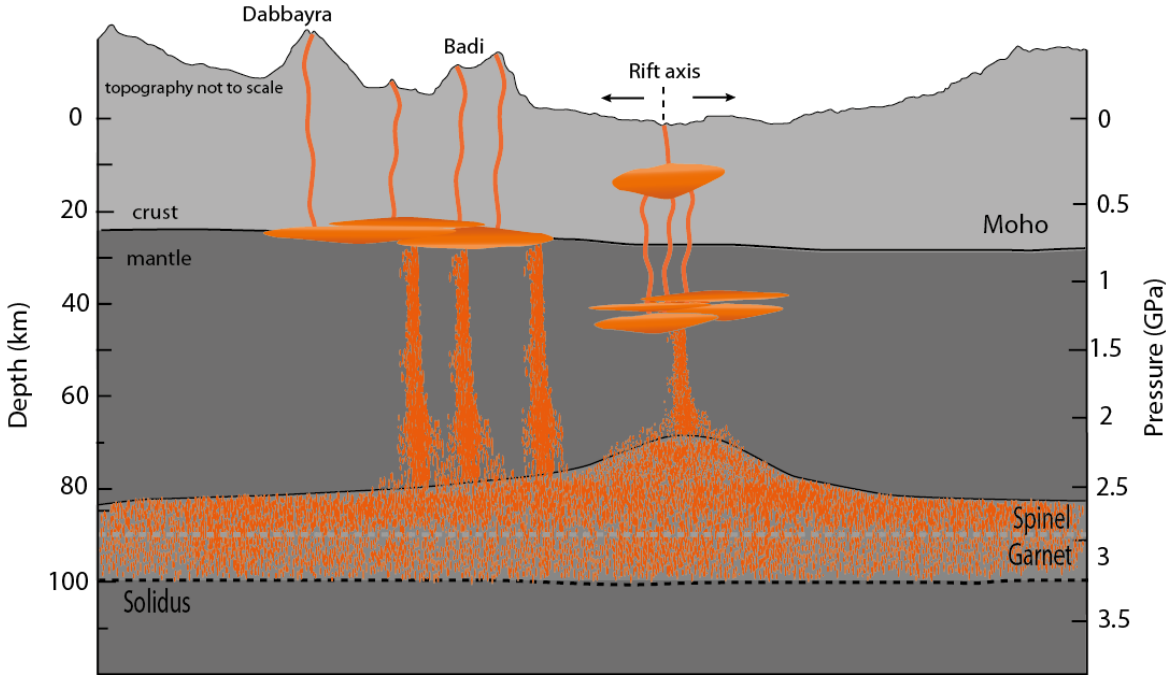

Figure 5.21 Schematic illustration of the magmatic system at the DMH rift segment based on the petrological constraints on melt generation and storage discussed in this chapter. Partial melts are generated in upwelling mantle between 100 – 75 km depth. These melts are stored and fractionated prior to eruption at the rift axis or at the off-axis volcanoes.

evolve prior to being erupted. The higher degree melts that feed the axial eruptions initially accumulate in a storage region at ~40km where fractionation occurs. Evolved liquids with ≥ 10 wt% MgO from this accumulation zone then feed a shallower region in the crust ~8 km below the rift axis, where further fractionation occurs and from which dykes propagate along the rift axis (e.g. Ebinger et al., 2011).

5.9 Comparison with geophysical observations

As discussed in early chapters, recent (and on-going) geophysical studies have provided some new constraints on the sub-surface structure and processes at the DMH rift system (i.e. Keir et al., 2009; Belachew et al., 2011; Hammond et al., 2011). Studies on the deeper (> 50 km) parts of the subsurface are currently being conducted and these should provide important constraints on the deeper regions identified here as zones of partial

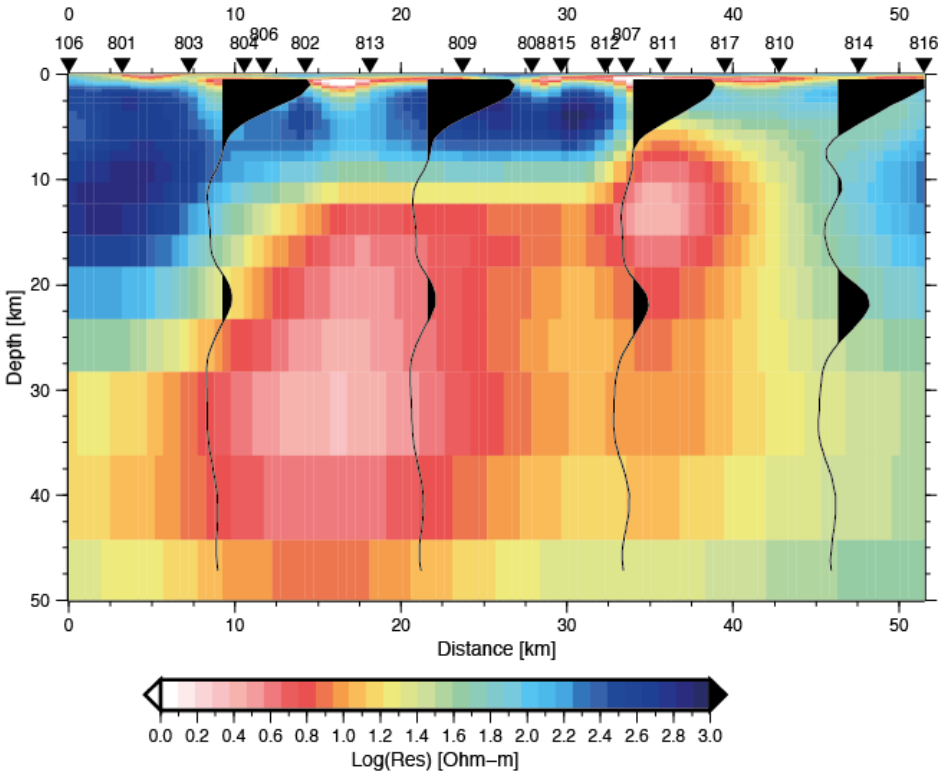

Figure 5.22 Conductivity model of the crust and upper mantle below the DMH segment based on magnetotelluric data by N. Johnson at the University of Edinburgh (Johnson et al., in prep). The profile line measured by Johnson et al is shown in the location map in Fig 5.4. The numbers and symbols on the top indicate measurement sites (rift axis is at site 811). The line of the profile is the same as the topographic section at the top of Fig 5.21. The most conductive regions are colured red/white, while the most resistive are blue. This dataset, measured in 2007-2008, identifies a large region of highly conductive material in the upper mantle to the east of the rift axis, interpreted to be a magma chamber/region of high partial melt fraction. A shallower conductive body is located beneath the rift axis (top right) and corresponds well with the axial magma chamber inferred to be feeding recent dyke intrusion and eruptions. As discussed in the text the overall conclusions from the petrological data agree well with this dataset.

melting. Some information on the shallow structure of the rift system and on the recent magmatic processes, however is available from recent seismic, geodetic and magnetotelluric (MT) investigations.

Seismic imaging shows that the crust beneath the DMH segment is ~22 km thick with an upper-lower crustal transition at ~6 km depth (Hammond et al., 2011). Seismicity associated with the recent dyke intrusions indicates that dykes propagate from the centre of the rift beneath the AVC complex (Kier et al., 2009) and the earthquakes are distributed between depths of 0-10 km (Ebinger et al., 2008;Belachew et al., 2011), indicating a storage region below this depth. The most important available dataset for

imaging melt distributions in the crust and upper mantle beneath the DMH rift is an MT profile (shown in Fig 5.22) measured in 2008 across the rift axis and immediately to the south of the Badi volcano (Johnson et al., in prep). The MT data identifies two significant regions of high conductivity beneath the rift. The shallowest of these is located directly beneath the rift axis at ~10-20 km depth and corresponds reasonably well to the region of shallow storage identified in the petrological data at ~8 km depth (0.2 GPa) (Fig 5.21) and also agrees with the seismic evidence from dyke propagation. It is likely therefore that this represents a sub-rift magma chamber where melts are stored prior to intrusion and eruption. The largest region of partial melt identified in the MT data is located below the crust, offset to the east of the axis and with maximum conductivity recorded at depths > 30 km. The structure of this region below ~30 km is not well resolved as the highly conductive material in the upper mantle limits the ability of the MT technique to measure the conductive properties of material at greater depths. The upper part of this region, at ~20 km depth, is located beneath the off-axis volcanoes and is also in broad agreement with the fractionation depths indicated by the petrological data. The deeper region of melt storage proposed for the axial lavas, where primary melts initially evolve, prior to shallow storage is in agreement with the deeper part of this conductive zone.

As shown in Fig 5.18, an important result from the trace element modelling is that lavas erupted at the off-axis volcanoes, which have greater incompatible element concentrations, represent lower melt fractions than those supplied to the axis. The preservation of these geochemical signatures in the erupted lavas imposes the key constraint on melt supply, that primary melts, parental to the lavas erupted at each location, do not mix prior to extraction from the mantle. Given the large dimensions of

the conductive region imaged by the MT data segregating melts prior to eruption may seem unlikely, however, it is important to remember that at the surface the off-axis volcanoes represent a discrete region of volcanism and that the MT inversion technique provides an averaged result for subsurface conductivity perpendicular to the profile line. The discrete nature of the off-axis volcanism demonstrates that melt supply to areas away from the rift axis is not common and therefore a separate plumbing system feeding this region from depth may not be unfeasible.

5.10 Summary

This chapter has presented a variety of geochemical data for basaltic rocks erupted across the field area and has developed various geochemical arguments for the constraints this dataset allows on magmatism at the DMH rift system. The isotopic and trace element compositions of the lavas demonstrate that they are produced from melting of fertile mantle material and all the lavas are enriched compared to typical MORB's. Results from both the major and trace element modelling shows that melting beneath the DMH segment begins at a pressure >3 GPa in the garnet stability field and that the observed compositions can be well modeled at melt fractions of ~4-6 %. An important result from this chapter is that the melts erupted in the main rift and at the off-axis volcanoes are chemically distinct and therefore do not mix prior to eruption. The major and trace element differences between these lavas can be explained by variable extents of melting of a common mantle source followed by differing fractionation histories and storage regimes, as illustrated in Fig 5.21. Comparing this model with recent geophysical studies, particularly the MT data (Fig 5 22), shows good agreement with respect to regions of melt storage in the crust and upper mantle.

Chapter 6

Petrogenesis of silicic lavas

6.1 Introduction

The preceding chapters in this thesis have focused on the processes connected to the generation, storage and eruption of the basaltic magmas found across the central DMH segment and at off-axis volcanoes. The intrusion of basaltic melts in dykes along the axis of the DMH segment is central to rifting here and the magmatic system is intimately linked to the tectonic evolution of this part of the Afro-Arabian plate boundary. However, as described in Chapter 2, a significant amount of silicic volcanism has also occurred across this study region, and lavas with evolved compositions form the majority of the subaerial volume of Badi and the rifted fragments of the Ado Ale volcanic complex (AVC). The overall theme of this thesis is the development of a 'source to surface' model of magmatism at the DMH rift system and the eruption of these evolved melt compositions has important implications for the processes of melt generation and/or modification in the sub-rift region. Although a detailed investigation of the origin of silicic melts has not been undertaken, it is prudent to consider at least some general aspects of the genetic processes responsible for the generation of evolved magma compositions. This chapter presents major and trace element and some isotopic data for a suite of silicic lavas, sampled from Badi and the eastern part of the AVC, and examines current evidence for the links between these evolved melts and their basaltic counterparts.

6.2 Silicic volcanism in Ethiopia

6.2.1 Overview

The volcanic activity associated with both the Eocene flood lavas in the Ethiopian and Yemeni plateaus and the rift related activity in the MER and Afar is typically considered to be largely basaltic in nature, and most studies have focused on basaltic magmatism. However, silicic volcanism is also a common feature of both these regions and evolved lavas represent a volumetrically significant part of the lava flux. In the Ethiopian and Yemeni plateaus, evolved lavas, including large ignimbrite deposits, are found within the flood basalt sequence (Mohr, 1983; Ayalew et al., 2002; Ayalew and Yirgu, 2003; Peate et al., 2005) and in Ethiopia it is estimated that these account for ~20% of the total volume of the flood lavas. Trachytic and rhyolitic lavas are also commonly found at many volcanoes in the MER (e.g. Cole, 1969; Mohr, 1969; Gibson, 1975; Woldegabriel et al., 1992; Webster et al., 1993; Chernet et al., 1998; Peccerillo et al., 2003; Kurz et al., 2007; Rampey et al., 2010) and this region hosts several large caldera systems that are associated with thick regional tephra deposits (Pyle, 1999; Hart et al., 2003). Relatively few of the silicic volcanoes in the MER have been studied in any detail and with the exception of a few (e.g. Chernet et al., 1998; Kurz et al., 2007; Rampey et al., 2010) the eruptive history/stratigraphy of most of the silicic systems in the MER is unknown. In both the flood lava sequence and in the MER lava compositions have a strong bimodal character and intermediate compositions appear to be very scarce.

The distribution of silicic volcanism in Afar has been previously discussed in Chapters 1 and 4. Although with respect to areal extent basaltic lavas are by far the most common

rock type found across the depression and form the prevailing substrate, evolved lavas account for a significant portion of the total erupted volume across Afar (Wiart and Oppenheimer, 2005). Several large silicic calderas are located around the margins of the depression (i.e. Ma'alalta, Barberi et al. 1974; Nabro, Wiart and Oppenheimer, 2005; see Chapter 4) and effusive silicic centres, similar to the AVC and Badi, are common along many rift zones and grabens (Lahitte et al., 2003ab).

The most significant silicic volcanism in the DMH segment has occurred at the Dabbahu volcano at the northern end of the segment, where an almost complete basalt-rhyolite compositional series has been erupted (Barberi et al., 1975; Field, 2011). A similar range of lava compositions has also been reported for volcanoes from the Erta Ale segment (Barberi and Varet, 1970; Bizourd et al., 1980; Barrat et al., 1998). A notable feature of many silicic lavas in Afar is the effusive nature of their emplacement and obsidian/finely crystalline lavas flows and domes are common. In general, explosive silicic eruptions, leading to caldera formation and/or deposition of significant pyroclastic material, appear to be limited to volcanoes on the margins of the Afar along the transverse structures (e.g. Ma'alalta, Nabro etc; see Fig 4.1).

6.2.2 Petrogenesis

A common petrological feature of silicic volcanism in the MER and Afar is the occurrence of lavas with peralkaline compositions (i.e. Barberi et al., 1974, 1975; Peccerillo et al., 2003). Peralkaline lavas are defined on the basis of the agpaitic or peralkaline index (PI), which is found from the molecular ratio of (Na + K)/Al and in peralkaline melts is > 1, signifying a relative depletion in Al compared to the alkaline

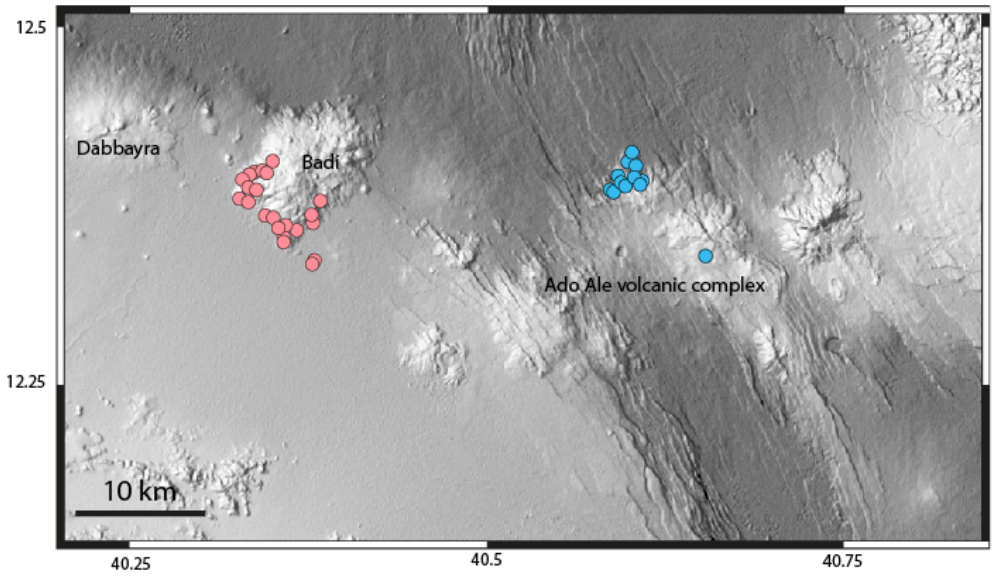

Figure 6.1 General locations of silicic lava samples from the NE part of the AVC and Badi. Photos and field descriptions of these lavas is presented in chapter 2.

components. Within the peralkaline field further divisions can be on the basis of Fe and Al content using the scheme of Macdonald (1974), which classes the trachytic and rhyolitic lavas from Afar and MER as pantellerites (Fig 6.2a) (defined as having $Al_2O_3 < 1.33*FeO^T + 4.4$ and signifying enrichment in Fe compared Al). Following the study of the Dabbahu lava series by Barberi et al (1975) this volcano became a type locality for the generation of peralkaline rhyolites from extensive low-pressure crystal fractionation of a transitional/mildly alkaline basaltic parent. The conclusions of Barberi et al (1975) have been largely confirmed by recent work by Field (2011) who showed that although melt storage at Dabbahu probably occurs over a range of depths, the final stage of liquid evolution most likely occurs at low pressures (~2 kb). An investigation of a bimodal suite of basaltic and pantelleritic lavas erupted at Gedemsa volcano in the MER by Peccerillo et al (2003) also concluded that low pressure fractionation, with possible minor crustal assimilation, rather than melting of crustal or basaltic material, was responsible for generating liquids with evolved compositions. Analysis of dissolved water contents in glass inclusions in lavas from Dabbahu (Field, 2011) and at Fantale

volcano in the MER (Webster et al., 1993) suggests relatively high pre-eruptive water contents for these magmas of~3-4 wt%.

6.3 Geochemistry of lava from Badi and the AVC

A suite of 46 samples of lavas and pumice deposits, which were identified in the field as rhyolitic/trachytic, were collected from Badi (33 samples) and the AVC (13 samples). Sampling locations are shown in Fig 6.1. Field observations on these silicic lavas and minor pyroclastic deposits are presented in Chapter 2.

6.3.1 Methods

Bulk concentrations of major element oxides and trace elements were measured by XRF for obsidian, crystalline lava and pumice samples from Badi (33 samples) and the AVC (13 samples). These samples include all of the textural varieties encountered, which vary between holohyaline obsidians, crystalline lavas and pumice. The results of the analyses are listed in Table 6.1. High precision trace element measurements using ICP-MS were also made on 5 samples from Ado Ale and 6 from Badi and these are also listed in the Table. XRF measurements were made at the University of Leicester, UK and ICP-MS measurements at the Washington State University, USA. The analytical details for these are the same as for the basaltic samples reported in Chapter 5 and are described in appendix B.

Radiogenic isotopic ratios for $^{206}Pb/^{204}Pb$, $^{207}Pb/^{204}Pb$, $^{208}Pb/^{204}Pb$ were determined for 4 silicic samples from the AVC and 2 from Badi and $^{143}Nd/^{144}Nd$ ratios were determined for 2 samples from each location. All isotopic ratios (plus $^{87}Sr/^{86}Sr$) were also determined for the trachy-andesite lava from the base of Dabbayra (sample 2909), which were reported in Chapter 5. The isotopic analyses were conducted at Woods Hole

Oceanographic Institution and the samples were co-prepared and analysed with the basaltic lavas using the same procedures outlined for these in Chapter 5 and appendix B. Measurements of the ratio of the stable silicon isotopes $^{30}Si/^{28}Si$ have also been made on 2 obsidian samples from the AVC and one pumice from Dabbahu by Savage et al (2011). This study also analysed $^{30}Si/^{28}Si$ for 3 basaltic lavas from the study area (2 axial lavas and 1 from Badi) and these are listed alongside the isotopic data for the silicic lavas in Table 6.2.

6.3.2 Results

6.3.2.1 Major elements

The results of the major element analyses are listed in Table 6.1. Lavas vary from mildly to strongly peralkaline (P.I. varies from 1.07 – 2.15) and according to the classification scheme of Macdonald (1974) are all classed as pantellerites (Fig 6.2a). Peralkaline lavas are particularly sensitive to post-eruptive alkali loss and it is important to assess whether this may have occurred before using geochemical data for petrogenetic studies. Using the criteria of White et al (2003), shown in Fig 6.2b, which compares the less mobile elements Fe, K and Al to the peralkaline index, alkali loss in all the analysed samples appears to be very minor. Variation plots of the major element concentrations versus SiO_2 data are shown in Fig 6.3. The compositional data from the basaltic lavas presented in Chapter 5 is also included in these plots and these therefore illustrate the entire compositional range of lavas sampled from across the study area.

The compositions of the trachytic and rhyolitic lavas from both regions are broadly similar although like the basaltic lavas, some variations do occur between lavas from

Table 6.1 Major (wt%) and trace (ppm) element compositions of Badi and AVC lavas measured by XRF

Location	AVC	AVC	AVC	AVC	AVC	AVC	AVC	AVC	AVC
Sample	**27-01**	**29-01**	**28-03**	**29-03**	**28-06**	**28-07**	**28-08**	**28-09**	**28-10**
Lithology	trachyte	rhyolite	trachyte	rhyolite	rhyolite	rhyolite	obsidian	rhyolite	obsidian
Latitude	12.333	12.410	12.396	12.397	12.392	12.391	12.393	12.393	12.391
Longitude	40.657	40.607	40.590	40.611	40.590	40.590	40.591	40.591	40.593
SiO_2	68.10	73.49	68.19	73.18	73.95	74.81	75.05	73.39	75.21
TiO_2	0.50	0.24	0.46	0.24	0.23	0.24	0.23	0.23	0.22
Al_2O_3	13.26	10.86	13.56	10.43	10.68	10.92	10.85	10.82	10.72
Fe_2O_3	6.17	4.03	6.02	3.86	3.89	3.97	3.97	3.95	3.79
MnO	0.199	0.085	0.200	0.081	0.079	0.082	0.082	0.083	0.077
MgO	0.06	<0.023	<0.024	0.13	<0.023	<0.023	<0.023	<0.024	<0.023
CaO	1.18	0.41	0.98	1.23	0.69	0.42	0.19	0.82	0.18
Na_2O	5.51	4.99	5.52	4.79	4.70	4.63	5.25	5.07	5.19
K_2O	4.799	4.441	5.002	4.392	4.483	4.476	4.326	4.462	4.382
P_2O_5	0.056	0.004	0.032	0.005	0.000	0.002	0.002	0.006	0.002
SO_3	0.023	0.019	<0.002	0.139	0.585	0.105	0.015	0.551	0.015
LOI	-0.02	1.19	0.04	1.18	0.30	0.29	0.18	0.45	0.17
Total	99.82	99.76	100.01	99.65	99.59	99.93	100.15	99.83	99.95
P.I.	1.08	1.20	1.07	1.21	1.18	1.14	1.23	1.22	1.24
Ba	481	17	429	11	<3.1	<3.2	<3.1	39	<3.1
Ce	151	249	158	231	249	250	250	228	245
Co	1.62	4.18	3.56	4.28	4.12	3.14	4.10	5.70	2.61
Cr	<0.7	<0.6	<0.7	<0.6	<0.6	<0.6	4.7	2.7	<0.6
Cs	<1.7	7.3	<1.7	5.4	9.7	7.0	7.8	4.9	10.4
Cu	6.8	3.9	1.9	2.1	3.6	1.0	<0.4	2.2	<0.4
Ga	29.0	33.6	32.0	31.1	34.3	33.0	32.6	31.5	31.0
La	68	108	72	107	110	110	109	85	113
Mo	3.1	6.2	2.7	2.0	1.3	2.5	6.9	4.6	6.2
Nb	89	126	92	122	107	126	129	125	128
Nd	75	117	77	108	116	114	116	90	114
Ni	<0.6	<0.6	<0.6	1.39	<0.6	<0.6	<0.6	<0.6	<0.6
Pb	9.6	15.4	9.6	12.6	12.3	14.3	15.8	15.1	15.7
Rb	92	133	91	134	148	150	150	145	151
Sc	2.14	<1.0	1.99	1.21	1.59	1.09	<1.0	<1.0	<1.0
Sr	27.3	10.4	13.3	21.0	13.6	13.0	3.2	21.9	2.8
Th	8.5	15.8	8.7	13.9	15.0	15.9	15.9	15.7	16.5
U	1.97	4.27	1.74	1.93	1.74	3.57	4.20	3.12	4.35
V	3.12	2.83	3.56	5.79	<0.7	2.03	<0.7	7.54	<0.7
Y	82	131	81	119	165	135	141	95	136
Zn	143	194	144	171	162	189	198	190	193
Zr	594	972	595	945	957	998	1017	990	1011

Location	AVC	AVC	AVC	AVC	BADI	BADI	BADI	BADI	BADI
Sample	**28-13**	**28-13b**	**29-02**	**29-05a**	**29-05b**	**01-01**	**03-01**	**22-01**	**31-01**
Lithology	trachyte	rhyolite	rhyolite	obsidian	rhyolite	obsidian	rhyolite	rhyolite	rhyolite
Latitude	12.410	12.409	12.410	12.397	12.397	12.396	12.354	12.372	12.37
Longitude	40.601	40.601	40.607	40.611	40.611	40.341	40.353	40.323	40.392
SiO_2	68.84	68.96	70.10	74.72	75.74	73.24	72.84	71.37	75.73
TiO_2	0.47	0.42	0.41	0.24	0.25	0.21	0.19	0.18	0.18
Al_2O_3	13.31	13.25	13.27	10.76	10.91	9.32	8.79	8.57	10.84
Fe_2O_3	5.82	5.50	5.29	4.03	4.05	6.91	7.08	7.01	3.30
MnO	0.180	0.180	0.164	0.085	0.087	0.182	0.192	0.194	0.063
MgO	0.05	<0.024	<0.024	<0.023	<0.023	<0.023	0.06	<0.023	<0.023
CaO	1.07	0.92	0.77	0.20	0.21	0.27	0.39	0.44	0.17
Na_2O	5.45	5.52	5.49	5.28	5.30	6.36	5.15	6.84	5.06
K_2O	4.839	5.036	4.818	4.439	4.293	3.902	4.276	4.128	4.399
P_2O_5	0.055	0.028	0.020	0.002	0.002	0.009	0.009	0.009	0.000
SO_3	0.013	0.026	0.012	0.014	0.015	0.022	0.007	0.041	0.011
LOI	-0.06	-0.07	-0.08	0.15	0.16	0.10	0.92	0.41	0.25
Total	100.04	99.77	100.27	99.92	101.01	100.53	99.92	99.18	100.01
P.I.	1.07	1.10	1.07	1.25	1.23	1.58	1.49	1.84	1.21
Ba	257	260	179	4	<3.1	11	3	<3.1	<3.0
Ce	165	168	162	246	246	363	482	517	232
Co	4.19	5.15	4.60	3.29	4.46	5.00	4.62	4.42	2.91
Cr	<0.7	<0.7	<0.7	2.0	1.0	15.4	4.9	<0.7	4.4
Cs	5.6	2.6	3.2	8.6	7.3	10.2	17.7	17.7	6.7
Cu	1.2	1.8	<0.5	<0.4	<0.5	7.2	12.4	5.0	<0.4
Ga	30.8	32.3	30.3	32.1	32.6	35.3	44.1	46.0	31.2
La	71	81	71	114	112	161	246	230	103
Mo	3.1	2.3	1.9	7.3	7.3	7.1	4.9	8.7	5.6
Nb	94	96	97	124	125	263	335	387	142
Nd	80	81	78	114	114	150	221	212	109
Ni	<0.6	<0.6	<0.6	<0.6	<0.6	2.77	4.04	<0.7	<0.6
Pb	8.7	10.0	8.4	14.1	15.0	16.6	29.1	29.4	18.6
Rb	94	92	101	144	146	173	202	261	173
Sc	2.70	<1.1	1.63	<1.0	1.66	<1.0	<1.1	<1.1	<1.0
Sr	26.3	11.1	10.1	3.2	3.4	6.7	20.0	10.3	2.2
Th	9.4	10.0	8.8	14.9	15.4	22.6	29.7	34.7	18.8
U	1.67	1.19	<0.4	3.79	4.38	5.86	7.88	9.57	5.55
V	8.59	6.84	5.85	1.97	0.81	2.02	<0.8	1.88	<0.7
Y	70	87	67	135	135	155	270	228	146
Zn	139	145	144	196	198	288	367	410	198
Zr	631	642	657	962	967	1372	1903	2220	1159

Location	BADI	BADI	BADI	BADI	BADI	BADI	BADI	BADI	BADI
Sample	**01-02**	**02-02**	**22-02**	**24-02**	**25-02**	**01-03**	**02-04**	**03-03**	**24-03**
Lithology	pumice	trachyte	rhyolite	obsidian	rhyolite	pumice	trachyte	rhyolite	rhyolite
Latitude	12.396	12.360	12.373	12.359	12.354	12.397	12.346	12.355	12.359
Longitude	40.342	40.349	40.328	40.389	40.371	40.342	40.351	40.360	40.389
SiO_2	69.69	68.94	69.67	72.25	71.29	69.17	69.32	70.00	71.76
TiO_2	0.23	0.46	0.17	0.25	0.21	0.49	0.46	0.24	0.18
Al_2O_3	8.77	10.15	8.34	8.26	8.85	10.75	10.21	7.45	8.70
Fe_2O_3	6.50	7.88	6.84	7.78	6.81	7.83	7.85	8.97	7.14
MnO	0.173	0.256	0.190	0.243	0.182	0.253	0.255	0.319	0.193
MgO	0.08	<0.024	0.33	<0.023	0.03	<0.024	0.12	<0.023	<0.023
CaO	0.71	0.47	1.76	0.24	0.90	0.55	0.86	0.40	0.40
Na_2O	5.19	6.00	4.92	6.67	5.22	5.84	5.06	7.07	5.92
K_2O	4.477	4.575	3.982	4.172	4.354	4.639	4.593	4.063	4.157
P_2O_5	0.017	0.012	0.008	0.010	0.074	0.016	0.015	0.015	0.009
SO_3	0.045	0.024	1.483	<0.002	0.484	0.020	0.086	0.006	0.019
LOI	3.93	0.20	1.32	-0.18	0.91	0.41	0.79	0.32	0.80
Total	99.81	98.98	99.01	99.69	99.32	99.97	99.61	98.85	99.29
P.I.	1.53	1.46	1.49	1.88	1.51	1.36	1.30	2.15	1.64
Ba	6	25	9	3	<3.2	22	22	14	22
Ce	359	292	527	441	487	346	352	686	539
Co	5.61	5.48	3.31	3.02	1.44	5.89	5.66	7.37	2.30
Cr	23.2	4.2	<0.7	<0.7	9.3	14.0	<0.7	12.2	<0.7
Cs	11.5	9.4	14.0	12.7	13.6	9.8	12.7	23.0	16.9
Cu	6.8	6.9	7.9	9.0	11.0	7.8	8.4	14.3	10.8
Ga	33.1	41.1	45.0	38.6	42.3	43.5	45.0	40.5	44.2
La	172	165	311	203	186	159	165	318	250
Mo	6.8	3.2	2.1	12.4	2.2	9.1	2.6	16.2	6.7
Nb	258	257	368	323	347	250	264	527	390
Nd	157	147	256	196	183	141	147	284	226
Ni	4.45	0.89	1.18	1.26	1.78	<0.7	<0.7	3.58	4.07
Pb	16.7	11.7	29.4	23.5	26.2	16.0	17.3	37.8	28.6
Rb	198	161	208	223	242	172	183	321	246
Sc	<1.1	<1.1	1.52	<1.1	2.15	<1.1	<1.1	<1.1	1.18
Sr	19.5	7.1	31.9	5.1	29.7	24.6	27.8	12.6	15.8
Th	22.1	12.9	33.2	28.1	31.2	20.2	21.3	46.6	34.6
U	5.77	2.77	3.45	7.58	5.29	3.88	5.86	11.70	7.32
V	8.25	2.54	2.58	<0.8	0.83	1.11	<0.8	3.03	0.99
Y	161	117	256	216	160	116	159	312	231
Zn	291	308	402	367	335	295	318	569	406
Zr	1355	1382	2129	1921	2055	1341	1419	2991	2243

Location	BADI	BADI	BADI	BADI	BADI	BADI	BADI	BADI	BADI
Sample	**30-03**	**01-04**	**02-04**	**03-04**	**3004**	**01-07**	**01-09**	**01-10**	**29-10**
Lithology	rhyolite	pumice	rhyolite	rhyolite	pumice	trachyte	trachyte	obsidian	trachy-andesite
Latitude	12.389	12.397	12.347	12.354	12.3894	12.400	12.399	12.396	12.424
Longitude	40.337	40.342	40.352	40.357	40.337	40.346	40.348	40.341	40.292
SiO_2	72.38	69.82	71.50	72.20	68.59	67.28	68.02	72.09	59.96
TiO_2	0.29	0.50	0.34	0.34	0.21	0.33	0.33	0.26	1.19
Al_2O_3	8.75	10.33	9.05	9.15	8.95	11.96	11.88	8.84	15.84
Fe_2O_3	7.51	8.05	8.17	8.10	7.06	5.91	5.77	7.85	9.17
MnO	0.234	0.250	0.233	0.260	0.211	0.165	0.160	0.260	0.210
MgO	<0.023	<0.024	<0.023	<0.023	<0.023	0.15	0.18	0.21	1.47
CaO	0.34	0.49	0.29	0.54	0.38	1.52	1.05	0.43	3.62
Na_2O	4.67	5.63	5.58	5.26	6.30	6.07	5.64	4.20	4.93
K_2O	4.448	4.486	4.478	4.535	4.438	4.809	4.749	4.401	3.149
P_2O_5	0.009	0.013	0.030	0.015	0.012	0.028	0.023	0.014	0.432
SO_3	0.012	0.018	0.025	0.011	0.039	0.089	0.023	0.020	0.018
LOI	0.57	0.29	0.33	0.64	2.92	1.40	0.95	0.77	-0.15
Total	99.22	99.88	100.03	101.02	99.11	99.71	98.76	99.34	99.83
P.I.	1.43	1.37	1.55	1.48	1.70	1.27	1.21	1.32	0.73
Ba	4	21	8	47	<3.2	57	50	68	965
Ce	776	349	360	458	355	347	312	522	140
Co	3.04	5.20	4.82	5.75	3.14	5.19	4.89	6.11	11.32
Cr	<0.7	15.2	<0.7	<0.7	<0.7	<0.7	1.6	11.9	<0.7
Cs	22.3	7.9	8.2	11.8	9.7	7.6	6.8	17.0	<1.7
Cu	9.9	8.0	9.8	9.3	6.3	12.1	14.0	11.8	3.7
Ga	38.6	43.5	42.4	43.6	34.5	39.4	38.0	41.7	26.0
La	232	168	123	206	167	136	181	205	69
Mo	2.2	1.9	5.1	5.7	9.6	4.0	2.2	3.0	4.6
Nb	371	264	337	327	271	278	265	410	90
Nd	212	147	122	179	152	122	153	181	65
Ni	2.05	1.67	<0.7	2.62	1.59	2.41	2.26	2.32	<0.7
Pb	23.4	17.3	21.7	21.5	15.6	19.7	15.4	28.5	8.3
Rb	249	176	202	188	185	193	183	290	74
Sc	2.44	<1.1	<1.1	<1.1	<1.1	1.42	2.62	1.52	15.51
Sr	30.1	26.8	9.8	20.0	10.7	24.5	18.6	23.5	356.2
Th	40.2	21.0	26.7	26.7	22.3	22.9	21.3	36.1	8.3
U	5.66	3.74	2.77	4.65	5.99	3.79	1.08	8.99	2.35
V	25.00	1.21	3.86	2.85	0.80	4.39	3.10	3.11	20.68
Y	224	163	73	165	157	90	130	166	58
Zn	404	316	329	370	293	235	217	433	117
Zr	2139	1437	1852	1774	1330	1498	1431	2341	593

Location	BADI	BADI	BADI	BADI	BADI	BADI	BADI	BADI	BADI
Sample	**30-10**	**30-12**	**02-06A**	**02-06B**	**3004a**	**3004b**	**3004c**	**3004d**	**30-12**
Lithology	pumice	obsidian	trachyte	rhyolite	pumice	pumice	pumice	pumice	obsidian
Latitude	12.389	12.392	12.329	12.329	12.389	12.389	12.389	12.389	12.392
Longitude	40.337	40.340	40.379	40.377	40.337	40.337	40.337	40.337	40.340
SiO_2	73.07	73.46	67.28	72.58	72.58	72.99	73.16	72.47	73.67
TiO_2	0.22	0.19	0.44	0.21	0.21	0.38	0.30	0.29	0.18
Al_2O_3	9.37	8.97	13.08	9.33	9.45	9.16	9.08	9.07	8.96
Fe_2O_3	6.92	6.68	5.64	7.45	7.40	8.16	7.91	7.73	6.68
MnO	0.176	0.178	0.186	0.203	0.220	0.260	0.246	0.236	0.181
MgO	<0.023	<0.023	0.15	0.10	<0.024	0.06	0.03	<0.023	<0.023
CaO	0.26	0.21	1.87	0.37	0.25	0.50	0.42	0.43	0.21
Na_2O	5.74	6.61	5.28	4.32	6.95	5.08	4.98	5.17	6.48
K_2O	3.991	4.185	4.899	4.450	3.867	4.494	4.472	4.567	3.938
P_2O_5	0.004	0.005	0.026	0.011	0.010	0.019	0.006	0.012	0.005
SO_3	0.016	0.017	0.109	0.011	0.029	0.074	0.013	0.040	0.017
LOI	0.22	-0.09	0.95	0.60	0.04	0.52	0.52	0.63	-0.07
Total	99.98	100.41	99.91	99.61	101.01	101.69	101.14	100.65	100.26
P.I.	1.47	1.72	1.07	1.28	1.66	1.44	1.44	1.48	1.67
Ba	13	<3.1	280	25	7	5	39	46	<3.1
Ce	246	372	155	501	360	433	398	313	373
Co	3.54	4.43	1.88	3.36	5.36	5.05	4.25	4.23	5.35
Cr	<0.7	<0.7	<0.7	<0.7	<0.7	<0.7	<0.7	<0.7	<0.7
Cs	9.5	11.6	<1.7	13.1	10.5	12.8	10.7	12.6	12.3
Cu	1.2	<0.5	1.6	6.0	0.8	3.7	4.2	3.9	1.3
Ga	40.2	36.4	29.6	46.2	37.6	43.1	42.3	41.7	36.0
La	122	177	69	48	169	198	202	232	177
Mo	2.6	7.2	3.5	3.7	10.2	1.6	3.1	4.5	7.2
Nb	268	276	89	340	280	309	359	363	281
Nd	103	160	75	86	155	176	174	196	160
Ni	<0.6	<0.6	<0.6	<0.7	<0.7	<0.7	1.14	<0.7	<0.7
Pb	14.1	18.0	9.0	22.2	16.1	21.2	27.4	31.9	18.6
Rb	175	191	87	217	188	216	253	252	193
Sc	<1.0	<1.0	1.87	1.38	<1.0	<1.0	1.30	<1.1	<1.0
Sr	9.7	3.3	21.7	18.4	6.0	39.9	32.2	27.9	3.5
Th	12.8	24.3	8.3	29.1	23.6	25.8	39.1	24.8	25.0
U	4.94	6.29	2.05	0.45	5.92	4.34	4.88	3.57	6.81
V	1.44	<0.8	12.11	2.34	<0.8	9.64	21.02	10.48	<0.8
Y	105	171	80	29	163	173	240	177	174
Zn	298	307	137	368	305	362	425	416	312
Zr	1412	1445	579	1972	1372	1675	2226	2018	1471

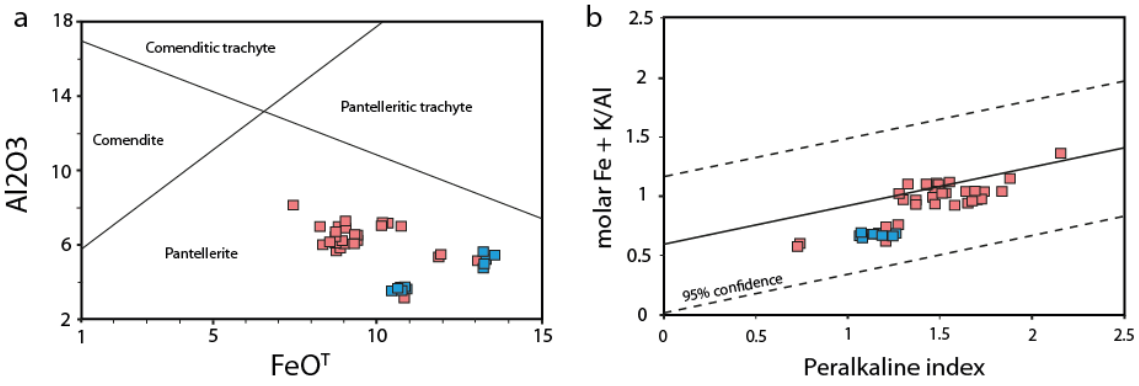

Figure 6.2 (a) Discrimination diagram for peralkaline trachytes and rhyolites after Macdonald (1974). All lavas from Badi and the AVC are classed as pantellerites, indicating an enrichment in Fe over Al. (b) Plot of (molar) Fe + (K/Al) vs. Peralkaline Index ((molar) Na + (K/Al)). This plot is used to assess post-eruptive alkali by comparing less mobile elements with the peralkaline index. The solid line equals (Fe +K/Al) = 0.6727(P.I) + 0.5954 and is based on the criteria of White et al (2003). According to this criterion no significant alkali loss has occurred form these lavas. Red symbols: Badi lavas, blue symbols: AVC lavas.

Badi and those erupted in the rift centre. Like the basaltic lavas there is greater scatter in the data for the off-axis silicic lavas, although this may be partly related to a larger number of samples. One notable variation is that the off-axis lavas trend to more peralkaline compositions (P.I. = 1.21 – 2.15) than those from the main rift (P.I. = 1.07 – 1.25), which is largely due to elevated Al contents in the latter. Many of the major elements, including CaO, TiO_2, Fe_2O_3, MgO, show consistent trends between the mafic and felsic compositions. Although the two intermediate (~60 wt% SiO_2) trachy-andesite samples demonstrate that some intermediate melt compositions are erupted, the overall distribution of compositions within the current sample suite is strongly bimodal and dominated by basaltic and rhyolitic melts. This is in contrast to the range of lavas erupted ~25 km further north at Dabbahu (Barberi et al., 1975; Field, 2011), which does include a significant proportion of products of intermediate composition.

6.3.2.2 Trace elements

The trace element results are listed in Tables 6.1 and 6.2. Variation diagrams of trace elements versus SiO_2 are shown in Fig 6.4 and log-log plots between incompatible

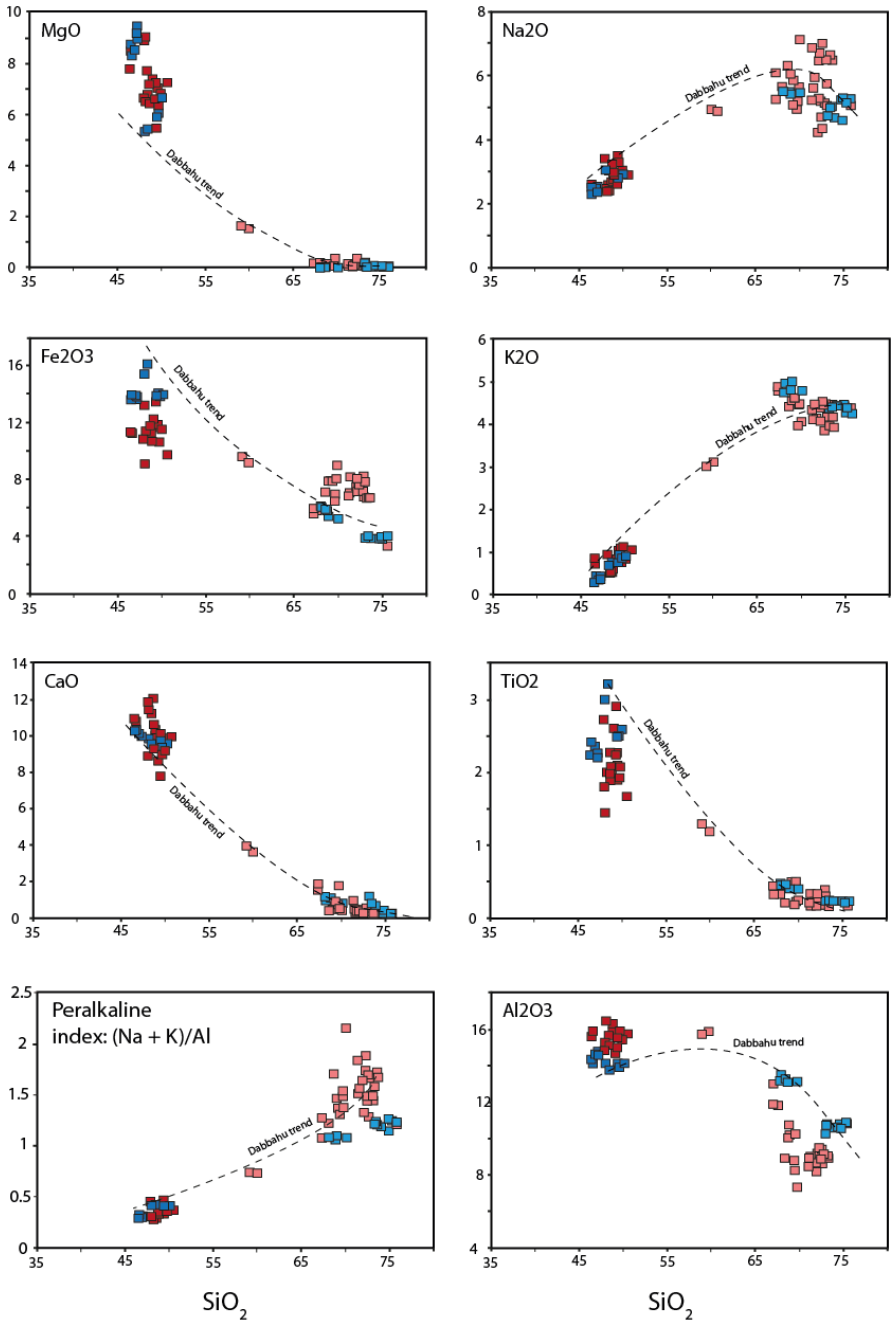

Figure 6.3 major element variation plots for all the samples analysed in this thesis. Data for the basaltic and intermediate lavas is listed in Table 5.1. The compositional trend for the Dabbahu lavas identified by Barberi et al (1975) is also shown. See text for discussion. Symbols are: dark red - off-axis basalts/intermediates, light red - off-axis rhyolites/trachytes (Badi), dark blue - axial basalts, light blue - axial trachytes/rhyolites (AVC).

Table 6.2 Trace element concentrations for selected samples analysed by ICP-MS

Location	AVC	AVC	AVC	AVC	AVC	AVC	BADI	BADI	BADI	BADI
Sample	**2701**	**2803**	**2810**	**2813**	**2813b**	**2902**	**2202**	**0304**	**3010**	**3012a**
Lithology	trachyte	trachyte	obsidian	trachyte	trachyte	rhyolite	rhyolite	rhyolite	pumice	obsidian
La	68	69	113	49	77	69	301	198	127	180
Ce	149	151	239	114	162	155	489	410	251	359
Pr	17.9	18.1	28.0	13.6	19.6	18.5	63.1	43.6	28.3	40.5
Nd	72	72	108	55	78	72	234	159	104	151
Sm	15.5	15.7	23.2	12.4	16.7	15.2	46.0	32.4	20.3	31.0
Eu	3.42	3.39	2.60	2.84	3.15	2.74	2.51	4.14	3.05	4.29
Gd	14.6	14.9	22.5	11.7	16.1	13.8	43.6	29.5	18.3	29.0
Tb	2.47	2.50	3.94	2.01	2.70	2.34	7.37	5.19	3.16	4.98
Dy	15.1	15.3	24.7	12.1	16.6	14.2	44.6	32.3	19.6	30.8
Ho	3.08	3.09	5.05	2.44	3.39	2.84	9.13	6.50	4.06	6.30
Er	8.3	8.3	13.9	6.6	9.1	7.8	24.6	17.7	11.3	16.9
Tm	1.23	1.24	2.04	0.95	1.34	1.18	3.54	2.61	1.69	2.44
Yb	7.9	8.0	12.6	6.1	8.6	7.8	21.8	16.8	11.1	15.1
Lu	1.29	1.30	1.91	1.00	1.41	1.29	3.40	2.61	1.78	2.29
Ba	469	410	15	255	265	181	22	51	24	14
Th	8.9	8.9	16.8	6.4	9.8	9.3	32.6	26.0	13.7	23.3
Nb	79	82	117	60	86	87	342	303	261	254
Y	75	74	128	55	80	62	231	151	103	157
Hf	13.1	13.1	23.4	10.0	14.2	14.7	45.9	38.0	33.6	31.9
Ta	5.00	5.06	8.00	3.84	5.36	5.51	21.74	19.08	17.90	16.37
U	1.86	1.65	4.81	1.08	0.52	0.29	3.50	4.26	5.44	6.44
Pb	9.2	9.1	16.1	6.0	9.6	8.4	27.6	20.5	12.9	17.2
Rb	86	85	146	59	87	95	192	175	162	178
Cs	0.77	0.25	1.89	0.26	0.08	0.22	0.43	0.30	0.61	1.59
Sr	26.44	12.10	1.80	146.64	9.52	8.73	28.76	16.67	5.96	2.45
Sc	5.38	3.80	3.86	18.68	3.40	3.09	6.30	5.75	4.18	5.24
Zr	546	551	962	430	598	619	2015	1683	1444	1351

elements (La, Nb, Th, Rb and Ba) versus Zr in Fig 6.5. REE profiles are shown in Fig 6.6. Similar to peralkaline trachytes and rhyolites elsewhere (e.g. Black et al., 1998; Peccerillo et al., 2003) these lavas show very strong enrichments in elements such as Zr (≤ 2991 ppm), Nb (≤ 527 ppm) and REE's and depletions in Sr (≤ 40 ppm) and Co (≤ 7.4 ppm). Ba contents show a wide variation from 481 to < 3 ppm. Similar to the major element data, the lavas from Badi display a wider range of trace element

Table 6.3 Nd, Pb and Si isotopic data for silicic and basaltic lavas

Sample	Lithology	$^{144}Nd/^{143}Nd$	$^{206}Pb/^{204}Pb$	$^{206}Pb/^{204}Pb$	$^{206}Pb/^{204}Pb$
2803	trachyte	-	18.60	15.56	38.42
2813	trachyte	0.512878	18.59	15.55	38.39
2813b	rhyolite	0.512879	18.60	15.56	38.43
2902	rhyolite	0.512856	18.59	15.56	38.42
2909	andesite	0.512864	18.69	15.57	38.52
3010	pumice	0.512856	18.96	15.59	38.92
BADI07		0.512896	18.78	15.58	38.67

Si isotopic data from Savage et al (2011)

		$\delta^{31}Si$	2σ (±)
2808	obsidian	-0.19	0.05
2907	trachyte	-0.16	0.03
DAB	pumice	-0.12	0.1
BADI05	basalt	-0.29	0.15
2805	basalt	-0.28	0.05
2007	basalt	-0.31	0.05

The $^{30}Si/^{28}Si$ ratio is reported using the $\delta^{31}S$ notation, which indicates the deviation of the measured ratio from a standard value. See Savage et al (2011) for full details.

concentrations and form less well-defined trends in SiO_2 discrimination plots, which are distinct from the trend of the axial lavas. Like the off-axis basalts, the Badi lavas are also typically more enriched in highly incompatible elements (e.g. Rb, Nb,) and have higher La/Sm than their axial counterparts (Fig 5.6f). With the exception of strong Eu anomalies all the silicic lavas have smooth REE patterns that are similar in shape to the basaltic lavas (Fig 6.6). In most log-log plots of highly incompatible elements (e.g. those shown for Zr vs. Rb, La and Th; Fig 6.4) all the silicic samples show strong positive linear trends, while elements that are variably compatible during crystallisation (e.g. Ba and Sr) show negative trends that are less well defined, although the difference between the sample groups is still discernible.

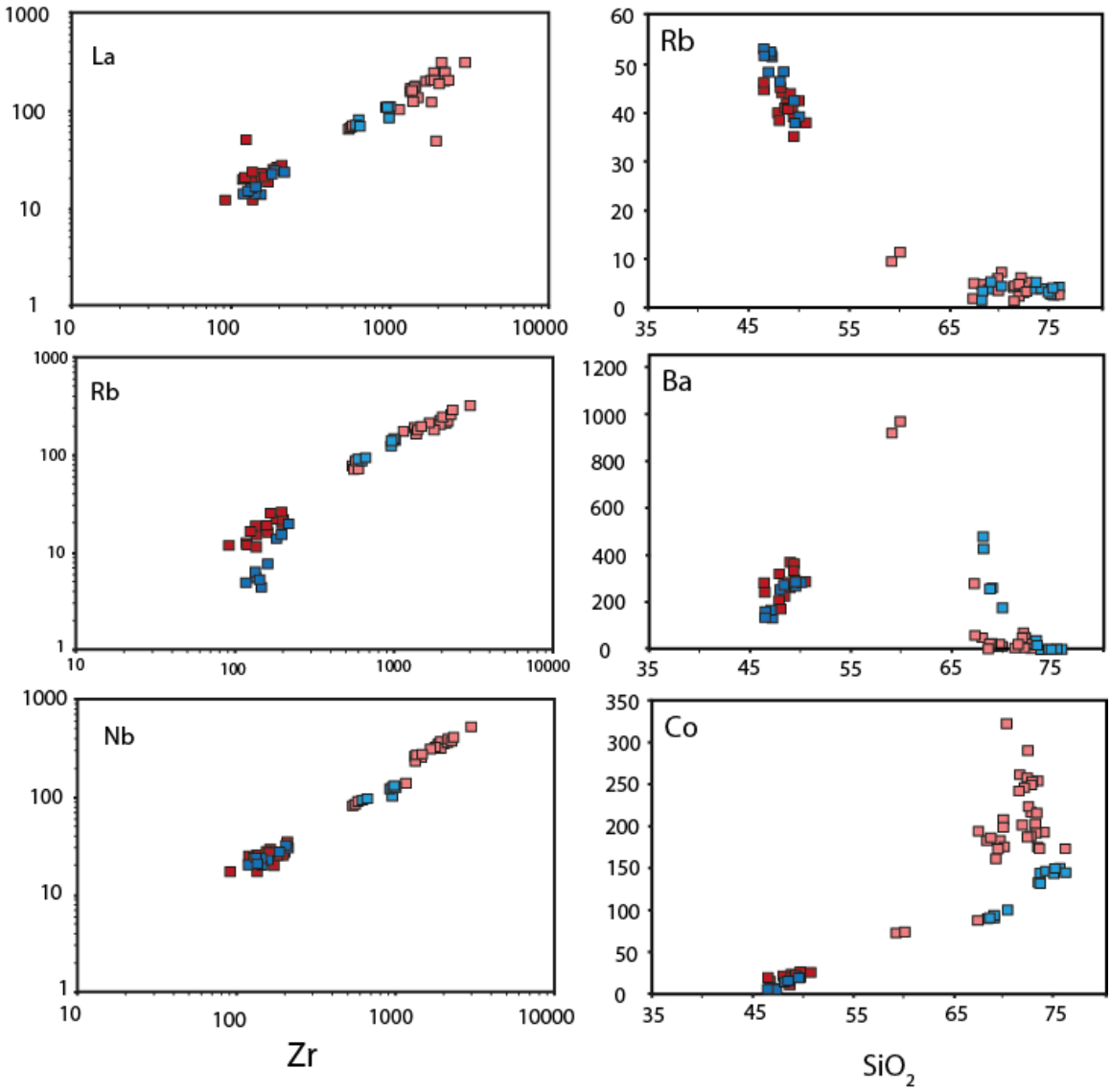

Figure 6.4 Trace element plots showing variations of selected elements versus SiO_2 or Zr (log-log plots) for all the lavas analysed in this thesis. Data for silicic lavas (SiO2 > 65 wt%) is in table 6.1. Basaltic and intermediate compositions are from chapter 5. SiO_2 is in wt%, all trace elements are in ppm. Symbols are the same as in Fig 4.3.

6.3.2.3 Nd, Sr and Si isotopes

Although relatively few isotopic measurements have been made on the silicic lavas, these do provide a key line of evidence when investigating the provenance of the evolved melts. The isotopic data are listed in Table 6.2. Fig 6.5a-e shows a comparison between Nd and Pb isotopic ratios for the silicic lavas with those for the basaltic melts, presented in Chapter 5. $^{143}Nd/^{144}Nd$ values for the silicic lavas are indistinguishable

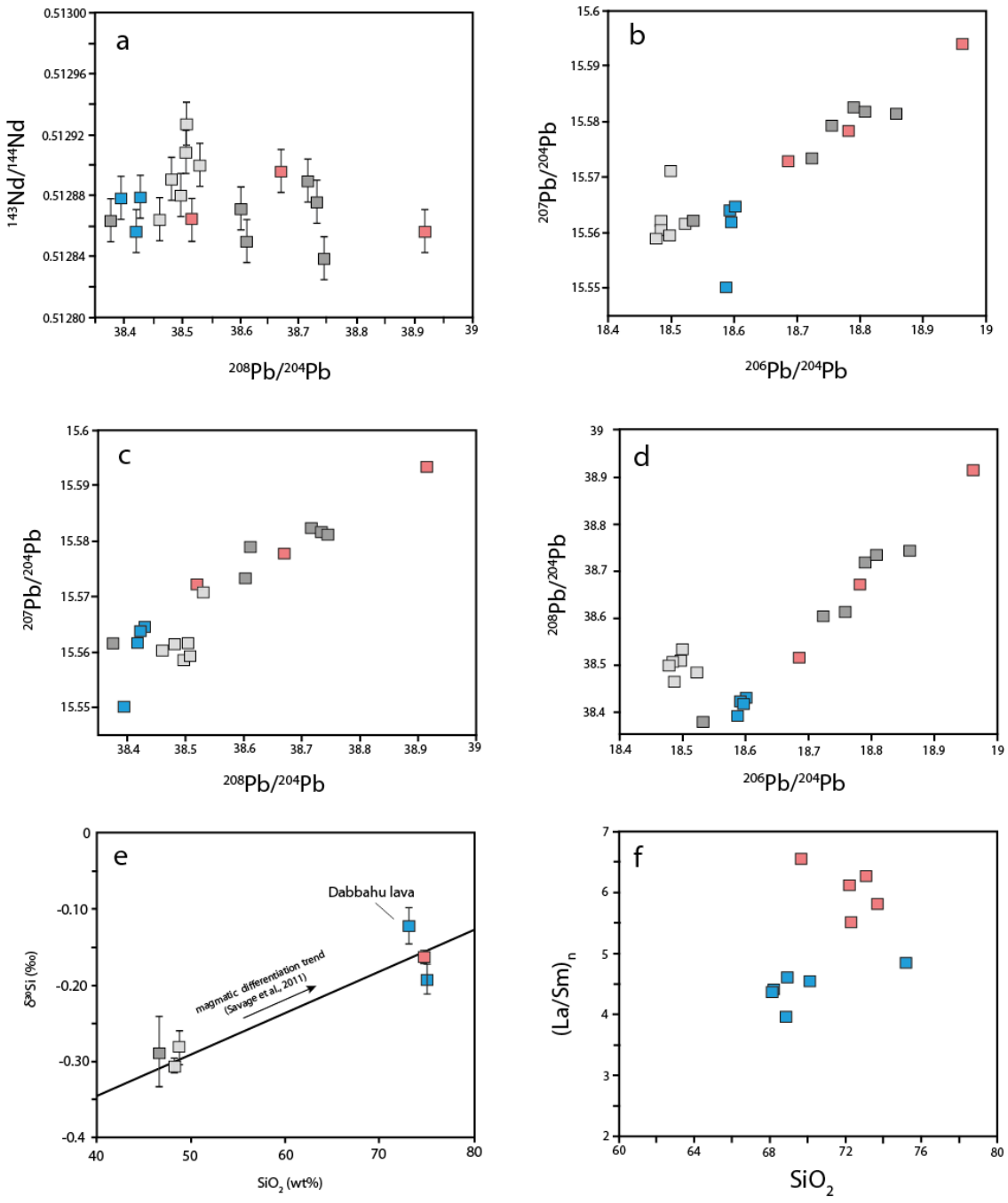

Figure 6.5 (a-e) variation plots comparing the isotopic compositions of silicic and basaltic lavas erupted in the field area. (data listed in table 6.3 and in chapter 5). Coloured symbols represent silicic compositions (Badi: red, AVC: blue), off-axis basalts (and one trachy-andesite) are dark grey, axial basalts are light grey. Although only a few silicic lavas have been analysed the Nd and Pb isotopic values for these samples are very similar to the basalts. The Si isotopic data is from Savage et al (2011) (see Table 6.3 for explanation of $\delta^{31}Si$ notation). The differentiation trend is from analyses of a suite of basaltic and rhyolitic by Savage et al (2011) who found that differentiated lavas have consistently higher $\delta^{31}Si$ values. (f) Plot of $(La/Sm)_n$ vs. SiO_2. Similar to the basaltic lavas the Badi trachytes and rhyolites show greater fractionations of highly to moderately incompatible elements compared to the Ado Ale (i.e. axial) samples. La/Sm normalized to primitive mantle as in Fig 6.6.

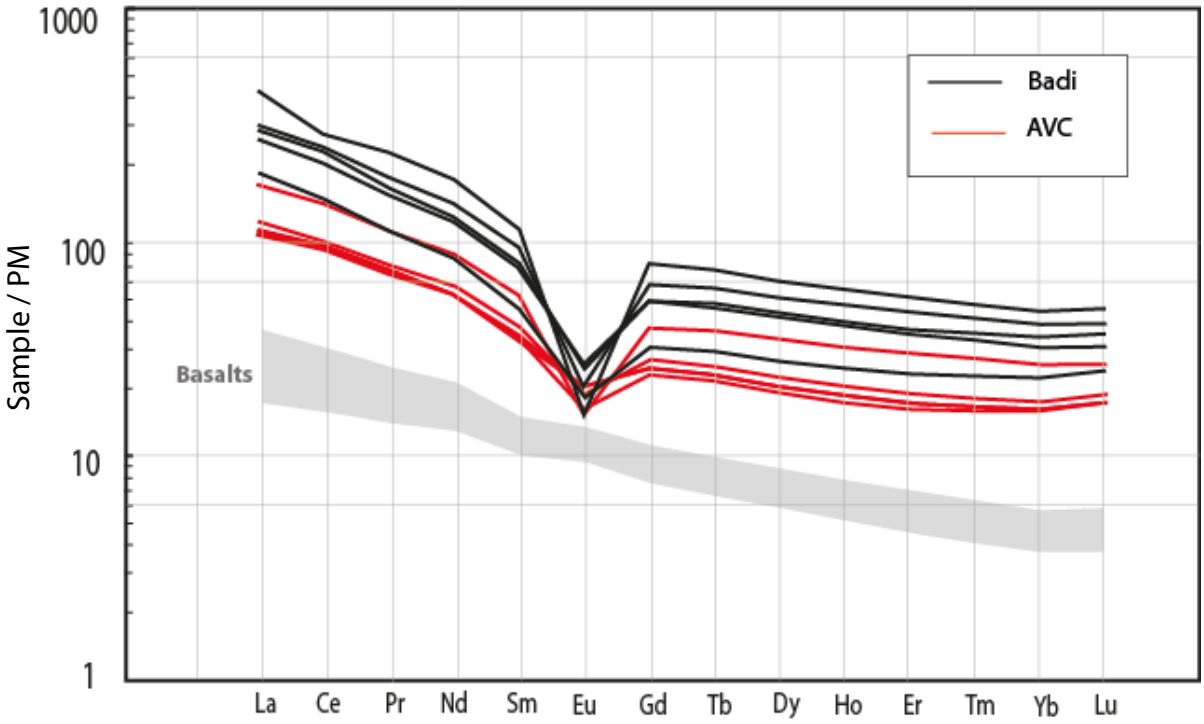

Figure 6.6 Primitive mantle normalized rare earth element profiles for silicic lavas from Badi and the AVC. Normalizing values from Sun and McDonough (1989). All lavas have very similar patterns with large Eu anomalies. . Like the basaltic lavas samples from Badi are enriched in LREE's (La/Sm: 5.5 – 6.54) compared to the AVC lavas (La/Sm: 4.85 – 3.97). Grey area shows the same data for the basaltic lavas, which also have similar patterns.

from the array defined by the basaltic lavas and the entire sample suite for all compositions shows very minor variations with almost all samples have the same value when analytical uncertainties are considered. The $^{206}Pb/^{204}Pb$, $^{207}Pb/^{204}Pb$ and $^{208}Pb/^{204}Pb$ values largely mimic those for the basaltic lavas from both the on and off axis regions. The $^{208}Pb/^{204}Pb$ values for the AVC lavas are more similar to those for the off-axis lavas than the axial basalts, which lie slightly off the linear array defined by these. An important feature of the isotopic results for the silicic lavas is the similarity of these values to the basaltic lavas and this strongly indicates that these melts are derived from a common source with respect to isotopic composition. The $^{30}Si/^{28}Si$ measurements by Savage et al (2011) (reported as $\delta^{30}Si$ values in Table 6.3) are identical within analytical error for the AVC samples and are very close to a Dabbahu pumice sample measured at the same time ($\delta^{30}Si = -0.12 \pm 0.1$).

6.4 Discussion

6.4.1 Petrogenesis of peralkaline rhyolites

Theories regarding the origin of peralkaline rhyolites have typically focused on two processes; extensive fractionation of basaltic parents (e.g. Barberi et al., 1975; Harris et al., 1983; Mungall and Martin, 1995; Civetta et al., 1998; Peccerillo et al., 2003) or partial melting of crustal material (e.g. Macdonald et al., 1987; Black et al., 1997; Mahood et al., 1990). In some locations, such as Pantelleria, Italy, conflicting studies have proposed both these processes (i.e. Mahood et al., 1990; Civetta et al., 1998), however, in other locations there is clear evidence for either extensive fractionation of basaltic melts (e.g, Peccerillo et al., 2003) or the direct involvement of crustal material (e.g. Black et al., 1997). The Nd and Pb isotopic data for the Badi and AVC rhyolites and trachytes strongly suggests that they share a common source with the basaltic melts and therefore that evolved liquids were derived by either fractionation of these basaltic magmas or were generated by partial melting of material that shares the same isotopic composition, such as cumulates from these magmas.

The possible scenarios for a genetic link between the mafic and felsic lavas are similar to those considered by Peccerillo et al (2003) for a bimodal lava suite in the MER. It is notable that the major element trends for the lava analysed here are, in most cases, consistent with the evolutionary trend from the Dabbahu lava series (shown in Fig 6.3), where magma evolution has been clearly shown to be the result of extensive fractionation (Barberi et al., 1975; Field, 2011). The evidence from the major element trends, along with the extreme enrichments observed in some incompatible elements, such as Zr (≤ 2991 ppm) and Ce (≤ 776 ppm), suggests that crystal fractionation is the

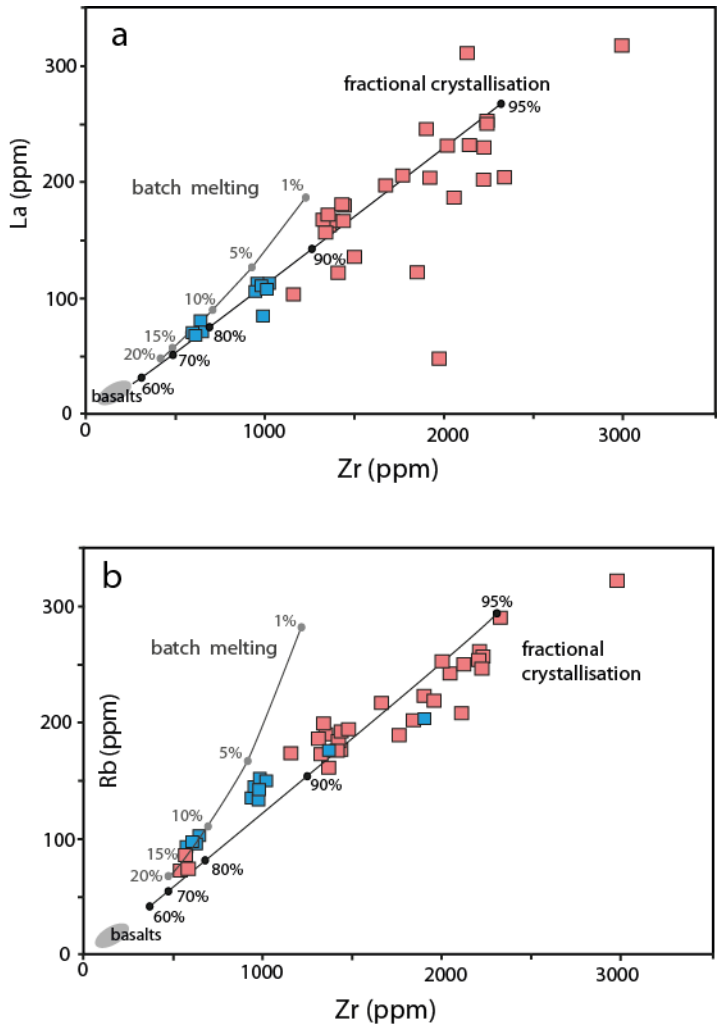

Figure 6.7 Plots of (a) Zr vs La and (b) Zr vs Rb comparing the compositions of the silicic lavas to batch melting of a gabbroic source and fractional crystallisation a basaltic liquid. The batch melt is calculated using a source composition typical of the basalts from the field area (Zr: 170 ppm, La: 17 ppm and Rb: 17 ppm). Partition coefficients are calculated for a gabbroic lithology of 0.9 Olv + 0.2 Cpx + 0.1 Plag and are D_{Rb} = 0.05, D_{La} = 0.08 and D_{Zr} = 0.127. Fractional crystallisation is calculated for the same crystallizing assemblage.

mostly likely mechanism for generation of the evolved lavas erupted at Badi and AVC. Before investigating fractionation processes, however, the alternative of partial melting of previously crystallized basaltic material will be briefly considered.

6.4.1.1 Origin by partial melting

The Nd and Pb isotopic constraints, shown in Fig 6.5, limit the potential source material or parental melts for the evolved melts as being essentially co-genetic with the basaltic lavas. Experimental studies have shown that it is possible for silicic rich melts to be generated from partial melting of mafic material under various conditions (e.g.

Holloway and Burnham, 1972; Wolf and Wyllie, 1994; Kawamoto, 1996; Koepke et al., 2004) and Peccerillo et al (2003) suggest that the major element composition of peralkaline rhyolites from the MER could be matched by ~10-30% partial melting of a gabbroic source. Melting of intruded or under-plated mafic material beneath the DMH rift could therefore in theory account for the generation of the silicic melts and would be consistent with the similar isotopic compositions between the basaltic and silicic lavas. This mechanism avoids the requirement, implicit in fractionation models, that relatively large volumes of basaltic melt are stored and processed beneath the rift.

Although detailed investigation of gabbroic melting is not presented here, and some aspects of this process may merit future investigation, the feasibility of producing the observed silicic compositions by partial melting can be briefly examined by comparing the trace element concentrations calculated for partial melts from a gabbroic source wit the observed compositions. Fig 6.6 shows Zr vs. Rb and Zr vs. La for a series of batch melts calculated for a gabbroic lithology which has a composition similar to the basaltic lavas. The source mineralogy and partition coefficients used in the calculation are listed in the caption. Even at very small melt fractions (F = 0.01%) the Zr and La concentrations in the batch melt fail to match the most enriched lavas and can only reproduce the highest Rb concentrations observed at relatively low melt fractions (F = ~1 %). At higher melt fractions (~20 %) the incompatible element compositions of some of the least evolved lavas can be reproduced. In comparison, a simplified fractionation trend for (olv + cpx + plag) calculated for the same source/melt composition, also shown in Fig 6.7, produces a much better representation of the variations in trace element concentrations. It should be noted that since the bulk source composition used for the batch melting and fractional crystallisation models shown in

the Fig 6.7 is identical, once a melt fraction is reached where the melt composition closely approximates that of the less evolved lavas (in this case at F = ~20 %) it is impossible to discriminate between fractionation of this new melt compared to fractionation of the original more mafic melt. However, there is no evidence to support this complex two stage processes (i.e. such as fluid contamination) and the coherence in the incompatible element trends between the basaltic and silicic lavas (Fig 6.5) suggests that the straightforward fractionation model provides a more consistent explanation of the data.

6.4.1.2 Fractional crystallisation

As demonstrated by the simple crystal fractionation model for Zr, Rb and La shown in Fig 6.6 the trends between these incompatible elements can be well reproduced by prolonged fractionation of a source with a similar composition to the erupted basalts. In most of the variation plots shown in Figs 6.3, 6.4 and 6.5 relatively consistent liquid lines of descent can be identified from the basaltic to silicic compositions. The variation in major elements concentrations closely approximates the Dabbahu trend, which is well constrained due to the unusual abundance of intermediate lavas. The Si isotopic data by Savage et al (2011) also argues for an origin for the silicic melts by crystal fractionation from a basaltic parent. Magmatic differentiation causes observable mass dependent fractionations in stable Si isotopes and the variation in $^{30}Si/^{28}Si$ values between the silicic and basaltic lavas from the field area, shown in Fig 6.4, is consistent with this process.

To further investigate fractionation processes the major element compositions of liquids produced by progressive fractionation of basaltic parental magma have been calculated using the thermodynamic model Rhyolite-MELTS by Gualda et al (submitted). This is a revised version of the MELTS model by Ghiroso and Sack (1995), modified to

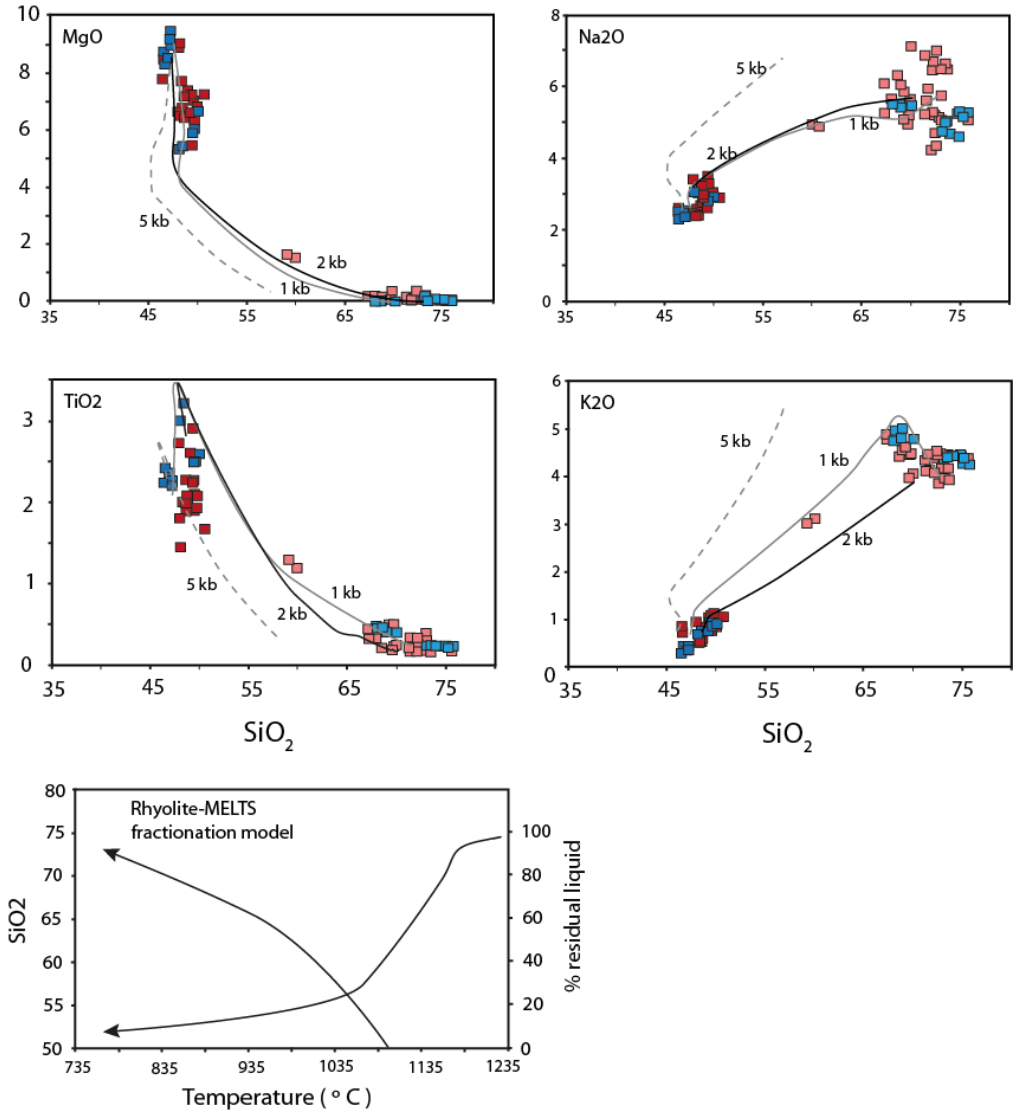

Figure 6.8 Fractionation trends calculated using the Rhyolite-MELTS software (Gualda et al., Submitted).

.

produce more accurate predictions of plagioclase-quartz saturation in melts with elevated SiO_2 contents. The silicic lava samples from the AVC and Badi are ideal for comparisons with fractionation models due to their crystal poor nature and high glass contents. Following the experimental work of Scaillet and Macdonald (2002) the oxygen fugacity (fO_2) conditions in the fractionation model was set at just below the Quartz-Fayalite-Magnetite buffer (*QFM -1*). No information is currently available on the volatile contents of the basaltic lavas in the DMH rift, however, dissolved water

contents measured in glass inclusions in rhyolites from Dabbahu by Field (2011) reach ~3-4 wt%. In order to account for the effects of water on the fractionation process, an initial H_2O content of 0.3 wt% was used for the parental melt in the model.

Fractionation trends were obtained for various pressures of crystallisation using basaltic melts erupted in the field area as starting compositions. Illustrative results from these models are shown in Fig 6.8. The best fitting results were obtained for low-pressure conditions (≤ 2 kbar). This is consistent with previous studies that argue that peralkaline melts are the products of fractionation at moderately low pressures (Barberi et al., 1975; Scaillet and Macdonald, 2002; Peccerillo et al., 2003). To reach the observed silicic compositions requires high degrees of crystallisation of ≥ 80% and Fig 6.8e illustrates how the SiO_2 content of the melt evolves with increasing fractionation.

6.4.1.3 Crustal assimilation

Assimilation processes in magmas are best investigated using radiogenic isotopic ratios, which are unaffected by melting/crystallisation but will be altered if material of a different composition is assimilated into a magma. The dataset of isotopic analyses for these rhyolites is currently limited to the small number of Nd and Pb analyses listed in Table 6.3 and so conclusion based on the isotopic composition are necessarily tentative. However, as noted above, the current isotopic data is very consistent with the array defined by the basaltic lavas and on this basis there is no evidence for significant contamination by material, which is isotopically different to the mantle source inferred for the basalts. Ce/Pb and La/Nb ratios are also commonly used to infer crustal contamination of mantle derived melts (i.e. Hofmann et al., 1986). Fig 5.14 (in Chapter 5) showed the co-variation of these ratios for the basaltic lavas and was used to argue that there was no evidence for in these lavas for deviations from the low La/Nb (< 1)

and high Ce/Pb (20 – 30) typical of mantle material. La/Nb ratios in the silicic rocks vary between 0.5 - 1 (Table 6.1) and are indistinguishable from the basalts. However, the available analyses of Ethiopian crustal material, also shown in Fig 5.14, show that many crustal samples also have low La/Nb so contamination from this crust would be hard to detect on this basis. Ce/Pb ratios, listed in Table 6.1, in the silicic lavas vary between 15 – 21 and are notably lower than the basaltic lavas (Ce/Pb = 16 - 31) and below the commonly accepted mantle range of Ce/Pb = 25 ± 5 (Hofmann et al., 1986). There may be evidence therefore that some assimilation of material of typical crustal compositions has occurred, as may be expected during a protracted fractionation process. Further investigation of this would be best conducted via more isotopic measurements, particularly analysis of $^{87}Sr/^{86}Sr$ and $\delta^{18}O$ as these proved to be sensitive indicators of crustal contamination in rift settings such as Iceland (e.g. Sigmarsson et al., 1992); however a more extended investigation would also benefit from better knowledge of the crustal composition in this region.

6.4.2 Implications for melt storage

The results of the fractionation model suggest that the evolution to high SiO_2 contents occurs at relatively low pressures, most likely at or below 2 kbar. This is lower than the fractionation/storage pressures estimated for the basaltic lavas in Chapter 5, which are ~6-8 kbar for the off-axis lavas and ~3-5 kbar for the axial lavas. In the case of the central rift zone it is feasible that late stage fractionation occurs in the upper part of the storage region at sufficiently low pressures. This is unlikely for the case for the off-axis region where the storage depths indicated by the basalts appear too deep for generation of the evolved melts.

The petrogenetic model for the basaltic melts summarised in Fig 5.21 is partly based on the important observations that the various geochemical differences that exist between lavas erupted in the on and off-axis regions eruptions indicate that these two areas are fed by separate plumbing systems. Many of these variations, such as the enrichments in incompatible elements in the off-axis (Badi) lavas (i.e. higher Zr, Rb, Nb, REE's) (Figs 6.5 and 6.6) and Pb isotopic concentrations (Fig 6.4), appear to be inherited by the silicic lavas from the respective locations. This implies that, like the basaltic lavas, the evolved melts that erupted at Badi evolved separately from those at the AVC. The only available age constraint for the silicic volcanism in this region is the K-Ar age of 290 ± 4 ka for the base of Badi (Lahitte et al., 2003), however, based on the erosional state of all the silicic flows forming Badi and the AVC, and the significant rifting of the AVC lavas, there is no evidence for recent eruptions of any significant volume of silicic lavas. The emplacement of Badi and the AVC lavas may therefore represent a discrete period of silicic volcanism in this part of the DMH rift system at ~300 ka. A possible explanation for this event may be a period of reduced melt flux to the sub-rift region, allowing more extensive fractionation to occur and the generation of silicic melts. A temporary region of shallow melt storage beneath Badi at this time could allow differentiation at pressures consistent with the fractionation models. If this is the case, the absence of a shallow conductive region beneath Badi in the recently acquired magnetotelluric data (Johnson et al., in prep; shown in Fig 5.22) indicates that this is not a permanent feature of the magmatic system. The total subaerial volume of silicic lavas forming Badi and the AVC is ~48 km^3. Based on the fractionation model the generation of this volume by differentiation of a basaltic parent would require ~240 km^3 of parental melt (with ~80% crystallisation), around 80 times the volume of magma intruded/erupted since 2005.

6.5 Summary

This chapter has presented a brief overview of some of the geochemical features of the silicic lavas erupted in the study area and has outlined the evidence for the generation of these lavas by extensive low-pressure fractionation of a basaltic parent. This conclusion is in line with the results of the studies of peralkaline trachytes and rhyolites erupted at Dabbahu (Barberi et al., 1975) and in the MER (Peccerillo et al., 2003). The limited isotopic data do suggest that there may only be a limited role for crustal contamination, however the lower Ce/Pb ratios in the silicic lavas do imply that some assimilation of crustal material may have occurred. Further isotopic data, and future studies, are required to test this. Based on the field evidence presented in Chapter 2 there is little evidence for recent silicic eruptions and the one existing K-Ar age of 290 ± 4 ka for Badi (Lahitte et al., 2003) may well be a good working estimate for the date when most of the silicic lavas were emplaced.

Chapter 7

Conclusions

7.1 Introduction

The aim of this thesis has been to develop a broad understanding of how magma is generated, stored and erupted at the DMH rift segment and to examine how these processes interact with the extensional tectonics related to continental break-up. The recent rifting activity at the DMH segment (i.e. Wright et al., 2006; Ebinger et al., 2010) has made this part of Afar an important location for understanding magmatic rifting and continental break-up, however, with the exception of the Dabbahu volcano (Barberi et al., 1975), there has been no prior geochemical or geochronological studies on lavas from this rift zone. In light of the wide array of geophysical information that has recently become available on magmatic and tectonic processes here (e.g. Hamling et al., 2009, 2010; Keir et al., 2009, 2011; Grandin et al., 2009, 2010; Belachew et al., 2011; Hammond et al., 2011; Johnson et al., in prep) this project has provided a timely complement to these studies and has provided an alternative perspective on magmatic processes. It has also provided important geological context for observations of the most recent magmatic, volcanic and tectonic activity. Due to the lack of previous geochemical studies on the DMH segment the approach in this thesis has been deliberately broad and has been undertaken with the intention of characterizing a range of the 'source to surface' processes relating to magmatism and volcanism in the DMH rift system.

7.2 Volcanic tectonic interactions at the rift surface

7.2.1 Current volcanic activity

The eruptions along the axis of the DMH segment between 2007-2010 provided a rare opportunity to observe fissure eruptions that were associated with active rifting and fed by intrusions that have been well characterised by seismic (Belachew et al., 2011) and geodetic (Hamling et al., 2009; Grandin et al., 2010) studies. The context for understanding these eruptions within their tectonic setting was limited as no detailed observations have ever been made on an active fissure eruption at a mid-ocean ridge and although much effort has been made to understand the physical aspects of lava emplacement in these settings (e.g. Perfit and Chadwick, 1998) these have been restricted by the obvious logistical limitations. The 1974-1981 Krafla rifting period in Iceland has provided an important analogue for the recent Afar activity and in Chapter 3 was used as a comparison for the physical characteristics of individual eruptions and the mass balance between intruded and extruded magma during a rifting phase. A clear result of this analysis is that, consistent with numerical models of successive dyking events (Buck et al., 2006), the intrusive to extrusive magma ratio evolves during a rifting phase, with eruptions becoming more likely as greater amounts of extension are achieved. The cumulative erupted volume from the current Afar rifting phase is relatively low (~16 x 10^6 km^3) and when the ratio of intruded to erupted (I:E) melt of ~260:1 is compared to I:E estimates for volcanic systems worldwide (i.e. White et al., 2006) this is approximately a factor of 10 lower than may be expected. Although the comparisons made with the Krafla activity are currently limited by the on-going nature of the Afar phase it has provided a useful framework for evaluating the prospect of further eruptions in the near future. To a first-order, eruptions in the DMH segment are

considered more likely to occur over the next ~5-10 years than either during the initial part of the current rifting phase or during a future inter-rifting period.

7.2.2 Development of volcano-tectonic structures during continental break-up

The recent eruptions and dyke intrusions along the DMH rift axis have shown that magma is currently strongly focused along the DMH axial zone and the rift zone can be considered to have reached a relatively mature stage of evolution. On a regional scale recent volcanism in Afar is clearly closely linked to tectonic structures and most Quaternary eruptions (at least since ~1 Ma) appear to have occured almost exclusively at either axial rift segments or along the transverse volcanic structures found around the margins of the depression. This is in contrast to the widespread activity associated with emplacement of the stratoid series of basaltic lavas from 1-3 Ma, which were erupted across a large area. There is clearly therefore a strong link between crustal or mantle structures and the focusing of melts along these recent volcanic-tectonic zones. In the case of the axial rift zones, these are also the locus of extension/strain accommodation and their magmatic development is key to understanding continental break-up in Afar.

7.2.2.1 The Dabbahu-Manda Hararo magmatic segment

The age constraints presented in Chapter 4 for the basaltic lavas erupted in the main DMH segment and along the adjacent Badi-Dabbayra transverse volcanic zone provide new information on the formation of both these structures. Although limited in number, the pattern of ages from the main part of the DMH segment, from ~200 ka on the eastern flank to 0 ka for the most recent axial eruptions, provide some key constraints

on the history of volcanic and tectonic processes here. In the region sampled, north of the central Ado Ale volcanic complex on the eastern rift flank, the large fault scarp that separates the rift flank from the axial graben was shown to be younger than ~30 ka. The development of this structure marks an important event in the topographic evolution of the rift zone and this result suggests a non-steady state evolution in rift topography, which may be linked to a period of increased tectonic extension causing graben formation or a reduction in the lava flux. It is unfortunate that the deformation and erosion of lavas on the rift flanks prohibits the identification of individual eruptive fissures and therefore any interpretation of the spatial distribution of sample ages is controversial. However, as shown by the comparison of the observed age-profile to an age-distance curve drawn from the axial graben and based on the current Afro-Arabian extension rate the distribution of ages across the rift flank can be explained by axial emplacement and subsequent transport outwards at ~10 mm yr^{-1}. A regression analysis of the age distance data also produces a similar result. The significance of the new age data is that it provides evidence that volcanic processes have been focused along the DMH axis for at least ~200 ka. It also suggests that the magmatic axis of the rift zone, distinct from the 'topographic' axis in the graben centre and where the recent dykes have been intruded, has been stable in its present location since this time. In the northern part of the rift this axis is located ~1 km east of the graben centre.

The model of rift evolution by Hayward and Ebinger (1996) proposes that the development of mature rift segments results from a narrowing of the region across which magma is intruded and erupted which is driven by a structural response to increasing attenuation of the lithosphere. The lava chronology for the DMH rift is consistent with this melt focusing process (i.e. eruptions focused at the rift axis) and

constrains the formation of the DMH magmatic segment, and therefore the onset of axially focused magmatism, to > 200 ka. If the age model for lavas on the eastern flank is extrapolated to the outer edge of the segment, i.e. to the edge of the older stratoid series lavas, an age of ~800 ka is estimated for the entire DMH segment. Although this is currently speculative and unconstrained by any observational data, this age is consistent with an existing K-Ar age of 757 ± 40 ka, for a lava flow sampled at the outer edge on the opposite margin on the western flank by Lahitte et al (2003). The extension rates observed during the active rifting phase (~2 m yr^{-1} since 2005) demonstrate that axial intrusion is currently a highly effective means of accommodating extension across the DMH rift and it seems likely that since the onset of axially focused magmatism, prior to 200 ka and possibly at 800 ka, that the axial part of the DMH segment has been accommodating essentially all Afro-Arabian extension. This marks a crucial stage in the development of the new plate boundary and tectonic evolution of Afar. Based on the recent activity this would require a rifting event of similar magnitude to the 2005 - 2010 phase every ~500-700 years.

7.2.2.2 Transverse volcanism at Badi-Dabbayra

The Badi-Dabbayra transverse volcanic zone stretches from the margin of the DMH segment to the western scarp separating Afar from the Ethiopian highlands, ~60 km to the west. The age data presented for basaltic lavas erupted in this region record volcanism from ~450 – 25 ka and shows no clear temporal-spatial pattern. It is significant that while volcanism elsewhere has become focused along the DMH segment a melt supply system has also been developed here, feeding contemporaneous eruptions along this volcanic-tectonic lineation. The new age constraints for these lavas are limited to flows sampled near the eastern end of the volcanic lineation, closest to the rift segment and it is unknown how eruption ages may vary further towards the

marginal scarp. However, it may be broadly concluded that volcanism here has been largely coeval with activity along the DMH segment and has been significant only since ~1 Ma. By comparison with analogue models of volcanic loading (i.e. Van wyk de vries and Merle, 1996) it was shown that the emplacement of the Badi edifice may have affected patterns of faulting in the central part of the DMH segment causing faults to deviate from the 'axial trend' and leading the fault and fracture zone that connects the rift segment with the Badi-Dabbayra volcanic lineation.

None of the transverse volcanic zones across Afar are directly related to active extensional processes and the persistence of volcanic activity along these structures, and their association with existing ~EW structures in the regional scarp between Afar and the pre-rift succession, suggests a strong control by lithospheric structures on the melt supply to the crust. The orientation of the transverse zones, approximately perpendicular to the rift axes, is consistent with theoretical models of dyke intrusion along pre-existing fractures (Ziv et al., 2000).

7.3 Melt generation beneath the DMH rift

7.3.1 Basaltic melts

The geochemical data presented for the basaltic (Chapter 5) and silicic (chapter 6) lavas provides an important context to the geological and geochronological observation of volcanism at the rift surface. A significant observation from the geochemical data is that while isotopic compositions show only minor variations across the study area and between compositional varieties, there are clear differences in other chemical features (i.e. major element trends and trace element concentrations) between lavas erupted in each region, implying differing petrogenetic histories. In Chapter 5 it was shown that, following corrections for fractionation, the major and trace element geochemistry of the

basaltic lavas is consistent with melting of fertile mantle with elevated potential temperature at depths near the garnet spinel transition. Melt fractions vary between ~4-6% and higher degree partial melts are consistently erupted in the central rift zone compared to the off-axis volcanoes. This imposes an important constraint that axial lavas are derived from a longer melting column and suggests that the geometry of the melting region in the mantle is contoured to create a focused upwelling beneath the rift segment.

The major element trends for basaltic lavas sampled for each location are distinct and were used to develop a model of melt storage beneath the main rift zone and off-axis volcanoes. Lavas erupted at the rift axis were related to primary melt compositions by a two stage polybaric fractionation regime, with initial melt storage at ~45 km in the upper mantle which supplied fractionated liquids to a shallow magma chamber ~10 km below the rift axis. In contrast the evolutionary trend of the off-axis magmas are consistent with a single fractionation process, which occurs in a storage region near the base of the crust at a depth of ~25 km. These results showed good agreement with the available geophysical constraints on melt storage, particularly the conductivity profile of the crust and upper mantle from the recent MT survey by Johnson et al (in prep).

7.3.2 Silicic melts

Unlike the basaltic activity, rhyolitic volcanism does not appear to be an on-going process in this part of the DMH system and there is no good field evidence for recent silicic eruptions. The one available K-Ar age for a silicic lava dome from Badi of 290 ± 4 ka (Lahitte et al., 2003) may provide a reasonable benchmark for the emplacement of most of the silicic lava encountered in this area, however the chronology of these

eruptions is not currently known. Although not explored in the same detail as the basaltic magmatism, the chemistry of the silicic lavas is most consistent with an origin from extensive shallow fractionation of a basaltic parent. This is similar to the process inferred for melt generation and Dabbahu. In the main part of the rift zone the shallow storage region identified from the basaltic geochemistry provides an obvious location for this low-pressure fractionation process. However, it is unclear where the silicic lavas that form Badi evolved as there is no evidence from either the basaltic chemistry or in the recent MT data for shallow melt storage, at least at the present time. Although not based on a detailed investigation, the difference in chemistry between the evolved lavas from Badi and Ado Ale Complex, mirroring those of the basaltic lavas, seemingly precludes a common source region for these and this issue remains unresolved. It is notable that the relatively large volumes of rhyolitic products that comprise Badi and the AVC have been erupted in a consistently effusive manner and it is uncommon for rhyolitic volcanoes not to be associated with collapse structures.

7.4 Linking source to surface processes

The recent dyke intrusions in the DMH segment demonstrate that magmatism plays a key role in maintaining extension here and is closely linked to the topographic development of the segment (Rowland et al., 2007). An important distinction that has been made between segmented rift zones in the Main Ethiopian rift and mid ocean ridge segments is that the former do not correlate with focused mantle upwellings (Bastow et al., 2005, 2008; Rooney et al., 2011). This is an important observations at it implies that melt focusing to the rift segments is originally controlled by lithospheric structures and processes (e.g. Corti, 2008). However, as rift segments evolve towards ocean ridges they must at some stage begin to influence the flow of the shallow sub-lithospheric

mantle. An important link can be made between the evidence for a focused neo-volcanic zone in the rift axis (compared to the off-axis eruptions) and the results from the petrogenetic model suggesting that axial lavas are the products of greater extents of mantle melting. It is unlikely that mantle solidus depth varies between these regions and it is more likely that the variation in melt fractions indicates that the top of the melting region is contoured to create a longer melting column beneath the axis. Although the difference in melt fraction in the model in Chapter 5 is relatively small (~2 %) it is a consistent feature seen in all the lavas erupted in each area and could be used as evidence for the initial stages of development of a focused mantle upwelling correlated with the DMH magmatic segment. The physical processes of lava emplacement at the rift surface bears many similarities to eruptions at Icelandic rift zones and slow spreading oceanic rifts and the volcanic architecture of the DMH segment is more similar to these environments than to continental rift zones elsewhere, including those found along the segmented (most mature) part of the MER axis (e.g. Rooney et al., 2011).

A significant result from the geochemical analyses is that, despite their relative proximity and structural connection via a zone of faulting and fractures, there is a clear difference in the composition of lava erupted in the main DMH segment and at the off-axis volcanoes. Although it has been proposed that it is lithospheric structures that control the supply of melts to the Badi-Dabbayra lineation, separate magma plumbing systems are seemingly maintained for melts erupted in each location. The results from geochronological analyses show that these different compositional varieties were being erupted simultaneously ~20 km apart and there exists a strong association between volcano-tectonic structures at the surface and the melt supply from depth.

7.5 Future investigations

This thesis has provided an overview of various aspects of the magmatism and volcanism at the DMH segment and presents important constraints on melt generation processes and the volcanic-tectonic history of the rift zone and adjacent volcanoes. There are many ways in which these themes can be developed by future research on melting processes, melt storage and differentiation, and the chronology of volcanism and faulting and there exists great potential for integrating the data in this thesis, and from future studies, with several ongoing geophysical investigations of the DMH system.

The geochronological data presented here are limited by sample availability and the analytical complexities associated with geochronology of young lavas and it would be a worthwhile endeavor to expand this dataset. This should be partly achieved by ongoing work on exposure dating of lava flow surfaces and fault scarps in the axial region by Williams et al (2008, 2009) and this work will provide valuable constraints on the chronology of faulting and volcanism. Integrating the geochronological data with results from structural analysis of high-resolution topographic data currently being undertaken by Hofmann et al (2010) has the potential to develop an integrated understanding of the processes of volcanic accretion and fault growth in the DMH rift segment.

Further research on melting process should seek to integrate the results from geochemical studies with seismic data on mantle structure currently being analysed at the University of Bristol. Important information on melt generation can also be derived from understanding melting rates and the geochemical dataset for the samples presented in this thesis is currently being expanded through analyses of uranium-series isotopes.

The interpretation of this new isotopic data requires constraints on melting processes and source compositions and the results presented in chapter 5 provide an important background for understanding this new data. A further potential avenue for integrating seismic and geochemical studies is to investigate the effects of active mantle upwelling beneath Afar on melting processes and the implication for the growth and structure of the crust.

As noted above, the extent of effusive rhyolitic volcanism in this region is unusual and a more detailed study of the geochemistry, petrography and physical volcanology of the silicic lavas from Badi and the AVC may provide important insights in understanding the generation and eruption of effusive rift-related rhyolitic lavas. Furthermore, although Afar is a key region for understanding continental break-up, the entire geochemical dataset for lavas of all compositions from across the region, particularly with regards to high quality isotopic and trace element analyses, remains very limited. It would therefore be of great benefit to improve this situation with further analytical work on other lava suites either from other parts of the DMH segment or from other Afar rift segments, which apart from the Erta Ale and Asal-Ghoubbet rift zones, are largely absent from the current geochemical catalogue.

Finally, although the intensity of intrusive activity in the DMH segment has now reduced from the peak period of dyke intrusion and eruptions during 2005 - 2009, the evidence from the final years of the Krafla rifting phase suggests that should a sufficient volume of melt still reside beneath the rift segment it is in the period following the major intrusive phase that further and potentially larger eruptions may occur. Although the hazard posed by these events is relatively modest due to the low population density

in the rift centre, this region should continue to be monitored. From a geochemical perspective, analyses of fresh lava samples from future eruptions could be used along with existing samples from the 2007 and 2009 eruptions to investigate the short-term compositional evolution and crystallisation processes in the sub-rift magma chamber.

References

Abdallah, A., Courtillot, V., Kasser, M., Le Dain, A.Y., Lépine, J.C., Robineau, B., Ruegg, J.C., Tapponnier, P., Tarantola, A., 1979, Relevance of Afar seismicity and volcanism to the mechanics of accreting plate boundaries. Nature, 282, 17–23

Acocella, V., 2006. Regional and local tectonics at Erta Ale caldera, Afar (Ethiopia). Journal of Structural Geology, 28, 10, 1808-1802

Acocella, V., 2010. Coupling volcanism and tectonics along divergent plate boundaries: Collapsed rifts from central Afar, Ethiopia. Geological Society of America Bulletin, 122, 1717-1728

Acocella, V., Abebe, B., Korme, T., Barberi, F., 2008. Structure of Tendaho Graben and Manda Hararo Rift: Implications for the evolution of the southern Red Sea propagator in Central Afar. Tectonics, 27, TC4016

Altherr, R., Henjes-Kunst, F., Baumann, A., 1990. Asthenosphere versus lithosphere as possible sources for basaltic magmas erupted during formation of the Red Sea: Constraints from Sr, Pb and Nd isotopes. Earth Planetary Science Letters, 96, 269-286.

Annen, C., Blundy, J. D., Sparks, R. S. J. 2006. The genesis of intermediate and silicic magmas in deep crustal hot zones. Journal of Petrology, 47, 3, 505-539

Armitage, J. J., Henstock, T. J.. Minshull, T. A., Hopper, J. R. 2009. Lithospheric controls on melt production during continental breakup at slow rates of extension: Application to the North Atlantic, Geochemistry Geophysics Geosystems, 10, Q06018

Audin, L., Quidelleur, X., Coulié, E., Courtillot, V., Gilder, S., Manighetti, I., Gillot, P.-Y., Tapponnier, P., Kidane, T. 2004. Palaeomagnetism and K-Ar and 40Ar/39Ar ages in the Ali Sabieh area (Republic of Djibouti and Ethiopia): constraints on the mechanism of Aden ridge propagation into southeastern Afar during the last 10 Myr. Geophysical Journal International, 158: 327–345.

Ayalew, D., Gibson, S. A. 2009. Head-to-tail transition of the Afar mantle plume: Geochemical evidence from a Miocene bimodal basalt-rhyolite succession in the Ethiopian Large Igneous Province. Lithos, 112 3-4, 461-476.

Ayalew, D., Yirgu, G., 2003. Crustal contribution to the genesis of Ethiopian plateau rhyolitic ignimbrites: basalt and rhyolite geochemical provinciality, Journal of the Geological Society of London, 160, 47–56.

Ayele, A., Jacques, E., Kassim, M., Kidane, T., Omar, A., Tait, S., Nercessian, A., de Chabalier, J.B., King, G., 2007. The volcano-seismic crisis in Afar, Ethiopia, starting September 2005. Earth and Planetary Science Letters, 255, 177–187

Baker, J.A., Thirlwall, M.F., Menzies, M.A., 1996. Sr – Nd – Pb isotopic and trace element evidence for crustal contamination of plume-derived flood basalts: oligocene flood volcanism in western Yemen. Geochimica Cosmochimica Acta, 60, 2559–2581

Baker, J. A., Cahzot, G., Menzies, M. A., Thriwall, M. 2002. Lithospheric mantle beneath Arabia: A Pan-African protolith modified by the Afar and older plumes, rather than a source for continental flood volcanism? In: Menzies, M. A., Klemperer, S. L., Ebinger, C., Baker, J. Volcanic Rifted Margins, Geological Socitey of America Special Paper, 362 65-80

Barberi, F., Santacroce, R. 1980. The Afar Stratoid Series and the magmatic evolution of the East African rift system: Bulletin de la Société Geologique de France, 6, 891–899.

Barberi, F., Tazieff, H., Varet, J., 1972. Volcanism in the Afar depression: its tectonic and magmatic significance. Tectonophysics, 15, 19–29.

Barberi, F., Varet, J., 1970. The Erta `Ale volcanic range. Bulletin Volcanologique, 34, 848- 917.

Barberi, F., Varet, J., 1977. Volcanism in Afar: small-scale plate tectonic implications, Bulletin of the Geological Society of America, 88, 1251–1266.

Barberi, F., Varet, J., 1975. Recent volcanic units of Afar and their structural significance. In: A. Pilger and A. Rosler, Editors, Afar depression of Ethiopia, proceedings of an international symposium on the Afar region and rift related problems, Bad Bergzabren, Germany, 1974, vol. 1, E. Schweizerbart'sche Verlagsbuchhandlung, Stuttgart, Germany, 174–178.

Barberi, F., Borsi, S., Ferrara, G., Marinelli, G., Varet, J., 1970. Relations between tectonics and magmatology in the northern Danakil Depression (Ethiopia). Philosophical Transactions of the Royal Society of London, A267, 293 – 311.

Barberi, F. Bonati, E., Marinelli, G., Varet, J., 1974. Transverse tectonic during the split of continent: Data from the Afar rift. Tectonophysics, 23, 17–19.

Barberi, F., S. Borsi, G. Ferrarea, G. Marinelli, R. Santcroce, H. Tazief., J. Varet., 1972. Evolution of the Danakil Depression (Afar Ethiopia) in light of radiometric age determination. Journal of Geology, 80, 720–729.

Barberi, F., Ferrara, G., Santacroce, R., Treuil. M., Varet, J., 1975. A transitional basalt-pantellerite sequence of fractional crystallisation, the Boina centre (Afar rift, Ethiopia). Journal of Petrology, 16, 22–56.

Barisin, I., Leprince, S., Parsons, B., Wright, T., 2009. Surface displacements in the September 2005 Afar rifting event from satellite image matching: Asymmetric uplift and faulting. Geophysical Research Letters, 36, 7.

Barnie, T., Oppenhiermer, C., 2010 Estimating lava effusion rates from high temporal resolution satellite image time series. [abstract]. Geophysical Research Abstracts, 12, EGU2010-6895

Barrat, J.A., Jahn, B.M., Joron, J.L., Auvray, B., Hamdi, H., 1990. Mantle heterogeneity in Northeastern Africa: evidence from Nd isotopic compositions and hygromagmaphile element geochemistry of basaltic rocks from the Gulf of Tadjoura and Southern Red Sea regions. Earth and Planetary Science Letters, 101, 233–247.

Barrat, J.A., Jahn, B.M., Fourcade, S., Joron, J.L., 1993. Magma genesis in an ongoing rifting zone: the Tadjoura Gulf. Geochimica Cosmochimica Acta, 57, 2291–2302.

Barrat, J.A., Fourcade, S., Jahn, B.M., Chemine´e, J.L., Capdevila, R., 1998. Isotope (Sr, Nd, Pb, O) and trace-element geochemistry of volcanics from the Erta' Ale range (Ethiopia). Journal of Volcanology and Geothermal Research, 80, 85–100.

Barrat, J.A., Joron, J.L., Taylor, R.N., Fourcade, S., Nesbitt, R.W., Jahn, B.M., 2003. Geochemistry of basalts from Manda Hararo, Ethiopia: LREE-depleted basalts in Central Afar. Lithos, 69, 1-13

Bastow, I., Keir, D., 2011. The protracted development of the continent–ocean transition in Afar. Nature Geoscience, 4, 248-250

Bastow, I., Stuart, G.W., Kendall, J.-M., Ebinger, C., 2005. Upper mantle seismic structure in a region of incipient continental breakup: northern Ethiopian rift. Geophysical Journal International, 162, 479–493.

Bastow, I.D., Nyblade, A.A., Stuart, G.W., Rooney, T.O., Benoit, M.H., 2008. Upper mantle seismic structure beneath the Ethiopian hot spot: Rifting at the edge of the African low-velocity anomaly. Geochemistry, Geophysics, Geosystems, 9, 12, Q12022

Beattie, P., 1993. Olivine-melt and orthopyroxene-melt equilibria. Contributions to Mineralogy and petrology, 115, 103-111

Behle, A., Makris, J., Baier B., Delibassis N., 1975. Salt thickness near Dallol (Ethiopia) from seismic reflection measurements and gravity data. Pilger, A., Rösler, A., (Editors). Afar Depression of Ethiopia, Vol. I Schweizerbart, Stuttgart, 156–167.

Bendick, R., McClusky, S., Bilham, R., Asfaw, L., Klemperer, S., 2006. Distributed Nubia–Somalia relative motion and dike intrusion in the Main Ethiopian Rift. Geophysical Journal International, 165, 1, 303–310.

Belachew, M., Ebinger, C., Cote, D., Keir, D., Rowland, J. V., Hammond, J. O. S., Ayele, A., 2011, Comparison of dike intrusions in an incipient seafloor-spreading segment in Afar, Ethiopia: Seismicity perspectives. Journal of Geophysical Research, 116, B06405,

Betton, P.J., Civetta, L., 1984. Strontium and neodymium isotopic evidence for the heterogeneous nature and development of the mantle beneath Afar (Ethiopia). Earth and Planetary Science Letters, 71, 59–70.

Beyene, A., Abdelsalam, M., 2005. Tectonics of the Afar Depression: A review and synthesis. Journal of African Earth Sciences, 41, 41-59.

Berhe, S.M., Desta, B., Nicoletti, M., Teferra. M., 1987. Geology, geochronology and geodynamic implications of Cenozoic magmatic province in W and SE Ethiopia, Journal of the Geological Society of London, 144, 213–226

Berckhemer, H., Baier, B., Barteisen, H., Behle, A., Burkhardt, H., Gebrande, H., Makris, J., Menzel, H., Miller H., Vees, R., 1975. Deep seismic soundings in the Afar region and on the highland of Ethiopia, Pilger, A., Rösler, A., (Editors). Afar Depression of Ethiopia, Vol. I Schweizerbart, Stuttgart, 89–107.

Bertrand, H., Chazot, G., Blichert-Toft, J., Thoral, S., 2003. Implications of widespread HIMU volcanism on the Arabian Plate for the composition of the Afar mantle plume and lithosphere. Chemical Geology, 198, 47-61.

Beutel, E., Jan Wijk, J., Ebinger, C., Keir D., Agostini A., 2010. Formation and stability of magmatic segments in the Main Ethiopian and Afar Rifts. Earth and Planetary Science Letters, 298, 225-235.

Bilham, R., Bendick, R., Larson, K., Mohr, P., Braun, J., Tesfaye, S., Asfaw, L., 1999. Secular and tidal strain across the Main Ethiopian Rift. Geophysical Research Letters, 26, 18, 2789–2792

Bizourd, H., barberi, F., Varet, J., 1979. Mineralogy and Petrology of Erta Ale and Boina Volcanic Series, Afar Rift, Ethiopia. Journal of Petrology, 21, 2, 401-436

Bjornsson, A., Saemundsson, K., Einarsson, P., Tryggvason, E., Gronvald, K., 1977. Current rifting episode in North Iceland. Nature, 266, 318–323.

Bjornsson, A., Johnsen, G., Sigurdsson, S., Thorbergsson, G., Tryggvason, E., 1979. Rifting of a plate boundary in North Iceland 1975–1978. Journal of Geophysical Research, 84, 3029–3038.

Black, S., Macdonald, R., Kelly, M. R., 1997. Crustal origin of peralkaline rhyolites from Kenya: evidence from U-series disequilibria and Th-isotopes. Journal of Petrology, 38, 277–297.

Blundy, J. D., Wood, B. J., 1994. Prediction of crystal-melt partition coefficients from elastic moduli. Nature, 372, 452-454

Blundy, J. D., Robinson, J. A.C., Wood, B. J., 1998. Heavy REE are compatible in clinopyroxene on the spinel lherzolite solidus'. Earth Planetary Science Letters, 160, 493-504

Boccaletti, M., Getaneh, A., Mazzuoli, R., Tortorici, L., Trua, T., 1995. Chemical variations in a bimodal magma system; the Plio-Quaternary volcanism in the Dera Nazret area (Main Ethiopian Rift, Ethiopia). Africa Geoscience Review 2, 1, 37–60.

Buck W. R., 2004. Consequences of asthenospheric variability on continental rifting. In Rheology and Deformation of the Lithosphere at Continental Margins. Karner, D., Taylor, B., Driscoll, N., Kohlstedt, B., (Editors) 92–137. New York: Columbia Univ. Press

Buck, W. R., 2006. The role of magma in the development of the Afro-Arabian Rift System, in The Afar Volcanic Province within the East African Rift System. Yirgu, G., Ebinger, C. J., Maguire, P. K. H. (Editors) Geological Society of London Special Publication, 259, 43-54.

Buck, W.R., Einarsson, P., Brandsdottir , B., 2006. Tectonic stress and magma chamber size as controls on dike propagation: Constraints from the 1975–1984 Krafla rifting episode. Journal of Geophysical Research, 111, B12404

Calvert, A. T., Lanphere, M. A., 2006. Argon geochronology of Kilauea's early submarine history. Journal of Volcanology and Geothermal Research, 151, 1-3

Casey, M., C. Ebinger, D. Keir, R. Gloaguen., Mohamed. F., 2006. Strain accommodation in transitional rifts: Extension by magma intrusion and faulting in Ethiopian rift magmatic segments, in The Afar Volcanic Province within the East African Rift System. Yirgu, G., Ebinger, C. J., Maguire, P. K. H. (Editors) Geological Society of London Special Publication, 259, 143-164.

Cattin, R., Doubre, C., De Chabalier, J-B., King, G., Vigny, C., Avouac, J-P., Ruegg, J-C., 2005. Thermo-mechanical modelling of quaternary deformation and post-seismic displacement in the Asal-Ghoubbet (Djibouti, Afar). Earth and Planetary Science Letters, 239, 352–367.

Chadwick, W.W., Embley, R.W., Fox, C.G., 1995. SeaBeam depth changes associated with recent lava flows, Co-Axial segment, Juan de Fuca Ridge: Evidence for multiple eruptions between 1981–1993. Geophysical Research Letters, 22, 167–170

Chazot, G., Bertrand, H., 1993. Mantle sources and magma-continental crust interactions during early Red Sea–Aden rifting in Southern Yemen: elemental and Sr, Nd, Pb isotope evidence. Journal of Geophysical Research, 98, 1819–1835.

Chen, C.Y., Frey, F.A., Rhodes, J.M., Easton, R.M., 1996. Temporal geochemical evolution of Kilauea Volcano: comparison of Hilina and Puna Basalt. In: Basu, A., Hart, S.R. (Editors). Earth Processes: Reading the Isotopic Code. Geophysical Monograph 95, 161–181.

Chernet, T., Hart, W.K., Aronson, J.L., Walter, R.C., 1998. New age constraints on the timing of volcanism and tectonism in the northern Main Ethiopian Rift—Southern Afar transition zone (Ethiopia). Journal of Volcanology and Geothermal Research, 80, 267–280.

Chu, D., Gordon, R.G., 1998. Current plate motions across the Red Sea. Geophysical Journal International, 135, 313–328.

Civetta, L., De Fino, M., La Volpe L., Lirer, L., 1974. Geochemical trend in the alkali basaltic suite of the Assab range (Ethiopia). Chemical Geology, 13, 149-162

Civetta, L., D'Antonio, M., Orsi, G., Tilton, G. R., 1998. The geochemistry of volcanic rocks from Pantelleria island, Sicily Channel: petrogenesis and characteristics of the mantle source region. Journal of Petrology, 39, 1453 -1491.

Clocchiatti, R., Métrich, N., Weiss, J., 1980. Petrologie et mineralogie des basaltes d'Asal, Afar: Bulletin CNRS-PIRPSEV (Centre National de la Recherche Scientifique, Prévision et Surveillance des Eruptions Volcaniques), no. 10, 18 p

CNR - CNRS Afar team., 1973. Geology of northern Afar (Ethiopia). Revue de Geographie Physique et de Geologie Dynamique, 15, 443- 490.

Cole, J.W., 1969. Gariboldi Volcanic Complex, Ethiopia. Bulletin Volcanologique, 33, 566–578.

Corti, G., 2008. Control of rift obliquity on the evolution and segmentation of the main Ethiopian rift. Nature Geoscience, 1, 258-262

Cornwell, D., Mackenzie, G., England, R., Maguire, P., Asfaw, L., Oluma, B., 2006. Northern Main Ethiopian rift crustal structure from new high-precision gravity data, in The Afar Volcanic Province within the East African Rift System. Yirgu, G., Ebinger, C. J., Maguire, P. K. H. (Editors) Geological Society of London Special Publication, 259, 307-321.

Cornwell, D. G., Maguire, P. K. H., England, R. W., Stuart, G. W., 2010. Imaging detailed crustal structure and magmatic intrusion across the Ethiopian Rift using a dense linear broadband array. Geochemistry Geophysics Geosystems, 11, Q0AB03, 22, 20

Courtillot, V., Jaupart, C., Manighetti, I., Tapponnier, P., Bess, J., 1999. On causal links between flood basalts and continental breakup. Earth and Planetary Science Letters, 166, 3-4, 177-195

Dainelli, G., 1943. Geologia dell' Africa orientale. Roma: R. Accad. d'Italia

Daly, E., Keir, D., Ebinger, C. J., Stuart, G. W., Bastow, I. D., Ayele, A., 2008. Crustal tomographic imaging of a transitional continental rift: the Ethiopian rift. Geophysical Journal International, 172, 3, 1033 – 1048,

Dalrymple, G.B., 1989. The GLM continuous laser system for 40Ar/39Ar dating; description and performance characteristics, in Shanks, W.C., III, and Criss, R.E., (Editors). New frontiers in stable isotopic research; laser probes, ion probes, and small- sample analysis: U.S. Geological Survey Bulletin 1890, 89-96

Dalrymple, G.B., Clauge, D. A., 1976. Age of the Hawaiian-Emperor bend. Earth and Planetary Science Letters, 31, 3, 313-329

Dalrymple, G.B., Duffield, W.A., 1988. High precision 40Ar/39Ar dating of Oligocene rhyolites from the Mogollon-Datil volcanic field using a continuous laser system. Geophysical Research Letters, 15, 463-366,

Dalrymple, G.B., Alexander E.C., Jr., Lanphere, M.A., Kraker, G.P., 1981, Irradiation of samples for 40Ar/39Ar dating using the Geological Survey TRIGA reactor. US Geological Survey Professional Paper 1176.

Danyushevsky, L. V., 2001. The effect of small amounts of H2O on crystallisation of mid-ocean ridge and backarc basin magmas. Journal of Volcanology and Geothermal Research, 110, 265–280

Danyushevsky, L. V., Plechov, P., 2011. Petrolog3: Integrated software for modeling crystallization processes. Geochemistry Geophysics Geosystems, 12, Q07021,

Davis, P., Slack, P., 2002. The uppermost mantle beneath the Kenya dome and relation to melting, rifting and uplift in East Africa. Geophysical Research Letters, 29, 1117 - 1120

De Chabalier, J.-B., Avouac, J. P., 1994. Kinematics of the Asal Rift (Djibouti) determined from the deformation of Fieale Volcano. Science, 265, 1677–1681.

De Fino, M., La Volpe L., Lirer, L., 1973. Volcanology and petrology of the Assab Range (Ethiopia). Bulletin of Volcanology, 37, 1, 95-110

Deniel, C., Vidal, P., Coulon, C., Vellutini, P.J., 1994. Temporal evolution of mantle sources during continental rifting—The volcanism of Djibouti (Afar). Journal of Geophysical Research, 99, 2853–2869.

Donnelly, K. E., Goldstein, S. L., Langmuir, C. H., Spiegleman, M., 2004. Origin of enriched ocean ridge basalts and implications for mantle dynamics. Earth and Planetary Science Letters, 226, 347-366

Draxler, R.R., Rolph, G.D., 2003. HYSPLIT (HYbrid Single-Particle Lagrangian Integrated Trajectory) Model access via NOAA ARL READY Website (http://www.arl.noaa.gov/ready/hysplit4.html). NOAA Air Resources Laboratory, Silver Spring, MD.

Dupre, B., Blanc, G., Boulegne, J., Allegre, C.J., 1988. Metal mobilization at a spreading centre studied using lead isotopes. Nature 333, 165-167.

Eagles, G., Gloaguen, R., Ebinger, C., 2002. A model for the creation of a microplate: kinematics of the Danakil microplate. Earth and Planetary Science Letters, 203, 607–620.

Einarsson, P., 1991. The Krafla rifting episode 1975–1989. In: Gardarsson, A., Einarsson, P., (Editors.) N´att´ura Myvatns, The Nature of Lake Myvatn. Icelandic Nature Science Society, Reykjavic, 97–139

Eissen, J. L., Juteau, T., Joron, J. L., Dupre, B., Humler, E., Al'Mukhamedov, A.I., 1989. Petrology and geochemistry of the basalts from the axial rift of the Red Sea at 18°N. Journal of Petrology, 30, 791-839

Ebinger, C. J., 2005. Continental breakup: The East African Perspective. Astronomy & Geophysics, 46, 2 2.16-2.21

Ebinger, C., Sleep, N., 1998. Cenozoic magmatism throughout East Africa resulting from impact of a single plume. Nature, 395, 788.

Ebinger, C., Keir, D., Ayele, A., Calais, E., Wright, T., Belachew, M., Hammond, J., Campbell, E., Buck, R., 2008. Capturing magma intrusion and faulting processes during continental rupture: Seismicity of the Dabbahu Afar rift. Geophysical Journal International, 174, 1138 – 1152

Ebinger, C. J., Ayele, A., Keir, D., Rowland, J. V., Yirgu, G., Wright, T., Belachew, M., Hamling, I., 2010. Length and time scales of rift faulting and magma intrusion: The Afar rifting cycle from 2005 to present. Annual Reviews in Earth and Planetary Science, 38, 437–464

Embley, R.W., Chadwick, W.W., Clague, D.A., Stakes, D., 1999. 1998 eruption of Axial Volcano: Multibeam anomalies and sea-floor observations. Geophysical Research Letters, 26, 3425–3428

Embley, R.W., Chadwick, W.W., Perfit, M.R., Smith, M.C., Delaney, J.R., 2000. Recent eruptions on the CoAxial segment of the Juan de Fuca Ridge: Implications for mid-ocean ridge accretion processes. Journal of Geophysical Research, 105, 16,501– 16,526

Ewart, J.A., Voight, B., Bjornsson, A., 1991. Elastic deformation models of Krafla Volcano, Iceland, for the decade 1975 through 1985. Bulletin of Volcanology, 53, 436–459.

Feigenson, M.D., Bolge, L.L., Carr, M.J., Herzberg, C.T., 2003. REE Inverse Modeling of HSDP2 Basalts: Evidence for Multiple Sources in the Hawaiian Plume. Geochemistry Geophysics Geosystems, 4, 806

Ferguson, D.J., Barnie, T.D., Pyle, D.M., Oppenheimer, D., Yirgu, G., Lewi, E., Kidane, T., Carn, S., Hamling, I., 2010. Recent rift-related volcanism in Afar, Ethiopia. Earth and Planetary Science Letters, 292, 409-418

Field, L., 2011. The magmatic evolution of Dabbahu volcano, and the 2010 eruption of Erta Ale, Afar, Ethiopia. PhD Thesis, University of Bristol, UK

Field, L., Barnie, T.D., Blundy, J.D., Keir, D., Lewi, E., Saunders, K., Submitted. The November 2010 eruption of Erta Ale: ground, satellite and petrological observations. Submitted to Earth and Planetary Science Letters

Fink, J. H., 1983. Structure and emplacement of a rhyolitic obsidian flow: Little Glass Mountain, Medicine Lake Highland, northern California. Bulletin of the Geological Society Of America, 94, 3, 362-380

Fowler, M. R. C., 1990. The Solid Earth: An Introduction to Global Geophysics, Cambridge University Press, Cambridge, 1990, 283

Furman, T., 2007. Geochemistry of East African Rift basalts: an overview. Journal of African Earth Sciences. Journal of African Earth Sciences, 48, 147–160

Furman, T., Bryce, J., Rooney, T., Hanan, B., Yirgu, G., Ayalew, D., 2006. Heads and Tails: 30 million years of the Afar plume. in The Afar Volcanic Province within the East African Rift System. Yirgu, G., Ebinger, C. J., Maguire, P. K. H. (Editors) Geological Society of London Special Publication, 259, 95-119

Frey, F. A., Pringle, M., Meleney, P., Huang, S., Piotrowski, A., 2011. Diverse mantle sources for Ninetyeast Ridge magmatism: Geochemical constraints from basaltic glasses. Earth and Planetary Science Letters, 303, 215-224

Gazel, E., Hoernle, K., Carr, M. J., Herzberg, C., Saginor, I., van den Bogaard, P., Hauff F., Feigenson, M., Swisher, C., 2011. Plume–subduction interaction in southern Central America: Mantle upwelling and slab melting. Lithos, 121, 117.134

George, R., Rogers, N., 1999. The petrogenesis of Plio-Pleistocene alkaline volcanic rocks from the Tosa Sucha region, Arba Minch, southern Main Ethiopian Rift. Acta Vulcanologica, 11, 1. 121–130.

George, R., Rogers, N., Kelley, S., 1998. Earliest magmatism in Ethiopia: Evidence for two mantle plumes in one flood basalt province. Geology, 26, 923–926.

Ghiorso, M. S., Sack, R. O., 1995. Chemical transfer in magmatic processes: IV. A revised and internally consistent thermodynamic model for the interpolation and extrapolation of liquid–solid equilibria in magmatic system at elevated temperatures and pressures. Contributions to Mineralogy and Petrology, 119, 197–212

Gibson, I. L., 1975. A review of the geology, petrology and geochemistry of the volcano Fantale. Bulletin of Volcanology, 38, 2 791-802

Goldstein, S. J., Perfit, M. R., Batixa, R., Fornari, D. J., Murrell, M. T., 1994. Off-axis volcanism at the East Pacific Rise detected by uranium-series dating of basalts. Nature, 367, 157-159

Grandin, R., Socquet, A., Binet, R., Klinger, Y., Jacques, E., de Chabalier, J.B., King, G.C.P., Lasserre, C., Tait, S., Tapponier, P., Delorme, A., Pinzuti, P., 2009. September 2005 Manda Hararo-Dabbahu rifting event, Afar Ethiopia: Constraints provided by geodetic data. Journal of Geophysical Research, 114, B08404

Grandin, R., Socquet, A., Doin, M.-P., Jacques, E., de Chabalier, J.-B., King, G. C. P., 2010. Transient rift opening in response to multiple dike injections in the Manda Hararo rift (Afar, Ethiopia) imaged by time-dependent elastic inversion of interferometric synthetic aperture radar data. Journal of Geophysical Research, 115, B09403,

Gualda G. A. R., Ghiorso M. S., Lemons R. V., Carley T. L. (submitted) Rhyolite-MELTS: A modified calibration of MELTS optimized for silica-rich, fluid-bearing magmatic systems. Submitted to Journal of Petrology.

Gurnis, M., Mitrovica, J.X., Su, W.J. van Heijst, H. 2000. Constraining mantle density structure using geological evidence of surface uplift rates: The case of the African plume. Geochemistry Geophysics Geosystems, 1, 7, 1999GC000035

Halliday A., Lee D-C., Tommasini, S., Davies, G. R., Paslick, C. R.,Fitton, G. J., James, D. E., 1995. Incompatible trace elements in OIB and MORB and source enrichment in the sub-oceanic mantle. Earth and Planetary Science Letters, 133, 379-395.

Hamling, I. J., Ayele, A., Bennati, L., Calais, E., Ebinger, E.J., Keir, D., Lewi, E., Wright, T., Yirgu, G., 2009. Geodetic observations of the ongoing Dabbahu rifting episode: new dyke intrusions in 2006 and 2007. Geophysical Journal International, 178, 989-1003

Hammond, J. O. S., Kendall, J-M., Stuart, G. W., Keir, D., Ebinger, C., Ayele, A., Belachew, M., 2011. The nature of the crust beneath the Afar triple junction: evidence from receiver functions. Geochemistry Geophysics Geosystems. in press

Harris, A. J. L., Murray, J. B., Aries, S. E., Davies, M. A., Flynn, L. P., Wooster, M. J., Wright, R., Rothery, D. A., 2000. Effusion rate trends at Etna and Krafla and their implications for eruptive mechanisms. Journal of Volcanology and Geothermal Research, 102, 237-270

Hart, S. R., Blusztajn, J., 2006. Age and geochemistry of the mafic sills, ODP site 1276, Newfoundland margin. Chemical Geology, 235, 3-4, 15, 222-237

Hart, S. R., Workman, R. K., Ball, L., Blusztajn, J., 2004. High precision Pb isotope techniques from the WHOI NEPTUNE PIMMS. WHOI Plasma Facility Open File Technical Report 10

Hart, W. K., Woldegabriel, G., Walter, R. C., Mertzman, S. A., 1989. Basaltic volcanism in Ethiopia: constraints on continental rifting and mantle interactions. Journal of Geophysical Research, 94, 7731–7748.

Hart, W. K, Walter, R., WoldeGabriel, G., 1992. Tephra sources and correlations in Ethiopia: Application of elemental and neodymium isotope data. Quaternary International, 13-14, 1992, 77-86

Haase, K. M., Muhe, R., Stoffers, P., 2002. Magmatism during extension of the lithosphere: geochemical constraints from lavas of the Shaban Deep, northern Red Sea. Chemical Geology, 166, 225–239

Hayward, N. J., Ebinger, C. J., 1996. Variations in the along-axis segmentation of the Afar Rift System. Tectonics, 15, 244–257

Heizler, M. T., Perry, F. V., Crowe, B. M., Peters, L., Appelt, R., 1999. The age of Lathrop Wells volcanic center: An 40Ar/39Ar dating investigation, Journal of Geophysical Research, 104, B, 761-804

Herzberg, C., 2006. Petrology and thermal structure of the Hawaiian plume from Mauna Kea volcano. Nature, 444, 605–609.

Herzberg, C., Asimow, P.D., 2008. Petrology of some oceanic island basalts: PRIMELT2. XLS software for primary magma calculation. Geochemistry Geophysics Geosystems, 9, Q09001.

Herzberg, C., Gazel, E., 2009. Petrological evidence for secular cooling in mantle plumes. Nature, 458, 619–683.

Herzberg, C., O'Hara, M.J., 2002. Plume-associated ultramafic magmas of Phanerozoic age. Journal of Petrology, 43, 1857–1883.

Herzberg, C., Asimow, P.D., Arndt, N., Niu, Y., Lesher, C.M., Fitton, J.G., Cheadle, M.J., Saunders, A.D., 2007. Temperatures in ambient mantle and plumes: constraints from basalts, picrites, and komatiites. Geochemistry Geophysics Geosystems, 8, Q02006.

Hofmann A. W., Jochum K. I., Seufert M., White W. M., 1986. Nb and Pb in oceanic basahs: new constraints on mantle evolution. Earth and Planetary Science Letters, 79, 33-45.

Hofmann, B., Wright, T. J., Rowland, J. V., Paton, D. A., Abebe, B., 2010. Analysing fault growth at the continental break up zone in Afar, Ethiopia. Abstract. EOS Transaction of AGU, Fall Meeting 2010, T31B-2156

Hofman, C., Courtillot, V., Feraud, G., Rochette, P., Yirgu, G., Ketefo, E., Pik, R., 1997. Timing of the Ethiopian flood basalt event and implications for plume birth and global change. Nature, 389, 6653, 838–841.

Holloway, J. R., Burnham C. W., 1972. Melting relations of basalt with equilibrium water pressure less than total pressure. Journal of Petrology, 13, 1–29

Huneke., J. C., Smith, S. P., 1976. The realities of recoil: 39Ar recoil out of small grains and anomalous patterns in 39Ar-40Ar dating. Geochimica Cosmochimica Acta, Supplement 7 (Proceedings of the Seventh Lunar Science Conference), 1987-2008.

Irvine T. N., Baragar, W. R. A., 1971. A guide to the chemical classification of the common volcanic rocks. Canadian Journal of Earth Sciences, 8, 5, 523-548,

Ito, G., Shen, Y., Hirth, G., Wolfe, C. J., 1999. Mantle flow, melting, and dehydration of the Iceland mantle plume. Earth and Planetary Science Letters, 165 81-96.

Johnson, J. S., Gibson, S. A., Thompson, R. N., Nowell, G. M., 2005. Volcanism in the Vitim volcanic field, Siberia: geochemical evidence for a mantle plume beneath the Baikal Rift zone. Journal of Petrology, 46, 7, 1309-1344.

Kawamoto, T., 1996. Experimental constraints on differentiation and H2O abundance of calc-alkaline magmas. Earth and Planetary Science Letters, 144, 577–589

Kebede, T., Koeberl, C., Koller, F., 1999. Geology, geochemistry and petrogenesis of intrusive rocks of the Wallagga area, western Ethiopia. Journal of African Earth Sciences, 29, 4 715–734.

Keir, D., Hamling, I., Ayele, A., Calais, E., Ebinger, C., Wright, T.J., Jacques, E., Mohammed, K., Hammond, J.O.S., Belachew, M., Baker, E., Rowland, J.V., Lewi, E., Bennati, L., 2009. Evidence for focused magmatic accretion at segment centers from lateral dike injections captured beneath the Red Sea rift in Afar. Geology, 37, 59–62

Kelemen, P. B., Hirth, G., Shimizu, N., Spiegelman., M., Dick, H. J. B., 1997. A review of melt migration processes in the asthenospheric mantle beneath oceanic spreading centers. Philosophical Transactions of the Royal Society of London, A355, 283-318

Kelley, D. F., Barton, M., 2008. Pressures of Crystallization of Icelandic Magmas. Journal of Petrology, 49, 3, 465-492

Kendall, J.-M., Stuart, G., Ebinger, C., Bastow, I., Keir, D., 2005. Magma-assisted rifting in Ethiopia. Nature, 433, 146–148.

Kidane, T., Tapponnier, P., Manighetti, I. P., Audin L., Lahitte, P., Quidelleur, X., Gillot, P. Y., Gallet, Y., Carlut, J., Haile, T., 2003. New paleomagnetic and geochronologic results from Ethiopian Afar: Block rotations linked to rift overlap and propagation and determination of a ~2 Ma reference pole for stable Africa. Journal of Geophysical Research, 108, 2102,

Kieffer, B., Arndt, N., Lapierre, H., Bastien, F., Bosch, D., Pecher, A., Yirgu, G., Ayalew, D., Weis, D., Jerram, D.A., Keller, F., Meugniot, C., 2004. Flood and shield basalts from Ethiopia: magmas from the African superswell. Journal of Petrology, 45 4, 793–834.

King, S. D., Ritsema, J., 2000. African Hot Spot Volcanism: Small-Scale Convection in the Upper Mantle Beneath Cratons. Science, 290, 5494, 1137-1140

Kinzler, R. J., Grove, T. L., 1992. Primary magmas of mid-ocean ridge basalts, I: Experiments and methods. Journal of Geophysical Research, 97, 6885-6906

Koepke, J., Feig, S. T., Snow, J., Freise M., 2004. Petrogenesis of oceanic plagiogranites by partial melting of gabbros: an experimental study. Contributions to Mineralogy and Petrology, 146, 4, 414-432

Klein, E. M., Langmuir, C. H., 1987. Global correlations of ocean ridge basalt chemistry with axial depth and crustal thickness. Journal of Geophysical Research, 92, 8089-8115

Knaack, C., Cornelius, S., Hooper, P. R., 1994. Trace element analysis of rocks and minerals by ICP-MS. Open File Report, Department of Geology, Washington State University.

Krotkov, N. A., Carn, S. A., Krueger, A. J., Bhartia, P. K., Yang, K., 2006. Band Residual Difference algorithm for retrieval of SO_2 from the Aura Ozone Monitoring Instrument (OMI). IEEE Transactions on Geoscience and Remote Sensing 445, 1259–1266

Kushiro, I., 2001. Partial melting experiments on peridotite and origin of mid-ocean ridge basalt. Annual Review of Earth and Planetary Sciences, 29, 71-107

Kurz, T., Gloaguena, R., Ebinger, C., Caseye, M., Abebe, B., 2007. Deformation distribution and type in the Main Ethiopian Rift (MER): A remote sensing study. Journal of African Earth Sciences, 48, 2-3, 100-114

Lahitte, P., Gillot, P.Y., Courtillot, V., 2003a. Silicic central volcanoes as precursors to rift propagation: the Afar case. Earth and Planetary Science Letters, 207, 103–116.

Lahitte, P., Gillot, P.Y., Kidane, T., Courtillot, V., Bekele, A., 2003b. New age constraints on the timing of volcanism in central Afar, in the presence of propagating rifts. Journal of Geophysical Research, 108, B2, 2123

Langmuir, C. H., Bender, J. F., Bence, A. E., G.N., Hanson, G. N., Taylor, S. R., 1977. Petrogenesis of basalts from the FAMOUS area: Mid-Atlantic Ridge. Earth and Planetary Science Letters, 36, 1, 133-156

Langmuir, C., Klein, E., Plank, T., 1992. Petrological systematics of mid-ocean ridge basalts: Constraints on melt generation beneath ocean ridges. AGU Geophysical Monograph, 71, 183-280

Lanphere, M.A., Dalrymple, G.B., 1976. Identification of excess 40Ar by the 40Ar/39Ar age spectrum technique. Earth and Planetary Science Letters, 32, 2, 141-148

Lanphere, M.A., Dalrymple, G.B., 2000, First-principles calibration of 38Ar tracers: Implications for the ages of 40Ar/39Ar fluence standards. U.S. Geological Survey Professional Paper 1621, 10 pp.

Lanphere, M. A., Champion, D. E., Melluso, L, Morra, V., Perrotta, A., Scarpati, C, Tedesco, D., 2007 40Ar/39Ar ages of the 79 AD eruption of Vesuvius, Italy. Bulletin of Volcanology, 69, 259-263

Lee, J, Marti, K, Severinghaus, J. P., Kawamura, K., Yoo, H., Lee, J., Kim, J. S., 2006. A redetermination of the isotopic abundances of atmospheric Ar. Geochimica et Cosmochimica Acta,, 70, 4507-4512.

Levelt, P.F., van den Oord, G.H.J., Dobber, M.R., Mälkki, A., Visser, H., de Vries, J., Stammes, P., Lundell, J.O.V., Saari, H., 2006. The Ozone Monitoring Instrument. IEEE Transactions on Geoscience and Remote Sensing, 44, 1093–1101.

Lipman, P. W., Calvert, A. T., 2011. Early growth of Kohala volcano and formation of long Hawaiian rift zone. Geology, 39, 7, 659-662

Mackenzie, G. D., Thybo, H., Maguire, P. K. H., 2005. Crustal velocity structure across the Main Ethiopian Rift: results from two-dimensional wide-angle seismic modelling, Geophysical Journal International, 162, 3, 994–1006.

McDonald, G.A., 1968. Composition and origin of Hawaiian lavas. In: Coats, R.R., Hay, R.L., Anderson, C.A. (Eds.), Studies in Volcanology: A Memoir in Honour of Howel Williams. Geological Society of America memoirs, 116, 477–522.

Macdoanld, R., 1974. Nomenclature and petrochemistry of the peralkaline oversaturated extrusive rocks. Bulletin of Volcanology, 38, 2, 498-516

Macdonald, R., Davies, G. R., Bliss, C. M., Leat, P. T., Bailey, D. K., Smith, R. L., 1987. Geochemistry of high-silica rhyolites, Naivasha, Kenya rift valley. Journal of Petrology, 28, 979--1088.

Maclennan, J., McKenzie, D. P. , Gronvöld, K., 2001. Plume-driven upwelling under central Iceland. Earth and Planetary Science Letters, 194, 67-82

Mahood, G. A., Halliday, A. N., Hildreth, W., 1990. Isotopic evidence for the origin of pantellerites in a rift-related alkalic suite: Pantelleria, Italy. In: IAVCEI Abstracts, International Volcanological Congress. Mainz.

Manighetti, I., Tapponnier, P., Courtillot, V., Gruszow, S., Gillot, P-Y., 1997. Propagation of rifting along the Arabia-Somalia plate boundary: The gulfs of Aden and Tadjoura. Journal of Geophysical Research, 102, 2681– 2710.

Manighetti, I. P., Tapponnier, P., Gillot, P. Y., Jacques, E., Courtillot, V., Armijo, R., Ruegg, J. C., King, G., 1998, Propagation of rifting along the Arabia-Somalia plate Boundary: Into Afar. Journal of Geophysical Research, 103, 4947–4974

Manighetti, I., Tapponnier, P., Courtillot, V., Gallet, Y., Jacques, E., and Gillot, Y., 2001, Strain transfer between disconnected, propagating rifts in Afa. Journal of Geophysical Research. 106, 13, 613– 13,665

Makris, J., Menzel, H., Zimmermann J., Gouin, P., 1975. Gravity field and crustal structure of north Ethiopia, A. Pilger, A. Rösler. (Editors). Afar Depression of Ethiopia, Vol. I Schweizerbart, Stuttgart, 135–144.

Makris J., Ginzburg A., 1987. The Afar Depression: transition between continental rifting and sea floor spreading. Tectonophysics, 141, 199–214

Marty, B., Pik, R., Yirgu, G., 1996. Helium isotopic variations in Ethiopian plume lavas: nature of magmatic sources and limit on lower mantle contribution. Earth and Planetary Science Letters, 144, 223 – 237.

Menzies, M. A., Klemperer, S. L., Ebinger, C., Baker, J., 2002. Characteristics of volcanic rifted margins. In: Menzies, M. A., Klemperer, S. L., Ebinger, C., Baker, J. (Editors) Volcanic Rifted Margins, Geological Society of America Special paper, 362, 1-14

McDade, P., Blundy, J. D., Wood, B. J., 2002. Trace element partitioning on the Tinaquillo Lherzolite solidus at 1.5 GPa. Physics of Earth and Planetary Interiors, 139, 129-147

McDougall, I., Harrison, T. M., 1999. Geochronology and thermochronology by the 40Ar/39Ar method. Oxford University Press, Oxford, UK

McKenzie, D., 1985. The extraction of magma from the crust and mantle. Earth and Planetary Science Letters, 74, 81-91

McKenzie, D., Bickle, M. J., 1998. The volume and composition of melt generated by extension of the lithosphere. Journal of Petrology, 29 625-679.

McKenzie, D. P., Morgan, W. J., 1969. Evolution of triple junctions. Nature, 224, 125–133.

Mckenzie, D., O'Nions, R. K., 1991. Partial melt distributions from inversion of Rare Earth Element concentrations. Journal of Petrology, 32, 1021-1091.

McKenzie, D. P., Davies, D., P. Molnar, P., 1970. Plate tectonics of the Red Sea and East Africa. Nature, 224, 125–133.

McClusky, S., Reilinger, R., Ogubazghi, G., Amleson, A., Healeb, B., Vernant, P., Sholan, J., Fisseha, S., Asfaw, L., Bendick, R., Kogan, L., 2010. Kinematics of the southern Red Sea–Afar Triple Junction and implications for plate dynamics. Geophysical Research Letters, 37, L05031,

McDougall, I., Harrison, M. T., 1999. Geochronology and Thermochronology by the 40Ar/39Ar Method. Oxford University Press.

Merrihue, C., Turner G., 1966. Potassium-Argon Dating by Activation with Fast Neutrons, Journal of Geophysical Research, 71, 11, 2852–2857,

Mohr, P., 1978. Afar. Annual reviews of Earth and Planetary Sciences, 6, 145-172

Mohr, P., 1983. Ethiopian flood basalt province. Nature, 303, 577–584.

Mohr, P. A., Zanettin, B., 1988. The Ethiopian flood basalt province. In: MacDougall, J. D. (Editor) Continental Flood Basalts. Kluwer Academic, Dordrecht, 63-110.

Morgan, W. J., 1972. Deep Mantle Convection Plumes and Plate Motions. Bulletin of the American Association of Petroleum Geology, 56, 203-213

Mungall, J. E., Martin, R. F., 1995. Petrogenesis of basalt-comendite and basalt-pantellerite suites, Terceira, Azores, and some implications for the origin of ocean-island rhyolites. Contributions to Mineralogy and Petrology, 119, 1, 43-55,

Nesbitt, L. M., 1935. Hell-Hole of Creation: The Exploration of Abyssinian Danakil. Alfred A. Knopf New York

Nielsen, T. K., Hopper, J. R., 2004. From rift to drift: Mantle melting during continental breakup. Geochemistry Geophysics Geosystems, 5, Q07003

Niu, Y., 1997. Mantle Melting and Melt Extraction Processes beneath Ocean Ridges: Evidence from Abyssal Peridotites. Journal of Petrology, 38, 8, 1047-1074

Niu, Y., Hekinian, R., 1997. Spreading rate dependence of the extent of mantle melting beneath ocean ridges. Nature, 385, 326–329.

Nyblade, A. A., Robinson, S. W., 1994. The African superswell. Geophysical Research Letters, 21, 9, 765-768

O'Hara, M. J., 1985. Importance of the 'shape' of the melting regime during partial melting of the mantle. Nature, 314, 58-62

O'Neill, H. S. C., 1981. The transition between spinel lherzolite and garnet lherzolite, and its use as a geobarometer. Contributions to Mineralogy and Petrology, 77, 185 – 194,

Oppenheimer, C., Francis, P., 1997. Remote sensing of heat, lava and fumerole emissions from Erta'Ale volcano, Ethiopia. International Journal of Remote Sensing, 18, 1661–1692

Pagli, C., Wright, T. J., Ebinger, C., Barnie, T., Ayele, A., 2009, Inflate, Pause, Erupt, Recharge: the 2008 Alu eruption in the Erta 'Ale volcanic system (Ethiopia): [abs.]: Eos (Transactions, American Geophysical Union), 90, T31B-1813

Peate, I. U., Baker, J. A., Al-Kadasi, M., Al-Subbary, A., Knight, K. B., Riisager, P., Thirlwall, M. F., Peate, D. W., Renne, P. R., Menzies, M. A., 2005. Volcanic stratigraphy of large-volume silicic pyroclastic eruptions during Oligocene Afro-Arabian flood volcanism in Yemen. Bulletin of Volcanology, 68, 2, 135-156

Peccerillo, A., Barberio, M. R., Yirgu, G., Ayalew, D., Barbieri, M., Wu, T., 2003. Relationships between Mafic and Peralkaline Silicic Magmatism in Continental Rift Settings: a Petrological, Geochemical and Isotopic Study of the Gedemsa Volcano, Central Ethiopian Rift. Journal of Petrology, 44, 11, 2003-2032

Peccerillo, A., Donati, C., Santo, A. P., Orlando, A., Yirgu, G., Ayalew, D., 2007. Petrogenesis of silicic peralkaline rocks in the Ethiopian rift: Geochemical evidence and volcanological implications. Journal of African Earth Sciences, 48, 2-3, 161-173

Perfit, M. R., Chadwick, W.W., 1998. Magmatism at mid-ocean ridges: Constraints from volcanological and geochemical investigations. In: Buck W.R., Delaney, P.T., Karson, J.A., Lagabrielle, Y., (Editors) Faulting and Magmatism at Mid-Ocean Ridges. Geophysical Monograph 106, AGU, Washington, D. C. 59-115

Pik, R., Deniel, C., Coulon, C., Yirgu, G., Hofman, C.Ayalew, D., 1998. The northwestern Ethiopian Plataeu flood basalts: classification and spatial distribution of magma types. Journal of Volcanology and Geothermal Research, 81, 91-111.

Pik, R., Deniel, C., Coulon, C., Yirgu, G., Marty, B., 1999. Isotopic and trace element signatures of Ethiopian flood basalts; evidence for plume-lithosphere interactions. Geochimica et Cosmochimica Acta, 63, 2263-2279.

Pik, R., Marty, B., Hilton, D., 2006. How many mantle plumes in Africa? The geochemical point of view. Chemical Geology, 226, 100-114,

Plank, T., Langmuir, C. H., 1992. Effects of the melting regime on the composition of the oceanic crust. Journal of Geophysical Research, 97, 19749-19770

Prodehl, C., Mechie, J., 1991. Crustal thinning in relationship to the evolution of the Afro-Arabian rift system: a review of seismic-refraction data. Tectonophysics, 198, 311–327

Pyle, D. M., 1999. Widely dispersed Quaternary tephra in Africa. Global and Planetary Change, 21, 95–112

Pyle, D M., Collins, S. J., Sims, K. W., Reagan, M., Blundy, J. D., Oppenheimer, C., Yirgu, G. 2006. Rhyolites From the September 2005 Da'Ure (Dabbahu) Eruption, Afar, Ethiopia. [abs.]: Eos (Transactions, American Geophysical Union), 90 , T41B-1560

Staudacher, T., Jessberger, E. K., Dorflinger, J., Kiko, J., 1978. A refined ultrahigh-vacuum furnace for rare gas analysis. Journal of Physics, 781-784.

Steiger, R. H., Jager, E., 1977. Sub-commission on geochronology: Convention on the use of decay constants in geo- and cosmochronology. Earth and Planetary Science Letters, 36, 359-362.

Stewart, K., Rogers, N., 1996. Mantle plume and lithosphere contributions to basalts from southern Ethiopia. Earth and Planetary Science Letters, 139, 195--211.

Rampey, M.L., Oppenheimer, C., Pyle, D.G., Yirgu, G., 2010. Caldera-forming eruptions of the Quaternary Kone Volcanic Complex, Ethiopia. Journal of African Earth Sciences, 58, 51–66.

Renne, P. R., Sharp, W. D., Deino. A. L., Orsi, G., Civetta, L., 1997. 40Ar/39Ar Dating into the Historical Realm: Calibration Against Pliny the Younger. Science, 29, 277, 5330, 1279-1280

Richards, M. A., Duncan, R. A., Courtillot, V., 1989. Flood Basalts and Hot-Spot Tracks: Plume Heads and Tails. Science, 246, 4926, 103-107

Ritsema, J., van Heijst, H.J. Woodhouse, J.H., 1999. Complex shear wave velocity structure beneath Africa and Iceland. Science, 286, 1925-1928.

Roeder, P. L., Emslie, R. F., 1970. Olivine-liquid equilibrium. Contributions to Mineralogy and Petrology, 29, 275 – 289

Rogers, N. W., 1993. The isotope and trace element geochemistry of basalts from the volcanic islands of the southern Red Sea. In: Prichard, H.M., Alabaster, T., Harris, N. B. W., Neary, C. R. (Editors). Magmatic Processes and Plate Tectonics. Geological Society of London Special Publication, 76, 455-467.

Rogers, N. W., 2006. Basaltic magmatism and the geodynamics of the East African Rift System, in The Afar Volcanic Province within the East African Rift System. Yirgu, G., Ebinger, C.J., Maguire, P.K.H. (Editors). Geological Society of London, Special Publication, 259, 77-94.

Roger, N., Macdonald, R., Fitton, G., Georgea, R., Smith, M., Barreiroe, B., 2002. Two mantle plumes beneath the East African rift system: Sr, Nd and Pb isotope evidence from Kenya Rift basalts. Earth and Planetary Science Letters, 176, 387-400

Rooney, T. O., 2010. Geochemical evidence of lithospheric thinning in the southern Main Ethiopian Rift. Lithos, 117. 33–48

Rooney, T. O., Furman, T., Yirgu., G., Ayalew, D., 2005. Structure of the Ethiopian lithosphere: Xenolith evidence in the Main Ethiopian Rift. Geochimica Cosmochimica Acta, 69, 3889– 3910.

Rooney, T., Furman, T., Bastow, I., Ayalew, D., Yirgu, G., 2007. Lithospheric modification during crustal extension in the Main Ethiopian Rift. Journal of Geophysical Research, 112, B10, B10201

Rooney, T. O., Bastow, I., Keir, D., 2011. Insights into extensional processes during magma assisted rifting: Evidence from aligned scoria cones. Journal of Volcanology and Geothermal Research, 201, 1-4, 83-96

Rowland, J.V., Baker, E., Ebinger, C.J., Keir, D., Kidane, T., Biggs, J., Hayward, N., Wright, T.J., 2007. Fault growth at a nascent slow-spreading ridge: 2005 Dabbahu rifting episode, Afar. Geophysical Journal International. 171, 1226– 1246

Rubin, A. M., Pollard, D. D., 1988. Dike-induced faulting in rift zones of Iceland and Afar. Geology, 16, 413-417

Savage, P., Georg, R. B., Williams, H. M., Burton, K., Halliday, A., 2011. Silicon isotope fractionation during magmatic differentiation. Geochimica et Cosmochimica Acta, 75, 6124-6139

Scaillet, B., Macdonald, R., 2003. Phase relations of peralkaline silicic magmas and petrogenetic implications. Journal of Petrology, 42, 4, 825-284

Shaw, D. M., 1970. Trace element fractionation during anatexis. Geochimica et Cosmochimica Acta, 34, 237-243

Schilling, J.-G. 1973. Afar mantle plume: Rare earth evidence. Nature, 242, 2–5.

Soule, S. A., Fornari, D. J., Perfit, M. R., Rubin, K. H., 2007. New insights into mid-ocean ridge volcanic processes from the 2005-2006 eruption of the East Pacific Rise, 9° 46'N 9° 56'N. Geology 35, 1079-1082

Sifeta, K., Roser, B. P., Kimur. J. I., 2005. Geochemistry, provenance, and tectonic setting of Neoproterozoic metavolcanic and metasedimentary units, Werri area, Northern Ethiopia, Journal of African Earth Sciences, 41, 3, 212– 234.

Sigmarsson, O., Condomines, M., Fourcade. S., 1992. Mantle and crustal contribution in the genesis of Recent basalts from off-rift zones in Iceland: Constraints from Th, Sr and O isotopes. Earth and Planetary Science Letters, 110, 1-4, 149-162

Sims, K. W. W., DePolo, D. J., 1997. Inferences about mantle magma sources from incompatible element concentration ratios in oceanic basalts. Geochimica et Cosmochimica Acta, 61, 4, 765-784,

Sinton, J., Bergmanis, E., Rubin, K., Batiza, R., Gregg, T. K. P., Gronvold, K., Macdonald, K.C., White, S.M., 2002. Volcanic eruptions on mid-ocean ridges: New evidence from the superfast spreading East Pacific Rise, 17–19S. Journal of Geophysical Research, 107, B2115

Singer, B. S., Pringle, M. S., 1996. Age and duration of the Matuyama-Brunhes geomagnetic polarity transition from $^{40}Ar/^{39}Ar$ incremental heating analyses of lavas. Earth and Planetary Science Letters, 139, 47-61

Singer, B. S., Brown, L. L., Rabassa, J. O., Guillou, H., 2004. 40Ar/39Ar chronology of Late Pliocene and early Pleistocene geomagnetic and glacial events in southern Argentina. in: Channell, J.E.T., Lowrie, W., and Meert J. (Editor). Timescales of the Internal Geomagnetic Field, American Geophysical Union, Geophysical Monograph

Singh, S. C., Crawford, W. C., Carton, H., Seher, T., Combier, V., Cannat, M., Canales, J. P., Dusunur, D., Escartin, J., Miranda, M., 2006. Discovery of a magma chamber and faults beneath a Mid-Atlantic Ridge hydrothermal field. Nature, 442, 1029-1032

Smithsonian Institution., 2007. Manda Hararo, Bulletin of the Global Volcanism Network 32, 7

Smithsonian Institution., 2009. Manda Hararo, Bulletin of the Global Volcanism Network 34, 6

Smithsonian Institution., 2011. Nabro, , Bulletin of the Global Volcanism Network 36, 6

Spampinato, L., Calvari, S., Oppenheimer, C., Lodato, L., 2008. Shallow magma transport for the 2002–3 Mt. Etna eruption inferred from thermal infrared surveys. Journal of Volcanology and Geothermal Research, 177, 301-312

Standish, J. J., Sims, K. W. W., 2010. Young off-axis volcanism along the ultraslow-spreading Southwest Indian Ridge. Nature Geoscience, 3, 286–292

Stracke, A., Hofmann, A. W., Hart, S. R., 2005. FOZO, HIMU, and the rest of the mantle zoo, Geochemistry Geophysics Geosystems, 6, Q05007,

Sun, S-s., McDonough, W. F., 1989. Chemical and isotopic systematics of oceanic basalts: implications for mantle composition and processes. Geological Society London Special Publication, 42, 1, 313-345

Tadesse, G., Allen. A., 2005, Geology and geochemistry of the Neo- proterozoic Tuludimtu Ophiolite suite, western Ethiopia, Journal of African Earth Sciences, 41, 3, 192–211.

Tazieff, H., Varet, J., Barberi, F., Giglia, G., 1972. Tectonic significance of the Afar (or Danakil) Depression. Nature, 235, 144-147

Teklay, M., Scherer, E. E., Mezger, K. Danyushevsky, L., 2010. Geochemical characteristics and Sr–Nd–Hf isotope compositions of mantle xenoliths and host basalts from Assab, Eritrea: implications for the composition and thermal structure of the lithosphere beneath the Afar Depression. Contributions to Mineralogy and Petrology, 159, 731–751

Thesiger, A., 1998. The Danakil Diary. Flamingo, London.

Todt, W., Cliff, R.A., Hanser,, A., Hofmann, A. W., 1996. Evaluation of a 202Pb-205Pb double spike for high-precision lead isotope analysis. In: Basu, A., Hart, S.R. (Editors). Earth Processes: Reading the Isotopic Code. Geophysical Monograph 95, 429-437. AGU.

Trua, T., Deniel, C., Mazzuoli, R., 1999. Crustal control in the genesis of Plio-Quaternary bimodal magmatism of the Main Ethiopian Rift (MER); geochemical and isotopic (Sr, Nd, Pb) evidence. Chemical Geology 155, 3-4, 201–231.

Tryggvason, E., 1984. Widening of the Krafla fissure swarm during the 1975– 1981 Volcano-tectonic Episode. Bulletin of Volcanology, 471, 47– 69.

Vidal, Ph., Deniel, C., Vellutini, P.J., Piguet, P., Coulon, C., Vincent, J., Audin, J., 1991. Changes of mantle sources in the course of a rift evolution: the Afar case. Geophysical Research Letters, 18, 1913–1916.

Vigny, C., Huchon, P., Ruegg, J.C., Khanbari, K., Asfaw, L.M., 2006. Confirmation of Arabia slow motion by new GPS data in Yemen. Journal of Geophysical Research, 111, B02402

Volker, F., McCulloch, M. T., Altherr, R., 1993. Submarine basalts from the Red Sea: New Pb, Sr, and Nd isotopic data. Geophysical Research Letters, 20, 927-930.

Volker, F., Altherr, R., Jochum, K-P., McCulloch, M. T., 1997. Quaternary volcanic activity of the southern Red Sea: new data and assessment of models on magma sources and Afar plume-lithosphere interaction. Tectonophsyics, 278, 15-29

Walker, D., Shibata, T., DeLong, S. E., 1979. Abyssal tholeiites from the Oceanographer Fracture Zone II. Phase equilibria and mixing. Contributions to Mineralogy and Petrology, 70, 2, 111-115

Walter, M. J., 1998. Melting of garnet peridotite and the origin of komatiite and depleted lithosphere. Journal of Petrology, 39, 29–60

Wang, K., Plank, T., Walker, J. D., Smith, E. I., 2002. A mantle melting profile across the basin and range, SW USA. Journal of Geophysical Research, 107, B1, 2017.

Waters, C. L., Sims, K. W. W., Perfit, M., Blichert-toft, J., Blusztajn, J., 2011. Perspective on the Genesis of E-MORB from Chemical and Isotopic Heterogeneity at 9’108N East Pacific Rise. Journal of Petrology, 52, 3, 565-602

Watson, S., McKenzie, D., 1991. Melt Generation by Plumes: A Study of Hawaiian Volcanism. Journal of Petrology, 32, 3501-537.

Webster, J. D., Taylor, R. P., Bean, C., 1993. Pre-eruptive melt composition and constraints on degassing of a water-rich pantellerite magma, Fantale Volcano, Ethiopia. Contributions to Mineralogy and Petrology, 114 , 1, 53–62.

Wiart, P. A. M., and Oppenheimer, C., 2000. Largest known historic eruption in Africa: Dubbi volcano, Eritrea, 1861, Geology, 28, 291-294.

Wiart, P. A. M., Oppenheimer, C., 2005, Large magnitude silicic volcanism in north Afar: The Nabro Volcanic Range and Ma'alalta volcano, Bulletin of Volcanology, 67, 99-115.

Wiart P. A. M., Oppenheimer, C., Francis, P., 2000, Eruptive history of Dubbi volcano, northeast Afar (Eritrea), revealed by optical and SAR image interpretation, International Journal of Remote Sensing, 21, 911-936.

Williams, A., Pik, R., Burnard, P., Lahitte, P., Yirgu, G., Adem, M., 2008. Tectonic-volcanic interplay in the Dabbahu Segment of the Afar Rift from cosmogenic 3He constraints. Abstract. EOS Transaction of AGU, Fall Meeting 2008 T43A-1984

Williams, A., Pik, R., Burnard, P., Medynski, S., Yirgu, G., 2009. Tectonic-magmatic interplay during the early stages of oceanic rifting: temporal constraints from cosmogenic 3He dating in the Dabbahu rift segment, Afar. Abstract. EOS Transaction of AGU, Fall Meeting 2009, T31B-1816

White, J. C., Holt, G. S., Parker, D. F., Ren, M., 2003. Trace-element partitioning between alkali feldspar and peralkalic quartz trachyte to rhyolite magma. Part I: Systematics of trace-element partitioning, American Mineralogist 88, 316–329

White, R. S., 1993. Melt production rates in mantle plumes. Philosophical Transactions of the Royal Society of London A, 342, 137-153

White, R. S., McKenzie, D., 1995. Mantle plumes and flood basalts. Journal of Geophysical Research, 100, B9, 17,543-17,585

White, R. S., Spence, G., Fowler, S. R., McKenzie, D. P., Westbrook, G. K., Bowen, A. N., 1987. Magmatism at rifted continental margins. Nature, 330, 439-444

White, S. M., Crisp, J. A., Spera, F.J., 2006. Long-term volumetric eruption rates and magma budgets. Geochemistry Geophysics Geosystems, 7, Q03010

White, T. D., Asfaw, B., Beyene, Y., Haille-Sellaise, Y., Suwa, G., Woldegabriel, G. 2009. Ardipithecus ramidus and the Paleobiology of Early Hominids. Science, 326, 75-86

WoldeGabriel, G., Walter, R., Aronson, J. L., Hart, W., 1992. Geochronology and distribution of silicic volcanic rocks of Plio-Pleistocene age from the central sector of the Main Ethiopian Rift. Quaternary International, 13-14, 69-76

WoldeGabriel, G., Haile-Selassie, Y., Renne, P. R., Hart, W. K., Ambrose, S. H., Asfaw, B., Heiken, G., White, T., 2001. Geology and paleontology of the Late Miocene Middle Awash valley, Afar rift, Ethiopia, Nature, 412, 175 - 178

Wolf, M. B., Wyllie, P. J., 1994. Dehydration-melting of amphibolite at 10 kbar: the effects of temperature and time. Contributions to Mineralogy and Petrology, 115:, 69–383

Wolfenden, E., Ebinger, C., Yirgu, G., Renne, P., Kelley, S.P., 2005. Evolution of the southern Red Sea rift: birth of a magmatic margin. Bulletin of the Geological Society of Americ, 117, 846–864.

Wright, R., Flynn, L. P., Garbeil, H., Harris, A. J. L., Pilger, E., 2004. MODVOLC: near-real-time thermal monitoring of global volcanism. Journal of Volcanology and Geothermal Research, 135, 29–49

Wright, T.J., Ebinger, C., Biggs, J., Ayele, A., Yirgu, G., Keir, D., Stork, A., 2006. Magma-maintained rift segmentation at continental rupture in the 2005 Afar dyking episode. Nature, 442, 291–294

Yang, H.-J., Kinzler, R. J., Grove, T. L., 1996. Experiments and models of anhydrous, basaltic olivine-plagioclase-augite saturated melts from 0.001 to 10 kbar. Contributions to Mineralogy and Petrology, 124, 1–18

Yang, K., Krotkov, N. A., Krueger, A. J., Carn, S. A., Bhartia, P. K., Levelt, P. F., 2007. Retrieval of large volcanic SO2 columns from the Aura Ozone Monitoring Instrument: Comparison and limitations. Journal of Geophysical Research, 112, D24S43

Yihunie, T., Adachi, M., Yamamoto, K., 2006, Geochemistry of the Neoproterozoic metabasic rocks from the Negele area, southern Ethiopia: Tectonomagmatic implications. Journal of African Earth Sciences, 44, 3, 255–269.

Yirgu, G., Ayele, A., Ayalew, D., 2006. Recent Seismovolcanic Crisis in Northern Afar, Ethiopia. Eos, Transaction of AGU 87, 325-326

Zimmer, M. M., Plank, T., Hauri, E. H., Yogodzinski, G. M., Stelling, P., Larsen, J., Singer, B., Jicha, B., Mandeville, C., Nye, C. J., 2011. The Role of Water in Generating the Calc-alkaline Trend: New Volatile Data for Aleutian Magmas and a New Tholeiitic Index. Journal of Petrology, 51, 12, 2411-2444.

Ziv, A., Rubin, A. M., Agnon, A., 2000. Stability of dike intrusion along preexisting fractures. Journal of Geophysical Research, 105, 5947-5961

APPENDIX A

40Ar/39Ar Analytical techniques

Samples were first inspected in thin section to select those with textures that were as close to holocrystalline and equigranular as possible and to identify the appropriate size fraction required for a groundmass separate. Selected samples were then crushed and sieved to collect the desired size fraction. This was then thoroughly cleaned in an ultrasonic bath with successive rinses of DI water and isopropyl alcohol. After cleaning samples were passed through a FRANTZ magnetic separator to increase the proportion of groundmass to phenocryts. Around 250mg of groundmass material was then handpicked using a binocular microscope.

For irradiation, ~250 mg groundmass sample were packaged in Cu foil and placed in a cylindrical quartz vial, together with fluence monitors of known age and K-glass and fluorite to measure interfering isotopes from K and Ca. The quartz vials were wrapped in 0.5 mm-thick Cd foil to shield samples from thermal neutrons during irradiation. The samples were irradiated for one (IRR279) or two (IRR276) hours in the central thimble of the U.S. Geological Survey TRIGA reactor in Denver, Colorado (Dalrymple et al., 1981). The reactor vessel was rotated continuously during irradiation to avoid lateral neutron flux gradients. Reactor constants determined for these irradiations were indistinguishable from recent irradiations, and a weighted mean of constants obtained over the past five years yields 40Ar/39ArK = 0.0010 +/- 0.0004, 39Ar/37ArCa = 0.00071 +/- 0.00005, and 36Ar/37ArCa = 0.000281 +/- 0.000006. TCR-2 sanidine from the Taylor Creek Rhyolite (Dalrymple and Duffield, 1988) was used as a fluence monitor with an age of 27.87 Ma. This monitor is a secondary standard calibrated against the primary intralaboratory standard, SB-3, that has an age of 162.9 ± 0.9 Ma (Lanphyre and Dalrymple, 2000). Fluence monitors were analyzed using a continuous CO2 laser system and mass spectrometer described by (Dalrymple, 1989). Argon was extracted from groundmass and mica separates using a Mo crucible in a custom resistance furnace modified from the design of Staudacher et al (1978) attached to the above mass spectrometer. Heating temperatures were monitored with an optical fiber thermometer and controlled with an Accufiber Model 10

controller. Gas was purified continuously during extraction using two SAES ST-172 getters operated at 4A and 0A.

Mass spectrometer discrimination and system blanks are important factors in the precision and accuracy of 40Ar/39Ar age determinations of Pleistocene lavas because of low radiogenic yields. Discrimination is monitored by analyzing splits of atmospheric Ar from a reservoir attached to the extraction line and for these samples D1amu = 1.007504 ± 0.000279. All isotopic ratios are mass discrimination corrected using 40Ar/36Ar = 295.5 (Steiger and Jager, 1977). A recent determination of atmospheric argon (40Ar/36Ar = 298.56 ± 0.31; Lee et al., 2006) is more precise, but acceptance is controversial and that ratio has no impact on this study because normalizing to a different value does not change the age. Typical system blanks including mass spectrometer backgrounds were 1.5x10-18 mol of m/z 36, 9x10-17 mol of m/z 37, 3x10-18 mol of m/z 39 and 1.5x10-16 mol of m/z 40, where m/z is mass/charge ratio.

In the incremental-heating experiments, the extraction line is isolated from pumping systems and the sample is heated to a specified temperature for 10 minutes, cooled for 3-5 minutes, and transferred to an isolated mass spectrometer. The gas is exposed to getters during the entire extraction. Isotopic ratios are measured and corrected for instrumental blanks, mass discrimination and interfering isotopes generated in the reactor. In these experiments we separated and loaded enough material to do 12-18 steps on each unknown in order to carefully characterize the argon release. The incremental heating data are plotted both as an age spectrum diagram and as an isotope correlation (isochron) diagram. For the age spectrum, apparent ages are calculated assuming that non-radiogenic Ar is atmospheric (40Ar/36Ar = 295.5) in composition and are plotted against the cumulative 39Ar released during the experiment. In cases with several contiguous steps yielding ages within analytical error, we calculate and report plateau ages by weighing individual ages by the inverse of their analytical error. Most groundmass age experiments do not yield identical ages across the entire spectrum due to minor alteration, recoil of 39Ar during irradiation or modest excess 40Ar. Generally accepted criteria for a meaningful incremental heating age are: (1) well-defined plateau (horizontal age spectrum) for more than 50% of the 39Ar released; (2) well-defined isochron for the plateau gas fractions; (3) concordant plateau and isochron ages; and (4) 40Ar/36Ar isochron intercept not significantly different from 295.5. For isochron plots, data are not corrected using an atmospheric ratio. Isochron ages include plateau steps on well-behaved samples or a subset of data that yield a reasonable goodness of fit. We show normal isochron plots for these low-radiogenic rocks because the data are easier to visualize. Inverse isochron results are indistinguishable. Isochron ratios are particularly vulnerable to mobilization of argon isotopes

during irradiation, particularly in fine-grained volcanic rocks. 39Ar produced from 39K in the reactor recoils ~0.1μm causing different degassing rates during analysis (Huneke and Smith, 1976). Recoil moves ratios along the x-axis of isotope correlation plots with low-T steps moved to lower values (loss of 39Ar) and high-T steps moved toward higher values (deeply implanted 39Ar). In this case, the isochron line becomes shallow, yielding a high 40Ar/36Ar ratio and young isochron age. We interpret this as an irradiation artifact. The most reliable results generally include gas from the middle of the release spectrum with consistent K/Ca ratios and concordant isochron data with 40Ar/36Ar intercepts within error of air. Ages and isotopic ratios reported below are 1!

Tabaulated data from each Ar-Ar step heating experiment

SA02 Basalt

Temp(°C)	Age(ka)	%40Ar*	K/Ca	K/Cl	moles 40Ar*	Σ39Ar	40Ar	39Ar	38Ar	37Ar	36Ar
550	2100.9±302.5	-8.02	-0.1	3686	-2.39E-15	-0.01	1.085421±0.002609	-0.013392±0.000088	0.000557±0.000020	0.098743±0.000943	0.003995±0.000021
600	-31.1±138.3	-0.16	0.06	1594	-5.28E-17	0	1.222986±0.002487	0.020243±0.000047	0.001092±0.000029	0.184395±0.001170	0.004197±0.000024
650	-79.9±53.7	-0.72	0.06	5649	-4.82E-16	0.05	2.451987±0.004944	0.071906±0.000145	0.002551±0.000028	0.671826±0.002177	0.008546±0.000028
700	17.4±35.3	0.25	0.06	9469	1.61E-16	0.12	2.354589±0.004750	0.110262±0.000222	0.002967±0.000063	0.973454±0.002466	0.008222±0.000029
750	1.4±26.9	0.03	0.06	4356	1.78E-17	0.21	2.257848±0.004556	0.147331±0.000296	0.003483±0.000072	1.250080±0.002687	0.007990±0.000031
800	28.4±21.1	0.67	0.06	4945	3.89E-16	0.31	2.143828±0.004328	0.164656±0.000331	0.003625±0.000038	1.383196±0.002840	0.007595±0.000025
850	-7.2±21.0	-0.18	0.06	4926	-9.75E-17	0.41	2.019243±0.004149	0.161334±0.000324	0.003512±0.000052	1.345349±0.002764	0.007223±0.000025
900	-15.0±22.2	-0.34	0.06	4256	-2.05E-16	0.51	2.195842±0.004502	0.164614±0.000331	0.003694±0.000054	1.362705±0.002821	0.007839±0.000027
950	-39.6±28.5	-0.72	0.07	2512	-4.57E-16	0.6	2.315136±0.004740	0.137366±0.000276	0.003487±0.000045	0.997415±0.002736	0.008171±0.000030
1000	-71.5±36.0	-0.99	0.1	2331	-7.72E-16	0.68	2.867255±0.005844	0.129299±0.000260	0.003736±0.000057	0.667383±0.001379	0.009986±0.000034
1050	-194.6±46.6	-2.02	0.13	1599	-1.89E-15	0.75	3.394544±0.006993	0.114972±0.000233	0.003978±0.000041	0.466900±0.001273	0.011851±0.000038
1125	-180.2±62.4	-1.25	0.12	1795	-2.04E-15	0.83	5.940279±0.011905	0.134521±0.000271	0.005858±0.000034	0.606015±0.003043	0.020524±0.000051
1200	53.2±86.0	0.26	0.06	469	4.48E-16	0.89	6.346921±0.012719	0.100220±0.000203	0.006218±0.000029	0.900669±0.002230	0.021677±0.000049
1300	172.3±92.9	0.75	0.02	1109	2.49E-15	1	12.060061±0.024145	0.174126±0.000352	0.010569±0.000084	4.715786±0.009662	0.041831±0.000088

Packet IRR279-RI, Experiment #10z0146, 0.2442 g Basalt, all errors ±1 sigma
J = 0.000180238±3.60E-07

40Ar* is radiogenic argon, isotopes in volts (2.75e-14 moles/volt), corrected for blank, background, discrimination, and decay
Calculated K2O = 0.39%wt., Calculated CaO = 8.74%wt., Calculated Cl = 0.2ppm

Total Gas Age = -36.0 ± 11.3 ka

Maximum Age = 18.0 ± 15.0 ka (±1 sigma, including ±J), 26.1% 39Ar released
MSWD = 0.31 (Good fit, MSWD < 3.69)
Steps 3 of 14 (700,750,800°C)

Isochron Age = 52.9 ± 33.6 ka (±1 sigma, including ±J)
Isochron Age = 52.9 ± 27.9 ka (A Priori Errors, including ±J)
Isochron Age = 52.9 ± 74.0 ka (95% confidence, including ±J)
MSWD = 1.45 (Good fit, MSWD < 2.40)
40Ar/36Ar intercept = 291.9 ± 1.8 (±1 sigma)
40Ar/36Ar intercept = 291.9 ± 1.5 (A Priori)
40Ar/36Ar intercept = 291.9 ± 4.1 (95% confidence)
Steps 8 of 14 (650,700,750,800,850,900,950,1000°C)

2805 Basalt

Temp(°C)	Age(ka)	%40Ar*	K/Ca	K/Cl	moles 40Ar*	Σ39Ar	40Ar	39Ar	38Ar	37Ar	36Ar
550	30.8±31.6	1.45	0.07	####	1.67E-16	0.05	0.419231±0.001079	0.101302±0.000204	0.001569±0.000026	0.754031±0.002906	0.001610±0.000020
600	26.5±14.9	1.67	0.07	9239	2.00E-16	0.12	0.435355±0.000957	0.141341±0.000284	0.002165±0.000032	0.989785±0.002079	0.001727±0.000013
650	34.6±16.6	2.43	0.08	6291	4.12E-16	0.23	0.616212±0.001319	0.222155±0.000446	0.003403±0.000031	1.420481±0.002914	0.002434±0.000023
700	33.2±11.4	2.49	0.09	11673	4.62E-16	0.36	0.674379±0.001435	0.260038±0.000522	0.003868±0.000027	1.490925±0.003058	0.002644±0.000018
750	24.6±10.0	1.77	0.1	5282	3.53E-16	0.49	0.724985±0.001536	0.268583±0.000539	0.004132±0.000029	1.410629±0.002894	0.002806±0.000015
800	29.1±12.5	1.8	0.1	5424	3.87E-16	0.61	0.788222±0.001662	0.250062±0.000502	0.003911±0.000039	1.261036±0.002589	0.002974±0.000018
850	26.3±32.7	1.21	0.11	3940	2.71E-16	0.71	0.812641±0.002042	0.192784±0.000414	0.003201±0.000036	0.919144±0.002893	0.002975±0.000040
925	64.1±49.7	1.8	0.14	2021	7.30E-16	0.81	1.478783±0.003141	0.212472±0.000428	0.004101±0.000028	0.794604±0.001844	0.005138±0.000068
1000	22.6±31.1	0.5	0.16	1898	2.85E-16	0.93	2.073004±0.004329	0.235134±0.000474	0.004857±0.000048	0.761839±0.002090	0.007194±0.000041
1100	67.4±50.4	0.61	0.06	625	5.08E-16	1	3.041046±0.006265	0.142445±0.000289	0.004735±0.000035	1.305146±0.002683	0.010595±0.000030

Packet IRR276-Pd, Experiment #10z0050mod, 0.1997 g Basalt, all errors ±1 sigma
J = 0.000283515826±5.6703E-07

40Ar* is radiogenic argon, isotopes in volts (2.72e-14 moles/volt), corrected for blank, background, discrimination, and decay
Calculated K2O = 0.38%wt., Calculated CaO = 4.83%wt., Calculated Cl = 0.1ppm

Total Gas Age = 34.9 ± 8.1 ka

Weighted Mean Plateau Age = 29.6 ± 5.3 ka (±1 sigma, including ±J), 100.0% 39Ar released
MSWD = 0.18 (Good fit, MSWD < 2.11)
Steps 10 of 10 (550,600,650,700,750,800,850,925,1000,1100°C)

Isochron Age = 23.9 ± 8.8 ka (±1 sigma, including ±J)
MSWD = 0.15 (Good fit, MSWD < 2.19)
40Ar/36Ar intercept = 296.5 ± 2.7 (95% confidence)
Steps 10 of 10 (550,600,650,700,750,800,850,925,1000,1100°C)

2802 Basalt

Temp(°C)	Age(ka)	%40Ar*	K/Ca	K/Cl	moles 40Ar*	Σ39Ar	40Ar	39Ar	38Ar	37Ar	36Ar
550	-54.0±230.1	-0.15	0.3	1689	-9.41E-17	0.02	2.301159±0.004626	0.023196±0.000079	0.001814±0.000033	0.041093±0.000484	0.007811±0.000029
600	90.9±105.2	0.36	0.17	1789	5.98E-16	0.09	6.121180±0.012266	0.087620±0.000177	0.005194±0.000081	0.263223±0.000997	0.020714±0.000047
625	-44.3±91.9	-0.2	0.14	3837	-2.35E-16	0.14	4.229196±0.008482	0.070781±0.000143	0.003670±0.000044	0.262934±0.001682	0.014415±0.000034
660	110.0±81.4	0.58	0.12	1993	7.52E-16	0.21	4.744295±0.009512	0.090379±0.000182	0.004341±0.000044	0.384230±0.002008	0.016070±0.000040
695	29.5±71.9	0.17	0.11	3123	2.18E-16	0.29	4.666620±0.009357	0.098384±0.000198	0.004350±0.000032	0.483594±0.002134	0.015901±0.000036
745	5.7±62.7	0.04	0.1	8100	4.85E-17	0.37	4.611419±0.009246	0.113401±0.000228	0.004439±0.000077	0.622414±0.001352	0.015774±0.000038
795	-34.3±56.8	-0.26	0.09	2557	-3.57E-16	0.48	5.049208±0.010122	0.137806±0.000277	0.005213±0.000062	0.833307±0.002195	0.017365±0.000042
895	-58.8±44.8	-0.54	0.07	3632	-8.33E-16	0.63	5.614012±0.011287	0.187650±0.000377	0.006219±0.000053	1.307045±0.003687	0.019468±0.000041
945	-114.1±67.6	-0.75	0.07	2484	-9.56E-16	0.71	4.657300±0.009374	0.110871±0.000223	0.004593±0.000059	0.775245±0.002863	0.016096±0.000043
1000	-52.1±99.2	-0.22	0.08	1076	-3.08E-16	0.77	5.191018±0.010441	0.078206±0.000158	0.004612±0.000050	0.512639±0.002024	0.017749±0.000038
1050	139.3±126.3	0.45	0.09	1832	6.61E-16	0.82	5.387699±0.010835	0.063344±0.000129	0.004358±0.000069	0.363647±0.001451	0.018253±0.000039
1150	395.0±123.6	1.3	0.04	671	2.07E-15	0.87	5.768337±0.011596	0.069624±0.000141	0.004954±0.000040	0.922770±0.002635	0.019525±0.000042
1250	271.7±108.7	1.01	0.01	541	3.33E-15	1	12.114889±0.024289	0.167643±0.000339	0.011184±0.000092	6.931431±0.014203	0.042532±0.000089

Packet IRR279-RF, Experiment #10z0150, 0.1648 g Basalt, all errors ±1 sigma
J = 0.000200662±4.01E-07

40Ar* is radiogenic argon, isotopes in volts (2.72e-14 moles/volt), corrected for blank, background, discrimination, and decay
Calculated K2O = 0.41%wt., Calculated CaO = 10.19%wt., Calculated Cl = 0.3ppm

Total Gas Age = 50.4 ± 18.2 ka

Weighted Mean Plateau Age = -8.8 ± 24.7 ka (±1 sigma, including ±J), 62.6% 39Ar released
Weighted Mean Plateau Age = -8.8 ± 24.7 ka (A priori, without ±J)
MSWD = 0.71 (Good fit, MSWD < 2.29)
Steps 8 of 13 (550,600,625,660,695,745,795,895°C)

Isochron Age = -109.908 ± 62.339 ka (±1 sigma, including ±J)
Isochron Age = -109.908 ± 61.355 ka (A Priori Errors, including ±J)
Isochron Age = -109.908 ± 138.892 ka (95% confidence, including ±J)
MSWD = 1.03 (Good fit, MSWD < 2.40)
40Ar/36Ar intercept = 297.4 ± 1.1 (±1 sigma)
40Ar/36Ar intercept = 297.4 ± 1.1 (A Priori)
40Ar/36Ar intercept = 297.4 ± 2.5 (95% confidence)
Steps 8 of 13 (550,600,625,660,695,745,795,895°C)

2801 Basalt

Temp(°C)	Age(ka)	%40Ar*	K/Ca	K/Cl	moles 40Ar*	Σ39Ar	40Ar	39Ar	38Ar	37Ar	36Ar
550	16.6±178.2	0.04	0.45	1396	9.52E-17	0.03	9.178464±0.018396	0.137543±0.000278	0.007987±0.000058	0.158815±0.001441	0.031094±0.000064
570	257.9±172.9	0.61	0.41	1356	1.04E-15	0.05	6.280227±0.012641	0.097231±0.000197	0.005501±0.000058	0.125507±0.001143	0.021159±0.000044
590	73.9±150.6	0.2	0.29	1589	4.93E-16	0.08	9.003545±0.018087	0.159819±0.000323	0.008164±0.000046	0.292188±0.002470	0.030490±0.000064
610	303.9±132.7	0.93	0.23	1803	2.01E-15	0.12	7.885280±0.015851	0.158473±0.000320	0.007351±0.000044	0.357332±0.002587	0.026537±0.000055
630	269.5±116.0	0.94	0.2	2106	1.87E-15	0.15	7.252341±0.014585	0.166775±0.000336	0.007025±0.000064	0.440154±0.002807	0.024435±0.000051
650	189.0±101.7	0.77	0.18	2351	1.37E-15	0.19	6.467120±0.013015	0.173844±0.000350	0.006609±0.000061	0.494482±0.002182	0.021855±0.000050
675	228.9±84.2	1.15	0.18	2220	1.88E-15	0.23	5.938097±0.011957	0.197347±0.000397	0.006628±0.000049	0.566672±0.003660	0.020022±0.000049
700	225.7±65.6	1.43	0.18	4245	2.08E-15	0.28	5.323757±0.010728	0.222655±0.000448	0.006403±0.000055	0.642461±0.002538	0.017939±0.000042
735	206.5±51.8	1.73	0.18	4942	2.18E-15	0.33	4.610605±0.009738	0.254850±0.000513	0.006360±0.000046	0.742405±0.003343	0.015541±0.000040
775	127.2±37.3	1.42	0.19	7109	2.12E-15	0.41	5.462148±0.011441	0.402099±0.000808	0.008811±0.000060	1.123596±0.003285	0.018537±0.000041
825	108.7±29.2	1.59	0.19	6106	2.43E-15	0.52	5.553905±0.011624	0.535963±0.001076	0.010713±0.000097	1.447767±0.004841	0.018902±0.000046
875	78.9±27.2	1.24	0.19	5055	1.96E-15	0.65	5.781822±0.012080	0.595996±0.001196	0.011768±0.000049	1.614131±0.005420	0.019778±0.000046
910	53.6±34.4	0.64	0.18	4899	9.25E-16	0.74	5.229644±0.010521	0.413917±0.000831	0.008964±0.000045	1.182043±0.004529	0.017916±0.000040
950	-39.6±47.1	-0.35	0.17	4697	-5.64E-16	0.81	5.935436±0.011933	0.341452±0.000686	0.008466±0.000069	1.082158±0.004858	0.020460±0.000043
980	-124.3±71.5	-0.71	0.14	3366	-1.21E-15	0.86	6.220115±0.012502	0.234591±0.000472	0.007278±0.000042	0.852090±0.003364	0.021439±0.000045
1010	-55.6±100.9	-0.23	0.13	2009	-3.95E-16	0.89	6.249594±0.012561	0.170657±0.000344	0.006522±0.000049	0.670051±0.003526	0.021386±0.000049
1040	-282.5±122.8	-0.94	0.13	2616	-1.87E-15	0.93	7.217706±0.014497	0.158913±0.000320	0.006914±0.000035	0.638760±0.002755	0.024835±0.000052
1070	-196.4±142.1	-0.56	0.13	1423	-1.31E-15	0.96	8.480076±0.017022	0.160426±0.000324	0.007942±0.000047	0.664281±0.003504	0.029046±0.000060
1085	-63.1±162.8	-0.16	0.12	1371	-2.74E-16	0.98	6.310900±0.012684	0.104257±0.000211	0.005667±0.000058	0.466781±0.002161	0.021522±0.000045
1100	88.3±170.2	0.22	0.11	1511	3.11E-16	1	5.246422±0.010555	0.084535±0.000171	0.004640±0.000054	0.397784±0.002094	0.017828±0.000040

Packet IRR276-PG, Experiment #10z0075, 0.2032 g Basalt, all errors ±1 sigma
J = 0.000364493789 38±7.2899E-07

40Ar* is radiogenic argon, isotopes in volts (2.75e-14 moles/volt), corrected for blank, background, discrimination, and decay
Calculated K2O = 0.68%wt., Calculated CaO = 4.64%wt., Calculated Cl = 0.3ppm

Total Gas Age = 76.4 ± 11.6 ka

Weighted Mean Age = 86.0 ± 21.7 ka (±1 sigma, including ±J), 100.0% 39Ar released
MSWD = 2.87 (Poor fit, MSWD > 1.73)
Steps 20 of 20 (550,570,590,610,630,650,675,700,735,775,825,875,910,950,980,1010,1040,1070,1085,1100°C)

Isochron Age = 97.0 ± 39.5 ka (±1 sigma, including ±J)
MSWD = 5.67 (Poor fit, MSWD > 1.75)
40Ar/36Ar intercept = 295.2 ± 1.7 (95% confidence)
Steps 20 of 20 (550,570,590,610,630,650,675,700,735,775,825,875,910,950,980,1010,1040,1070,1085,1100°C)

2811 Basalt

Temp(°C)	Age(ka)	%40Ar*	K/Ca	K/Cl	moles 40Ar*	Σ39Ar	40Ar	39Ar	38Ar	37Ar	36Ar
550	-505.2±181.7	-1.14	0.67	1618	-7.70E-15	0.08	10.738784±0.021532	0.164102±0.000332	0.009405±0.000035	0.127977±0.000960	0.036790±0.000076
565	-478.5±182.3	-1.07	0.64	1384	-3.47E-15	0.11	5.122246±0.010281	0.078042±0.000158	0.004515±0.000029	0.064101±0.000667	0.017538±0.000036
590	-281.8±158.7	-0.72	0.43	1419	-4.04E-15	0.18	8.860281±0.017757	0.154490±0.000312	0.008090±0.000052	0.187275±0.000991	0.030253±0.000063
610	-4.3±143.9	-0.01	0.35	1463	-4.13E-17	0.23	5.327720±0.010692	0.102603±0.000207	0.004986±0.000030	0.155683±0.001212	0.018075±0.000038
640	85.3±118.4	0.29	0.27	2266	1.10E-15	0.29	5.943002±0.011922	0.138834±0.000280	0.005791±0.000024	0.265230±0.001242	0.020127±0.000042
675	197.9±95.0	0.85	0.22	2603	2.90E-15	0.37	5.432738±0.010902	0.157875±0.000318	0.005693±0.000023	0.370171±0.001865	0.018333±0.000039
725	188.7±71.5	1.07	0.19	3467	3.65E-15	0.46	5.404411±0.010845	0.208682±0.000420	0.006319±0.000025	0.583703±0.001999	0.018257±0.000038
775	174.9±58.0	1.22	0.17	4146	3.46E-15	0.56	4.481458±0.008998	0.213497±0.000429	0.005764±0.000035	0.673796±0.001682	0.015169±0.000032
825	162.4±49.3	1.34	0.15	5700	3.67E-15	0.67	4.341875±0.008719	0.243850±0.000490	0.006029±0.000030	0.875669±0.001814	0.014743±0.000031
875	174.4±48.0	1.48	0.13	4656	3.38E-15	0.77	3.617044±0.007269	0.208993±0.000420	0.005136±0.000026	0.856077±0.001774	0.012300±0.000026
925	221.5±52.1	1.73	0.11	3534	3.13E-15	0.84	2.874281±0.005784	0.152816±0.000307	0.003940±0.000021	0.698130±0.001892	0.009755±0.000021
975	147.0±63.7	0.98	0.12	2209	1.58E-15	0.89	2.541650±0.005118	0.115894±0.000233	0.003309±0.000023	0.523128±0.001846	0.008664±0.000021
1025	89.1±70.2	0.52	0.14	1912	8.31E-16	0.94	2.537390±0.005110	0.100645±0.000203	0.003117±0.000024	0.380340±0.002147	0.008649±0.000018
1100	27.8±78.3	0.15	0.15	1592	3.35E-16	1	3.649288±0.007334	0.130226±0.000262	0.004330±0.000024	0.450614±0.001935	0.012458±0.000027

Packet IRR276-PF, Experiment #10z0077, 0.1977 g Basalt, all errors ±1 sigma
J = 0.000376522450 57±7.5304E-07

40Ar* is radiogenic argon, isotopes in volts (6.31e-14 moles/volt), corrected for blank, background, discrimination, and decay
Calculated K2O = 0.71%wt., Calculated CaO = 4.73%wt., Calculated Cl = 0.3ppm

Total Gas Age = 43.7 ± 16.2 ka

Weighted Mean Plateau Age = 179.8 ± 22.0 ka (±1 sigma, including ±J), 59.9% 39Ar released
MSWD = 0.18 (Good fit, MSWD < 2.40)
Steps 7 of 14 (675,725,775,825,875,925,975°C)

Isochron Age = 165.0 ± 78.5 ka (±1 sigma, including ±J)
MSWD = 0.40 (Good fit, MSWD < 2.56)
40Ar/36Ar intercept = 295.8 ± 3.6 (95% confidence)
Steps 7 of 14 (675,725,775,825,875,925,975°C)

SA05 Basalt

Temp(°C)	Age(ka)	%40Ar*	K/Ca	K/Cl	moles 40Ar*	Σ39Ar	40Ar	39Ar	38Ar	37Ar	36Ar
550	-198.0±109.3	-0.74	0.43	1674	-1.98E-15	0.06	9.742334±0.019520	0.231414±0.000466	0.009764±0.000068	0.279295±0.002132	0.033291±0.000070
575	-7.8±102.5	-0.03	0.42	1462	-6.55E-17	0.11	7.713233±0.015490	0.195056±0.000393	0.007950±0.000065	0.242288±0.002853	0.026178±0.000055
590	-29.5±90.1	-0.13	0.34	1823	-3.23E-16	0.17	8.791730±0.017647	0.252993±0.000510	0.009405±0.000031	0.393650±0.001972	0.029902±0.000063
600	41.2±83.4	0.2	0.3	1978	3.69E-16	0.23	6.595112±0.013253	0.207077±0.000417	0.007266±0.000039	0.363621±0.002501	0.022375±0.000049
615	159.0±76.3	0.87	0.26	2057	1.29E-15	0.28	5.399709±0.010863	0.187507±0.000378	0.006181±0.000037	0.378242±0.002860	0.018221±0.000042
635	194.1±68.4	1.21	0.22	2757	1.71E-15	0.33	5.158778±0.010381	0.204283±0.000411	0.006162±0.000061	0.490027±0.002801	0.017385±0.000043
660	145.9±60.4	1.01	0.2	2768	1.29E-15	0.38	4.644705±0.009387	0.203973±0.000411	0.005842±0.000040	0.538154±0.001938	0.015711±0.000036
690	199.5±52.6	1.61	0.17	2770	2.22E-15	0.45	5.020011±0.010138	0.257757±0.000519	0.006834±0.000054	0.791625±0.004017	0.016937±0.000041
740	188.5±43.5	1.83	0.15	2763	2.81E-15	0.53	5.604052±0.011306	0.346012±0.000696	0.008465±0.000043	1.207519±0.003505	0.018957±0.000045
790	202.7±38.6	2.23	0.14	3541	3.42E-15	0.64	5.590030±0.011278	0.391597±0.000787	0.008967±0.000061	1.430150±0.003569	0.018897±0.000046
840	178.4±37.3	2.01	0.13	3363	2.89E-15	0.73	5.230770±0.010559	0.375406±0.000755	0.008550±0.000065	1.464948±0.005341	0.017757±0.000042
890	217.3±39.6	2.25	0.12	2706	2.79E-15	0.81	4.510865±0.009114	0.298222±0.000603	0.007100±0.000061	1.276850±0.003797	0.015280±0.000033
940	212.2±47.8	1.84	0.11	2629	2.17E-15	0.87	4.297468±0.008688	0.237774±0.000481	0.006119±0.000045	1.101998±0.003308	0.014585±0.000033
1000	258.8±59.4	1.9	0.11	1607	2.24E-15	0.92	4.284620±0.008662	0.200941±0.000408	0.005784±0.000029	0.992709±0.003107	0.014502±0.000038
1050	326.3±61.9	2.33	0.1	1479	2.43E-15	0.96	3.823410±0.007740	0.174362±0.000354	0.005116±0.000035	0.931905±0.003049	0.012899±0.000035
1100	332.8±60.9	2.41	0.08	1517	1.99E-15	1	3.041021±0.006175	0.140257±0.000286	0.004085±0.000026	0.890197±0.001998	0.010294±0.000027

Packet IRR276-PH, Experiment #10z0078, 0.2073 g Basalt, all errors ±1 sigma
J = 0.000352170 57232±7.0434E-07

40Ar* is radiogenic argon, isotopes in volts (2.72e-14 moles/volt), corrected for blank, background, discrimination, and decay
Calculated K2O = 0.56%wt., Calculated CaO = 4.31%wt., Calculated Cl = 0.3ppm

Total Gas Age = 150.2 ± 10.7 ka

Weighted Mean Plateau Age = 193.3 ± 15.8 ka (±1 sigma, including ±J), 64.1% 39Ar released
MSWD = 0.20 (Good fit, MSWD < 2.19)
Steps 9 of 16 (615,635,660,690,740,790,840,890,940°C)

Isochron Age = 231.2 ± 50.9 ka (±1 sigma, including ±J)
MSWD = 0.33 (Good fit, MSWD < 2.29)
40Ar/36Ar intercept = 294.5 ± 2.9 (95% confidence)
Steps 9 of 16 (615,635,660,690,740,790,840,890,940°C)

BAD5 Basalt

Temp(°C)	Age(ka)	%40Ar*	K/Ca	K/Cl	moles 40Ar*	Σ39Ar	40Ar	39Ar	38Ar	37Ar	36Ar
550	-8.3±26.6	-0.19	0.31	1403	-8.94E-17	0.08	1.751483±0.003966	0.105738±0.000214	0.002788±0.000033	0.176792±0.002323	0.005988±0.000028
600	18.6±20.7	0.42	0.26	2699	2.65E-16	0.18	2.269446±0.004844	0.139414±0.000282	0.003438±0.000034	0.278659±0.002652	0.007726±0.000024
650	13.9±19.6	0.33	0.21	2660	2.40E-16	0.3	2.680887±0.005666	0.168934±0.000341	0.004130±0.000025	0.423458±0.005725	0.009162±0.000026
700	23.9±25.1	0.51	0.17	2702	4.11E-16	0.42	2.913247±0.006130	0.168706±0.000341	0.004268±0.000029	0.534975±0.003136	0.009958±0.000040
750	49.2±24.6	0.9	0.14	2422	7.61E-16	0.52	3.087256±0.006495	0.151539±0.000308	0.004152±0.000025	0.584766±0.002900	0.010518±0.000029
800	71.2±35.8	1.05	0.12	1475	8.96E-16	0.61	3.094499±0.006509	0.123479±0.000252	0.003885±0.000034	0.555680±0.004895	0.010518±0.000041
850	156.6±47.6	1.85	0.11	1281	1.46E-15	0.68	2.861407±0.006043	0.091299±0.000188	0.003258±0.000036	0.438670±0.001843	0.009627±0.000042
900	15.5±48.6	0.16	0.11	900	9.86E-17	0.72	2.281275±0.004885	0.062564±0.000130	0.002544±0.000026	0.289981±0.003252	0.007789±0.000026
950	15.6±56.4	0.15	0.11	1468	7.28E-17	0.75	1.805906±0.003936	0.045759±0.000096	0.001864±0.000028	0.214401±0.002001	0.006163±0.000023
1000	2.7±58.4	0.02	0.1	865	1.16E-17	0.79	1.694222±0.003649	0.042978±0.000105	0.001838±0.000028	0.221194±0.002153	0.005794±0.000021
1075	202.5±57.6	1.54	0.05	838	1.85E-15	0.85	4.357833±0.008975	0.089712±0.000187	0.004337±0.000031	0.896941±0.002767	0.014772±0.000038
1150	274.8±53.7	2.11	0.02	1040	5.93E-15	1	10.223494±0.020705	0.215422±0.000447	0.010100±0.000054	6.148227±0.012616	0.035594±0.000075

Packet IRR268-KT, Experiment #09z0148mod2, 0.1876 g Basalt, all errors ±1 sigma
J = 0.000148907±2.98E-07

40Ar* is radiogenic argon, isotopes in volts (2.75e-14 moles/volt), corrected for blank, background, discrimination, and decay
Calculated K2O = 0.53%wt., Calculated CaO = 9.51%wt., Calculated Cl = 0.4ppm

Total Gas Age = 83.2 ± 9.2 ka

Weighted Mean Plateau Age = 27.3 ± 9.2 ka (including ±J), 78.5% 39Ar released
MSWD = 1.38 (Good fit, MSWD < 2.11)
Steps 10 of 12 (550,600,650,700,750,800,850,900,950,1000°C)

Isochron Age = -3.733 ± 32.345 ka (±1 sigma, including ±J)
MSWD = 1.88 (Good fit, MSWD < 2.19)
40Ar/36Ar intercept = 297.2 ± 3.8 (95% confidence)
Steps 10 of 12 (550,600,650,700,750,800,850,900,950,1000°C)

3016 Basalt

Temp(°C)	Age(ka)	%40Ar*	K/Ca	K/Cl	moles 40Ar*	Σ39Ar	40Ar	39Ar	38Ar	37Ar	36Ar
550	470.6±69.3	3.27	0.26	1128	2.96E-15	0.06	3.290383±0.006840	0.055609±0.000131	0.002937±0.000036	0.111126±0.002187	0.010802±0.000032
600	393.3±56.6	3.36	0.22	1689	3.71E-15	0.16	4.023698±0.008255	0.083432±0.000190	0.003742±0.000032	0.197871±0.002229	0.013215±0.000041
650	316.2±46.1	3.45	0.21	1865	3.63E-15	0.27	3.826405±0.007861	0.101494±0.000206	0.003873±0.000040	0.256791±0.002934	0.012574±0.000047
700	401.6±40.6	5.18	0.2	1445	4.76E-15	0.39	3.344554±0.006898	0.104811±0.000221	0.003662±0.000032	0.279704±0.001852	0.010811±0.000043
750	273.6±41.4	3.64	0.17	1564	2.87E-15	0.5	2.870495±0.005951	0.092999±0.000189	0.003199±0.000033	0.286849±0.003164	0.009441±0.000042
800	413.4±54.1	5.18	0.13	2561	3.35E-15	0.58	2.351020±0.005300	0.071695±0.000163	0.002452±0.000038	0.284597±0.003121	0.007624±0.000045
850	454.5±57.1	5.59	0.11	1469	3.26E-15	0.65	2.122392±0.004844	0.063539±0.000145	0.002272±0.000026	0.311422±0.003830	0.006869±0.000042
900	368.2±55.8	4.47	0.1	1792	2.12E-15	0.71	1.725704±0.004054	0.051013±0.000116	0.001823±0.000022	0.273761±0.002973	0.005656±0.000032
950	318.5±67.0	3.69	0.1	2207	1.49E-15	0.76	1.471723±0.003549	0.041473±0.000126	0.001512±0.000029	0.215401±0.002379	0.004857±0.000030
1000	201.1±52.5	2.08	0.12	3054	9.33E-16	0.8	1.634865±0.003621	0.041101±0.000088	0.001600±0.000022	0.186222±0.003419	0.005470±0.000022
1050	224.1±57.1	1.94	0.08	2081	1.25E-15	0.86	2.343331±0.005033	0.049451±0.000105	0.002194±0.000018	0.316913±0.002237	0.007865±0.000026
1100	342.8±47.5	3.01	0.03	1384	4.77E-15	1	5.776421±0.011891	0.124201±0.000257	0.005556±0.000041	1.868883±0.010988	0.019486±0.000043

Packet IRR268-KV, Experiment #09z0150mod, 0.1922 g Basalt, all errors ±1 sigma
J = 0.000134509±2.69E-07

40Ar* is radiogenic argon, isotopes in volts (2.75e-14 moles/volt), corrected for blank, background, discrimination, and decay
Calculated K2O = 0.36%wt., Calculated CaO = 4.38%wt., Calculated Cl = 0.2ppm

Total Gas Age = 353.2 ± 12.1 ka

Weighted Mean Plateau Age = 342.5 ± 23.4 ka (±1 sigma, including ±J), 100.0% 39Ar released
Weighted Mean Plateau Age = 342.5 ± 14.9 ka (A priori, without ±J)
MSWD = 2.44 (Poor fit, MSWD > 1.99)
Steps 12 of 12 (550,600,650,700,750,800,850,900,950,1000,1050,1100°C)

Isochron Age = 312.317 ± 118.566 ka (±1 sigma, including ±J)
Isochron Age = 312.317 ± 59.764 ka (A Priori Errors, including ±J)
Isochron Age = 312.317 ± 268.193 ka (95% confidence, including ±J)
MSWD = 3.94 (Poor fit, MSWD > 2.05)
40Ar/36Ar intercept = 296.4 ± 3.7 (±1 sigma)
40Ar/36Ar intercept = 296.4 ± 1.9 (A Priori)
40Ar/36Ar intercept = 296.4 ± 8.4 (95% confidence)
Steps 12 of 12 (550,600,650,700,750,800,850,900,950,1000,1050,1100°C)

O4O2 Basalt

Temp(°C)	Age(ka)	%40Ar*	K/Ca	K/Cl	moles 40Ar*	Σ39Ar	40Ar	39Ar	38Ar	37Ar	36Ar
550	517.4±164.2	1.36	0.31	3209	1.68E-15	0.04	4.505193±0.009076	0.043855±0.000093	0.003432±0.000028	0.074662±0.000531	0.015060±0.000037
600	294.5±165.7	0.74	0.21	5037	1.27E-15	0.09	6.288168±0.012689	0.058420±0.000120	0.004748±0.000038	0.142699±0.000519	0.021163±0.000047
630	399.3±154.3	1.05	0.15	1846	3.17E-15	0.17	10.972118±0.022056	0.107378±0.000219	0.008497±0.000072	0.370252±0.001661	0.036844±0.000078
660	653.0±178.5	1.9	0.18	1642	1.03E-15	0.19	0.857294±0.001732	0.009253±0.000020	0.000675±0.000013	0.026638±0.000203	0.002854±0.000011
690	465.2±140.3	1.34	0.11	1328	3.29E-15	0.27	3.882107±0.007782	0.041701±0.000085	0.003095±0.000025	0.202952±0.000496	0.013018±0.000027
720	578.0±120.1	1.94	0.09	1353	4.75E-15	0.36	3.870912±0.007759	0.048391±0.000098	0.003179±0.000032	0.297349±0.000737	0.012929±0.000027
750	375.7±97.2	1.56	0.06	807	3.59E-15	0.47	3.638468±0.007294	0.056428±0.000114	0.003296±0.000037	0.474872±0.000975	0.012254±0.000026
800	459.0±69.8	2.71	0.1	1264	4.81E-15	0.59	2.806080±0.005630	0.061672±0.000124	0.002731±0.000023	0.334598±0.001077	0.009332±0.000021
850	490.7±60.4	3.45	0.1	1043	4.63E-15	0.7	2.123675±0.004343	0.055533±0.000114	0.002241±0.000017	0.304236±0.000634	0.007024±0.000017
900	446.3±61.3	3.38	0.08	1437	3.35E-15	0.78	1.568908±0.003234	0.044232±0.000092	0.001662±0.000018	0.296020±0.000691	0.005213±0.000016
975	418.4±52.1	3.62	0.07	3260	3.13E-15	0.86	1.366550±0.002746	0.044079±0.000089	0.001462±0.000018	0.342732±0.000917	0.004553±0.000014
1050	407.9±58.6	3.58	0.06	1625	2.61E-15	0.94	1.153644±0.002320	0.037764±0.000076	0.001293±0.000021	0.324217±0.000859	0.003855±0.000015
1150	909.6±67.2	5.9	0.06	1030	5.21E-15	1	1.401292±0.002816	0.033833±0.000068	0.001413±0.000018	0.280882±0.000578	0.004541±0.000013

Packet IRR279-RE, Experiment #10Z0120, 0.1926 g Basalt, all errors ±1 sigma
J = 0.000205265±4.11E-07

40Ar* is radiogenic argon, isotopes in volts (6.31e-14 moles/volt), corrected for blank, background, discrimination, and decay
Calculated K2O = 0.32%wt., Calculated CaO = 4.06%wt., Calculated Cl = 0.2ppm

Total Gas Age = 462.7 ± 25.7 ka

Weighted Mean Plateau Age = 444.9 ± 23.7 ka (±1 sigma, including ±J), 93.6% 39Ar released
Weighted Mean Plateau Age = 444.9 ± 23.7 ka (A priori, without ±J)
MSWD = 0.50 (Good fit, MSWD < 1.99)
Steps 12 of 13 (550,600,630,660,690,720,750,800,850,900,975,1050°C)

Isochron Age = 429.318 ± 41.060 ka (±1 sigma, including ±J)
Isochron Age = 429.318 ± 41.060 ka (A Priori Errors, including ±J)
Isochron Age = 429.318 ± 91.465 ka (95% confidence, including ±J)
MSWD = 0.94 (Good fit, MSWD < 2.05)
40Ar/36Ar intercept = 295.8 ± 0.6 (±1 sigma)
40Ar/36Ar intercept = 295.8 ± 0.6 (A Priori)
40Ar/36Ar intercept = 295.8 ± 1.4 (95% confidence)
Steps 12 of 13 (550,600,630,660,690,720,750,800,850,900,975,1050°C)

2911 Basalt

Temp(°C)	Age(ka)	%40Ar*	K/Ca	K/Cl	moles 40Ar*	Σ39Ar	40Ar	39Ar	38Ar	37Ar	36Ar
550	407.4±37.8	3.61	0.14	3388	2.73E-15	0.05	2.755074±0.001031	0.072801±0.000115	0.002708±0.000063	0.277666±0.001149	0.009065±0.000031
600	196.7±20.2	3.48	0.15	25913	2.72E-15	0.14	2.840734±0.000988	0.150124±0.000181	0.003689±0.000037	0.529568±0.002766	0.009427±0.000034
650	137.7±10.6	4.89	0.2	5855	2.67E-15	0.27	1.987228±0.001068	0.210196±0.000172	0.004047±0.000058	0.563695±0.002414	0.006555±0.000025
700	94.6±9.2	4.59	0.27	4309	1.88E-15	0.41	1.487427±0.000811	0.214974±0.000205	0.003867±0.000030	0.417038±0.001943	0.004920±0.000022
750	57.2±10.3	2.89	0.34	4864	9.17E-16	0.52	1.153321±0.000520	0.173727±0.000180	0.003086±0.000063	0.266474±0.001689	0.003865±0.000020
800	62.1±15.7	2.65	0.38	11257	6.39E-16	0.59	0.878577±0.000615	0.111540±0.000133	0.002012±0.000045	0.154700±0.001244	0.002938±0.000020
850	80.2±19.9	2.88	0.35	4310	6.18E-16	0.64	0.781811±0.000583	0.083582±0.000129	0.001634±0.000034	0.123618±0.001445	0.002604±0.000019
925	30.3±17.8	0.97	0.31	5582	3.04E-16	0.71	1.146741±0.000548	0.109107±0.000124	0.002200±0.000045	0.186777±0.001330	0.003896±0.000022
1000	48.8±13.4	1.71	0.3	5536	7.76E-16	0.82	1.653249±0.000836	0.172681±0.000195	0.003374±0.000064	0.302163±0.001340	0.005584±0.000026
1100	52.8±11.9	1.24	0.08	1728	1.37E-15	1	4.024641±0.001381	0.282090±0.000192	0.006859±0.000064	1.863709±0.004228	0.013975±0.000036

Packet IRR282-Ud, Experiment #10z0296, 0.1401 g Basalt, all errors ±1 sigma
J = 0.000164991±3.30E-07

40Ar* is radiogenic argon, isotopes in volts (2.75e-14 moles/volt), corrected for blank, background, discrimination, and decay
Calculated K2O = 0.72%wt., Calculated CaO = 5.00%wt., Calculated Cl = 0.2ppm

Total Gas Age = 100.4 ± 4.4 ka

Weighted Mean Plateau Age = 54.5 ± 5.6 ka (±1 sigma, including ±J), 59.0% 39Ar released
Weighted Mean Plateau Age = 54.5 ± 5.6 ka (A priori, without ±J)
MSWD = 0.81 (Good fit, MSWD < 2.56)
Steps 6 of 10 (750,800,850,925,1000,1100°C)

Isochron Age = 64.410 ± 19.373 ka (±1 sigma, including ±J)
Isochron Age = 64.410 ± 19.373 ka (A Priori Errors, including ±J)
Isochron Age = 64.410 ± 45.817 ka (95% confidence, including ±J)
MSWD = 0.93 (Good fit, MSWD < 2.77)
40Ar/36Ar intercept = 294.5 ± 1.9 (±1 sigma)
40Ar/36Ar intercept = 294.5 ± 1.9 (A Priori)
40Ar/36Ar intercept = 294.5 ± 4.6 (95% confidence)
Steps 6 of 10 (750,800,850,925,1000,1100°C)

O111 Basalt

Temp(°C)	Age(ka)	%40Ar*	K/Ca	K/Cl	moles 40Ar*	Σ39Ar	40Ar	39Ar	38Ar	37Ar	36Ar
550	-11.5±65.8	-0.09	0.35	1374	-9.46E-17	0.03	3.990405±0.008030	0.102159±0.000252	0.004154±0.000052	0.152912±0.000661	0.013559±0.000039
600	-31.1±49.2	-0.3	0.3	1561	-2.37E-16	0.05	2.867097±0.005850	0.094402±0.000193	0.003288±0.000054	0.162385±0.001065	0.009777±0.000031
650	9.5±32.5	0.12	0.19	1731	1.71E-16	0.11	5.079686±0.010275	0.221796±0.000449	0.006605±0.000081	0.615279±0.002030	0.017342±0.000039
700	50.9±23.4	1.01	0.15	2631	9.36E-16	0.17	3.369292±0.006854	0.228110±0.000461	0.005413±0.000062	0.795386±0.003056	0.011510±0.000035
800	47.9±12.5	1.7	0.18	5744	1.72E-15	0.28	3.688288±0.007492	0.445229±0.000896	0.008341±0.000034	1.265934±0.003535	0.012625±0.000034
850	33.5±11.2	1.63	0.26	8787	8.29E-16	0.36	1.850600±0.003878	0.306133±0.000620	0.005225±0.000062	0.617703±0.002982	0.006334±0.000026
900	37.2±10.3	1.77	0.28	8916	1.09E-15	0.46	2.240537±0.004657	0.362074±0.000732	0.006206±0.000049	0.678006±0.002400	0.007639±0.000026
950	25.1±11.4	1.13	0.24	6918	6.40E-16	0.54	2.054100±0.004285	0.315810±0.000639	0.005530±0.000065	0.693856±0.002491	0.007067±0.000026
1000	49.0±13.3	2.01	0.19	5550	1.14E-15	0.62	2.055647±0.004288	0.287256±0.000582	0.005184±0.000050	0.812894±0.001688	0.007045±0.000029
1050	14.7±17.8	0.51	0.16	3960	2.53E-16	0.67	1.819496±0.003816	0.213546±0.000434	0.004120±0.000053	0.720533±0.002869	0.006329±0.000031
1125	6.3±21.3	0.14	0.14	4008	9.74E-17	0.72	2.455236±0.005087	0.191860±0.000391	0.004223±0.000044	0.701492±0.002164	0.008494±0.000028
1225	80.1±23.3	1.41	0.1	1486	2.91E-15	0.84	7.497848±0.015171	0.450600±0.000910	0.011786±0.000062	2.463953±0.005063	0.025708±0.000055
1275	60.8±20.8	1.23	0.04	2430	2.68E-15	0.98	7.945166±0.016066	0.550884±0.001112	0.013148±0.000095	7.759651±0.015906	0.028737±0.000061
1325	198.7±39.6	2.98	0.02	1744	1.06E-15	1	1.298472±0.002774	0.067651±0.000142	0.001877±0.000033	2.224701±0.004574	0.004889±0.000021

Packet IRR279-RH, Experiment #10z0148, 0.2322 g Basalt, all errors ±1 sigma
J = 0.000188355±3.77E-07

40Ar* is radiogenic argon, isotopes in volts (2.75e-14 moles/volt), corrected for blank, background, discrimination, and decay
Calculated K2O = 0.92%wt., Calculated CaO = 11.10%wt., Calculated Cl = 0.3ppm

Total Gas Age = 42.7 ± 4.5 ka

Weighted Mean Plateau Age = 36.5 ± 4.9 ka (±1 sigma, including ±J), 98.3% 39Ar released
Weighted Mean Plateau Age = 36.5 ± 4.5 ka (A priori, without ±J)
MSWD = 1.22 (Good fit, MSWD < 1.94)
Steps 13 of 14 (550,600,650,700,800,850,900,950,1000,1050,1125,1225,1275°C)

Isochron Age = 40.477 ± 10.997 ka (±1 sigma, including ±J)
Isochron Age = 40.477 ± 7.588 ka (A Priori Errors, including ±J)
Isochron Age = 40.477 ± 24.204 ka (95% confidence, including ±J)
MSWD = 2.10 (Poor fit, MSWD > 1.99)
40Ar/36Ar intercept = 295.1 ± 0.9 (±1 sigma)
40Ar/36Ar intercept = 295.1 ± 0.6 (A Priori)
40Ar/36Ar intercept = 295.1 ± 2.1 (95% confidence)
Steps 13 of 14 (550,600,650,700,800,850,900,950,1000,1050,1125,1225,1275°C)

2401 Basalt

Temp(°C)	Age(ka)	%40Ar*	K/Ca	K/Cl	moles 40Ar*	Σ39Ar	40Ar	39Ar	38Ar	37Ar	36Ar
550	287.0±50.6	5.94	0.08	19547	6.75E-16	0.02	0.413722±0.000918	0.041967±0.000086	0.000798±0.000022	0.263524±0.001790	0.001391±0.000014
600	196.3±28.3	4.99	0.09	####	1.07E-15	0.06	0.783210±0.001738	0.097585±0.000196	0.001733±0.000033	0.585436±0.001970	0.002683±0.000017
650	176.0±23.1	5.18	0.09	27775	2.18E-15	0.15	1.530231±0.003231	0.220586±0.000443	0.003799±0.000044	1.224364±0.004240	0.005254±0.000030
700	110.9±19.6	4.1	0.11	5797	1.79E-15	0.27	1.588829±0.003348	0.287496±0.000577	0.004880±0.000030	1.334453±0.004686	0.005531±0.000034
750	94.3±13.4	7.02	0.17	41635	1.45E-15	0.39	0.750957±0.001654	0.273354±0.000574	0.003981±0.000047	0.854285±0.003143	0.002603±0.000024
800	51.5±13.6	4.25	0.23	15435	8.96E-16	0.52	0.774930±0.001702	0.312154±0.000627	0.004560±0.000039	0.726428±0.002911	0.002715±0.000028
850	65.9±9.2	5.04	0.27	7860	1.06E-15	0.64	0.766154±0.001684	0.286642±0.000576	0.004291±0.000035	0.555305±0.002437	0.002618±0.000016
900	56.6±12.3	3.42	0.26	5253	7.25E-16	0.74	0.771886±0.001696	0.227864±0.000458	0.003579±0.000036	0.456467±0.002730	0.002651±0.000017
950	74.0±17.9	3.22	0.26	4132	7.13E-16	0.81	0.805756±0.001785	0.171317±0.000349	0.002867±0.000043	0.349065±0.002298	0.002737±0.000019
1025	73.9±18.9	2.38	0.27	2958	9.52E-16	0.91	1.456290±0.003084	0.229151±0.000464	0.004168±0.000027	0.442705±0.002433	0.004935±0.000024
1100	53.2±20.3	1.47	0.24	3254	6.38E-16	1	1.575763±0.003323	0.213264±0.000433	0.003998±0.000029	0.461011±0.002125	0.005383±0.000023

Packet IRR276-PE, Experiment #10z0074, 0.1936 g Basalt, all errors ±1 sigma
J = 0.000270516635805±4.5103E-07

40Ar* is radiogenic argon, isotopes in volts (2.75e-14 moles/volt), corrected for blank, background, discrimination, and decay
Calculated K2O = 0.48%wt., Calculated CaO = 3.41%wt., Calculated Cl = 8.0e-2ppm

Total Gas Age = 91.7 ± 5.0 ka

Weighted Mean Plateau Age = 62.1 ± 5.6 ka (±1 sigma, including ±J), 61.0% 39Ar released
MSWD = 0.40 (Good fit, MSWD < 2.56)
Steps 6 of 11 (800,850,900,950,1025,1100°C)

Isochron Age = 59.1 ± 13.0 ka (±1 sigma, including ±J)
MSWD = 0.55 (Good fit, MSWD < 2.77)
40Ar/36Ar intercept = 296.0 ± 4.5 (95% confidence)
Steps 6 of 11 (800,850,900,950,1025,1100°C)

2101 Basalt

Temp(°C)	Age(ka)	%40Ar*	K/Ca	K/Cl	moles 40Ar*	Σ39Ar	40Ar	39Ar	38Ar	37Ar	36Ar
550	110.7±46.8	1.26	0.21	1374	3.35E-16	0.03	0.966332±0.001991	0.028380±0.000058	0.001056±0.000018	0.069988±0.002318	0.003249±0.000013
600	46.4±38.7	0.59	0.17	910	2.82E-16	0.08	1.726174±0.003511	0.056923±0.000115	0.002084±0.000037	0.173754±0.003411	0.005856±0.000020
650	92.7±43.8	1.29	0.15	1222	8.25E-16	0.16	2.342055±0.004742	0.084369±0.000171	0.002843±0.000033	0.299190±0.003033	0.007907±0.000040
700	105.9±28.9	1.59	0.14	1804	1.14E-15	0.26	2.627236±0.005324	0.101533±0.000205	0.003182±0.000027	0.383470±0.002824	0.008858±0.000023
750	117.4±30.2	1.72	0.12	943	1.29E-15	0.36	2.756468±0.005582	0.104285±0.000211	0.003530±0.000028	0.444508±0.004482	0.009293±0.000025
800	81.5±29.4	1.16	0.11	2081	8.93E-16	0.46	2.814398±0.005698	0.103047±0.000209	0.003299±0.000039	0.477507±0.003100	0.009548±0.000022
850	104.6±31.6	1.39	0.1	731	9.83E-16	0.55	2.595828±0.005261	0.089116±0.000181	0.003290±0.000038	0.454083±0.005757	0.008790±0.000021
900	80.0±44.7	0.98	0.1	954	6.22E-16	0.62	2.321071±0.004729	0.073167±0.000159	0.002725±0.000049	0.369107±0.004963	0.007882±0.000032
950	170.3±47.5	2.12	0.1	1054	1.06E-15	0.67	1.817198±0.003705	0.058508±0.000119	0.002117±0.000027	0.308663±0.002834	0.006106±0.000029
1000	136.3±45.0	1.52	0.08	428	6.83E-16	0.72	1.644202±0.003509	0.047542±0.000104	0.002114±0.000025	0.303097±0.002486	0.005565±0.000019
1050	232.8±34.7	2.81	0.05	356	4.09E-15	0.88	5.304193±0.010827	0.165863±0.000341	0.007404±0.000074	1.738494±0.008981	0.017934±0.000041
1075	267.3±32.8	3.55	0.02	753	3.27E-15	0.99	3.386394±0.006992	0.117747±0.000244	0.004300±0.000072	2.970709±0.008500	0.011888±0.000029
1100	218.1±102.9	2.1	0.01	1283	2.31E-16	1	0.399684±0.001024	0.010535±0.000036	0.000436±0.000009	0.861558±0.005069	0.001566±0.000012

Packet IRR268-LB, Experiment #09z0165mod, 0.1934 g Basalt, all errors ±1 sigma
J = 0.000142667±2.85E-07

40Ar* is radiogenic argon, isotopes in volts (2.75e-14 moles/volt), corrected for blank, background, discrimination, and decay
Calculated K2O = 0.40%wt., Calculated CaO = 7.89%wt., Calculated Cl = 0.6ppm

Total Gas Age = 142.8 ± 8.6 ka

Weighted Mean Plateau Age = 94.6 ± 12.3 ka (including ±J), 61.7% 39Ar released
MSWD = 0.40 (Good fit, MSWD < 2.29)
Steps 8 of 13 (550,600,650,700,750,800,850,900°C)

Isochron Age = 179.9 ± 116.0 ka (±1 sigma, including ±J)
MSWD = 0.65 (Good fit, MSWD < 2.40)
40Ar/36Ar intercept = 292.0 ± 8.5 (95% confidence)
Steps 8 of 13 (550,600,650,700,750,800,850,900°C)

2909 Andesite

Temp(°C)	Age(ka)	%40Ar*	K/Ca	K/Cl	moles 40Ar*	Σ39Ar	40Ar	39Ar	38Ar	37Ar	36Ar
550	152.41±6.66	31.17	1.37	25699	3.14E-15	0.03	0.367120±0.001129	0.203137±0.000412	0.002790±0.000025	0.077950±0.001350	0.000877±0.000016
600	145.81±2.92	27.54	1.4	25228	7.38E-15	0.1	0.976051±0.002133	0.498728±0.001001	0.006905±0.000043	0.186899±0.003610	0.002446±0.000015
650	146.05±2.18	30.8	1.56	24341	1.30E-14	0.22	1.540668±0.003260	0.878998±0.001764	0.012061±0.000043	0.295944±0.003198	0.003691±0.000017
700	138.98±1.84	32.41	1.82	18320	1.67E-14	0.38	1.876869±0.003932	1.184238±0.002377	0.016211±0.000076	0.342206±0.003643	0.004389±0.000018
750	139.77±1.66	34.19	1.71	8652	1.93E-14	0.57	2.057537±0.004293	1.361949±0.002733	0.018934±0.000083	0.417081±0.003420	0.004699±0.000017
800	139.06±2.48	32.48	1.49	6223	1.77E-14	0.74	1.983906±0.004154	1.253931±0.002517	0.017735±0.000064	0.441891±0.003603	0.004657±0.000032
850	132.27±3.98	24.94	1.27	5085	1.09E-14	0.85	1.591497±0.003370	0.811888±0.001630	0.011817±0.000061	0.336400±0.003259	0.004137±0.000036
900	138.89±9.44	18.83	1.06	3215	6.03E-15	0.91	1.166893±0.002787	0.428000±0.000860	0.006641±0.000048	0.211515±0.002016	0.003265±0.000049
975	144.29±6.32	15.61	0.89	2195	6.11E-15	0.97	1.424687±0.003037	0.417022±0.000838	0.006907±0.000049	0.246432±0.002912	0.004138±0.000029
1075	125.33±12.29	5.13	0.18	974	2.61E-15	0.99	1.850132±0.003886	0.205419±0.000414	0.004651±0.000035	0.598050±0.002908	0.006108±0.000023
1150	114.45±37.07	2.29	0.06	717	4.68E-16	1	0.742996±0.001678	0.040489±0.000083	0.001226±0.000025	0.378209±0.003782	0.002563±0.000016

Packet IRR268-LA, Experiment #09z0151mod, 0.2049 g Andesite, all errors ±1 sigma
J = 0.000149948±3.00E-07

40Ar* is radiogenic argon, isotopes in volts (2.75e-14 moles/volt), corrected for blank, background, discrimination, and decay
Calculated K2O = 2.51%wt., Calculated CaO = 2.84%wt., Calculated Cl = 0.5ppm

Total Gas Age = 139.9 ± 1.1 ka

Weighted Mean Plateau Age = 138.9 ± 1.1 ka (including ±J), 78.3% 39Ar released
MSWD = 0.78 (Good fit, MSWD < 2.29)
Steps 8 of 11 (700,750,800,850,900,975,1075,1150°C)

Isochron Age = 140.6 ± 1.6 ka (±1 sigma, including ±J)
MSWD = 0.82 (Good fit, MSWD < 2.40)
40Ar/36Ar intercept = 294.0 ± 2.4 (95% confidence)
Steps 8 of 11 (700,750,800,850,900,975,1075,1150°C)

APPENDIX B

Analytical techniques

1. Major and Trace elements analysed by X-Ray Fluorescence

~200 grams of each sample for XRF analysis was crushed with a steel jaw crusher and and then milled to fine powdered using agate ball mill. Some larger samples were first cut up using a circular saw and in this case the fragments were cleaned in DI water in an ultrasonic path prior to crushing and milling.

Glass discs and powdered pellets for major and trace element analyses were prepared at the University of Leicester (with the assistance of Nick Marsh). For major and minor elements 0.1 g of powder was ignited for 1 hr at 1035°C and then re-weighed to determine loss on ignition (LOI). Ignited sample was mixed with 3g of lithium tetraborate flux and fused into a glass bead and then analysed using a PANalytical Axios Advanced XRF spectrometer. LOI provides a normal lower limit of detection (LLD) of 0.01 wt % with precision better than 0.5 wt % at 100 times the LLD. XRF calibration curves were established using 21 international and in-house reference standards.

2. Trace elements measured by solution ICP-MS

A smaller suite of samples was analysed for trace element concentrations by Inductively Coupled Palsma – Mass Spectrometry (ICP-MS) at the Geoanalytical Lab at Washington State University, USA. Samples were digested in acid and the solutions analysed using the procedure of Knaack et al., 1994.

The precision of the ICP-MS analysis can be estimated from analysis of rock standards and repeat analyses on the sample. Table B1 list analyses of USGS rock standards and repeat analyses of sample SA05.

Table B1 USGS rock standards and repeat analyses of SA05 by ICP-MS

	BCR-1 Basalt		**BHVO-1 Basalt**		**SA05 (1)**	**SA05 (2)**
	Accepted value	WSU	Accepted value	WSU		
Ba	681	683	139	130	240	239
La	24.9	25.9	15.8	15.6	25.64	25.41
Ce	53.7	54.3	39	38.0	56.77	56.41
Pr	6.8	7.06	5.7	5.44	7.43	7.30
Nd	28.8	29.0	25	24.6	31.84	31.43
Sm	6.59	6.73	6.2	6.11	7.64	7.67
Eu	1.95	1.96	2.06	2.06	2.40	2.43
Gd	6.68	6.56	6.4	6.19	8.25	8.24
Tb	1.05	1.05	0.96	0.93	1.39	1.38
Dy	6.34	6.43	5.2	5.33	8.58	8.46
Ho	1.26	1.32	0.99	1.00	1.76	1.74
Er	3.63	3.55	2.4	2.55	4.72	4.59
Tm	0.56	0.52	0.33	0.33	0.67	0.67
Yb	3.38	3.26	2.02	1.90	4.10	4.01
Lu	0.51	0.49	0.291	0.27	0.63	0.62
Rb	47.2	48.4	11	9.7	20.4	20.0
Y	38	35.6	28	26.4	43.56	42.77
Nb	14	11.3	19	17.2	31.20	30.65
Cs	0.96	0.96	0.13	0.10	0.22	0.22
Hf	4.95	4.98	4.38	4.44	5.60	5.50
Ta	0.81	0.79	1.23	1.17	2.10	2.07
Th	5.98	5.86	1.08	1.27	2.45	2.43
U	1.75	1.65	0.42	0.43	0.67	0.66
Sr	330	321	403	385	292	290
Pb	13.6	13.4	2.6	2.03	2.55	2.49
Sc	32.6	32.3	31.8	31.9	38.2	35.9
Zr	190	181	179	167	218	216

2. Sr, Nd and Pb isotopic analyses

Radiogenic isotopes were analysed at Woods Hole Oceanographic Institution (WHOI), USA. All the sample preparation was also done at WHOI in geochemical clean labs. Samples were prepared and analysed using the same procedures as Waters et al (2011).

Preparation

For Sr and Nd analyses ~500 mg of powdered sample was covered with a DI water acid mix (dilute HF/perchloric) and left on a hot plate at ~70°C. Once dried out, sample was mixed and dried out twice with 6.2 N HCl. 2.5 N HCl was then added and sampled was left to dissolve. Once dissolved sample was centrifuged and passed through resin columns for chemical separation.

For Pb isotopic analysis 500 mg of powder was mixed with DI water and a 3:1 solution of HF and HNO3 and left sealed on a hotplate for several hours. Sample was then dried out and the acid re-added and before drying out again. Samples were then mixed with 6.2 N HCl and dried out three times. This was then repeated with HBr.

Analysis

All the isotopic analyses were made at whoi using a ThermoFinnigan Neptune MC-ICP-MS. The Sr and Nd analyses have internal precision of 5-10 ppm. External precision after adjusting to standards NBS SRM 987 ($^{86}Sr/^{87}Sr$ = 0.71024) and La Jolla Nd Standard ($^{144}Nd/^{143}Nd$ = 0.511847) is estimated to be 15-30 ppm (2-sigma). Measurements of $^{208}Pb/^{204}Pb$, $^{207}Pb/^{204}Pb$, and $^{206}Pb/^{204}Pb$ have estimated internal precisions of 15-30 ppm and external precisions of 150-200 ppm (2-sigma). SRM 997 Tl was used as an internal standard, and measurements were then normalized to NBS 981 using the values of Todt et al. (1996). Further details of the analytical procedures can be found in Hart et al. (2004) and Hart and Blusztajn (2006). Procedural blanks were co-prepared and analysed for each isotopic measurement.